Petrogenetic Processes and their Timescales beneath Santorini, Aegean Volcanic Arc, Greece

Thesis

UNRESTRICTED

PETROGENETIC PROCESSES AND THEIR TIMESCALES BENEATH SANTORINI, AEGEAN VOLCANIC ARC, GREECE

A thesis presented for the degree of

Doctor of Philosophy

by

GEORG FLORIAN ZELLMER

B. A. (Hons.) *Cantab.* 1995

Department of Earth Sciences

The Open University

Milton Keynes, U. K.

DATE OF SUBMISSION: 17 DECEMBER 1998

DATE OF AWARD: 4 MARCH 1999

December 1998

"In a way you've got a quite well
constrained system there,
unfortunately."

Dr. R. M. M. George

Geological map of Santorini

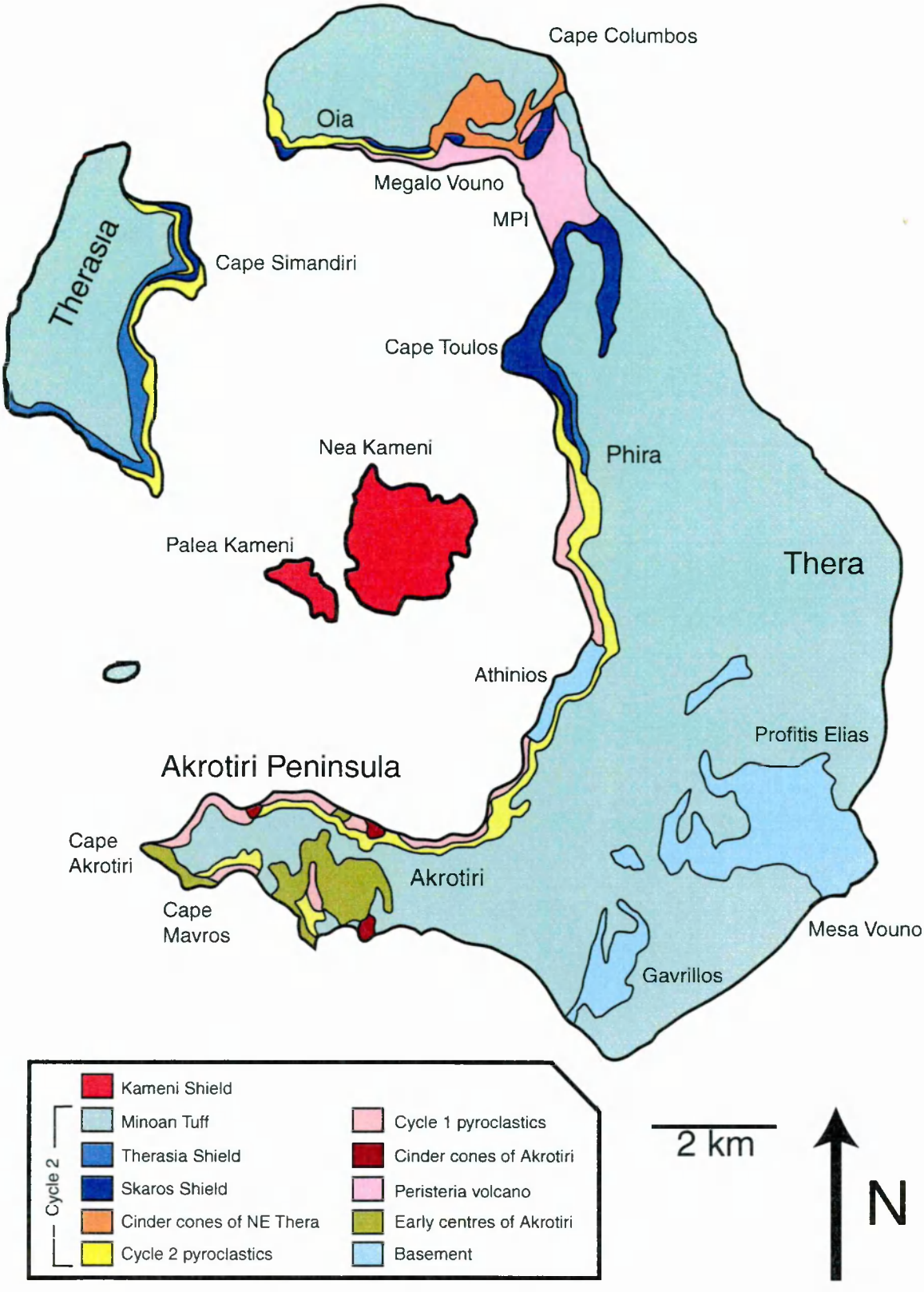

Abstract

An understanding of the timescales of petrogenetic processes at destructive plate margins is critical to assess models of fluid and magma transport through the mantle wedge and magma storage within the overriding crust.

The Aegean Volcanic Arc is formed by the northward subduction of the African Plate under the continental Aegean microplate. Shallow (<40 km) teleseismic activity in the South Aegean is concentrated at transform segments in the trench, and epicentres of intermediate depth (>65 km) teleseismic and microseismic activity in the subducting slab form linear trends from the transform segments in the trench towards the volcanic centres of Methana, Milos, Santorini and Nisyros. Epicentre trends are approximately collinear with the direction of subduction at the trench. This pattern implies fracturing of the slab at the trench due to the geometry of the plate margin, and subsequent slab deformation along zones of weakness. The coincidence of the seismicity with volcanic activity along the arc suggests that pore fluids are collected within fault zones and are released by hydraulic fracturing to trigger localised melting within the wedge.

Santorini, in the central part of the arc, has been volcanically active since the middle Pleistocene. The two youngest volcanic sequences are the second eruptive cycle (SEC; ~172 ka-3.6 ka) and the Kameni island lavas (46 AD to 1950). For the SEC, major and trace element and Sr and Nd isotope data ($^{87}Sr/^{86}Sr = 0.7035$-0.7052, correlated with $^{143}Nd/^{144}Nd = 0.51285$-$0.51267$) indicate that differentiation of the less evolved samples is dominated by fractional crystallisation from a primary magma with low H_2O content (<0.7 wt%), while open system processes become more important at >60 wt% SiO_2. The Kameni dacites have restricted major, trace and Sr and Nd isotope variations ($SiO_2 = 65$-68 wt%, $^{87}Sr/^{86}Sr \approx 0.70475$, $^{143}Nd/^{144}Nd \approx 0.51274$). They contain mafic enclaves with distinctly different incompatible element ratios.

Compared to N-MORB, samples are enriched in LREE, LILE, U and Th. The least evolved sample can be modelled using three components: batch melting (15-20% without residual garnet) of wedge peridotite, enriched by partial (1-3%) melts of subducted sediments that make up 0.2-0.4% of the source, and slab fluids that contribute 35-85% of the fluid mobile element budget. Samples from the SEC are in ^{230}Th-^{238}U radioactive equilibrium, suggesting that >350 ka have passed since U-Th differentiation by slab fluids. The Kameni dacites and some of their enclaves, however, have $(^{230}Th/^{232}Th) = 0.91$-$0.99$, correlated with $(^{238}U/^{232}Th) = 0.91$-$1.04$, dating the time since U-Th differentiation at 147 (+27/-21) ka (1σ). On the basis of comparison with the global dataset for fluid transfer times at arcs built on crust of variable thickness, most of these ages reflect long crustal magma storage times. U-Th WR-mineral isochrons from samples of the SEC and a Kameni dacite give ages of 85 (+22/-19) ka (1σ) and 18 (+19/-16) ka (1σ) respectively, indistinguishable from their eruption ages, suggesting that they date crystallization prior to eruption. Most Kameni dacites have $(^{226}Ra/^{230}Th) < 1$. This is not due to fluid mobility of Ra, but can be modelled by up to 40% plagioclase fractionation <1 ka prior to their eruption.

Using ion microprobe data of trace element traverses across plagioclase crystals from the Kameni dacites and Soufriere, St. Vincent, a model is developed that allows maximum plagioclase crystal residence times to be estimated from incomplete diffusion of Sr profiles. Three out of eight plagioclase phenocrysts have Sr concentration profiles that are not in diffusive equilibrium. For these, the diffusion model is employed to calculate maximum crystal residence times, ranging from 100 to 450 years. This emphasises the importance of distinguishing between crystal residence times and crustal magma storage times, that for Soufriere are thought to be in excess of 40 ka on basis of U-Th mineral isochron data.

Acknowledgements

First and foremost I would like to thank my supervisors Chris Hawkesworth and Simon Turner for their support, helpful comments and ideas, and especially their continued encouragement throughout the last three years. Thought provoking discussions with Simon Turner, Chris Hawkesworth, Steve Blake and Derek Vance have led to submission of parts of Chapters 2 and 5 of this thesis as manuscripts to Geology and CMP. Simon Turner and Chris Hawkesworth are co-authors of the submitted part of Chapter 2, while all of the above are co-authors of the submitted part of Chapter 5. Acknowledged is also the collection of many of the rock samples of Santorini by Simon Turner, Anthony Cohen, Peter van Calsteren and Rhiannon George in Summer 1995.

Scientific discussions with many members and visitors of the department have fostered this research. Special thanks go to Anthony Cohen for his advice on laboratory techniques, and Peter van Calsteren for explaining bits and pieces of the mass spectrometers and keeping it up and running for most of the time. Also, many thanks to Mabs Gilmour for continuous advice and help in the chemistry labs, and to Nick Rogers, Dave Peate, Carsten Israelson, Thomas Kokfelt, Ian Parkinson, Mike Widdowson, Nigel Harris and Simon Kelley for many helpful and interesting discussions. Thanks to Mark Davies for his excellent map of Santorini, Julie Hardiman for her helpful advice on how to get to Nisyros and where to stay and Rhiannon George for being a great field assistant. Gratefully acknowledged is also the help of Nick Rogers (INAA), Andy Tindle (EMP), Richard Hinton (IMP), John Watson and Peter Webb (rock powdering and XRF), Brian Ellis and Kay Green (rock cutting and sectioning), John Taylor and Andy Lloyd (Cartography), Janet Dryden, Anita Chhabra, John Holbrook for being Mr. H., and Liz Lomas.

Many thanks go to all my great office mates, especially to Louise Thomas for being really helpful whenever possible, to Adam Maciejewski for making tea, and to Christophe Prince, Rob Hughes, Elric Whittington, Mark Davies, Cheryl Williams, Linda Kirstein and Kirsta Galloway. To Cheryl Williams for many good times and a trip to the Carribean. To the Mad Kows Ultimate Frisbee team and Eva Nyström for lots of fun. To Marianne Kendall, John, Andrea, Martin, Bonnie, Janie and Normski, and also to Helen Williams and Jo Rhodes, for being there when times went bad. To Lin and Richard Bulloch, Jane and Mervin Bradford, and Andrew Bell. To my "mates", including former housemates Liz, Matt and Tony, Tubbs and Gavin, and Paul, Steve and Julie. And to Bruce Charlier and Mark Cooper, Dàvid Szüts, Balàzs Szendröi, Harm Pralle, Johannes Röhl, Andreas Kühl, Birgit Grunewald, Daniele Carbone and Jan Ehlers for being good friends and keeping in touch...

...and to Allister, Charles, Pete, Aussi Bruce, Nicki, Nicky, Steve, Sarah, Glyn, Hazel, Yvonne, Simon, Jessica, Vince, Rob, Ben and all the others who I have not forgotten.

Last not least I am most grateful to my parents for their continued support. Without them I would not have written this thesis.

Table of Contents

Chapter 3

Chapter 4

Appendix C

Appendix D

Appendix E

List of Figures

Chapter 1

Chapter 2

Chapter 3

Chapter 4

Chapter 5

Appendix A

Appendix C

List of Tables

Chapter 3

Chapter 5

Appendix A

CHAPTER 1

Introduction

1.1 Significance of destructive plate margins

Modern plate tectonics is the principle mechanism for the Earth to lose its heat, and it requires that the growth of oceanic plates at mid-ocean ridges is balanced by the subduction of oceanic plates into the mantle. Volcanic arcs are the surface expression of plate subduction, and the magmatic flux at destructive plate margins may be the most important mechanism for additions to the continental crust. Furthermore, subduction of oceanic crust and sediments back into the mantle contributes to upper mantle heterogeneity sampled at ocean-islands. Thus, destructive plate margins can be considered a key to the geochemical evolution of the continental crust and the upper mantle, and to gain insights into this evolution it is necessary to investigate the mechanisms and rates of element transfer at subduction zones. In addition, explosive volcanic activity at island arcs and continental margins is the most hazardous on Earth, and cataclysmic eruptions may wipe out entire civilisations as in the case of the Minoan eruption at Santorini 3600 years ago.

1.2 Temperature constraints on the magma source

A fundamental problem in destructive plate margin petrogenesis is the production of significant amounts of magma in an environment where cold oceanic lithosphere is being subducted. Green and Ringwood (1968) first demonstrated experimentally that partial melting of subducted oceanic crust could generate magmas of andesitic composition, the dominant magma type at many volcanic arcs. Slab melting by advection of heat from the mantle wedge was thought to produce arc magmas directly (e. g. Marsh, 1979; Brophy

and Marsh, 1986). Temperatures greater than ~700°C are required to melt the subducting hydrous gabbroic crust (Peacock et al., 1994). Theoretical modelling of the thermal structure of subducting slabs (Davies and Stevenson, 1992; Davies and Rowland, 1997; Kincaid and Sacks, 1997) and seismicity in the uppermost parts of the subducting slab (Fukao et al., 1983), however, suggest that the majority of slabs are too cold to melt. Recent geochemical studies have again invoked an important role for slab melting in particular areas (Defant and Drummond, 1990), e. g. beneath the southern Andes (Stern and Kilian, 1996; Sigmarsson et al., 1998) and the Aleutians (Kay, 1978; Yogodzinski et al., 1995). However, this requires special circumstances such as slow subduction of young, hot lithosphere (Peacock, 1993) or high potential temperatures within the mantle as, for example, in the Archaean (Kincaid and Sacks, 1997).

Thus, despite the fact that subduction of cold material lowers the wedge temperature, it was concluded that melt generation beneath volcanic arcs occurred within the mantle, by partial melting of wedge peridotite (e. g. Gill, 1981). The mechanisms invoked to account for melt generation in a relatively cold wedge are mantle metasomatism by the addition of fluids that lower the mantle solidus (Wyllie, 1984; Tatsumi, 1986), and decompression melting due to mantle upwelling and diapirism (e. g. Plank and Langmuir, 1988). Fluids are thought to originate from dehydration reactions within the subducting slab (Tatsumi, 1989).

In addition, there may be a contribution from subducted sediments to arc magmas (e. g. White and Dupre, 1986). Melting experiments on pelagic clays indicate that subducted sediments may melt at temperatures of ~650°C (Nichols et al., 1994), and theoretical temperature modelling indicates that the slab surface temperature may reach 650°C at ~100 km depth. However, the depth of sediment melting may be shallower if shear heating is important (Peacock, 1993).

1.3 Geochemical constraints on the magma source

1.3.1 Geochemical characteristics of arc magmas

The geochemistry of arc magmas may provide important constraints on the source components of destructive plate margin magmatism. In terms of trace element geochemistry, general enrichments of large ion lithophile elements (LILE) relative to high field strength elements (HFSE), and of uranium, thorium, and light rare earth elements (LREE) relative to heavy rare earth elements (HREE) when compared to mid-ocean ridge basalts (MORB) are characteristic of destructive plate margin rocks (Gill, 1981; Pearce, 1982; Pearce and Parkinson, 1993; Davidson, 1996). While elevated LREE/HREE ratios are also a feature of ocean-island basalts (OIB), basalts from destructive plate margin magmas also have distinctly low Nb and Ta abundances, with Ba/Ta ratios generally greater than 450 (Gill, 1981). Furthermore, they are generally enriched in Th and Pb, and depleted in Ti relative to other HFSE (e. g. Pearce, 1982). As temperature constraints suggest that melting occurs within the mantle wedge, it is reasonable to assume that at oceanic arcs, destructive plate margin magmas are generated from a MORB-source, although melt extraction may progressively deplete the mantle wedge in incompatible elements (e. g. Ewart and Hawkesworth, 1987). Hence, the distinctive geochemical signatures of these magmas are thought to be derived from the subducted slab. At continental margins, the situation can be complicated by previous subduction events that may lead to enrichment of the mantle wedge in slab derived elements (Reagan et al., 1994).

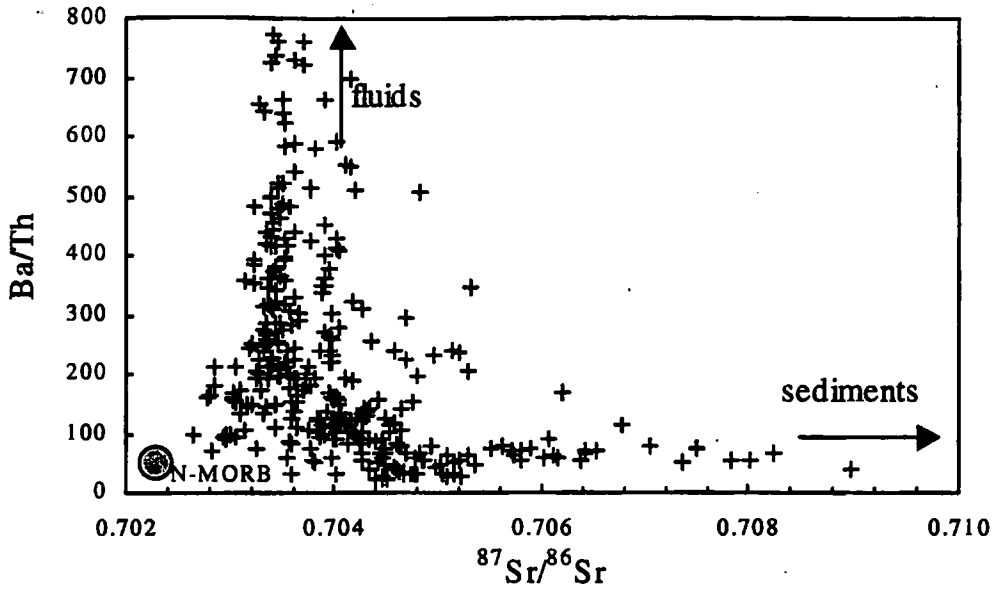

Figure 1-1: Ba/Th versus $^{87}Sr/^{86}Sr$ for the global arc dataset. High Ba/Th ratios are found at intraoceanic arcs with little sediment input, e. g. the Marianas, Tonga Kermadec and Vanuatu. High $^{87}Sr/^{86}Sr$ ratios in mafic lavas from arcs close to or built on continental crust, e. g. Indonesia, the Aeolian islands and the Philippines, are interpreted to reflect subducted sediments being introduced into the magma source region.

Figure 1-1 is a diagram of Ba/Th versus $^{87}Sr/^{86}Sr$ for the global arc dataset. As Ba is much more fluid mobile than Th (Brenan et al., 1995), high Ba/Th ratios can be considered to originate from slab derived fluids. In contrast, average subducted sediments have lower Ba/Th ratios of ~110, and elevated $^{87}Sr/^{86}Sr$ ratios of 0.71736 (Plank and Langmuir, 1998). In addition, N-MORB has low Ba/Th of ~50 and low Sr isotope ratios of ~0.7023. Thus, the data may be explained using a three-component model that involves mixing between slab derived fluids, sediments and mantle melts. Further support for subducted sediments, rather than for example crustal contamination, as a source for the high $^{87}Sr/^{86}Sr$ component is provided by negative Ce anomalies observed in some arc magmas, for example in the Mariana oceanic arc (Figure 1-2). Seawater has a negative Ce anomaly that is inherited by pelagic clays, and negative Ce anomalies in the Mariana arc magmas, correlated with $^{143}Nd/^{144}Nd$ (Woodhead, 1989;

Elliott et al., 1997), hence provide evidence for contributions for subducted sediments in the magma source region.

1.3.2 The fluid component

As discussed in Section 1.2, fluids are necessary to lower the mantle solidus and to induce melting. Relative to the HFSE, the LILE are mobile in aqueous fluids (Loughnan, 1969; Brenan et al., 1995). For this reason, fluids from dehydration reactions in the subducting slab are considered to enrich the mantle wedge with LILE (Pearce, 1982; Tatsumi, 1986; Tatsumi, 1989). Direct evidence for slab-derived fluids in the mantle wedge is provided by mantle xenoliths. Elevated oxygen isotope ratios in glass inclusions within crystals from these xenoliths suggest that subducted crustal materials are part of the source (Eiler et al., 1998). Elsewhere, elevated B/Be ratios in arc lavas indicate that the mantle was metasomatised by slab-derived fluids (Morris et al., 1990; Leeman et al., 1994; Ryan et al., 1995). In addition to the LILE, U^{6+} is fluid mobile (Bailey and Ragnarsdottir, 1994; Brenan et al., 1995; Shock et al., 1997), and limited fluid mobility of the LREE has also been suggested recently (You et al., 1996).

Low Sr and Pb isotopic compositions of samples with strong fluid signatures, such as high U/Th and Ba/Th ratios (e. g. Turner et al., 1996; Turner and Hawkesworth, 1997), indicate that the geochemistry of slab fluids may dominantly originate from the subducted oceanic crust rather than from subducted sediments, and that the fluid and sediment component are decoupled (cf. Figure 1-1).

1.3.3 The sediment component

Strong depletion of Nb and Ta relative to Ce, and a general enrichment in Th and Pb, and depletion in Ti relative to other HFSE, characteristic of arc lavas, is also a pattern displayed by subducting sediments (Ben Othman et al., 1989; Plank and Langmuir, 1998), albeit at much higher concentrations than those observed in the most depleted

destructive plate margin magmas. This suggests that subducted sediments may be entrained into the magma source region. Elevated Pb isotope ratios in many primitive arc magmas relative to MORB supports a sedimentary origin for some of the Pb (e. g. Armstrong, 1971; Hawkesworth, 1982; Barreiro, 1983). Experimental studies indicate that LREE and Th are not very fluid mobile (Loughnan, 1969; Bailey and Ragnarsdottir, 1994; Brenan et al., 1995). Again, enrichments of LREE in arc magmas are attributed to contributions from subducted sediments to the mantle wedge (Pearce, 1982; Turner et al., 1996; Hawkesworth et al., 1997a). In addition, although fluids may be responsible for some enrichment in fluid mobile LILE, in some arcs the sedimentary component may in fact dominate the LILE budget (Plank and Langmuir, 1993).

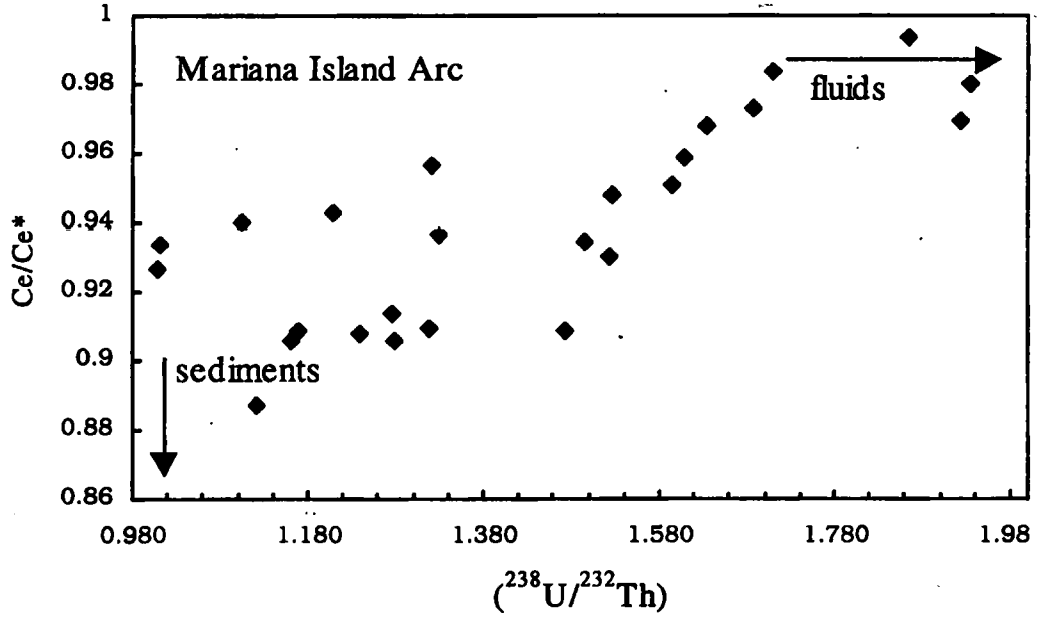

Figure 1-2: Ce/Ce* versus ($^{238}U/^{232}Th$) for the Mariana Island Arc. Ce/Ce* was calculated from $Ce_N/Ce^*_N = Ce_N/((La_N^2 \times Nd_N)^{1/3})$, cf. Appendix B. Low Ce/Ce* are interpreted to result from contributions of the sediment component, while high ($^{238}U/^{232}Th$) activity ratios are indicative of contributions from the slab fluid component.

Further evidence for contributions from a sedimentary component comes from trace amounts of the cosmogenic radionuclide ^{10}Be in many arc magmas (Tera et al., 1986;

Monaghan et al., 1988; Morris et al., 1990). ^{10}Be is abundant in young subducting sediments but not found within old crust or the mantle as it decays to ^{10}B with a half-life of 1.51 Ma (Hofmann et al., 1987). Its occurrence in arc magmas provides inescapable evidence that sediments are recycled (Monaghan et al., 1988; Morris et al., 1990).

Finally, contributions from subducted sediments are evident in negative Ce anomalies in some arc magmas, e. g. the Marianas. Figure 1-2 shows that samples with the most pronounced anomaly have generally low U/Th ratios, whilst samples with the $Ce/Ce^{*}\approx1$ display the highest U excesses. As U is fluid mobile (Brenan et al., 1995; Shock et al., 1997), this again demonstrates decoupling of the sedimentary component with low Ce/Ce^{*}, $(^{238}U/^{232}Th)\approx1$, from the fluid component, with high $(^{238}U/^{232}Th)$, $Ce/Ce^{*}\approx1$.

Given the evidence for contributions of subducted sediments in arc magmas, it is important to understand the mechanism by which sediments are added to the source region. While bulk addition by physically scraping sediments off the descending slab seems conceivable, Elliott et al. (1997) favour sediment addition as partial melts that infiltrate and vein the wedge. Their arguments are based on trace element and Th and Nd isotope constraints and will be discussed in Section 1.5.2. Further evidence for sediment melting comes from low Ta/Nd ratios and Pb isotopic constraints, and high Th/Ce ratios (Hawkesworth et al., 1997a; Turner et al., 1997a).

1.4 Mechanisms of fluid transfer and melt generation

1.4.1 Dehydration reactions and conditions of fluid release

Much of the pore fluids with the subducted sediments are probably expelled at relatively shallow levels of subduction zones and escape towards the surface (cf. Langseth and Moore, 1990; Moore and Vrolijk, 1992). A comparatively small part is subducted in the form of hydrous minerals. Subducted metasediments contain chlorite and biotite, and

metabasalts and gabbros are characterised by amphibole, epidote and chlorite (Anderson et al., 1976). In addition, subducted ultramafic material contains some serpentine (Nicholls and Ringwood, 1973). With increasing pressure and temperature, dehydration reactions result in fluid release into the mantle wedge. Breakdown of hydrous minerals predominantly occurs at pressures less than ~2.5 GPa, when hornblende breaks down (e. g. Delany and Helgeson, 1978), and at temperatures between 600 and 700°C, when serpentine, chlorite, talc and Fe-rich biotite decompose (Kitahara et al., 1966; Delany and Helgeson, 1978; Banno et al., 1986). A good summary of the dehydration reaction is given by Tatsumi (1989). Most of the subducted slab fluids will be released at depths shallower than ~80 km from parts of the slab underlying the fore-arc region, where mantle wedge temperatures are below the hydrous peridotite solidus (Kincaid and Sacks, 1997). A mechanism is required for slab fluid transfer into hotter regions of the mantle.

1.4.2 Fluid transfer through the wedge

Slab fluids released into the mantle wedge may be absorbed into amphibole and carried to greater depths and temperatures by subduction induced mantle wedge flow (e. g. McKenzie, 1969; Andrews and Sleep, 1974; Toksoz and Hsui, 1978). At pressures greater than ~3 GPa amphibole breakdown may then result in partial melting beneath the volcanic front, close to the slab (Tatsumi, 1989). Alternatively, Davies and Bickle (1991) and Davies and Stevenson (1992) proposed a model whereby slab-parallel movement of amphibole by induced mantle flow, coupled with vertical fluid movement upwards through the wedge, result in a net horizontal motion away from the slab into hotter regions of the mantle. More recent work by Davies and Rowland (1997) suggests that faults within the subducting slab will locally collect pore fluids before they fail. If sufficient water is available, this may cause hydraulic fractures that propagate (perpendicular to the least compressive stress) into the mantle wedge. Large hydraulic

fractures may propagate tens of kilometres into the hottest part of the mantle, where they may trigger partial melting at temperatures higher than the wet peridotite solidus (~1000°C; Green, 1973; Wyllie, 1979; Takahashi, 1990). An understanding of fluid transfer times through the mantle wedge (Section 1.5) is essential to distinguish between these possibilities. Clearly, long transfer times would favour slow fluid migration into the melting region as suggested by Davies and Stevenson (1992), while short transfer times would favour rapid transfer by hydraulic fracturing.

While it is widely accepted that the addition of slab fluids into the mantle wedge is required in order to facilitate partial melting (cf. Sections 1.2 and 1.3.2), based on major element criteria it has also been suggested that decompression melting due to mantle diapirism may play an important role (Plank and Langmuir, 1988). Hydrous peridotite is less dense than anhydrous peridotite and consequently it will tend to rise. Relatively low HREE abundances relative to MORB can be modelled by relatively high degrees of mantle melting (15-30%) beneath most arcs, with the highest degrees of melting beneath arcs built on thin lithosphere (Pearce and Parkinson, 1993). If hydrous fluxing cannot account for more than ~8% melting (Davies and Bickle, 1991), then this indicates that the degree of mantle melting may be dominated by decompression. However, if slab fluids are transferred into the melting region by hydraulic fracturing, they may induce massive melting directly and quickly (Davies and Rowland, 1997). Fluid and magma transfer times through the mantle wedge are again critical in order to distinguish between these melt generation models. If magma transfer times through the mantle wedge are short, magma may rise upwards via channelled flow through long wide fissures in the wedge. Alternatively, longer magma transfer times may favour decompression melting and magma transport in melt pockets within mantle diapirs.

1.5 Timescales of fluid and sediment transfer at volcanic arcs

1.5.1 Transfer of the slab fluid component

With the discovery of ^{238}U-^{230}Th radioactive disequilibria in recent volcanics it became clear that the U decay system could be used to date processes that lead to the fractionation of U from Th (Allègre and Condomines, 1982; Condomines et al., 1988). For a recent review of the U-series dating techniques, see Dickin (1997), and the summary in Appendix B. Many subduction-related volcanic rocks show variable ^{238}U excesses over ^{230}Th (Gill and Williams, 1990; McDermott and Hawkesworth, 1991), and this is generally attributed to wedge metasomatism by U-rich slab fluids (e. g. (Gill and Williams, 1990; Hawkesworth et al., 1997a).

Early alpha-spectrometry work on Andean arc magmas by Sigmarsson et al. (1990) suggested that the time interval between the fluid induced U-Th fractionation in the mantle and eruption of the magmas is ≤20 ka. The precision of U-Th data was significantly improved using thermal ionisation mass spectrometry (TIMS) (Chen et al., 1986; Edwards et al., 1986/87; Goldstein et al., 1989; van Calsteren and Schwieters, 1995), and several recent studies have successfully used along-arc variations in U-series disequilibria to elucidate rates of element transport and melt generation beneath island arcs. A whole rock (WR) pseudo-isochron of ~30 ka was obtained for the Marianas (Elliott et al., 1997), and reference lines through WR samples with low ($^{230}Th/^{232}Th$) activity ratios reveal ages of 30-50 ka for the Tonga-Kermadec island arc and the Aleutians, and ≥150 ka for Kamchatka (Turner et al., 1997b; Turner et al., 1998). Furthermore, modelling of ^{230}Th ingrowth due to unsupported initial U excesses indicate that in the Lesser Antilles, ~90 ka have elapsed since U-Th differentiation in the mantle wedge (Turner et al., 1996; Heath et al., 1998a).

If these ages indeed date slab fluid addition to the mantle, they may be interpreted as a combination of slab fluid and magma transfer time through the mantle wedge, and the magma storage time within the overriding crust. Thus, it is critical to determine whether magma storage times are significant beneath arc volcanoes and must therefore be subtracted from the total transit times to isolate the wedge transfer time. In general, variations in isotope disequilibria within individual volcanoes remain to be investigated to constrain the timescales of magmatic differentiation within the crust (Section 1.6), and to justify the feasibility of along arc studies that use a limited number of samples from each volcano.

1.5.2 Transfer of the sedimentary component

There are a number of constraints on the timescales of sediment transfer from the subducting slab into the melting region. These are based on Be, Th and Pb isotopes and are discussed below.

(a) The presence of ^{10}Be with a half-life of 1.51 Ma appears to provide an upper estimate of sediment transfer times of less than a few million years. However, $^{10}Be/^{9}Be$ ratios are often higher in arc magmas with a strong fluid signal, e. g. high Ba/Th and U/Th ratios, than in those with a strong sediment signal, e. g. negative Ce anomalies and high Th/Nb and $^{87}Sr/^{86}Sr$ ratios (Sigmarsson et al., 1990; Elliott et al., 1997; Hawkesworth et al., 1997b; Turner et al., 1998), and You et al. (1994) found that Be may in fact be fluid mobile. Thus slab fluids may scavenge some ^{10}Be from the sediments, potentially precluding its use in determining transfer times of the bulk sediment, or sediment melt component.

(b) Due to the high Th content and low ($^{230}Th/^{232}Th$) activity ratios of subducted sediments relative to the mantle wedge, small contributions of sediments result in very low ($^{230}Th/^{232}Th$) activity ratios of ~0.7 of the source. Initial ($^{230}Th/^{232}Th$)

activity ratios in the Mariana island arc are greater than 1 (Elliott et al., 1997), and this has been interpreted to reflect ingrowth of ^{230}Th from excess uranium. Uranium excesses within the sedimentary component may be generated by partial melting in the presence of accessory phases with $D_{Th} > D_U$. As the low U/Th samples of lavas from the Mariana arc are close to U-Th radioactive equilibrium, any initial U-Th disequilibrium introduced to the source by sediment melting must have decayed before the addition of slab fluids. This suggests that the transfer time of the sediment component is greater than 350 ka (Elliott et al., 1997), implying that the sediment component and the fluid component are decoupled (cf. Sections 1.3.2 and 1.3.3).

(c) Turner and Hawkesworth (1997) used high $^{206}Pb/^{204}Pb$, high Ta/Nd volcaniclastic sediments as a geochemical tracer in the northern Tonga-Kermadec island arc, and constrained the time between subduction of the sediments and their signature being observed in the arc lavas to 2-4 My. The rate of subduction beneath Tonga is 150-240 mm a^{-1}, and at this rate the sediments would arrive at the source region beneath the volcanoes in <1 My. This suggests that the wedge may only be partially coupled to the subducting slab, and that sediments enrich the wedge at shallow levels and are carried down to the melt generation zone at a rate of 20-40 mm a^{-1}. Although in general the directions of mantle flow appear to be unrelated to the overlying plate motions (Turner and Hawkesworth, 1998), this rate is similar to the half-spreading rates of the back-arc spreading centre in the Lau basin. In addition, slow mantle convection combined with fast subduction suggests that significant shear occurs against the subducting plate, and this may produce elevated slab surface temperatures (Molnar and England, 1995) and result in sediment melting at relatively shallow levels.

In conclusion, U-series data suggest that the fluid component may be transferred in as little as 30 ka, and that fluid addition is the trigger to melting. In contrast, the transfer timescale of the sediment component lies between 350 ka and probably a few million years. Beneath Tonga-Kermadec the sediment transfer time is constrained to 2-4 My. Thus, fluid and sediment components are decoupled.

1.6 Crustal residence times versus mantle wedge transfer times

In addition to implications for crystallisation processes and the thermal budget of magma chambers (e. g. Marsh, 1989), and volcanic hazard assessment (e. g. Fytikas et al., 1989), constraints on the timescales of magma storage within crustal magma chambers are required to resolve fluid and magma transfer times through the mantle wedge. Mineral isochron dating is a useful technique to estimate crustal residence times as mantle derived magmas may be expected to begin to crystallise as soon as they reach crustal levels and begin to cool. Again, the U-series decay scheme may be used to date crystallisation events that took place within the last 200-300 ka (Gill et al., 1991), although age precision is generally worse than ±10% (2σ) unless accessory phases such as apatite or zircon are available (Condomines, 1997). Mineral separates from Soufriere on St. Vincent, in the Lesser Antilles, were successfully dated using U-Th isochron techniques (Heath et al., 1998b), and those data suggest that crystallisation occurred up to 77 (+22/-19) ka (2σ) ago. In contrast, olivine gabbro xenoliths from Raoul in the Kermadec island arc form zero age U-Th isochrons with their host lavas (Turner et al., 1997a), implying that minimal time was spent in crustal magma chambers. Very short crustal residence times are also implied by lava-xenolith pairs from Adak in the Aleutian arc (Turner et al., 1998).

Thus, preliminary results indicate that fluid and magma transfer times through the mantle wedge may generally be around 30 ka, but that crustal residence times may differ

between volcanic arcs by tens of thousands of years. Again, more detailed studies of single destructive plate margin volcanoes are necessary to test such suggestions. In addition, the results from U-Th dating of mineral separates should be compared with other dating techniques that often indicate very different residence times and may be dating different stages of magmatic differentiation. For example, magma chamber residence times of hundreds of thousands of years have been suggested for rhyolitic systems on the basis of Rb-Sr isotope disequilibria of mineral-groundmass pairs (Halliday et al., 1989; Christensen and DePaolo, 1993; Davies et al., 1994), while crystal size distribution (CSD) studies (Marsh, 1988) imply residence times of as little as a few years during the period of crystallisation (Higgins, 1996b; Higgins, 1996a). Clearly, total magma storage times within the crust, and magma residence times derived from crystal populations of certain crystallisation intervals may not be the same, and the timescales of magmatic differentiation require further study.

1.7 Aim of study, and structure of this thesis

The aim of this thesis is to constrain the petrogenetic processes at volcanic arcs with particular emphasis on the timescales involved in fluid and melt transfer through the mantle wedge, and magmatic differentiation within the overriding crust. Santorini, in the Aegean Volcanic Arc, Greece, was chosen as a case study because its stratigraphy is well established. In addition, there are a large number of well-documented historic eruptions, beginning with the cataclysmic caldera-forming Minoan eruption in 1600 BC and followed by the formation of the intracaldera Kameni shield with subaerial eruptions from 197 BC to 1950. Furthermore, geochemical variations within an individual volcano need to be assessed to justify the feasibility of along arc studies, and to constrain the timescales of magmatic differentiation within the crust.

Chapter 2 introduces the tectonic regime of the south Aegean region. Then, the processes of fluid and magma transfer through the mantle wedge and the focussing of volcanic activity at the surface are addressed. This second part of the chapter is a manuscript, submitted to Geology in October 1998.

Chapter 3 summarises the geology and general geochemistry of Santorini. It serves as an introduction to the magmatic evolution of the volcano and is largely based on data from this study, although previously published data from Huijsmans (1985) and Edwards (1994) are presented for reference. The chapter concludes with a brief geochemical comparison of the volcanic centres along the Aegean Arc to review the geochemistry of Santorini in a regional context.

In Chapter 4, trace element and Sr and Nd isotope data are employed to quantify the magma source components and the processes of upper crustal differentiation. U-series results, including some Ra-Th data, are then discussed in terms of the timescales of melt generation and differentiation. This chapter has been structured in the form of a manuscript and will be submitted to Earth and Planetary Science Letters in slightly modified form.

Trace element traverses across plagioclase and pyroxene phenocrysts by ion microprobe are discussed in Chapter 5, which serve to support the results obtained in the previous chapter. The first part may be considered as an epilogue to Chapter 4 as it discusses the possibility of magma-fluid interactions affecting the Ra-Th system. The second part is a manuscript, submitted to Contributions to Mineralogy and Petrology in October 1998. Using Sr diffusion systematics, it describes a new method of estimating crystal residence times in upper crustal magma chambers and thus concentrates on the timescales of magmatic differentiation in the crust.

Chapter 6 summarises the results of this study. It is a synthesis and discusses the processes of fluid transfer, melt generation and magmatic differentiation, with emphasis on the rates of these processes. Some suggestions for future work in this field conclude this thesis.

CHAPTER 2

Tectonic setting and the controls on the distribution of volcanic centres in the Aegean

2.1 Chapter outline

This chapter is in two parts: The first part is a literature review and an introduction to the regional tectonics and the recent volcanic activity in south Aegean region. The second part is a paper submitted to Geology, on "Fracturing of the subducting slab in the Aegean: implications for fluid transfer mechanisms and the focussing of volcanic activity beneath island arcs". The paper links the tectonic aspects of the Hellenic subduction zone and melt generation at depth with associated arc volcanism at the surface. It thus serves as a link to Chapter 3 which deals with the general geochemistry of Santorini.

Part I

Regional tectonics and volcanism

2.2 Plate tectonic setting

The Mediterranean is a region of collisional tectonics ultimately driven by the convergence of Africa and Europe. In the Eastern Mediterranean, the northern edge of the African Plate is being subducted beneath the southern perimeter of the Aegean Sea. Active subduction beneath the Aegean region is accompanied by N-S extension in the southern Aegean as revealed by earthquake focal mechanisms and faulting patterns in central Greece (Taymaz et al., 1991). While back-arc extension is accommodated by roll-back of the slab southwards, the kinematics of the deformation are governed by two additional processes: the westward movement of Turkey relative to Europe; and the

continental collision between NW Greece-Albania with the Apulia-Adriatic platform in the west. This results in E-W shortening in the northern Aegean, which is compensated by fault block rotation and N-S extension in the back-arc region. This area of extension is the South Aegean region (Figure 2-1).

The Hellenic arc-trench region has all the characteristic geological features of an active convergent plate boundary: in the Hellenic Trough, a series of discontinuous basins are picked out by seismic reflection profiling and represent the location of the trench (Kastens, 1991). The subducting slab is delineated by the distribution of shallow and intermediate-depth earthquakes in the Aegean (Hatzfeld and Martin, 1992) and by seismic tomography (Hashida et al., 1987). The Cretan trough, a fore-arc basin, separates the sedimentary outer arc high of the central Peloponnesus, Kythera, Crete, Karpathos and Rhodes from the active volcanic arc. Finally, there is a region of back-arc extension, characterised by block faulting in the Aegean Sea, mainland Greece and western Anatolia (Taymaz et al., 1991).

2.3 Eastern Mediterranean sediments and the Mediterranean Ridge

As discussed in Section 2.6 below, the eastern Mediterranean sediments contain information about the history and kinematics of subduction. In addition, there may be a contribution from these sediments in the arc magma source region (Chapter 4).

The Deep Sea Drilling Program and the Ocean Drilling Program included several cruises into the Mediterranean (Legs 13, 42 and 160/161). The sediments of the eastern Mediterranean comprise late Cretaceous limestones and compact carbonates (cf. DSDP cores 127/128, and Le Pichon and Angelier, 1979), Palaeogene flysch deposits of the alpine orogeny, Miocene pelagic, hemipelagic and turbiditic sediments, including marls and pelagic shales (c. f. DSDP cores 126/377), evaporites of the Messinian salinity crisis (dolomite, gypsum, anhydrite, halite), and Pliocene to Recent sands, silts and marl oozes.

The thickness of these sediments is highly variable with the thickest sediment accumulation in the centre of the basins where they are estimated to extend to in excess of 5 km below sea floor (Le Pichon and Angelier, 1979). Furthermore, the sediments south of the trench form an accretionary complex, the so-called Mediterranean Ridge, that runs from Calabria south-eastwards and then parallel to and south of the Hellenic Trench system into the easternmost Mediterranean. On the basis of drill holes, seismic reflection profiling and seismicity north of the ridge, this structure is interpreted to be a sedimentary wedge formed by accretion of very thick piles of sediments in a compressional thin-skinned tectonic regime (Kastens, 1991). Accretion started in the middle Miocene (Biju-Duval et al., 1978; Robertson and Grasso, 1995) and continues today (Kastens, 1991). Southwest of Crete, the trend of the ridge is ~115° which is orthogonal to the earthquake slip vectors identified by Taymaz et al. (1990) that define the convergence direction between Crete and Africa.

The percentage of sediments that are being subducted is difficult to constrain. However, in the light of massive sediment accretion in a thin-skinned tectonic regime, probably only a small proportion of the sediments are being subducted, and these are likely to originate from the lower part of the thick sediment pile.

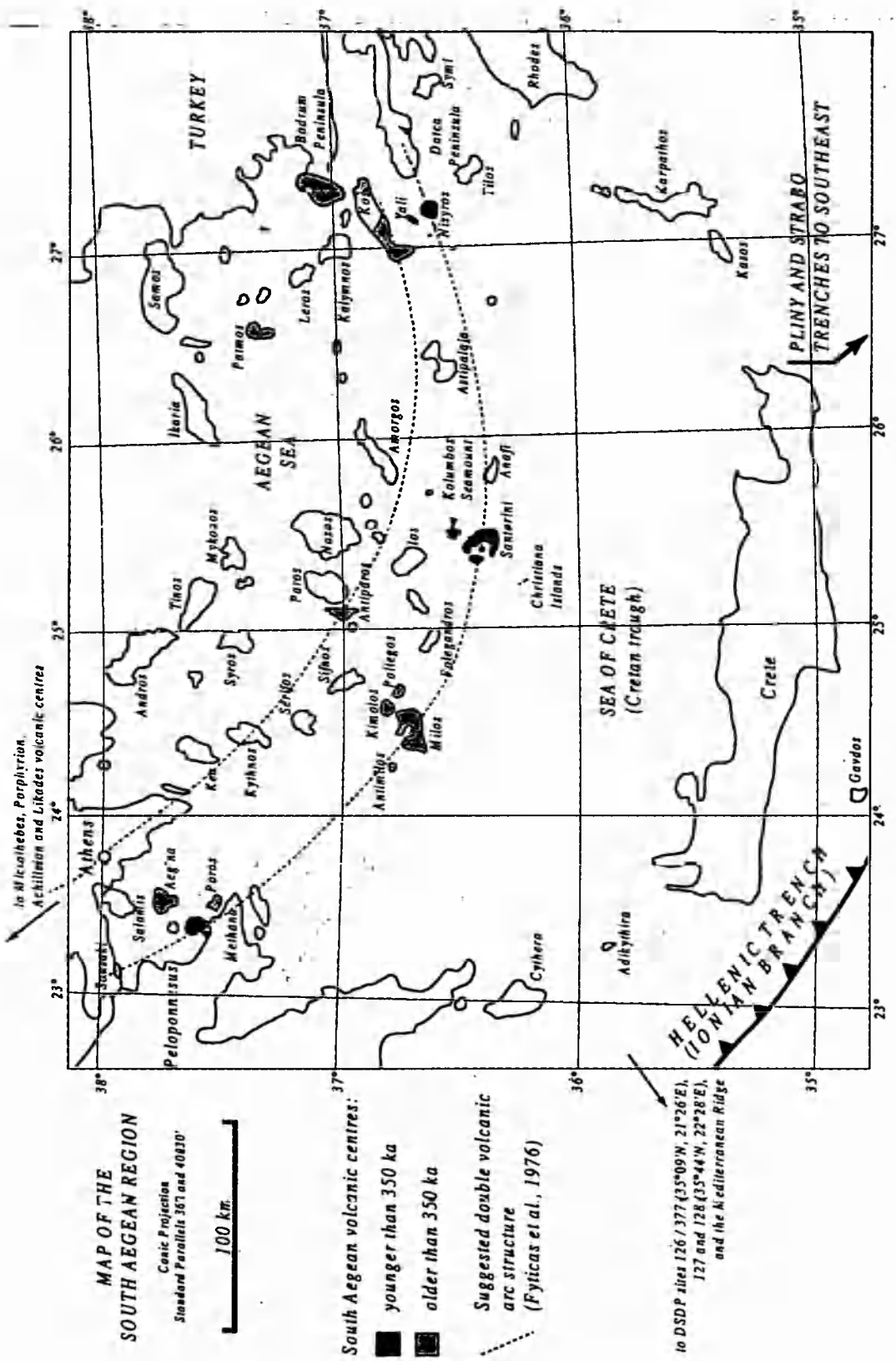

Figure 2-1: Map of the South Aegean Region.

2.4 The Hellenic Trench

The Hellenic Trench separates the Aegean Sea from the eastern Mediterranean. It is a complex system of graben and topographic ridges. To the southwest, the Aegean is bounded by the Ionian trench, whilst to the southeast, two parallel trenches occur, the inner Pliny trench and the outer Strabo Trench (c. f. Figure 2-1).

The results of a multi-narrow seabeam survey of the Hellenic trench system (Le Pichon et al., 1979) reveal a more detailed structure of the trench. Along the Ionian branch, the subduction system is dominated by thrust faulting, characteristically shown as divisions into small basins, partly filled with Pleistocene sediments. These are being deformed by a compressional stress perpendicular to the trench.

The Pliny and Strabo trenches, on the other hand, are sub-parallel to the motion of the African plate. Thus, transform motion dominates here. The area between the Pliny and Strabo trenches is affected by complex deformation as transform motion is progressively transferred from Pliny in the southwest to Strabo in the northeast (Jongsma, 1977). Numerous long narrow graben and ridges have developed in this area of left-lateral shear, and the paucity of Pleistocene sediment fill provides further evidence that transform motion dominates in this region.

Furthermore, within the Pliny trench itself, which is orientated 060°, there are en-echelon narrow troughs, orientated 040°. This is the direction of the regional slip vector determined by Le Pichon and Angelier (1979) and suggests that the trench is made of small portions of en-echelon transforms connected by right-lateral offsets along which the theoretical motion is mostly compressional with some right-lateral slip component.

2.5 The subducting slab

Due to the high reflectivity and thickness of the sediments in the Eastern Mediterranean, seismic reflection profiling cannot penetrate to the crust. However, the Ionian and Levantine basins in the eastern Mediterranean are thought to represent the remnants of the Tethys ocean and to have formed during Jurassic-Cretaceous rifting (Hsü and Bernoulli, 1978). Below the sediments of the eastern basins there should therefore be either oceanic crust of Mesozoic age, or intermediate thin crust, considering the proximity of the African passive margin (Le Pichon and Angelier, 1979).

Slab geometry is very variable along the arc, and the Benioff zone has a mean dip angle of 23° down to a depth of 100 km, then steepens with a mean dip angle of 38° (Papazachos et al., 1991). This has been attributed to internal deformation of the slab by both gravity forces and horizontal compression (Hatzfeld, 1994). Palaeomagnetic studies (Kissel and Lay, 1987) indicate that the Lower Miocene arc was sublinear with an E-W trend, and that it acquired its curvature due to fault block rotation which started in the Middle Miocene, less than 16 Ma ago. This is in agreement with an inferred change in subduction rate as outlined in section 2.6. Extension throughout the Aegean was active during the Plio-Quarternary, as shown by continued exhumation of metamorphic core complexes in the Cyclades (Lister et al., 1984; Avigad and Garfunkel, 1991).

2.6 Plate kinematics and history of subduction

Various estimates have been made about the length of the subducted slab, the rate of its subduction and the age of initiation of subduction. Papazachos and Hoogerduyn-Strating (1973) estimated the length of the seismically active part of the subducting slab to be ~280 km, reaching a depth of ~130 km below the volcanic front. Using ~3 Ma for the initiation of volcanism and a mean slab dip angle of 35°, Fyticas et al. (1976) estimated the rate of subduction to be ~18 mm a^{-1}, assuming melt was generated and erupted as

soon as the subducting slab reached a depth of 130 km. This gives an age of >15 Ma for initiation of subduction. More recent estimates of at least 50 mm a^{-1} for the shortening at the Hellenic Trench, using kinematic arguments, seismic moment rates and satellite laser ranging (Taymaz et al., 1990, and references therein), would require a much younger age of ~5 Ma for the initiation of the present subduction regime.

However, Wortel (1982) argued that no earthquakes are generated in the deeper parts of the subduction zone due to heating of the slab by the mantle wedge. Hence the slab may extend further than suggested by earthquake data. Tomographic imaging (Spakman et al., 1988) indeed shows a seismic low velocity zone that extends down to >600 km into the lower mantle, and more recent data (van der Hilst, 1998) indicates a down-dip slab length of ~1400 km.

Kastens (1991) placed further constraints on the history of subduction kinematics by studying the rate of outward growth of the Mediterranean Ridge accretionary complex using borehole information. Its growth rate was shown to have increased since subduction initiation 40-33 Ma ago (Spakman et al., 1988; Kastens, 1991), reflecting a corresponding increase in subduction velocity from an initial value that would have been that of the net convergence rate between Africa and Europe of ~10 mm a^{-1} (Livermore and Smith, 1985). The increase in rate of subduction to ~50 mm a^{-1} today may be explained by the onset of N-S back-arc extension in the Aegean Sea 12-16 Ma ago (Meulenkamp et al., 1988; Mercier et al., 1989; Druitt et al., 1996) in response to E-W shortening in the northern Aegean, followed by tectonic activation of the islands of Kos during the Messinian (Besenecker and Otte, 1977) and Rhodes during the late Pliocene (Meulenkamp, 1985).

2.7 Thickness of the overriding crust

The Aegean crust has been studied by deep seismic sounding (Makris, 1978). The main part is composed of thinned continental crust, with maximum thinning at the deep Cretan Sea trough, where crustal thickness is only 20 km, compared to 46 km on mainland Greece. Seismic sections indicate that the thickness of the crust is variable along the Aegean volcanic arc, ranging from 32-34 km below Methana in the northwest and Nisyros in the east to ~23-26 km in the central part below Santorini (Makris, 1977).

Sedimentary cover on the overriding crust is very unevenly distributed and confined to Neogene basins where sediments reach thicknesses of ~3 km. Large areas, including the Cyclades, almost totally lack sediments.

2.8 The volcanic arc: geography and geochronology

Areas of young volcanic activity in the south Aegean region are highlighted in Figure 2-1. The late Pliocene-Quaternary volcanic products in the South Aegean make up a volcanic front that includes the Saronic Gulf volcanic province (Sousaki / Crommyonia, Aegina, Methana, Poros), the Milos group (Milos, Antimilos, Kimolos, Poliegos), the Santorini group (Santorini, Christiana Islands, Columbos seamount), the Nisyros group (Nisyros, Yali, Strongyli), western Kos and the Datca Peninsular in Turkey (di Paola, 1974; Keller, 1982; Fytikas et al., 1989). This volcanic arc is attributed to subduction of the African plate under the Aegean microplate and will be referred to as the Aegean Volcanic Arc, following Innocenti et al. (1981).

Behind this belt of fumarolic and calc-alkaline magmatic activity are the more K-rich volcanic centres of Kammena Vourla, Microthebe, Porphyrion, Achilleion and Likades in the northwest (Pe, 1975), and Antiparos, eastern Kos, Bodrum and Patmos. Volcanic rocks on eastern Kos, Bodrum and Patmos are Miocene (Keller et al., 1989) and

consequently unrelated to the presently active magmatic arc. It is possible that they are associated with an earlier phase of subduction (Keller, 1982). The northwestern K-rich volcanic centres, Antiparos and eastern Kos have previously been interpreted as the inner arc of an active double arc structure in the South Aegean (Ninkovich and Hays, 1972). Later, the volcanic products of Antiparos were dated as Miocene by K-Ar (Innocenti et al., 1981), and it was found that the northwestern K-rich volcanic centres lie along and may be associated with a major transcurrent fault system bordering the Aegean microplate in the north (c. f. Taymaz et al., 1991, their figure 17). Hence, they are not necessarily related to subduction.

In conclusion, the currently active volcanic arc is a single arc, and only Methana, Santorini, and the Nisyros group are young enough for U-series studies. None of the volcanic centres north of this arc can unequivocally be associated with the present phase of subduction.

Part II

Fracturing of the subducting slab in the Aegean: implications for fluid transfer mechanisms and the focussing of volcanic activity beneath island arcs

A paper submitted to Geology, October 1998

2.9 Abstract

The controls on the distribution of magmatic centres along active plate margins remain controversial, and yet they may be central to models of slab fluid transfer and melt generation in the mantle wedge. Shallow earthquake (≤40 km) hypocentre locations from the South Aegean active margin indicate that at the trench, deformation within the subducting slab is localised and controlled by the geometry of the plate margin. Epicentres of intermediate depth earthquakes (≥65 km) form linear arrays, trending north-east from zones of localised shallow seismicity at the trench towards the volcanic centres of Methana, Milos, Santorini and Nisyros, respectively. Almost no intermediate depth seismicity is observed between these linear arrays. The data indicate that the trench geometry leads to localised deformation and segmentation of the subducting slab, and that deformation within the subducted slab is restricted to segment boundaries. The coincidence of intermediate depth seismicity and volcanic activity indicates a close link between tectonic features within the subducting slab and active magmatism above it. This suggests that melt generation is concentrated in zones above those parts of the slab that are heavily deformed and where pore fluids from dehydration reactions are focussed to be released into the mantle wedge via hydraulic fracturing.

2.10 Introduction

Direct evidence for the causes of partial melting, and the positioning of volcanic islands above subducting slabs is hard to find. Many geochemical studies have attributed the trigger for partial melting to lowering of the solidus in the mantle wedge by the addition of fluids from the slab (e. g. Hawkesworth et al., 1997). However, some workers have suggested a significant role for decompression melting (e. g. Plank and Langmuir, 1988). In detail, within the fluid-induced melting models there is further debate. Some models have fluid release occurring beneath the arc volcanoes and partial melting occurring close to the slab (e. g. Tatsumi, 1989), whilst others have slab-derived fluids migrating horizontally from the slab and inducing partial melting closer to the centre of the mantle wedge beneath the arc volcanoes (e. g. Davies and Stevenson, 1992). At present, geochemical data cannot easily distinguish between these various possibilities, and so independent evidence for the physical relationship between the positioning of arc volcanism and processes occurring at the slab-wedge interface would be invaluable. Such evidence may be contained in teleseismic and microseismic data from the Aegean arc.

2.11 Geological background

In the eastern Mediterranean, collisional tectonics are characterised by north-eastward subduction of the African plate beneath the Aegean microplate along the Hellenic Trench (e. g. Le Pichon and Angelier, 1979; Taymaz et al., 1990), evidenced by intermediate depth seismicity beneath the Aegean region (Hatzfeld and Martin, 1992) and by seismic tomography (Spakman et al., 1988). Estimates of the rate and direction of subduction vary from 30 to 60 mm a^{-1} and from N15°E to N50°E, respectively (Le Pichon et al., 1979; Taymaz et al., 1990; Robbins et al., 1995). The Benioff zone has a dip angle of ~23° down to the depth of 100 km, then steepens with a mean dip angle of 38° (Papazachos et al., 1991). The Aegean Volcanic Arc principally consists of the late

Pliocene to Quarternary volcanic centres of Sousaki, Methana, Milos, Santorini and Nisyros. They are located 120 to 140 km above the Benioff zone (Hatzfeld and Martin, 1992), 250 to 300 km behind the trench.

A link between intermediate depth seismicity and volcanic activity was initially suggested by Papazachos and Panagiotopoulos (1993) on the basis of ten strong ($M_S \geq 5.6$) intermediate depth earthquakes that have occurred directly beneath the volcanic arc since 1862, but their conclusion was speculative as they did not utilise the complete earthquake dataset. Recent teleseismic relocation of the hypocentres (Engdahl et al., 1998) allows us to re-evaluate the data for evidence of the association of seismicity and volcanism, and to place further constraints on the structure and deformation of the subducting slab.

2.12 Seismicity

In the following, relocated hypocentres for seismic events in the South Aegean from 1964 to 1995 from Engdahl et al. (1998), together with the data compiled by Papazachos and Panagiotopoulos (1993) and microseismic data from Hatzfeld et al. (1993) have been used (Figure 2-2). Shallow seismicity is observed throughout the Aegean, but the number of events increases towards the trench, where earthquakes cluster around transverse segments in the trench system at 35°40'N 22°E, 35°N 23°E, 34°30'N 24°E and 34°20'N 25°10'E. Fault plane solutions (Papazachos et al., 1991, and references therein) show that low-angle thrust faulting dominates the shallow depth seismicity near the trench, with slip vectors orientated at ~N50°E, and that strike-slip components are small or absent.

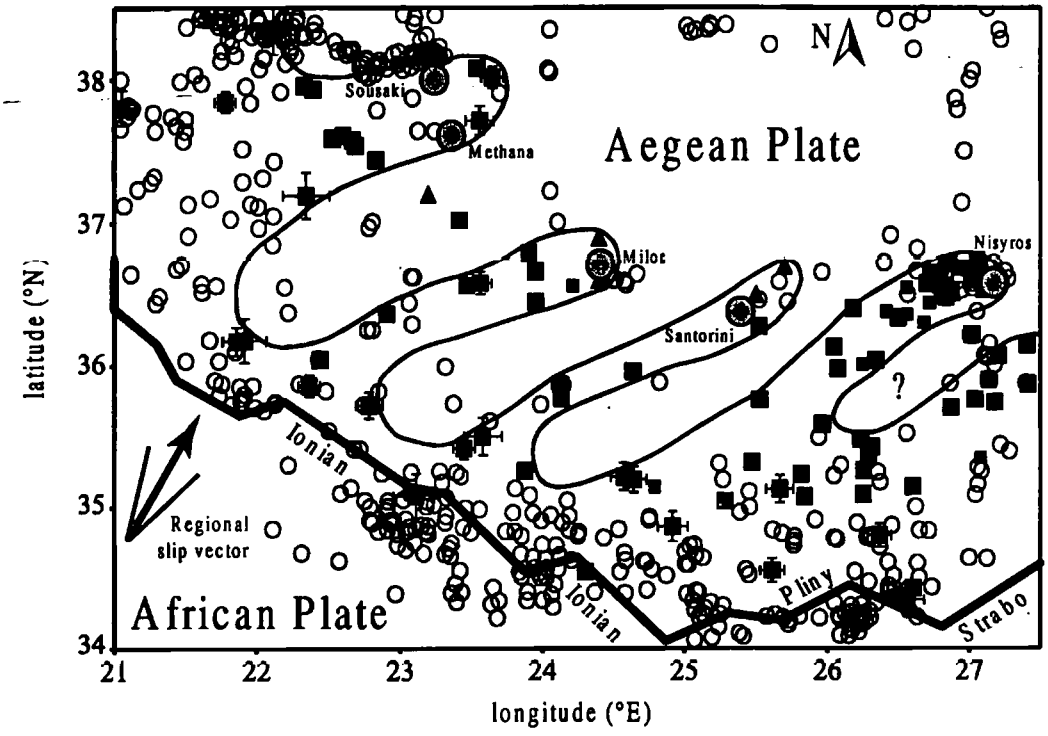

Figure 2-2: Earthquake map of the South Aegean. The thick dark line shows parts of the various branches of the Hellenic Trench, adapted from Le Pichon and Angelier (1979) The regional slip vector trends north-west at 30±17°(1σ) and is based on the direction of thrusting derived from shallow earthquakes at the trench (Papazachos et al., 1991). Earthquake epicentres are plotted for shallow (≤ 40 km, open circles) and intermediate (≥ 65 km, black squares) teleseismic events observed between 1964 and 1995 (Engdahl et al., 1998). Standard errors on epicentre location of shallow earthquakes are generally much better than ±15 km. For intermediate seismic events, they are smaller than symbol size unless indicated otherwise. Focal depths are generally known to better than ±10 km. In addition, intermediate depth epicentres from a compilation of Papazachos and Panagiotopoulos (1993)(black triangles) and from a microseismic study of Hatzfeld et al. (1993)(small black squares, with standard errors of less than ±20 km) are given. The thin dark line divides areas where intermediate depth earthquakes occur from areas where intermediate depth seismicity is almost absent.

Hatzfeld et al. (1993) note that for earthquakes with depths ranging from 40 to 80 km it is difficult to establish whether they were within the upper plate or the subducting slab. However, hypocentre relocation has improved the depth resolution to better than ±10 km, and crustal thickness does not exceed 55 km anywhere in the Aegean (Makris, 1978). Thus, earthquakes deeper than 65 km almost certainly occurred within the subducted slab. These are evenly distributed close to the trench, but away from the trench they form linear arrays of intermediate depth seismicity, which trend north-east from zones of localised shallow seismicity at the trench towards the volcanic centres of Methana, Milos, Santorini and Nisyros, respectively. Fault plane solutions (Papazachos et al., 1991; Hatzfeld et al., 1993) indicate reverse faulting, some with a considerable strike-slip component.

2.13 Plate deformation at the trench

The Hellenic trench (Figure 2-2) is segmented, with the Ionian trench system in the Southwest and the Pliny and Strabo trenches in the Southeast. The Ionian trench system consists of a series of topographic troughs, orientated roughly perpendicular to the regional slip vector of the shallow thrust-type earthquakes, and separated by transverse topographic trends along which transform motion occurs (Le Pichon et al., 1979). In contrast, the Pliny and Strabo trenches are sub-parallel to the regional slip vector, and are dominated by transform motion.

While shallow earthquakes in the Aegean are generally more frequent close to the trench than beneath the volcanic arc, in the Ionian trench system they are focussed at the transverse segments. This suggests that the African plate fractures at the transverse segments to accommodate subduction to the Northwest as well as transform motion along the transverse segment (Figure 2-3). The paucity of strike-slip events near the

trench is consistent with this interpretation, as slab deformation by dip-slip earthquakes alone is required as a response to the imposed stress field.

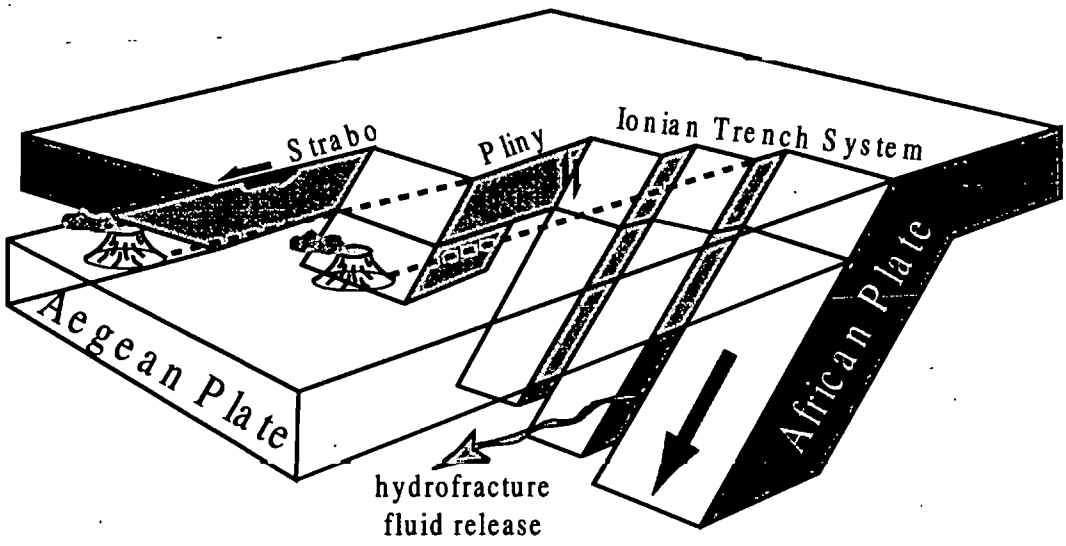

Figure 2-3: Model of the 3d-structure of the subducting slab beneath the South Aegean, looking from the North. At transverse segments in the trench, the slab is broken up by dominantly dip-slip movements, leading to linear slab segmentation at depth. Intermediate depth earthquakes are inferred to result from subsequent deformation between these segments, where the slab is structurally weakened. Faults are inferred to collect pore fluids from dehydration reactions and to control their localised release into the mantle wedge by hydraulic fracturing, resulting in the focussing of volcanic activity above.

2.14 Slab segmentation

Close to the trench, intermediate depth seismicity is uniformly distributed. This may reflect internal deformation of the slab along the whole length of the trench at the early stages of subduction. Away from the trench, however, three north-east trending zones of little intermediate depth seismicity (Figure 2-2) imply segmentation of the subducting

slab into at least three parts that do not deform internally (Figure 2-3). Most intermediate depth seismicity occurs along their boundaries. The focussing of shallow seismicity at the south-western end of each linear array of intermediate depth seismicity suggests that the slab is structurally weakened during subduction at the trench, and that any subsequent deformation within the slab occurs along those lines of weakness. Similar observations of slab deformation along fracture zones have been made at the Sumatran arc (Page et al., 1979; Fauzi et al., 1996).

The south-west - north-east orientation of the slab segments is consistent with earthquake slip vectors of shallow thrust faulting near the trench (Papazachos et al., 1991). In addition, their orientation is within error of the direction of motion of Africa relative to the Aegean microplate determined by satellite laser ranging in the southern Aegean (Robbins et al., 1995). Moreover, the linearity of intermediate depth seismicity implies that the direction of convergence has remained relatively constant over the last few million years.

Fault plane solutions of intermediate depth earthquakes beneath the Aegean are similar to those in other arcs in that T-axes plunge in the downdip direction of the slab. P-axes, however, are sub-horizontal and many are aligned parallel to the plane of the seismic zone, pointing to contortion of the subducted slab (Hatzfeld et al., 1993). This may be associated with the progressive change in direction of convergence between the plates, from north-eastwards in the west to north – north-eastwards in the east (Le Pichon and Angelier, 1979; Robbins et al., 1995), resulting in compressive stresses between the plate segments at depth.

2.15 Discussion

Volcanic activity above areas of intermediate depth seismicity in the Aegean provides first-order evidence for a direct relationship between deformation processes occurring within the subducting slab and the distribution of volcanic centres at the surface. Thus, the spacing of volcanic activity may not always be random, as suggested by de Bremond d'Ars et al (1995) for active margin volcanism globally, and the data argues strongly for a slab control on where mantle melting takes place.

It follows that partial melting of the mantle is triggered by addition of fluids from the dehydrating slab, and that decompression melting within the wedge due to mantle diapirism alone (Plank and Langmuir, 1988) cannot account for melt generation. In conjunction with recent short-lived isotope results, the data may be used to constrain the mechanism of fluid transfer. U-Th isotope disequilibria studies have indicated that the time between fluid release and partial melting is of the order of 20 to 30 ka (see Hawkesworth et al., 1997, for a recent review). Therefore it may be argued that there is insufficient time for slab-derived fluids to migrate more than a few kilometres into the wedge prior to partial melting (Turner and Hawkesworth, 1997). In the horizontal fluid transfer model, this would conflict with the location of arc volcanoes being generally some 100 to 300 km from the trench. As a possible solution to this dilemma, Davies and Rowland (1997) suggested that slab-derived fluids may be rapidly transported tens of kilometres into the mantle wedge from the subducting slab by hydraulic fracture. Furthermore, the high pore fluid pressure that counteracts the high confining pressure at depths greater than ~60 km may be the reason for the occurrence of intermediate depth seismicity globally (Green and Houston, 1995). The data from the Aegean provide a strong indication that localised brittle failure within the slab channels pore water (Davies and Rowland, 1997), and that hydraulic fractures propagating from the slab into the

hotter mantle control fluid release from the slab, thereby triggering focussed partial melting. Thus, the physical and geochemical data can be reconciled in a single model.

Evidence that this model may be more globally applicable comes from the observed increase (by a factor of two to five) in the relative size of the geochemically-traced slab fluid contribution to Aleutian arc volcanoes which lie above fractures in the down-going Pacific plate (Singer et al., 1996), associated with an increase in the degree of partial melting (e. g. Kay et al., 1982).

2.16 Conclusions

Shallow seismicity at the Hellenic Trench predominantly occurs due to segmentation of the subducting slab in response to stresses imposed by the geometry of the plate margin. Intermediate depth seismicity is confined to the slab segment boundaries where the slab has fractured and has been structurally weakened. This model is consistent with available earthquake fault plane solutions of both shallow and intermediate depth seismic events (Papazachos et al., 1991).

The coincidence of intermediate depth seismicity and volcanic activity implies that processes within the slab control melt generation in the wedge. It is inferred that fluids from dehydration reactions within the slab are channelled towards the slab-wedge interface by faults in the slab segment boundaries. Subsequently, focussed slab fluids are released into hotter regions of the mantle wedge via hydraulic fracturing. This results in increased melt generation in those parts of the mantle wedge that overlie the fracture zones, and determines the location of recent volcanic activity in the South Aegean. Thus, the distribution of volcanism in the South Aegean is not random, but rather controlled by tectonic processes within the subducting slab, initiated hundreds of kilometres away from the active volcanic arc.

CHAPTER 3

The geology and the general geochemistry of Santorini

3.1 Chapter outline

This chapter begins with a brief review of the general geology and the volcanological evolution of Santorini, based on published stratigraphic and geochronological data.

Following this general introduction, the major element constraints on the processes that lead to magmatic differentiation at Santorini are discussed, including some MELTS modelling (Ghiorso and Sack, 1995). Trace element constraints are used to assess and quantify these processes. Sr and Nd isotopic variations are then discussed. As this thesis is concerned with the application of uranium series disequilibria, this chapter focuses on samples that are young enough for uranium series dating. It is based on analyses undertaken as part of this study combined with data available from previous studies. Only samples younger than ~200 ka have been chosen for analysis. The chapter concludes by comparing the geochemical data from Santorini with that published from the other volcanic centres of the Aegean Volcanic Arc.

3.2 Geological background

Santorini, situated at 36°25'N, 25°25'E, ~107 km north of Crete, is a volcanic complex of five islands (Figure 3-1). Thera, Therasia and Aspronisi form a dissected ring around a flooded caldera complex containing the islands of Palea Kameni and Nea Kameni. The caldera is bounded by subaerial cliffs up to 300 m high and it represents a composite structure resulting from at least four collapse events, the last 3.6 ka ago (Druitt and Francaviglia, 1992). Santorini is split by a major tectonic lineament, the Kameni line (Heiken and McCoy, 1984), that trends NE-SW and intersects the caldera wall near the

town of Phira, where normal faulting is evident (Druitt et al., 1989). Magma ascending through prevolcanic basement of Mesozoic and early Tertiary age has exploited fissures along the Kameni line and along another NE-SW trending fault system to the north.

The stratigraphy of the pyroclastic deposits of Santorini is given by Druitt et al. (1989) and discussed in detail by Edwards (1994). More recent work (Druitt, 1999) has included the effusive units and has simplified the stratigraphy by combining some of the pyroclastic deposits, and this is the stratigraphy adopted in this thesis (Figure 3-2). The volcanological evolution of Santorini can be divided into four main stages:

(1) Early volcanic activity (~750 ka - ~300 ka) was characterised by the extrusion of the basaltic to hornblende-phyric rhyolitic lavas and tuffs on the Akrotiri peninsula and the basaltic to andesitic lavas, tuffs and breccias of Peristeria volcano in the Northeast at Mikro Profitis Ilias (MPI).

(2) These deposits are overlain by a sequence of dominantly andesitic to rhyolitic pyroclastic deposits of the first eruptive cycle (~360 ka - <200 ka) that is recognised on the basis of long-term trends in magma composition from mafic to more evolved nature. The cycle began with explosive venting of andesitic to dacitic magma, with interdispersed effusion of basaltic, andesitic and dacitic lavas, and culminated in a pair of major dacitic to rhyolitic explosive eruptions that were accompanied by caldera collapse (Druitt et al., 1989). The first eruptive cycle dominates the cliffs of southern Thera and Aspronisi.

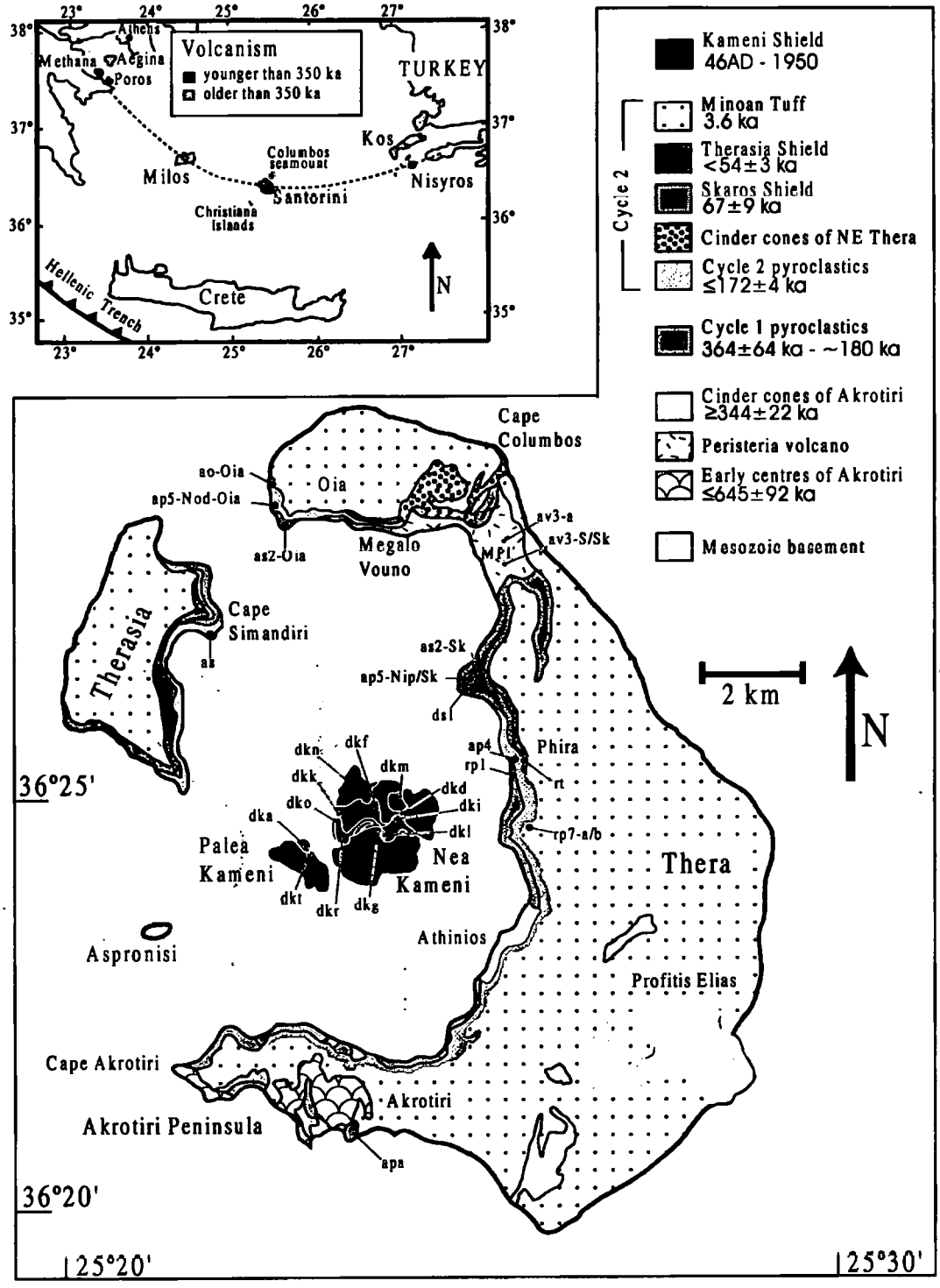

Figure 3-1: Geological Map, stratigraphy and geochronology of Santorini, modified from Druitt et al. (1996), including sample locations. Sample names refer to the stratigraphic units of Druitt (1999). Inset: Map of the Aegean region and the volcanic arc.

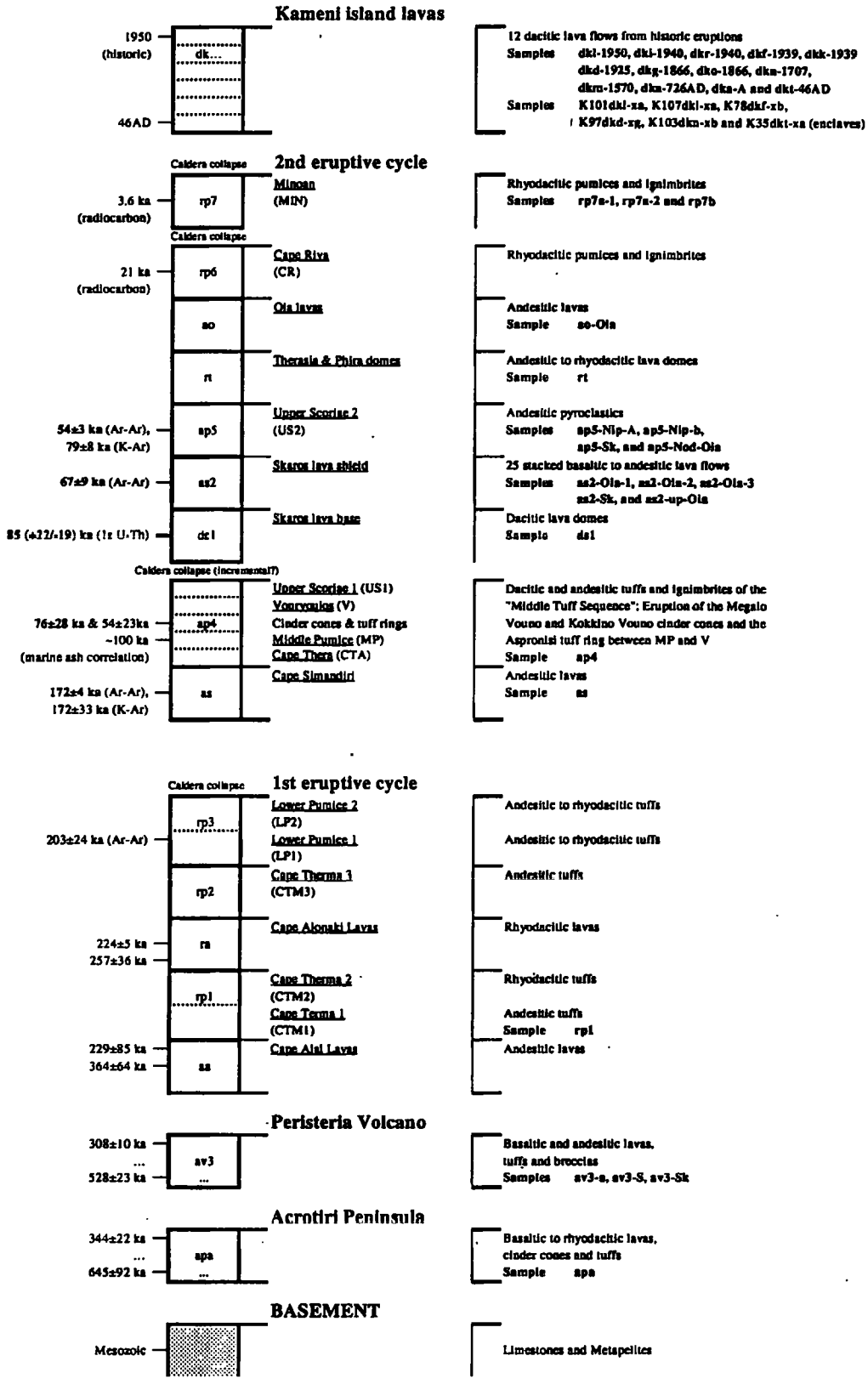

Figure 3-2: Stratigraphy of Santorini, adopted from Druitt et al. (1996) and Druitt (1999). For a key to the stratigraphic units, see Appendix C. The geochronometry is based on K-Ar whole rock ages unless otherwise stated (Druitt et al., 1996, and references therein). Also indicated is the relative stratigraphic position of analysed samples.

(3) The northern half of Thera and the whole of Therasia is dominated by basaltic to rhyolitic lavas and minor pyroclastic deposits of the second eruptive cycle (SEC, ~170 ka - ~3.6 ka), which again culminated in a pair of major dacitic to rhyolitic explosive eruptions. The SEC represents the products of at least three large shield complexes: Simandiri, Skaros, and Therasia. White rhyolitic pumice and ignimbrites of the caldera forming Minoan eruption ~3.6 ka ago essentially cover the islands of Thera, Therasia and Aspronisi.

The two eruptive cycles with a combined maximum thickness of up to 200 m are volumetrically most important.

(4) Submarine volcanic eruptions at the centre of the caldera recommenced shortly after caldera collapse, and lava flows emerged to above sea level in 197 BC. Since then, 12 dacitic lava flows were erupted, the last in 1950, forming the two Kameni islands, Palea Kameni and Nea Kameni. These are the subaerial expression of a ~2 km^3 intracaldera shield which rises to ~500 m above the caldera floor.

3.3 Petrography, mineral chemistry and crystallisation conditions

This section is restricted to the petrography of samples from the SEC and the Kameni dacites. For a petrographic study of the other volcanic units of Santorini, see Nicholls (1971). The samples studied as part of this work are mineralogically very similar to those previously described by Nicholls (1971), Huijsmans (1985) and Barton and Huijsmans (1986).

3.3.1 The second eruptive cycle (SEC)

Basalts and basaltic andesites sampled in this study are porphyritic with abundant phenocrysts of plagioclase, pyroxene and rare resorbed olivine crystals, set in a fine

grained groundmass dominated by plagioclase microlites, pyroxene, magnetite and ≤5% brown glass. Plagioclase crystals dominate the phenocryst assemblage, which in some cases may result from plagioclase accumulation (e. g. sample 'ap5-Nod-Oia'). They are euhedral to subhedral, generally less than 6 mm in length, and many contain abundant melt inclusions. Clinopyroxene and less abundant orthopyroxene are subhedral to anhedral, and generally less than 5 mm in length. Orthopyroxene gradually replaces olivine in the basaltic andesites. Olivine crystals are generally resorbed and often rimmed with pyroxene.

Andesites are dominated by plagioclase, clinopyroxene and orthopyroxene phenocrysts, all generally less than 2 mm in length. In addition, phenocrysts of magnetite (≤1 mm) become abundant, and the proportion of brown glass in the groundmass increases to up to 30%.

In the dacites and rhyolites (>63 wt% SiO_2), apatite (e. g. sample 'rt') joins the crystallising assemblage as acicular inclusions in subhedral plagioclase phenocrysts (5-20%) and in the groundmass which is dominated by plagioclase, pyroxene, magnetite and pale-brown glass. In addition, Huijsmans et al. (1988) reported biotite in the rhyolites, but biotite was not found in any of the samples studied here.

According to Nicholls (1971), plagioclase phenocryst composition ranges from An_{90}-An_{85} in the basalts to An_{50} in the dacites and rhyolites. Groundmass plagioclase crystals are generally more albitic, ranging from An_{75} in the basalts to An_{30} in the evolved samples. Olivine compositions generally range from Fo_{70} to Fo_{80}.

3.3.2 The Kameni dacites

The Kameni lavas are dacitic with gabbroic and basaltic to andesitic enclaves. The dacites have porphyritic textures with plagioclase (10-20%), pyroxene (<5%) and magnetite as phenocrysts set in a fine-grained groundmass dominated by plagioclase

microlites and brown glass. Apatite needles occur in the groundmass and as inclusions in phenocryst phases (Barton and Huijsmans, 1986).

In this study, two types of euhedral plagioclase phenocrysts could be distinguished according to their mineral chemistry. The first type (An_{41}-An_{53}) has a rim with a composition similar to the microlites (~An_{44}), suggesting that the two grew simultaneously. The second type is slightly more calcic in composition (An_{58}-An_{67}, e. g. sample 'dkr-1940'). Plagioclase phenocrysts are generally less than 1 mm in length and have abundant melt inclusions (10-15%). Larger (up to 2 mm) crystals of plagioclase also occur. They are much more anorthitic (An_{90}-An_{93}, dkl-1950), and on basis of their similarity to plagioclase crystals from the cognate xenoliths are considered to represent xenocrysts derived by disaggregation of the cognate xenoliths (Barton and Huijsmans, 1986).

Clinopyroxene crystals are subhedral to anhedral, generally ≤0.5 mm long, and show weak pleochroism. Their Mg# ranges from 0.69-0.74, calculated on the basis of 6 oxygens. Inclusions of magnetite are common. Orthopyroxene crystals are rarer but occur as euhedral to subhedral phenocrysts (≤1 mm). Their Mg# ranges from 0.59 to 0.68.

Magnetite phenocrysts (<0.5 mm) are subhedral to anhedral, whereas the magnetite microphenocrysts are euhedral. They are titaniferous with 14.0 - 16.4 wt% TiO_2 (Barton and Huijsmans, 1986). Olivine (Fo_{80-60}) has been reported as a rare phase not in equilibrium with the melt (Barton and Huijsmans, 1986), but it was not identified in any of the samples studied here.

3.3.3 Conditions of crystallisation

Huijsmans (1985) estimated pre-eruptive temperatures, pressures, oxygen fugacities and water contents for the entire compositional range of lavas erupted at Santorini.

Temperatures were calculated using olivine-liquid geothermometry, pyroxene geothermometry and Fe-Ti-oxide geothermometry. Pressures were calculated using the compositions of coexisting plagioclase, clinopyroxene and olivine phenocrysts. Pre-eruptive H_2O contents were calculated using the regular solution model of Ghiorso and Carmichael (1980). Oxygen fugacites were calculated from coexisting olivine and titano-magnetite crystals and from pairs of coexisting Fe-Ti oxides. For details on the calculations, see Huijsmans (1985) and references therein, and Barton and Huijsmans, (1986). The inferred ranges in pre-eruptive temperatures, pressures, oxygen fugacities and water contents are summarised in Table 3-1.

	Temperature	Pressure	Oxygen fugacity	Water content
Basalts	1150-1200°C	1-3 kbar	$\sim 10^{-7}$	<0.5wt%
Basaltic andesites	1050-1150°C	n. d.	n. d.	n. d.
Andesites	960-1050°C	1-3 kbar	$\sim 10^{-10}$	<1.5 wt%
Dacites and rhyolites	800-980°C	1-2 kbar	10^{-10}-10^{-12}	3-4 wt%

Table 3-1: Estimates of pre-eruptive temperatures, pressures, oxygen fugacities and water contents, after Huijsmans (1985) and Barton and Huijsmans (1986).

3.4 Major element geochemistry

Major element oxide concentrations of the SEC and the Kameni dacites have been analysed by XRF. Analytical techniques and the data tables are given in Appendix A and Appendix D, respectively. Although the suite of early eruptive products from Akrotiri is slightly more calc-alkaline in character than samples from subsequent cycles (Nicholls, 1971), in general the major element differentiation trends of the different eruptive units on Santorini are very similar (Huijsmans et al., 1988). The results from this section are restricted to observations from the SEC and the Kameni lavas, but they are also broadly

applicable to the earlier eruptive products from Akrotiri, Peristeria and those of the first eruptive cycle.

3.4.1 Results of the major element analysis

Relatively low Mg numbers of 54 even in the least evolved samples indicate that at Santorini, the erupted magmas have evolved considerably from primary magmas in equilibrium with the mantle (Mg# ≈ 73). Silica is used as the differentiation index throughout the following sections. In the SEC, increasing SiO_2 is accompanied by increasing K_2O. Na_2O increases up to ~67 wt% SiO_2 and then slightly decreases. P_2O_5 increases up to ~61 wt% SiO_2 and then decreases, although some samples plot at lower P_2O_5 at intermediate SiO_2 levels (Figure 3-3). TiO_2 shows a similar trend but peaks at ~58 wt% SiO_2. Fe_2O_3 increases only very little up to ~57 wt% SiO_2 and then decreases. MgO and CaO both decrease with increasing SiO_2. Al_2O_3 decreases rapidly with increasing SiO_2 within the basaltic andesite field (53-57 wt% SiO_2), stays relatively constant at andesitic compositions (57-63 wt% SiO_2) and then gently decreases at more felsic compositions (Figure 3-3).

The Kameni dacites have a restricted SiO_2 range of 64 - 69 wt%. They contain mafic enclaves of both cumulate and non-cumulate origin. The Kameni lavas generally fall within the major element trend displayed by the SEC, with the exception of the lower K_2O concentrations of the dacites relative to those in the SEC with similar SiO_2 content.

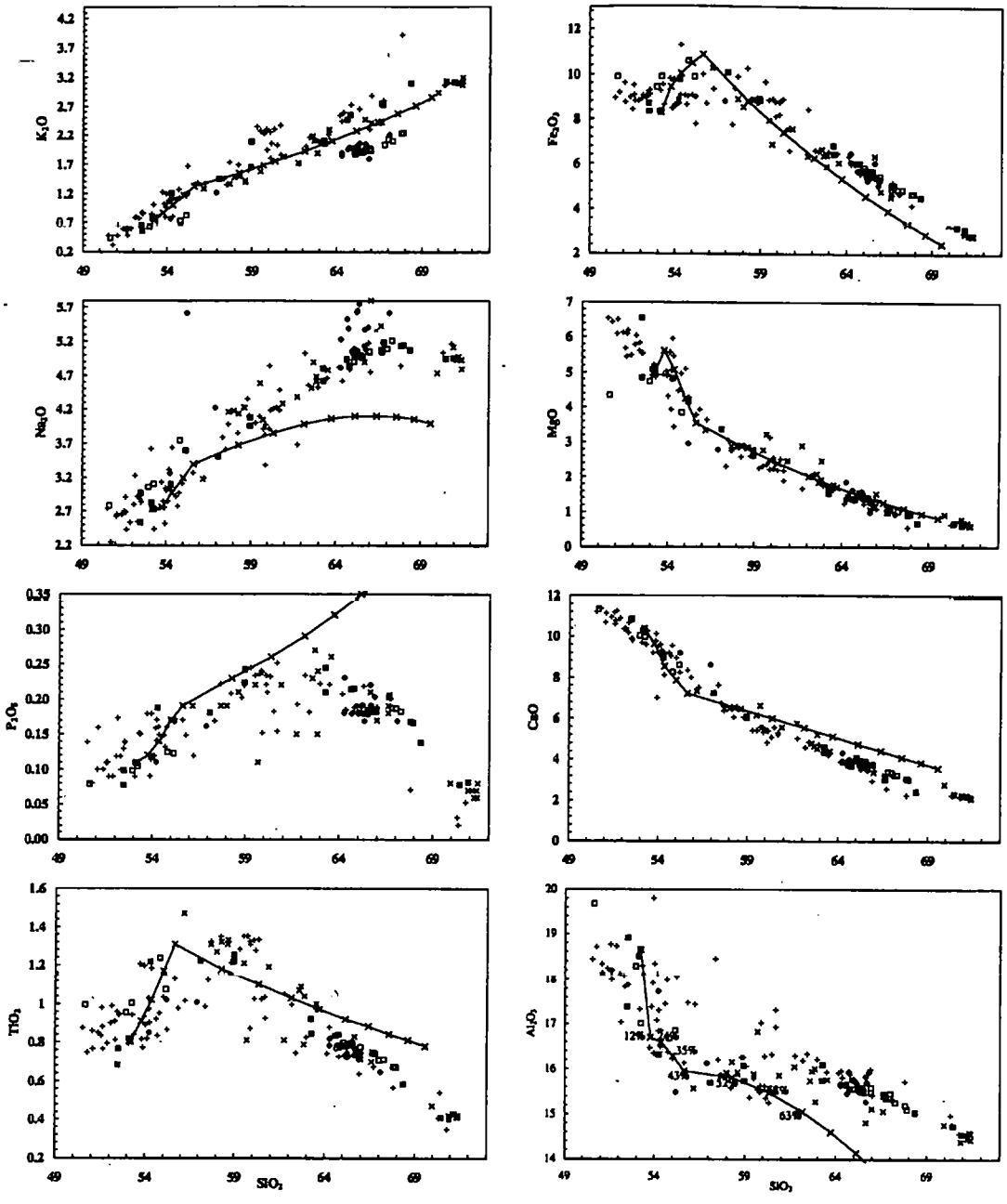

Figure 3-3: Major element trends with SiO_2 as differentiation index. Symbols as in Figure 3-4. MELTS modelling was performed at 1.5 kbar, using sample as2-Oia-1 as starting composition and an initial H_2O content of 0.7 wt%, an initial temperature of 1160°C (see text for details), and oxygen buffered at QFM+1. The amount of fractional crystallisation within each 20°C cooling interval is indicated on Al_2O_3 versus SiO_2. 50-60% crystal fractionation may produce andesites (up to ~60 wt% SiO_2) by fractional crystallisation from basaltic compositions. More felsic members of the SEC cannot be generated by fractional crystallisation.

3.4.2 Rock classification

Figure 3-4 shows that the analysed rock samples range from low-K basalts to high-K rhyolites. To classify the major element differentiation trends, previous workers have compared the development of calc-alkaline and tholeiitic rock suites on the basis of differences in their FeO^T/MgO ratio at different SiO_2 contents (Miyashiro, 1974; Figure 3-5a), and the relative variation in their total iron content using AFM diagrams (Figure 3-5b). Using Miyashiro's (1974) definition, most rock samples should be classified as tholeiitic due to their high FeO^T/MgO ratio. However, the position of the tholeiitic - calc-alkaline divide is somewhat arbitrary and the slope of a differentiation trend may thus be more informative than the composition of individual samples. Using this criterion, the Kameni dacites may be considered tholeiitic, while the scatter within the SEC precludes unambiguous classification as calc-alkaline or tholeiitic. On an AFM diagram (Figure 3-5b), the boundary of Kuno (1968) and of Irvine and Baragar (1971) have slightly different positions, but most samples from the SEC may be classified as calc-alkaline. Minor enrichments in total iron content, and hence tholeiitic affinities (Edwards, 1994), are evident for some samples at intermediate compositions and will be discussed in section 3.4.3. However, they are not pronounced enough to allow the entire sample suite to be classified as tholeiitic. It is concluded that classification of the sample suite depends on which criterion is employed, and that while it lies close to the tholeiite – calc-alkaline divide, many samples show little or no iron enrichment at intermediate compositions (Figure 3-5b) and may thus be considered to form part of a calc-alkaline suite.

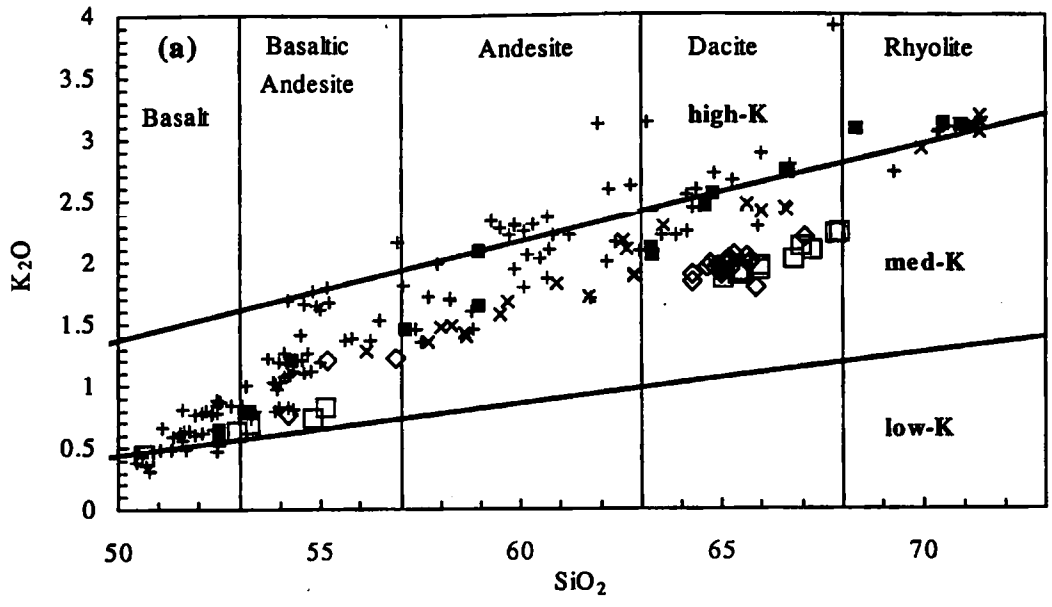

Figure 3-4: K_2O versus SiO_2 variation. The SEC (+,■) ranges compositionally from low K basalts to high K rhyolites. The Kameni lavas (◇,□) are dominantly dacitic, with some mafic xenoliths. Data sources: (+,◇) Huijsmans (1985), (×) Edwards (1994), (■,□) this study.

3.4.3 The generation of calc-alkaline magmatism at Santorini

The classification of volcanic rocks into tholeiitic and calc-alkaline on the basis of FeO^T/MgO ratios (Figure 3-5a) and iron enrichment trends (Figure 3-5b) has been practised for many years. A good discussion of the processes that may generate these trends was given by Edwards (1994) and is summarised here:

Iron enrichment at intermediate compositions is thought to be the result of early plagioclase fractional crystallisation of dry basaltic magma at low pressures (Grove and Baker, 1984). If the proportion of plagioclase in the early fractionating assemblage is reduced, Fe enrichment may be prevented and high-alumina basalts are generated. It has been suggested (Grove and Baker, 1984) that due to the shrinking of the plagioclase stability field at higher pressures (0.5 - 0.8 GPa) the proportions of olivine and augite in the fractionating assemblage increase, resulting in a considerable reduction in iron enrichment. Furthermore, H_2O destabilises plagioclase as an early crystallising phase,

resulting in an increased proportion of Fe-Mg silicates that crystallise early (Sisson and Grove, 1993), and if H_2O content reaches 4 wt%, magnetite will crystallise early as suggested by Osborn (1959) and Fe enrichment will be prevented (Conrey, 1997).

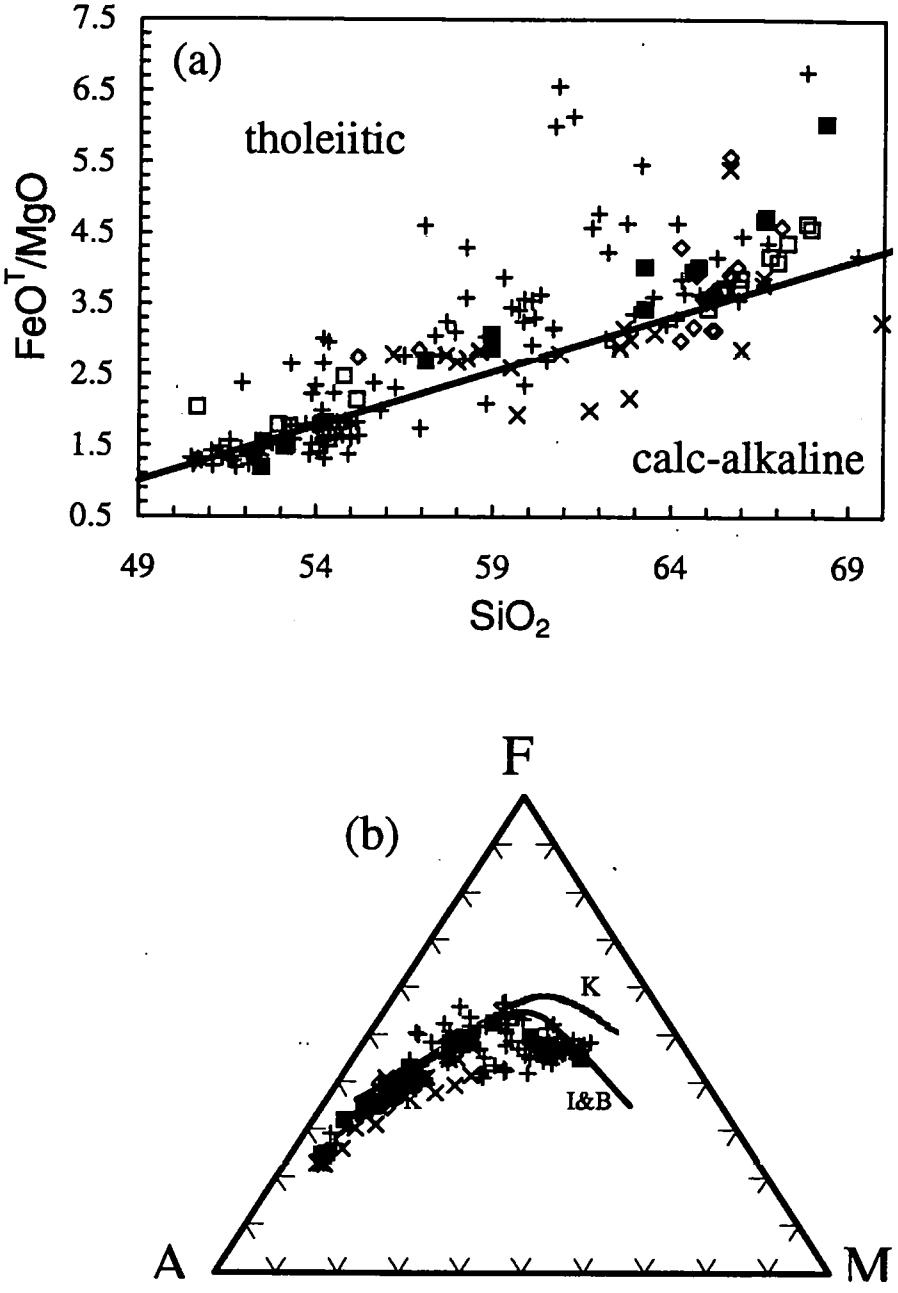

Figure 3-5: Symbols as in Figure 3-4. (a) FeO^T versus SiO_2. The straight line divides tholeiitic and calc-alkaline fields (Miyashiro, 1974). (b) AFM diagram. A = Na2O + K20, F = total Fe as FeO, M = MgO. Tholeiitic - calc-alkaline divides of Kuno (1968) and Irvine and Baragar (1971) are shown for reference. Where only FeO (T) was known, FeO was calculated assuming 85% of all Fe is FeO.

The scarcity of basaltic magmas (<53 wt% SiO_2) at Santorini makes it difficult to assess the processes responsible for their differentiation to andesitic compositions. However, if these processes are indeed dominated by fractional crystallisation, the low inferred H_2O contents of the basaltic andesites («1.5 wt%; Table 3-1) suggests that suppression of plagioclase crystallisation by high H_2O activities is unlikely. Furthermore, geobarometry limits pressure to less than 3 kbar for the basalts (Huijsmans, 1985), and although olivine and pyroxene are observed mineral phases, the observed crystallising assemblage is dominated by plagioclase. Thus, calc-alkaline magmatism at Santorini does not appear to originate from fractionation either at high pressures or from H_2O rich primary magmas.

Another way of generating a suite of calc-alkaline rocks is by mixing basic, relatively undifferentiated magmas, with more evolved silicic magmas (Sakuyama, 1983). Considering that shrinking of the plagioclase stability field is unlikely at low pressure and H_2O contents, magma mixing (Section 3.4.5) may indeed be of some importance in generating calc-alkaline trends at Santorini.

3.4.4 Fractional crystallisation modelling of the SEC

The major element patterns indicate that Na_2O and K_2O are broadly incompatible throughout the differentiation history of the SEC, although slight decreases in Na_2O at rhyolitic compositions are observed. MgO, CaO, Al_2O_3 and Fe_2O_3 remain broadly compatible. TiO_2 and P_2O_5 are incompatible at mafic compositions, but become compatible at andesitic (>57 wt% SiO_2) and dacitic compositions (>63 wt% SiO_2), respectively. Within the basalts and the basaltic andesites (<57 wt% SiO_2), these patterns are consistent with fractional crystallisation of the observed phenocrysts of calcic plagioclase + augite + olivine (Nicholls, 1971) (with olivine replaced by hypersthene at more intermediate compositions). At more felsic compositions, Fe_2O_3, TiO_2 and P_2O_5 behave compatibly, and this has been taken to reflect titanomagnetite and apatite

fractionation. Compatibility of Na_2O at rhyolitic compositions may indicate biotite fractionation (Huijsmans et al., 1988). Crystal fractionation is also consistent with the presence of gabbroic cumulates (Nicholls, 1971).

Least square mixing calculations were carried out by Mann (1983) to test if fractional crystallisation could quantitatively model the observed major element trends of the SEC. Using this method, basaltic andesites could be generated by up to 50% fractionation from a parental basalt, and andesites may be produced by up to 40% crystallisation from a basaltic andesite. The solid phases removed were calcic plagioclase, augite, and olivine. Dacites and rhyolites may be generated by up to 35% crystallisation from an andesite, removing plagioclase, clinopyroxene, orthopyroxene, Ti-magnetite and apatite. Discrepancies between the observed and calculated compositions, represented by the sum of the squares of the residuals, ranged from $\Sigma r^2 = 0.09$ to $\Sigma r^2 = 2.06$. Σr^2 values were generally greater than one during the early stages of crystallisation, indicating that discrepancies were small but significant.

While least square fractionation modelling produces the observed differentiation trends, it does not take into account available data on pre-eruptive pressure, temperature and oxygen fugacity constraints (Table 3-1). Thus, MELTS fractionation modelling has been conducted to see if simple fractional crystallisation is consistent with the available thermodynamic data, using MELTS Version 2.0.3 for the SUN workstation, released in March 1995. Although the MELTS calibration database is dominated by basaltic compositions, a considerable number of more evolved compositions have also been taken into account, notably at the relatively high total alkali contents also displayed by samples from Santorini. This suggests that the liquid-solid equilibria predicted by MELTS may be applicable to the entire compositional range observed at Santorini.

Sample 'as2-Oia-1' is the least evolved sample and was used as starting composition. A starting temperature of 1160°C was assumed, based on olivine-liquid geothermometry estimates on samples of similar SiO_2 content (Table 3-1). As pre-eruptive pressures have a limited range from 1-3 kbar to 1-2 kbar for mafic and felsic samples, respectively, isobaric crystallisation at 1.5 kbar was adopted in the MELTS models. Oxygen fugacities are buffered slightly above the Ni-NiO buffer (Huijsmans, 1985), and so MELTS modelling was conducted one log-unit above the quartz-fayalite-magnetite (QFM) buffer.

As the H_2O content of a cooling magma strongly influences the onset and extent of plagioclase crystallisation, and as plagioclase fractionation affects the Al_2O_3 content of the melt, Figure 3-6a serves to constrain the H_2O content of the starting composition. High H_2O contents inhibit early plagioclase fractionation. To model the relatively rapid decrease in Al_2O_3 with increasing SiO_2 within the basaltic andesites (53-57 wt% SiO_2), early plagioclase removal is required, thus constraining the H_2O content of the starting composition to ~0.7 wt%. This lies between the inferred H_2O contents of basalts and andesites from Santorini (Table 3-1). This H_2O content is low compared to estimates of >1.5 wt% inferred for more primitive samples from the Mariana arc (Stolper and Newman, 1994), but higher than H_2O abundances in more primitive samples from the Indonesian arc (0.21-0.38 wt% H_2O; Sisson and Bronto, 1998). However, as very primitive basalts have not been erupted at Santorini, the H_2O content of the primary magmas of Santorini is likely to be comparable to that of samples from the Indonesian arc. The latter were taken as evidence for the dominant control of decompression melting rather than slab fluid addition in the generation of destructive plate margin magmatism.

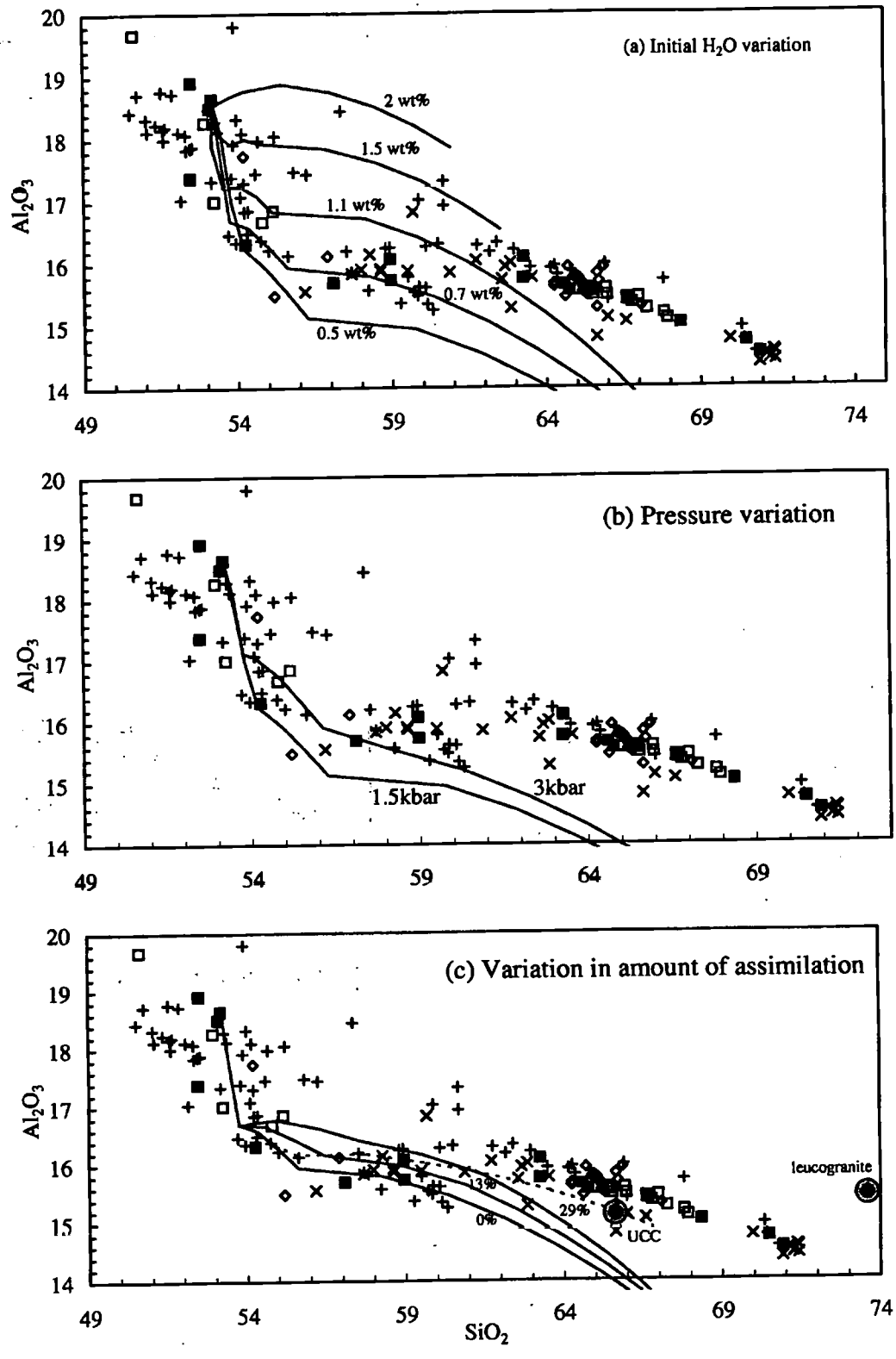

Figure 3-6: Symbols as in Figure 3-4. (a) Rapid initial decrease in Al_2O_3 at mafic compositions indicates relatively low H_2O contents of the basalts (≤0.7 wt%). (b) Fractional crystallisation trends are relatively insensitive to changes in pressure, and higher pressures do not seem to prevent plagioclase fractionation at more evolved compositions. Initial H_2O content was set to

0.5 wt%. (c) Assimilation of up to ~30% bulk UCC (solid line) and 30% leucogranite (dashed line). Initial H_2O content was set to 0.7 wt%. Again, the effect of crustal assimilation on the fractionation path is small. See text for discussion.

Closed system fractional crystallisation can explain the differentiation trends within the basaltic andesites and into andesitic compositions of the SEC, up to sample 'ap5-Sk' at ~59 wt% SiO_2 (Figure 3-3). At more evolved compositions, however, MELTS fractionation modelling fails to generate the observed differentiation trends, most notably for Al_2O_3 and Na_2O. At such compositions, and temperatures less than 1050°C, MELTS predicts extensive plagioclase fractionation which is not displayed to this degree by the data. In addition, MELTS overestimates the amount of albite fractionation relative to the amount of anorthite fractionation (cf. Na_2O and CaO trends in Figure 3-3). Increasing the modelling pressure to 3 kbar to suppress plagioclase fractionation does not have a significant effect on the modelled fractionation trends (Figure 3-6b). These observations either indicate that at more evolved compositions, closed system fractional crystallisation alone cannot be invoked to explain the observed differentiation trends within the SEC, or that the thermodynamic constraints on MELTS are insufficient to accurately predict the liquid line of descent at high silica compositions.

3.4.5 Alternative differentiation processes

Assimilation of crustal material in subvolcanic magma chambers is a well documented process (e. g. Bacon et al., 1989). In the South Aegean, the metamorphic basement mainly consists of glaucophane schists, eclogites, metavolcanic rocks (Kornprobst et al., 1979; Briqueu et al., 1986). Marbles are also abundant (Briqueu et al., 1986), and granitoids are found on Naxos (Andriessen et al., 1979; Pe-Piper et al., 1997), Serifos and Kos (Edwards, 1994). On Santorini, schists, quartzites, marbles and metamorphosed sandstones and meta-volcanites are found (Davies and Bastas, 1978). Given the large

variation in rock types in the Aegean basement (Table 3-2), upper continental crust (UCC; Taylor and McLennan, 1995) may be a first order approximation for the average composition of the Aegean basement.

	glaucophanite, Milos[1]	andesitic meta-volcanite, Santorini[2]	calc phyllite, Santorini[3]	quartzite, Santorini[3]	Upper Continental Crust[4]	Himalayan two-mica leucogranite[5]
SiO_2	57.25	59.21	36.10	86.40	65.61	73.59
TiO_2	1.70	1.13	0.15	0.10	0.50	0.13
Al_2O_3	15.50	19.87	4.60	2.30	15.13	15.44
Fe_2O_3	11.51	7.75	5.88	0.82	4.98	1.00
MnO	0.11	0.06	0.19	0.02	0.08	0.01
MgO	2.00	3.85	6.90	1.00	2.20	0.20
CaO	2.30	2.04	20.30	3.90	4.18	0.86
Na_2O	7.50	1.69	2.80	0.60	3.88	3.88
K_2O	0.70	5.00	1.60	1.50	3.36	5.00
P_2O_5	0.60	0.18			0.09	n. d.
H_2O			21.40	4.20		
quartz					16.75	32
orthoclase					19.86	21
albite					32.83	4
anorthite					13.94	33
diopsite					5.20	-
hypersthene					8.98	-
magnetite					0.86	-
ilmenite					0.95	-
apatite					0.21	-
muscovite					-	7
biotite					-	3

Table 3-2: Major element compositions of potential assimilants. Data sources: [1] Kornprobst et al. (1979), [2] Edwards (1994), [3] Davies and Bastas (1978), [4] Taylor and McLennan (1995), with calculated normative mineral assemblage, [5] Patiño Douce and Harris (1998), with mineralogy after Le Fort et al. (1987).

The effects of crustal assimilation were investigated using MELTS AFC facility (Figure 3-6c). The assimilated mineral assemblage (Table 3-2) was estimated by calculating the CIPW normative mineralogy of the major element composition of average UCC. In the absence of any direct constraints on the mineral assemblage of a potential assimilant, it is noted that this assemblage does not include any hydrous phases, and it is necessarily a very crude approximation. From Figure 3-6c it is apparent that assimilation of UCC does not result in significant deviations from the simple fractionation paths. Even 40% crustal assimilation is insufficient to increase modelled SiO_2 abundances by more

than ~3 wt% for andesitic compositions (at >15% Al_2O_3). Most notably, the steep slope of the modelled AFC trend towards very low Al_2O_3 abundances at dacitic compositions (63-68 wt% SiO_2) is retained. In summary, AFC processes that involve bulk rock assimilants are not able to produce the observed differentiation trend of the SEC at more evolved compositions.

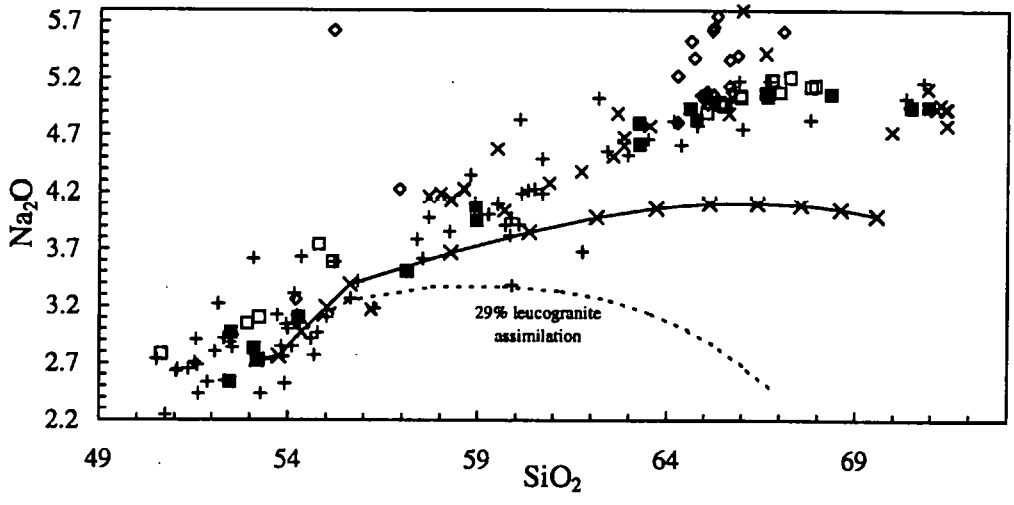

Figure 3-7: Na_2O versus SiO_2. Solid line and tick marks as in Figure 3-3. Dashed line represents 29% leucogranite assimilation. See text for discussion.

To establish if assimilating a partial melt of crustal material may generate the observed differentiation trends, a typical leucogranite has also been used as assimilated composition. Although leucogranites are not a major component of the Aegean crust (Edwards, 1994), they are found on Naxos (Pe-Piper et al., 1997), and melts of metapelites have been shown to be very similar in composition to leucogranites (Patiño Douce and Harris, 1998). The modelled differentiation path for ~30% assimilation of a leucogranite (Figure 3-6c) indicates that higher SiO_2 abundances may be reached without rapid decrease in Al_2O_3 content of the melt. However, relatively low Na_2O abundances in leucogranites compared to the dacites and rhyolites of Santorini result in rapid decrease of Na_2O with progressive AFC (Figure 3-7), and we conclude that assimilation by a crustal melt of composition similar to leucogranite is unlikely to generate the

differentiation trend of the SEC. Despite this conclusion, using MELTS modelling it is not possible to rule out assimilation of a magma generated by partial melting of crustal rocks, given the variety of rock types and possible residual mineralogies, and evidence from isotope constraints (Section 3.6).

In addition, there is evidence for magma mixing, based on the occurrence of compositionally banded pumices and hybrid andesites (Druitt et al., 1996), resorption textures within phenocrysts (Stamatelopoulou-Seymour et al., 1990) and crystal size distribution studies on dacitic lavas (Higgins, 1996). However, inflections of the major element differentiation trends at variable SiO_2 abundances (56 wt% SiO_2 for Fe_2O_3, MgO and Al_2O_3, 59 wt% SiO_2 for TiO_2, 62 wt% SiO_2 for P_2O_5, and 68 wt% SiO_2 for Na_2O; cf. Figure 3-3) limit the SiO_2 range for any mixing. The samples with relatively low P_2O_5 and TiO_2 abundances at intermediate compositions may be an exception (Figure 3-8). Their petrogenesis may be interpreted to reflect the rare case of mixing relatively mafic (< ~58 wt% SiO_2) with much more felsic (> ~65 wt% SiO_2) material.

3.4.6 The generation of high silica compositions: concluding remarks

This section is dedicated to Dr. Tim Elliott and Dr. Nick Rogers

MELTS fractionation modelling did not reproduce the observed differentiation trend at high SiO_2, particularly for Na_2O, CaO, Al_2O_3 and TiO_2. A number of explanations for this discrepancy may be put forward:

(1) Propagation of errors in the MELTS fractional crystallisation calculations will result in increasing uncertainties in the composition of the residual liquid with increasing SiO_2. Thus, it may be more appropriate to model the differentiation trend stepwise, using more than one starting composition with different silica values.

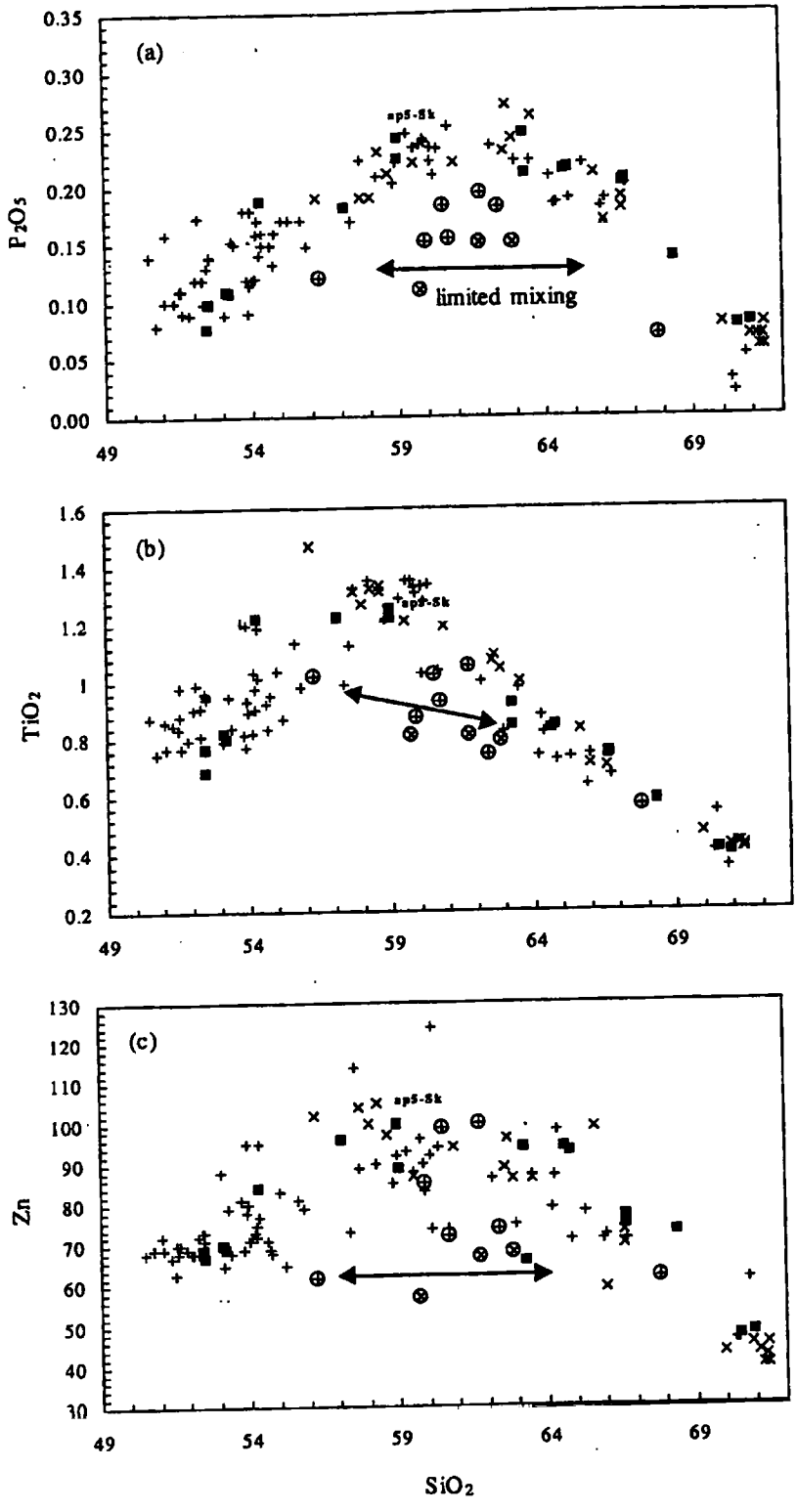

Figure 3-8: (a) P_2O_5 versus SiO_2, (b) TiO_2 versus SiO_2, and (c) Zn versus SiO_2. Symbols as in Figure 3-4. Samples with comparatively low P_2O_5 abundances are highlighted.

(2) Relatively few hydrous experiments are available in the calibration database of MELTS (Ghiorso and Sack, 1995). In addition, these are water saturated experiments, while natural magmas may be hydrous but undersaturated, which may have significant effects on the amount of plagioclase and magnetite crystallisation and the proportions of anorthite and albite (Panjasawatwong et al., 1995). Thus, the constraints on the fractionating assemblage used by MELTS may not be applicable to the dacites and rhyolites of the SEC.

(3) MELTS calculates the composition of a residual liquid that is crystal free. In contrast, samples from the SEC are porphyritic, and the dacites and rhyolites notably contain up to 20% plagioclase (Section 3.3.1). Consequently, these samples will have higher Al_2O_3 and Na_2O contents than predicted by MELTS fractionation modelling, as indeed is observed.

It is thus concluded that the petrogenesis of the dacites and rhyolites of the SEC may be *dominanted* by crystallisation processes, although there is evidence of crustal assimilation and limited magma mixing from the trace element (Section 3.5) and isotope (Section 3.6) data.

3.4.7 The Kameni lavas

Geochemical constraints on the petrogenesis of the Kameni dacites are poor because of their extremely restricted total range of composition. Nicholls (1971) interpreted the Kameni dacites as acid members of a rock suite whose more basic members are represented by the non-cumulate xenoliths of basaltic and basaltic andesite composition. However, the coincidence of the major element compositions of the Kameni enclaves with samples from the SEC suggests that as for the SEC, the dacites could not have been produced by simple crystal fractionation from magmas similar in composition to their mafic enclaves. In addition, MELTS modelling suggests that at dacitic compositions,

fractional crystallisation will produce a more rapid decrease in Al_2O_3 than displayed by the Kameni dacites. Hence, their small range in SiO_2 (65-68 wt%) is also unlikely to have been produced by differential crystal fractionation alone. The lack of intermediate compositions precludes major element modelling to constrain the petrogenesis of the Kameni dacites, and it is thus difficult to assess whether there is a geochemical relation between the dacites and their mafic enclaves or whether the mafic enclaves represent an entirely different suite of magmas that were incorporated into the dacites at a later stage.

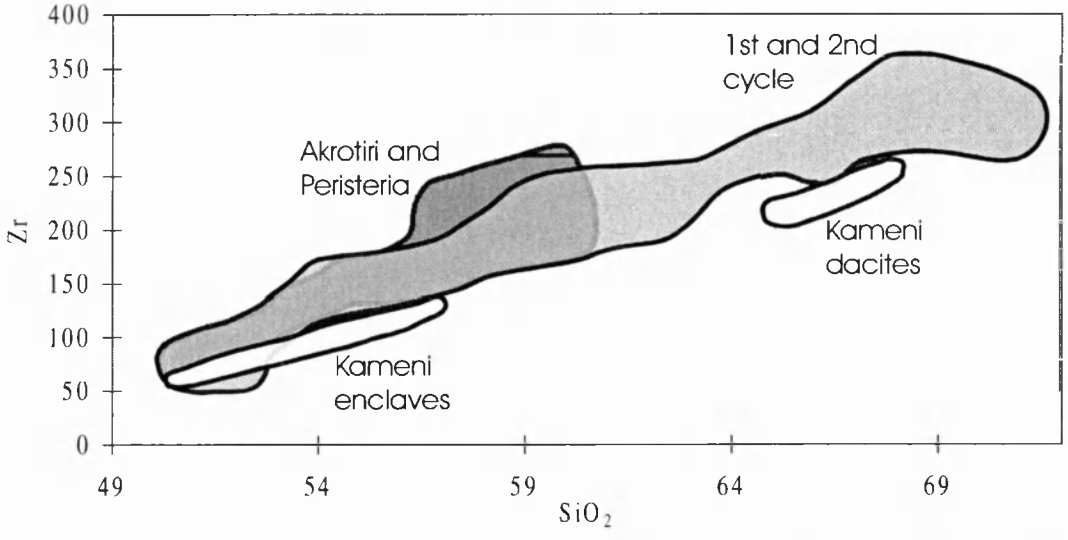

Figure 3-9: Slight decrease in incompatible element concentrations of the volcanic deposits of Santorini over time, illustrated on a diagram of Zr versus SiO_2.

3.5 Trace element geochemistry

The trace element and rare earth element abundances of the SEC and the Kameni dacites have been determined by XRF and INAA. The analytical techniques and data tables are given in Appendix A and Appendix D, respectively.

At Santorini, the incompatible trace element abundances of sample suites decrease slightly from the older volcanic products at Akrotiri and Peristeria to the deposits of the two eruptive cycles and the Kameni lavas at given SiO_2 contents (Figure 3-9). This is a

feature which Huijsmans et al. (1988) attributed to progressive incompatible element depletion of the upper mantle source region. However, the convergence of differentiation trends at mafic compositions suggest that the decreases in incompatible element abundancies may not be a source feature but could be due to slight differences in the differentiation paths of each sample suite. The trace element differentiation trends of individual suites of samples are nevertheless broadly similar, and those of the first eruptive cycle and SEC are indistinguishable. Again, the results from this section are restricted to observations from the SEC and the Kameni lavas, but they are applicable to the first eruptive cycle, and broadly to the earlier eruptive products from Akrotiri and Peristeria.

3.5.1 Results

With Ni and Cr contents generally well below 40 and 90 ppm, respectively, samples from the SEC are very evolved compared to primary magmas from the mantle which should have Ni and Cr contents above 200 ppm and 400 ppm, respectively (e. g. Smith et al., 1997). Within the SEC, increases in Ba, Nb, Zr, Y and Rb, and decreases in Sr (Figure 3-10) and more pronounced in Sc are observed with increasing SiO_2. Zn initially increases up to ~60 wt% SiO_2 and then decreases. V increases slightly up to ~57 wt% SiO_2 and then decreases sharply (Figure 3-10). The concentrations of the rare earth elements increase with increasing SiO_2, with the exception of Eu which increases slightly up to ~60 wt% SiO_2 and then decreases.

The Kameni dacites have lower incompatible trace element concentrations than the deposits of the SEC at similar SiO_2 contents. No significant compositional shift is observed for trace elements that behave compatibly at >63 wt% SiO_2 (Zn, Sr, Sc, V and Eu).

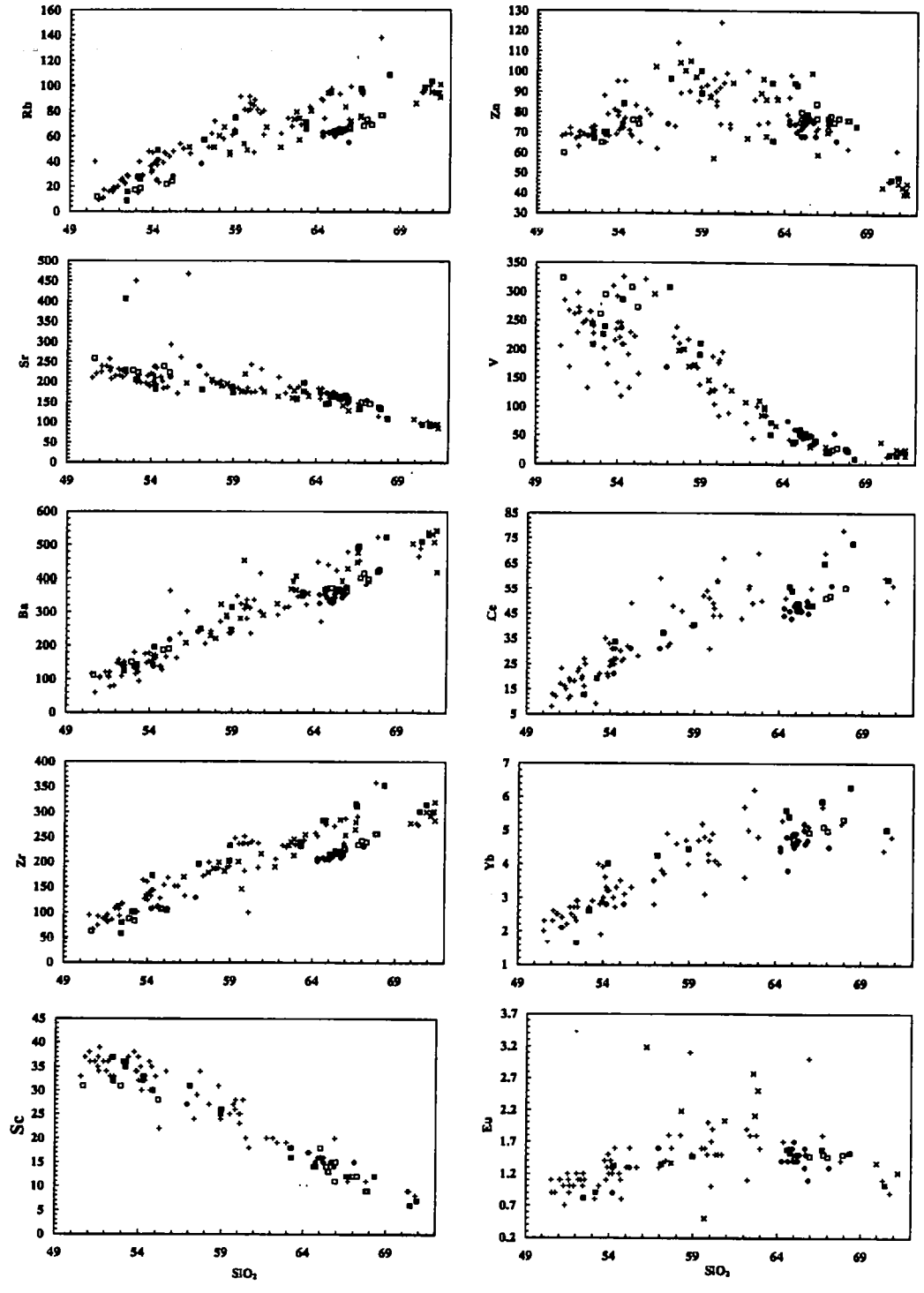

Figure 3-10: Trace element trends with SiO_2 as differentiation index. Symbols as in Figure 3-4. See text for discussion.

Figure 3-11 is a plot of incompatible trace elements normalised to N-MORB, including selected rare earth elements (REE). While the heavy REE have a broadly flat pattern and, for the most primitive samples, the heavy REE concentrations are similar to N-MORB, all samples show enrichments in light REE. Large ion lithophile elements (LILE) and U are significantly enriched compared to most high field strength elements (HFSE).

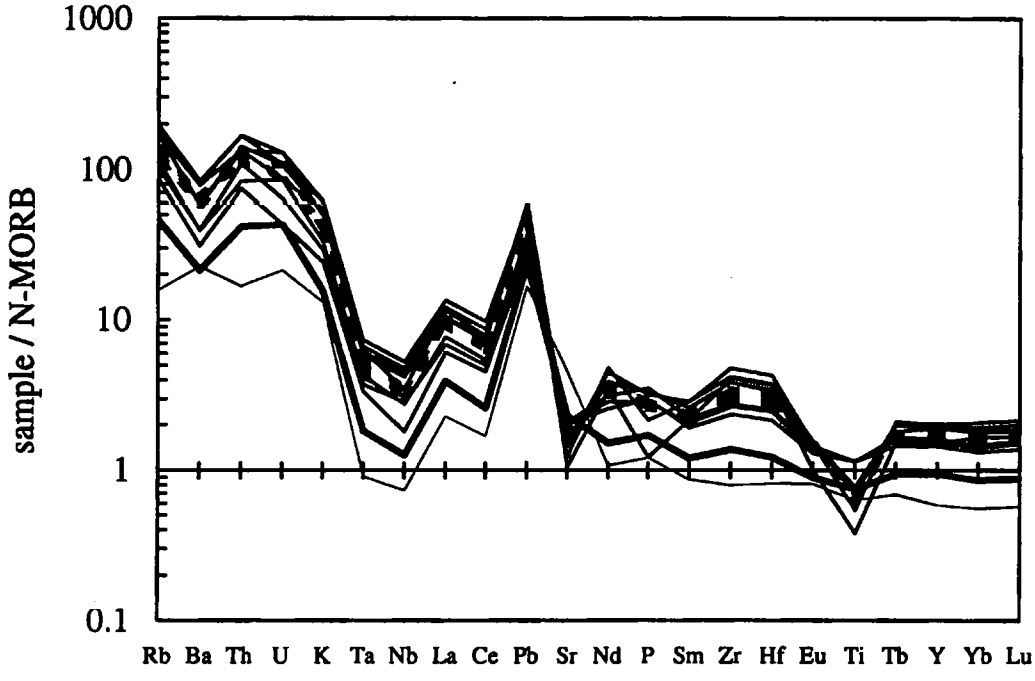

Figure 3-11: Incompatible trace element diagram. Thin solid line is sample 'ap5-Nod-Oia', thick solid line is sample 'as2-Oia-1'. Other solid lines are other SEC samples. Dashed lines are the Kameni dacites. Samples display enrichment of LREE over HREE, high LILE abundances, and negative Ta and Nb anomalies characteristic for destructive plate margin magmatism. See text for discussion.

3.5.2 Fractional crystallisation modelling

Mann (1983) modelled trace element variations in lavas of the SEC by simple fractionation. Considering the trace elements alone, the proposed generation of the entire compositional range of the SEC by crystal fractionation seems plausible (Figure 3-12a), although for the more evolved samples slight discrepancies are apparent between the

modelled and observed differentiation trends for some elements (Figure 3-12b-d). However, Mann (1983) found that the amount of fractionation required to generate the rhyolites was 15-20% higher than suggested by major element least square mixing calculations, and MELTS modelling has shown that simple crystal fractionation processes are unlikely to generate the major element trends of the dacites and rhyolites.

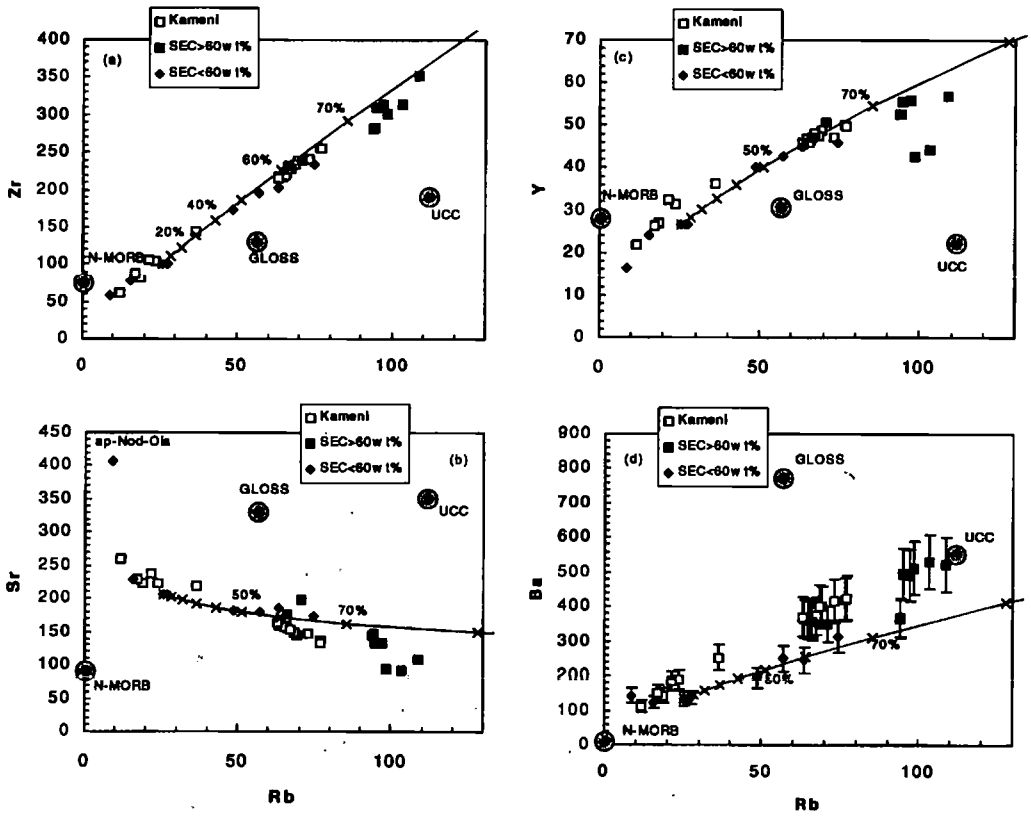

Figure 3-12: Trace element crystal fractionation modelling. The SEC is divided into samples with less than 60 wt% SiO_2 (◆) and samples with more than 60 wt% SiO_2 (■). Open symbols are the Kameni dacites and their mafic xenoliths. Using sample 'as2-Oia-1' as starting composition, andesites may be generated by up to 65% crystal fractionation. The fractionation trends do not satisfactorily reproduce the trace element compositions of the dacites and rhyolites. D_{Rb} was set to 0. Modelled partition coefficients were $D_{Zr} = 0.12$, $D_{Sr} = 1.2$, $D_Y = 0.4$ and $D_{Ba} = 0.3$. These correspond to bulk partition coefficients of $D_{Rb} = 0.057$, $D_{Zr} = 0.09$, $D_{Sr} = 0.78$, $D_Y = 0.14$ and $D_{Ba} = 0.40$ calculated for a fractionating assemblage of 63% plagioclase, 23% clinopyroxene and 14% orthopyroxene, as suggested by MELTS modelling of 50-60 wt% crystal fractionation at low initial H_2O contents. Mineral-melt partition coefficients used in the calculation are given in Appendix B8.

Thus in this study, fractional crystallisation modelling of trace element variations is only discussed for samples with less than 60 wt% SiO_2. Rb was used as a differentiation index in Figure 3-12 as it is a highly incompatible element in the fractionating assemblage of dominantly plagioclase and pyroxene, and its partition coefficient was set equal to zero. The partition coefficients of selected elements were modelled by adjusting the calculated fractionation trends to mirror the differentiation trends displayed by the trace element data, using sample 'as2-Oia-1' as endmember composition. This sample, although not the most mafic sample of this study, was chosen on basis of availability of INAA data. The modelled partition coefficients are of the same order of magnitude as the expected bulk partition coefficients of a fractionating assemblage involving 63% plagioclase, 23% clinopyroxene and 14% orthopyroxene, as suggested by MELTS modelling of 50-60 wt% crystal fractionation at low initial H_2O contents (see caption to Figure 3-12 for details). In addition, trace element modelling suggests that andesites may be generated by up to ~65 wt% fractional crystallisation from sample 'as2-Oia-1'. Thus, these independent estimates for major and trace element modelling are similar for fractionation modelling of the basalt to andesite differentiation trend (< ~60 wt% SiO_2), suggesting that both qualitatively and quantitatively, the differentiation trend of the less evolved samples may be dominated by simple crystal fractionation.

3.5.3 Open system differentiation processes

Assimilation of high SiO_2 crustal melts and magma mixing as identified in Section 3.4.5 is difficult to detect using trace element variation diagrams as differentiation trends are generally sublinear. A significant range in Zn abundances at intermediate compositions may be an exception (Figure 3-8c), and again demonstrates the scarcity of mixing of relatively mafic (< ~58 wt% SiO_2) with much more felsic (> ~65 wt% SiO_2) material. To assess the control of open system processes on the petrogenesis of the dacites and

rhyolites (> ~60 wt% SiO_2) on a more rigorous, quantifiable basis, incompatible trace element ratio diagrams have been employed (Figure 3-13). Modelled endmembers were the andesite 'ap5-Sk' (59 wt% SiO_2) and the Minoan rhyolite 'rp7a-2' (70.5 wt% SiO_2). The andesite was chosen on the basis of the extrapolation of major element trends at dacitic compositions (63-68 wt% SiO_2; Figure 3-3 and Figure 3-10) towards more mafic compositions. The rhyolite was chosen as the high silica endmember since there are no constraints on other, possibly more felsic endmember compositions. Element ratios have been chosen so that the effects of crystal fractionation are minimised.

The dacites and rhyolites form a linear array that is indicative for magma mixing and cannot be produced by fractional crystallisation, suggesting that open system processes may indeed dominate the petrogenesis of these samples. In addition, open system behaviour does not appear to control the differentiation of the more mafic samples of the SEC that show little consistent variation and a slightly smaller total range when sample 'ap5-Nod-Oia' is excluded. This sample has a positive Eu anomaly and a low $^{87}Sr/^{86}Sr$ ratio compared to other samples from the SEC. The Eu anomaly is interpreted as evidence for plagioclase accumulation, which may account for some of the shift to higher Tb/Yb ratios due to the relatively high Tb/Yb exchange partition coefficient (cf. Beattie et al., 1993) of plagioclase ($D_{Tb}/D_{Yb}>2$), although the concentration of these elements in plagioclase is very low. The higher La/Yb ratio of the other samples of the SEC may be due to assimilation of some crustal material during their petrogenesis, with upper crustal La/Yb ratios of 12-15. The influence of crustal assimilation is discussed in Section 3.6, which includes further evidence for the association of variations in trace element ratios with open system behaviour.

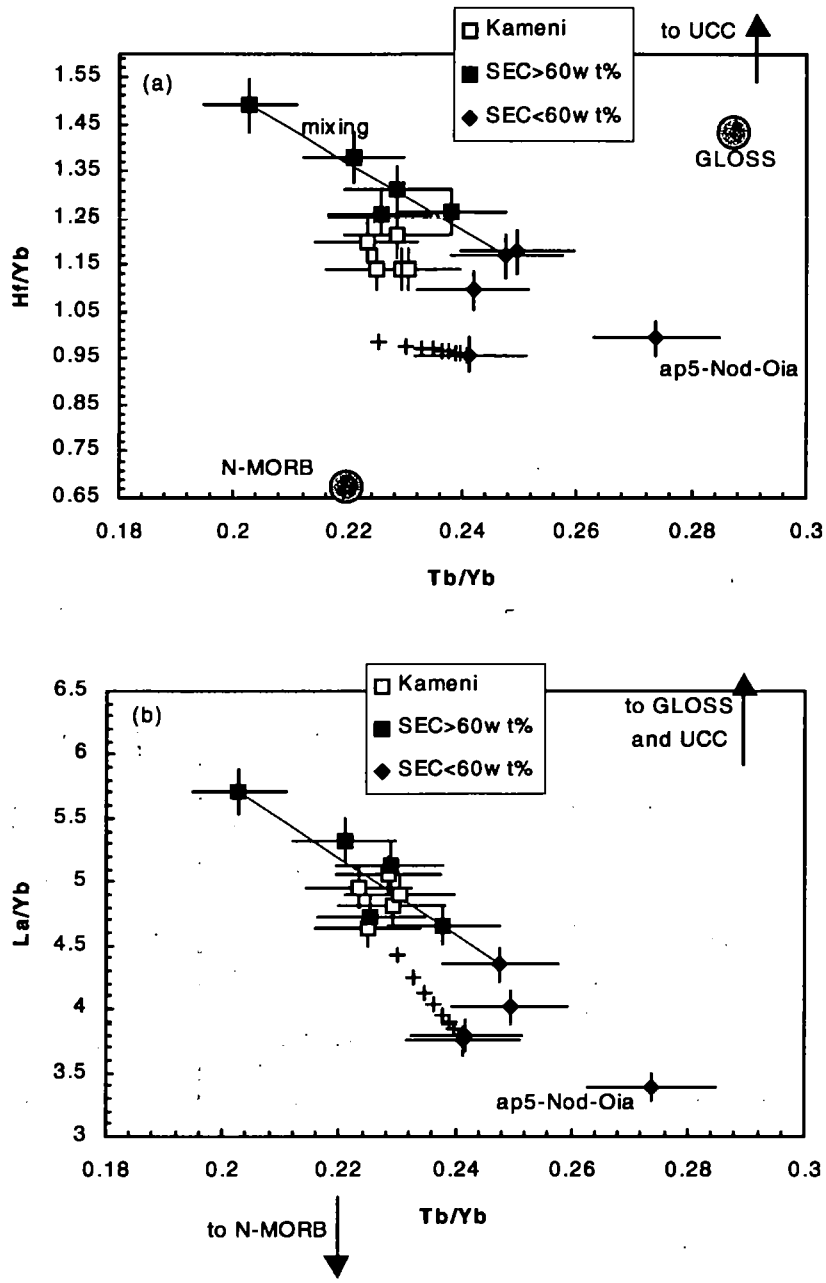

Figure 3-13: Trace element ratio diagrams. Symbols as in Figure 3-12. Fractionation modelling (+, at 10% intervals) indicates that the effect of crystal fractionation is negligible on such diagrams. See Appendix B8 for partition coefficients and text for discussion.

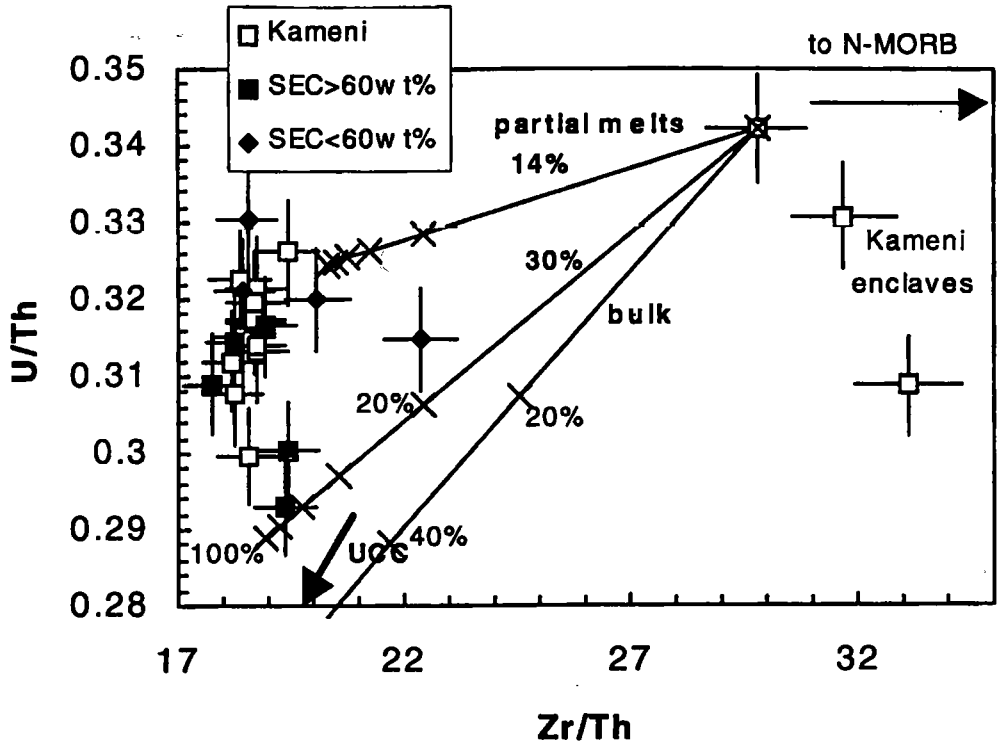

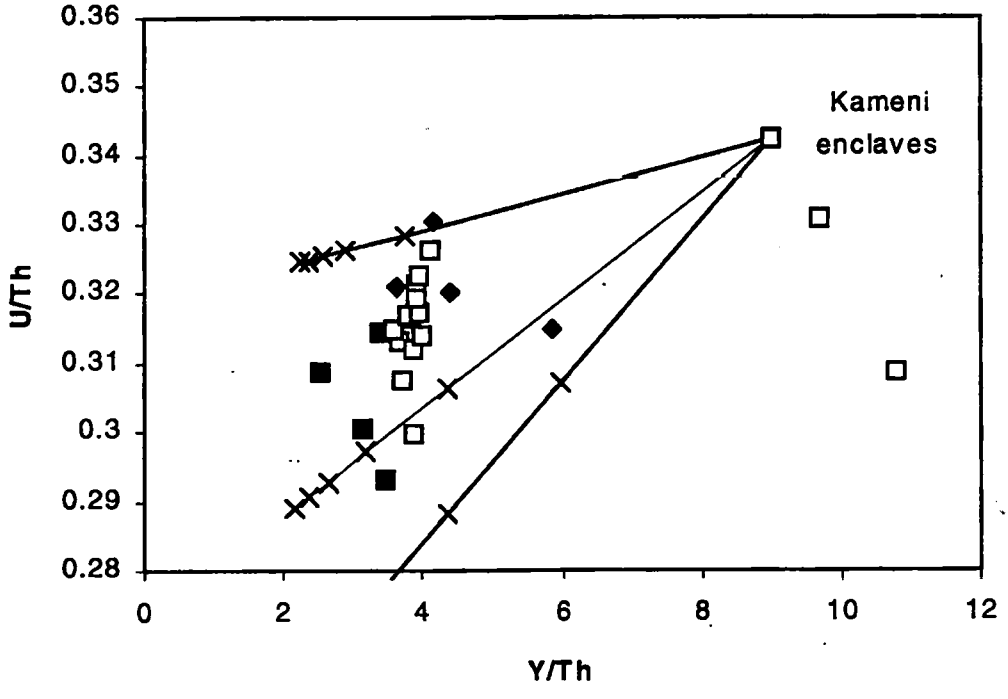

Figure 3-14: (a) U/Th versus Zr/Th. Symbols as in Figure 3-12. Mixing (at 20% intervals) of the high U/Th Kameni enclave with upper continental crust (UCC) from Taylor and McLennan (1995) and with partial melts of UCC (both 14% and 30%) are modelled. (b) U/Th versus Y/Th. Model endmembers and tick marks as in (a). See text for discussion.

3.5.4 The Kameni lavas

Due to the lack of intermediate compositions, trace element variation diagrams offer little insights into the petrogenesis of the Kameni dacites and their non-cumulate mafic enclaves. As no INAA data are available for the enclaves, only few incompatible trace element ratios can be used to assess a possible geochemical relation between the dacites and their enclaves. The U/Th ratios of both the dacites and the enclaves vary (Figure 3-14), with two of the enclaves displaying the highest U/Th ratios of the Kameni lavas. In addition, both Zr/Th and Y/Th ratios of the dacites are constant and much lower than those of the enclaves.

There is no evidence for abundant fractionation of accessory phases such as apatite or zircon that may differentiate U from Th. Alternative processes that may introduce the observed range in U/Th ratios in both the dacites and their enclaves are crustal assimilation or magma mixing, and differential uranium addition from slab fluids to their mantle source. While magma mixing is suggested by CSD studies (Higgins, 1996), it should be evident from variations in other trace element ratios if it is considered responsible for the range in U/Th. However, the relatively constant La/Yb, Tb/Yb and Hf/Yb ratios of the Kameni dacites suggest that magma mixing is unlikely to have introduced the observed range in U/Th ratios. Thus, differential U addition by slab fluids to the source region of the dacites may be a better explanation for U/Th variation in the Kameni lavas.

To assess if crustal assimilation may explain the differences in Zr/Th, Y/Th and U/Th ratios of the enclaves and the dacites, simple mixing of the high U/Th enclave with both bulk upper continental crust material and partial melts of crust has been modelled. To generate low Zr/Th ratios, ~80% bulk crustal addition is required, although this produces U/Th ratios lower than those observed in the Kameni dacites. Mixing with partial melts

of continental crust may result in higher U/Th ratios but fails to produce low Zr/Th ratios. This however assumes that no residual zircon is present during melting of the crustal assimilant. Residual zircon would result in considerable decrease in Zr/Th. Notably, the Y/Th ratios of the dacites could be produced from the high U/Th enclave by 20-30% assimilation of a partial (~15-30%) melt of UCC (Figure 3-14b). However, variable crustal assimilation is not consistent with constant REE ratios within the dacites. In conclusion, simple crustal assimilation is unlikely to have generated the dacites from compositions similar to the mafic enclaves, suggesting that the dacites are geochemically unrelated to their enclaves, and that the enclaves represent an influx of fresh, mafic and geochemically distinct magma into the dacitic host.

3.5.5 Implications of the incompatible element patterns

Incompatible element abundances are compared to N-MORB in Figure 3-11 to obtain information about the parental magmas. The pattern displays negative Sr and Eu anomalies for all but one sample, indicating early fractionation of plagioclase. Sample ap5-Nod-Oia has a small positive Eu anomaly and compared to all other samples it is enriched in Sr and Ba. This is interpreted to result from plagioclase accumulation, which is supported by its highly plagioclase phyric texture. Although mixing may be important within the dacites (63-68 wt% SiO_2), the depletion of Ti abundances in the dacites and rhyolites (Figure 3-11) suggests magnetite fractionation (cf. Section 3.3). Only the rhyolites display negative P anomalies, and these imply that apatite fractionation occurs within the very evolved samples. This is also apparent from the inflected P_2O_5 versus SiO_2 trend in Figure 3-3.

One of the less evolved samples (as2-Oia-1, [Ni] = 26 ppm, [Cr] = 42 ppm, Mg# = 54) may be used to obtain information about the primary magmas: for example, garnet readily accommodates HREE and Y, and at low degrees of melting would result in

strong fractionation of these elements in the primary magma relative to MORB (Figure 3-15). The flat HREE patterns (Figure 3-11) suggests that either mantle melting occurs at less than ~100 km depth in the spinel stability field, or that the degree of melting was so large that any residual garnet ceased to significantly affect LREE/HREE ratios. Incompatible trace element modelling (Chapter 4) suggests that the degree of mantle melting is high, between 15 and 20%, in agreement with previous estimates for subduction related source melts (Pearce and Parkinson, 1993), suggesting that beneath Santorini, melting in the garnet stability field may be possible without significantly fractionating the REE.

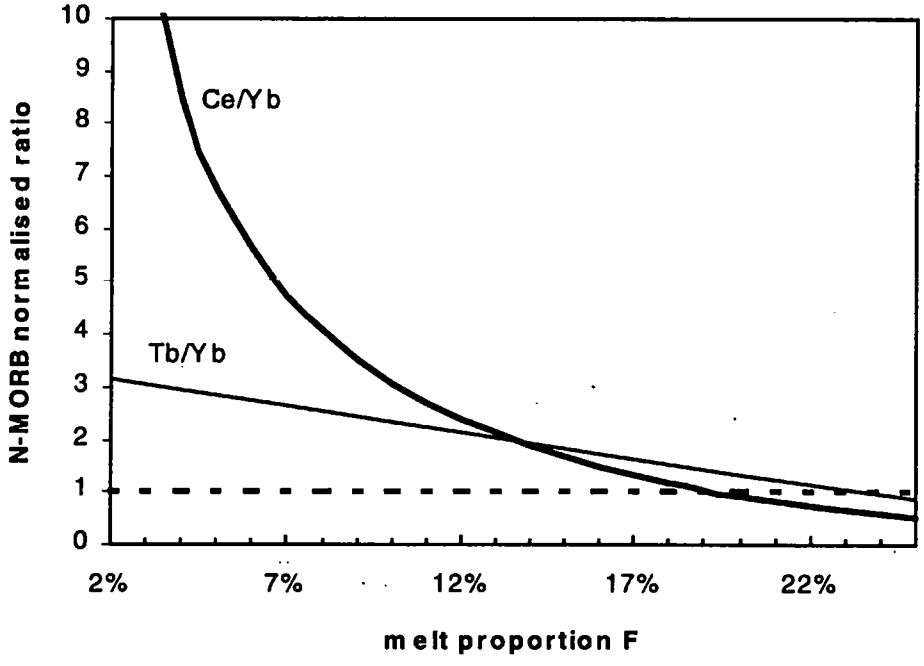

Figure 3-15: Effect of garnet as residual phase on REE ratios during non-modal mantle batch melting. At low degrees of melting, residual garnet fractionates the REE. Flat HREE profiles imply that either the degree of melting was high, or that garnet was not a residual phase during melting. Garnet lherzolite phase proportions (ol:opx:cpx:grt = 55:25:10:10) and melting mode (ol:opx:cpx:grt = 5:5:45:45) are from Greenough (1988).

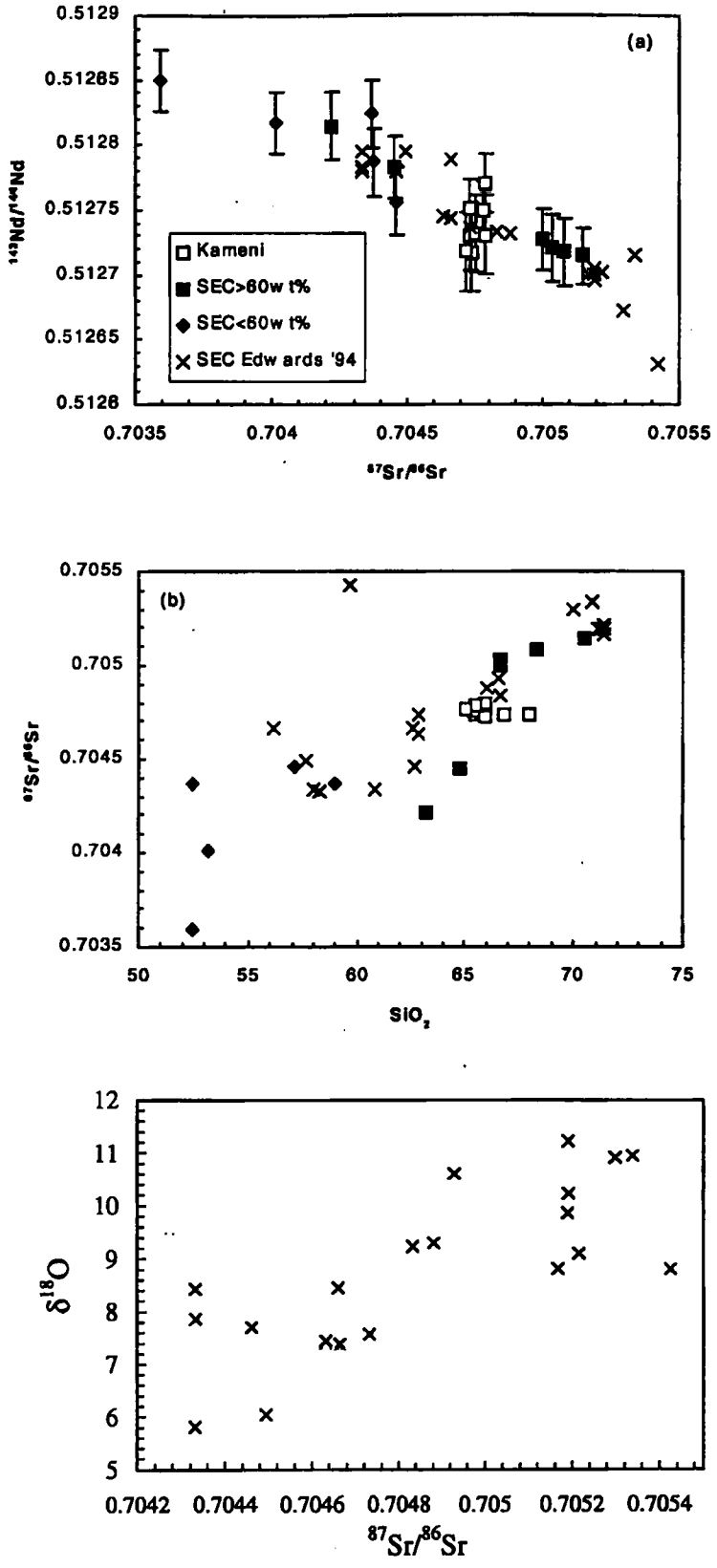

Figure 3-16: Sr and Nd isotopic variations. Symbols as in Figure 3-12. (a) $^{143}Nd/^{144}Nd$ versus $^{87}Sr/^{86}Sr$. (b) Sr isotopes versus SiO_2. (c) $\delta^{18}O$ versus $^{87}Sr/^{86}Sr$ (after Edwards, 1994). See text for discussion.

In consequence, relative enrichment of the LREE over the HREE is not due to low degrees of melting in the presence of residual garnet, but suggests that the source was enriched in light REE, possibly due to addition of subducted sediments. The LILE and U are amongst the most enriched elements. As all LILE and U^{6+} are fluid mobile (e. g. Brenan et al., 1995; You et al., 1996; Ayers, 1998), some of their enrichment may be attributed to addition of hydrous fluids from the subducted slab. Quantitative constraints on these processes may be obtained by incompatible trace element modelling (Chapter 4).

3.6 Sr and Nd isotope constraints

3.6.1 Results

$^{87}Sr/^{86}Sr$ and $^{143}Nd/^{144}Nd$ ratios of the SEC range from ~0.7036 to ~0.7054 and from ~0.51285 to ~0.51263, respectively, and are negatively correlated (Figure 3-16a). There is a broad positive correlation of Sr isotopes with SiO_2 (Figure 3-16b), although less pronounced in the less evolved samples (<60 wt% SiO_2), and Edwards (1994) has indentified a broad positive correlation of Sr isotope ratios with $\delta^{18}O$ values (Figure 3-16c). The Kameni dacites have constant Sr and Nd isotope ratios of ~0.70475 and ~0.51275, respectively.

3.6.2 Modelling of open system processes

The general increase of Sr isotope ratios with increasing silica suggests that the range in Sr and Nd isotopes was produced during magmatic differentiation, and the broad correlation with $\delta^{18}O$ values suggests that variable upper crustal contributions are responsible for the range in Sr and Nd isotopes. Thus, most samples contain a crustal component, although sample 'ap5-Nod-Oia' has been contaminated least, in agreement with results from trace element modelling (Section 3.5.3). Little crustal assimilation has

occurred during fractional crystallisation processes within the basaltic andesites (< 57 wt% SiO_2), as indicated by relatively constant Sr isotope ratios. The good positive correlation of Sr isotopes with SiO_2 at high silica abundances implies that open system behaviour is most pronounced for the dacites and rhyolites.

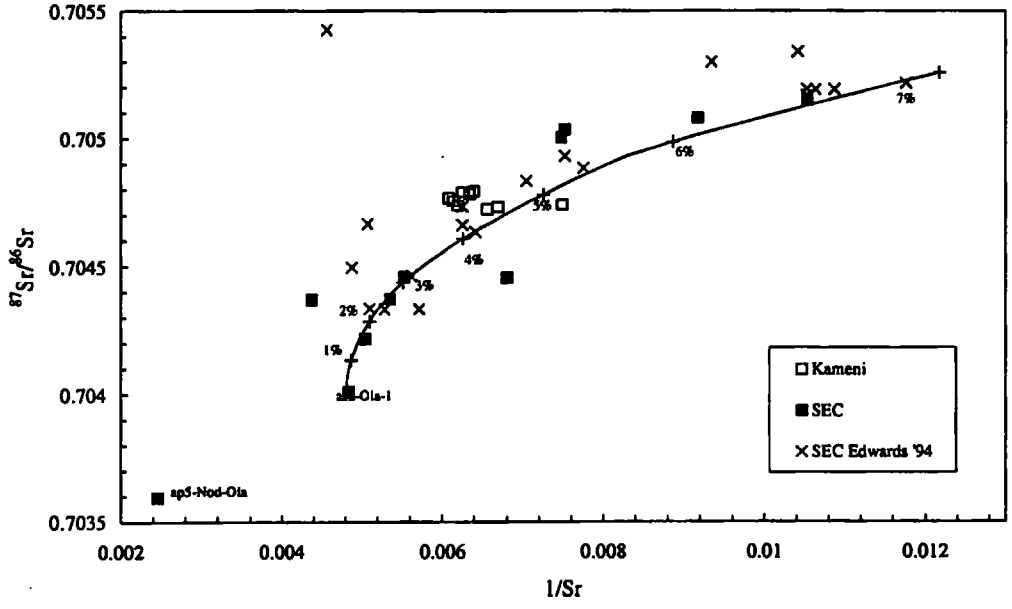

Figure 3-17: $^{87}Sr/^{86}Sr$ versus 1/Sr. Symbols as in Figure 3-12. AFC modelling, as envisaged by Edwards (1994), was performed using sample as2-Oia-1 as starting compositions. Up to 7% crustal assimilation would be required to produce the observed range in Sr isotopes. The crustal endmember was taken to have 350 ppm Sr, with and $^{87}Sr/^{86}Sr$ ratio of 0.7122. The bulk partition coefficient of Sr was continuously increased from 0.8 to 2.8 to account for changes in plagioclase composition during differentiation.

Edwards (1994) modelled trace element – isotope covariations by simple AFC processes (DePaolo, 1981, see Appendix B for details). However, during magmatic differentiation, Sr bulk partition coefficients are likely to change (Blundy and Wood, 1991), and this is not taken into account by the AFC equation. Hence in Figure 3-17, the range in Sr isotopes has been modelled with variable Sr partitioning. Starting composition was sample 'as2-Oia-1' ($^{87}Sr/^{86}Sr = 0.7040$, 207 ppm Sr). The assimilating endmember was taken to have 350 ppm Sr, equal to UCC (Taylor and McLennan, 1995), with an

$^{87}Sr/^{86}Sr$ ratio of 0.7122. Note that this Sr isotope ratio is considerably lower than that calculated for 1.5 Ga old average upper crust (~0.723) used by (Barton et al., 1983). The bulk partition coefficient of Sr was continuously increased from 0.8 to 2.8 to account for changes in plagioclase composition during differentiation. Assimilation of 6-7% crustal material can explain the range in Sr isotope ratios from basaltic andesites to rhyolites (Figure 3-17).

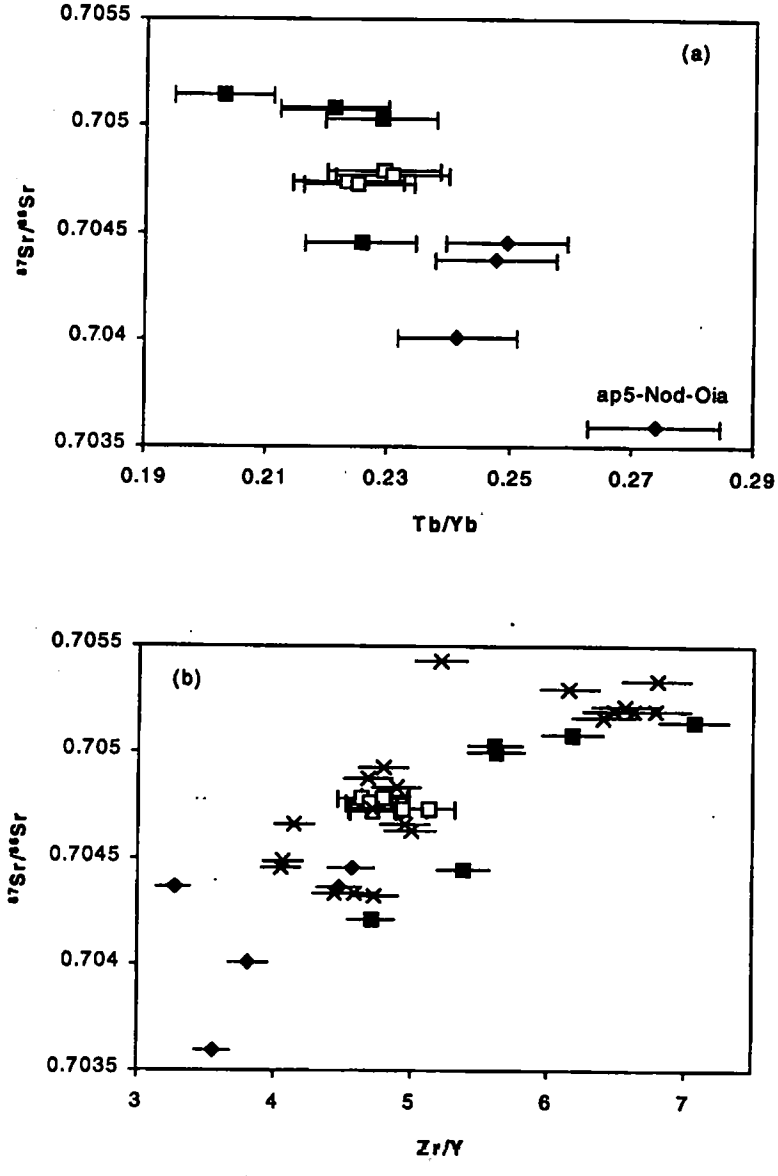

Figure 3-18: (a) $^{87}Sr/^{86}Sr$ versus Tb/Yb. (b) $^{87}Sr/^{86}Sr$ versus Zr/Y.

The coincidence of Sr and Nd isotope composition of the Kameni dacites with the trend of the SEC suggests that the Kameni dacites have suffered considerable amounts of crustal assimilation (Figure 3-16a). However, the constancy of both Sr and Nd isotope ratios implies that their degree of assimilation was very similar.

3.6.3 Combined trace element and isotope evidence

Figure 3-18a shows that Tb/Yb ratios are correlated with $^{87}Sr/^{86}Sr$ ratios. This supports the notion that open system processes such as crustal assimilation control the range in HREE ratios, and that closed system fractional crystallisation has comparatively little influence. $^{87}Sr/^{86}Sr$ ratios are plotted against Zr/Y in Figure 3-18b. Again, the range in incompatible trace element ratios is greater for the more evolved samples ($SiO_2 > 60$ wt%), suggesting that open system processes are more prominent at higher silica abundancies, and that early differentiation may be dominated by fractional crystallisation.

3.7 Along-arc geochemical variations

3.7.1 Introduction

With the exception of Santorini and Nisyros, little geochemical work has been done on the volcanic centres of the Aegean Arc. This section is an attempt to compare the general geochemistry of Santorini with other volcanic centres, namely Aegina, Methana, Poros and Milos in the Northwest and Nisyros in the East (Figure 2-1). In addition, fields for the low Ce/Yb, depleted Tonga-Kermadec arc and the high Ce/Yb, calc-alkaline Andes Central Volcanic Zone (CVZ) and Aeolian islands are given as a frame of reference.

The volcanic rocks of the Aegean Arc belong to a typical calc-alkaline suite and are dominated by andesitic to rhyolitic compositions (Keller, 1982). Only Santorini has significant amounts of basaltic lavas (Nicholls, 1971). The main processes for the

formation of the more felsic differentiates are thought to be fractional crystallisation (Nicholls, 1971; Pe, 1973; Mann, 1983), crustal assimilation (section 3.4.5) and magma mixing (Francalanci et al., 1995; Higgins, 1996).

3.7.2 Along-arc magma source variations

Early work by Mitropoulos et al. (1987) identified large variations in trace element abundances and ratios between the different volcanic centres and attributed this to heterogeneous source regions in the subcontinental lithosphere beneath the Aegean region. Since then, there has been evidence for multiple source components in the generation of destructive plate margin magmatism (e. g. Hawkesworth et al., 1993; Elliott et al., 1997; see also Chapter 1), and attempts are made here to compare the volcanic centres of the Aegean Arc in terms of sediment input, slab fluid input, and other source parameters. Incompatible trace element ratios are useful to identify such processes as they are not significantly differentiated by high level fractional crystallisation.

Subducted sediments have higher La/Nb ratios than the upper mantle, and so differential involvement of subducting sediments in the petrogenesis of magmas along the arc should be preserved in their La/Nb ratios. Figure 3-19a shows that the Aegean arc has similar La/Nb ratios to the Aeolian islands and the Andes CVZ, low compared to many samples from the Tonga-Kermadec arc which has La/Nb ratios has high as 20 and has been omitted on Figure 3-19a as it would compress the scale. La/Nb does not vary with degree of differentiation, and there is no evidence for differential sediment addition between Santorini and the northwestern centres of the arc. Nisyros is displaced to slightly lower La/Nb ratios. This may be interpreted as evidence for slightly lower sediment input in the eastern parts of the arc, where transform motion rather than subduction dominates at the trench, as evidenced by the paucity of Pleistocene sediment fill (Le Pichon et al., 1979).

Figure 3-19b shows that the Aegean Volcanic Arc has Ce/Yb ratios intermediate between the low Ce/Yb Tonga-Kermadec arc and the high Ce/Yb Aeolian islands and Andes CVZ. The high Ce/Yb of the latter are probably due to crustal assimilation (cf. Figure 3-20). While Ce/Yb ratios may be affected by differential sediment addition, Nisyros has in fact higher Ce/Yb ratios than Santorini. This would appear to contradict the argument that less sediment had been added to the source, or Ce/Yb ratios may be governed by another process. Differential crustal assimilation could account for differences in Ce/Yb ratios, but Sr isotopes suggest that the amount of crustal contributions to magmas from Santorini and Nisyros was similar (Figure 3-20). Finally, Ce/Yb exchange partition coefficients are well below 1, and variable degrees of melting may affect Ce/Yb ratios, even when garnet is not a residual phase in the source as implied by flat HREE patterns (Mitropoulos et al., 1987). The HREE are compatible in aluminous clinopyroxene in spinel lherzolite (Blundy et al., 1998). In consequence, slightly lower degrees of melting beneath Nisyros could potentially explain elevated Ce/Yb ratios relative to Santorini, and this is consistent with lower magma volumes erupted in the eastern part of the arc.

In addition, at Santorini there is a distinct difference between the older deposits from Akrotiri and Peristeria with higher Ce/Yb ratios of generally up to ~20 and the younger deposits from the two eruptive cycles and the Kameni islands with lower Ce/Yb ratios of generally less than ~15. As there is no evidence from Sr isotopes for differential amounts of crustal assimilation between the older and the younger samples (Edburg, pers. comm.), this by analogy may be interpreted to reflect an increase of the degree of melting beneath Santorini with time. However, the lack of more complete geochemical datasets for the entire history of the magmatic evolution of Santorini makes an assessment of this hypothesis difficult.

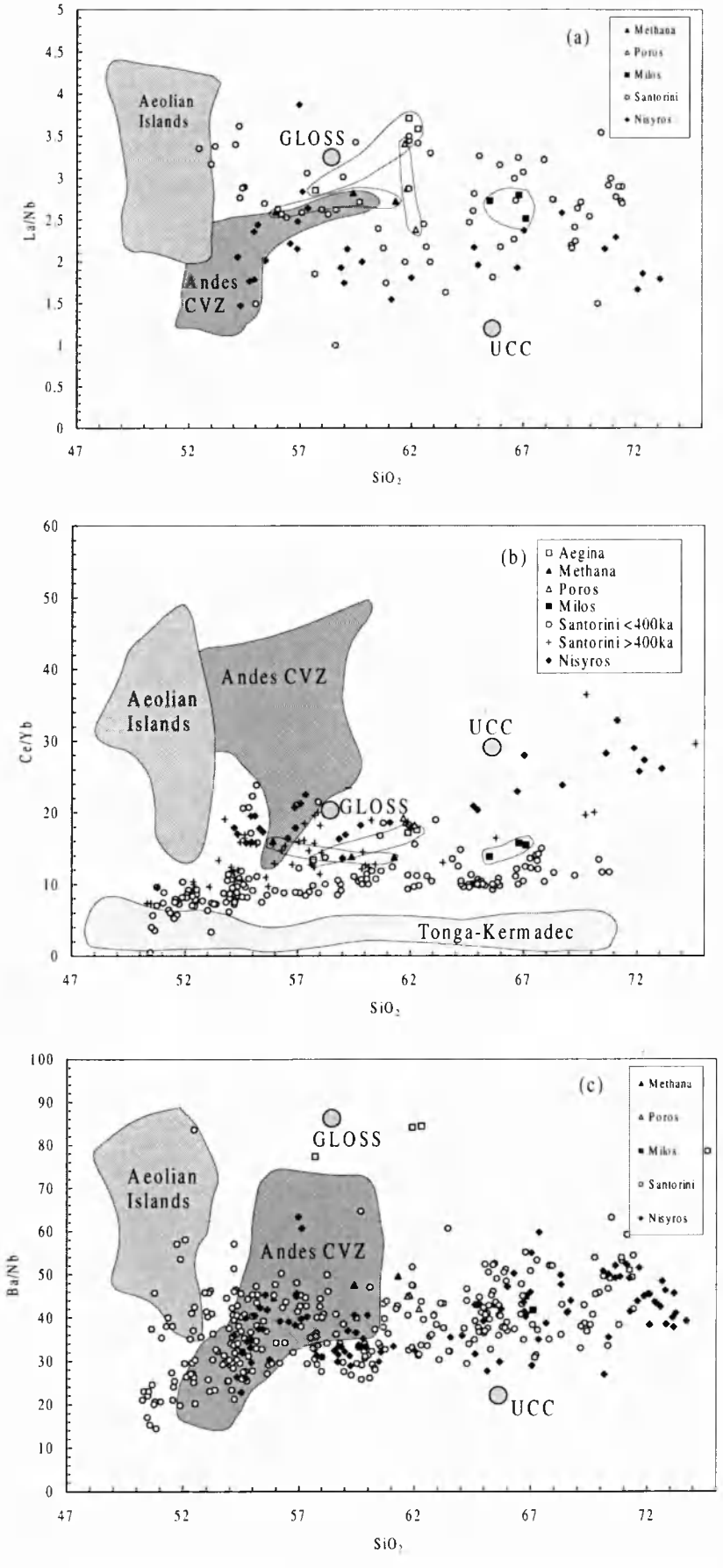

Figure 3-19: Along-variations in (a) La/Nb versus SiO_2, (b) Ce/Yb versus SiO_2, and (c) Ba/Nb versus SiO_2. See text for discussion.

Slab fluids are thought to carry fluid mobile LILE, and their Ba/Nb ratios are expected to be large compared to the mantle wedge. Differential Ba addition from slab fluids to the source region should thus be evident from along-arc changes in the Ba/Nb ratio of arc magmas. Figure 3-19c shows that Ba/Nb ratios are generally low compared to both the Tonga-Kermadec arc (Ba/Nb ~ 400, not plotted on Figure 3-19c) and the Aeolian islands, and this is compatible with low H_2O contents in the primary magmas of Santorini as inferred from MELTS modelling (Section 3.4.4). There are generally no along-arc variations in the Ba/Nb ratios of the Aegean arc, suggesting that fluid addition to the wedge may be relatively invariable. Aegina is an exception as it displays very high Ba/Nb ratios of ~80, but its proximity to Poros and Methana suggests that this cannot be attributed to large scale changes in mantle wedge geochemistry.

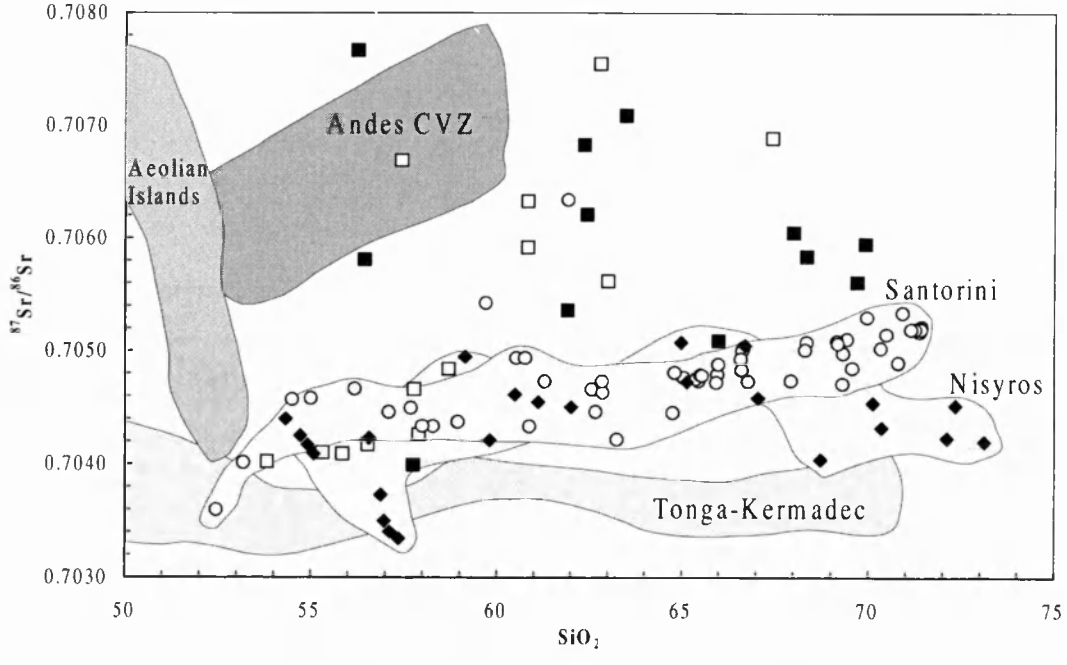

Figure 3-20: Along-arc variations in $^{87}Sr/^{86}Sr$ versus SiO_2, compared to Tonga-Kermadec, the Andes CVZ and the Aeolian Islands. Symbols as in Figure 3-19.

3.7.3 Sr isotope variations

Very little isotopic data exist for Aegina, and Milos, and major element, trace element and isotope data are generally not available for the same samples. Thus, only $^{87}Sr/^{86}Sr$ versus SiO_2 could be plotted to compare along-arc variations within the Aegean arc (Figure 3-20). Fields for the Tonga-Kermadec arc, the Andes CVZ, and the Aeolian islands are again given for comparison.

At Milos, Sr isotope ratios range from 0.7040 to 0.7077 but do not show systematic variations with SiO_2. In contrast, Sr isotope ratios from Aegina in the western part of the arc, with a similar total range, correlate with SiO_2. In Santorini at the central part of the arc, Sr isotope ratios have a much tighter range, but generally increase slightly from the most mafic samples, where $^{87}Sr/^{86}Sr$ ratios range from 0.7036 to 0.7044, to the most felsic samples, with $^{87}Sr/^{86}Sr$ ratios of up to 0.7055. Finally, Sr isotope ratios from Nisyros generally increase with degree of differentiation from 0.7033-0.7044 in the mafic samples to 0.7050 at 67 wt% SiO_2. In the rhyolites, however, $^{87}Sr/^{86}Sr$ ratios are much lower, ranging from 0.7040 to 0.7045.

Low Sr isotope ratios for the mafic magmas in the Aegean arc are consistent with their derivation from a mantle-derived parent. Clear correlations of Sr isotope ratios with degree of differentiation index in Aegina and Santorini indicate that crustal contributions generated the range in Sr isotope ratios. In contrast, the Sr isotope variations on Nisyros suggest that the most felsic magmas could not have evolved from the mafic endmembers of the suite, although crustal assimilation processes are evident within the less evolved samples. Finally in Milos there is no clear correlation of Sr isotope ratios with SiO_2, thus precluding an unambiguous identification of crustal assimilation as the origin of Sr isotopic variation. Due to the general lack of major and trace element constraints for these samples, an interpretation of the isotopic variations in Milos is not attempted.

Finally, at low SiO_2 abundances of the least evolved samples, $^{87}Sr/^{86}Sr$ ratios of the depleted Tonga-Kermadec arc and of Santorini, Nisyros and Aegina converge. This indicates that the mafic samples from the Aegean arc have suffered little crustal assimilation that has been suggested for many calc-alkaline arcs (e. g. Davidson, 1996) and that may be evident in the elevated $^{87}Sr/^{86}Sr$ isotope ratios of the Andes CVZ and the Aeolian islands.

3.8 Conclusions

1. MELTS modelling indicates that simple isobaric (1.5 kbar) crystal fractionation from basalts with relatively low H_2O content of less than ~0.7 wt% can produce basaltic andesites and andesites from their basaltic parent. Such low H_2O contents indicate that slab fluid addition to the mantle wedge alone cannot account for the large degrees of mantle melting (15-20%) required to account for the trace element budget. Hence, melting may at least in part be due to decompression by mantle diapirism.

2. Inflections in major and trace element trends indicate that mixing processes are generally limited. While crystallisation processes may hence also dominate the generation of more felsic members of the sample suite, trace element modelling indicates that open system processes such as magma mixing or assimilation of crustal materials are required in addition. However, simple assimilation of *bulk* basement rocks (Edwards, 1994) is unlikely to operate at Santorini.

3. Trace element evidence further suggests that the mafic enclaves within the Kameni dacites are not the mafic endmembers of a coeval suite of samples but are geochemically unrelated to their host. In addition, due to constant La/Yb, Tb/Yb, Hf/Yb and Zr/Th ratios of the Kameni dacites, their range in U/Th ratios is unlikely to result from magma mixing and is interpreted to reflect differential uranium addition to their source by slab fluids.

4. Minor variations in La/Nb ratios between Santorini and Nisyros suggest that in the eastern part of the arc, sediment addition to the mantle wedge may be slightly less pronounced. There is, however, no evidence from Ba/Nb ratios for differences in slab fluid addition to the mantle wedge. Along arc variations in Ce/Yb ratios may point to variable degrees of mantle melting, with lower degrees in the eastern part of the arc. If decompression melting is important, this may be due to a longer melting column (cf. Plank and Langmuir, 1988) due to thinner crust in the central part of the arc (Makris, 1978) compared to the eastern part.

5. On Santorini, lower Ce/Yb ratios of the younger volcanics of the two eruptive cycles and the Kameni dacites (<400 ka) compared to the older volcanic products of Akrotiri and Peristeria suggest that the degree of melting may have increased over time.

CHAPTER 4

Timescales and processes of magma formation, transfer and storage beneath Santorini, Aegean volcanic arc

4.1 Abstract

The timescales of element transfer at volcanic arcs give important insights into magma generation, movement and storage beneath destructive margin volcanoes. Here we present major, trace and Sr-, Nd- and U-series isotope data of <200 ka old samples from Santorini in the Aegean volcanic arc as a case study of a hazardous destructive margin volcano. Samples range from low K calc-alkaline basalts to high K rhyolites, and relative to N-MORB, they are enriched in LREE and fluid mobile trace elements and have negative Ta, Nb and Ti anomalies characteristic of arc magmatism. $^{87}Sr/^{86}Sr$ ratios range from 0.7035 to 0.7054 and are negatively correlated with $^{143}Nd/^{144}Nd$ ratios, ranging from 0.51285 to 0.51263. Whole rock samples from the second eruptive cycle are in U-Th radioactive equilibrium, and a WR-plagioclase-magnetite U-Th mineral isochron from a dacite that erupted ~67 ka ago yields an age of 85 (+22/-19) ka (1σ). Samples from the Kameni islands show small but significant U excesses, with $(^{230}Th/^{232}Th) = 0.91\text{-}0.97$, correlated with $(^{238}U/^{232}Th) = 0.91\text{-}1.04$. Selected Kameni samples show variable Ra depletion, with $(^{226}Ra/^{230}Th) = 0.92\text{-}0.99$.

The range in Sr and Nd isotope data reflects progressive crustal assimilation. Incompatible trace element modelling of the least evolved sample indicates that melt generation was governed by contributions from the mantle wedge, low degree partial melts of subducted sediments (0.2-0.4%) and slab-derived fluids. While the time between slab-derived fluid addition to the wedge and volcanic eruption is >350 ka for the second eruptive cycle, a Kameni island whole rock isochron yields an age of 147 (+27/-21) ka

(1σ). In contrast, a U-Th mineral isochron of the 1940 Kameni dacite yields an age indistinguishable form zero years, consistent with relatively recent (less than 1 ka) plagioclase crystal fractionation in the subvolcanic magma chamber estimated from the timing of Ra depletion.

On basis of global arc U-Th data, it is argued that crustal magma storage times may be strongly influenced by crustal thickness, and that in Santorini, crustal magma storage times are in excess of ~120 ka. However, the mineral isochrons and the Ra data indicate that the magma storage times in the plumbing system immediately below the volcano are much shorter, in the case of the Kameni dacites as little as a few hundred years or less.

4.2 Introduction

Destructive plate margin magmatism is important, both as a significant component of new crustal additions, and because many of the most hazardous historic volcanic eruptions have occurred in this tectonic setting. Thus, there is increasing interest in the timescales of magma formation, transfer and storage beneath volcanoes since these provide important insights into the physical processes of magma formation and may allow better prediction of eruptive hazards. For example, regional short-lived isotope studies of destructive plate margin magmatism have indicated that partial melting is induced by fluid release from the subducting oceanic crust and that this may typically occur 30-50 ka prior to eruption (Turner et al., 1996; Elliott et al., 1997; Hawkesworth et al., 1997; Turner and Hawkesworth, 1997; Turner et al., 1997). In contrast, contributions from the subducted sediments appear to occur separately, some 350 ka to 4 Ma before fluid addition and are presumably, therefore, not directly involved in triggering partial melting (Elliott et al., 1997; Hawkesworth et al., 1997; Regelous et al., 1997; Turner and Hawkesworth, 1997).

An outcome from the regional studies, mentioned above, is an increasing need for detailed studies of individual volcanic centres so that intra-arc variability can be assessed. Moreover, the detailed studies that have been performed clearly indicate that the effects and timescales of shallow level processes, such as residence times in upper crustal magma chambers, need to be carefully quantified (Pyle et al., 1988; Heath et al., 1998). Additionally, much of the available constraints from short-lived isotopes come from oceanic arcs, and the apparently contrasting and more complex results from continental arcs (Reagan et al., 1994) require further substantiation. In light of this, we present the results of a detailed study from Santorini in the Aegean continental volcanic arc. The results are used to place constraints on the processes and timescales of magma formation, transfer and storage beneath the volcano, the cataclysmic eruption of which led to the destruction of the Minoan civilisation in 1600 BC.

4.3 Geological Setting

The Aegean volcanic arc (inset to Figure 4-1) is a 450 km long chain of late Pliocene - Quarternary volcanoes formed by northward subduction, currently at ≥ 5 cm a^{-1}, of the African plate beneath the continental Aegean microplate (Taymaz et al., 1990). Volcanic activity at Santorini, situated in the central part of the arc on 23-26 km thick continental crust (Makris, 1978), commenced ~750 ka ago (Druitt, 1999). A geological map of Santorini, including sample locations, is given in Figure 4-1.

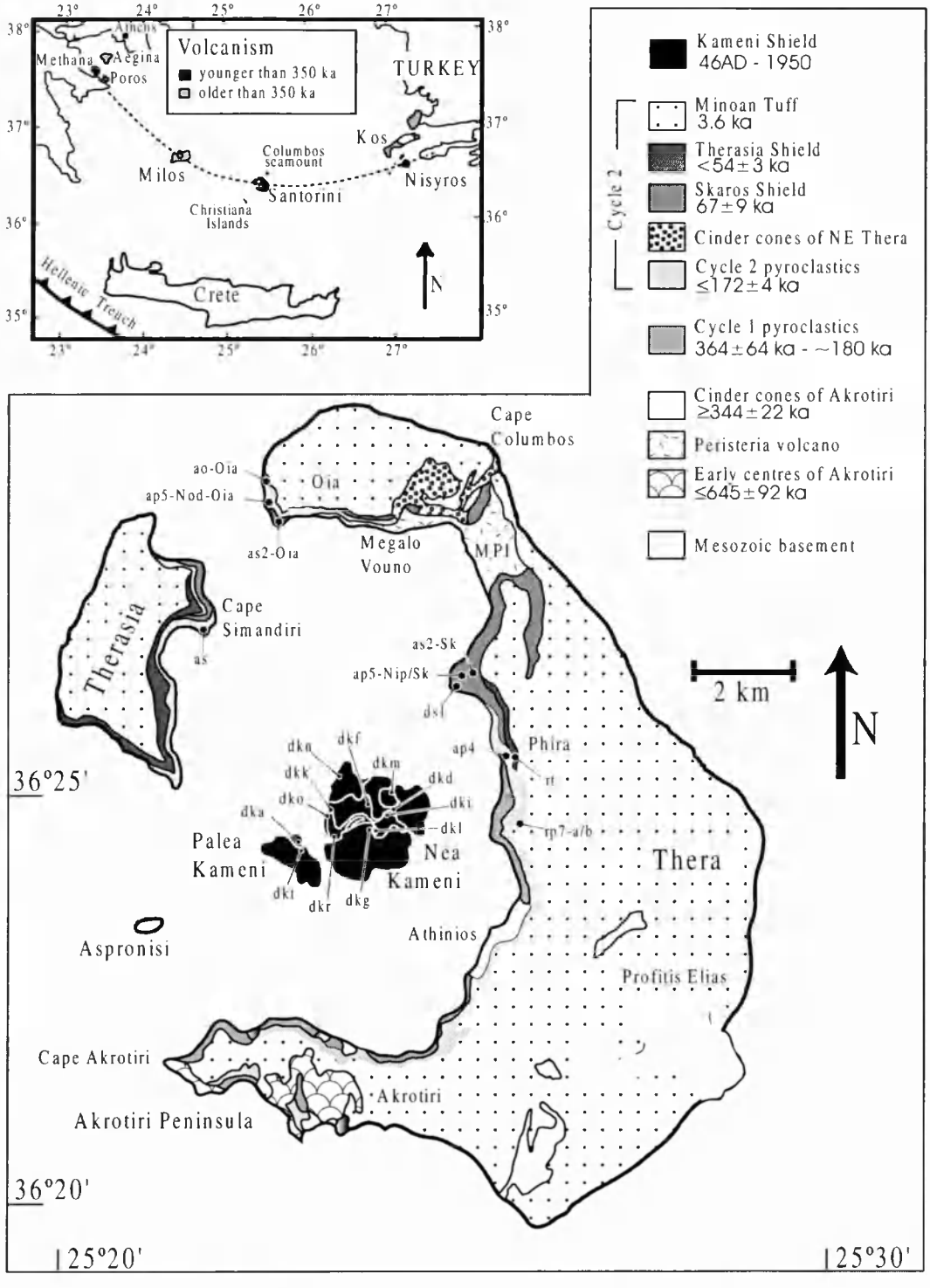

Figure 4-1: Geological Map, stratigraphy and geochronology of Santorini, modified from Druitt et al. (1996), including sample locations. Sample names refer to the stratigraphic units of Druitt and Davies (1999). Inset: Map of the Aegean region and the volcanic arc.

Early volcanic activity (~750 ka - ~350 ka) was characterised by the extrusion of the basaltic to hornblende-phyric rhyodacitic lavas and tuffs on the Akrotiri peninsula and the basaltic to andesitic lavas, tuffs and breccias of Peristeria volcano at Mikro Profitis Ilias (MPI) in the Northeast. These deposits are overlain by a sequence of dominantly andesitic to rhyodacitic pyroclastic deposits that form the first eruptive cycle (~360 ka - ~180 ka), which terminated in a caldera collapse, and by basaltic to rhyodacitic lavas and minor pyroclastic deposits of the second eruptive cycle (SEC) (~180 ka - ~3.6 ka). White rhyodacitic pumice and ignimbrites of the devastating caldera-forming Minoan eruption of 1600 BC cover the islands of Thera, Therasia and Aspronisi. Submarine volcanic eruptions at the centre of the caldera recommenced shortly after caldera collapse, and lava flows emerged above sea level in 197 BC. Since then, 12 dacitic lava flows have erupted, the last in 1950, forming the two Kameni islands, Palea Kameni and Nea Kameni (Figure 4-1). These are the subaerial expression of a ~2 km^3 intracaldera shield volcano which rises to ~500 m above the caldera floor.

4.4 Sample selection and analytical techniques

Only the SEC and the Kameni island samples are considered in this contribution, as the earlier deposits are too old for U-series studies. Samples were selected to cover the range of stratigraphic units, based on the stratigraphy of Druitt (1999). Eruption ages (shown on Figure 4-1 and listed in Appendix D) are well documented for the historic Kameni samples, and for the SEC they are constrained by the established stratigraphy and published ^{40}Ar-^{39}Ar age data (Druitt et al., 1996).

Major and trace elements were analysed by XRF, and Cs, Zn, Co, Ta, Hf and rare earth elements (REE) by INAA following standard techniques (Potts et al., 1985; Ramsey et al., 1995). Analytical techniques for the determination of Sr and Nd isotopes and of U-Th isotopes are given in the captions to Figure 4-3 and Figure 4-4, respectively. ^{226}Ra

concentrations were determined on a Finnigan MAT 262. Between 50 and 100 mg of sample, equivalent to ~50 fg ^{226}Ra, was spiked with a ^{228}Ra tracer aiming for a $^{228}Ra/^{226}Ra$ ratio of ~1. Samples were dissolved using HF-HNO_3-HCl in Teflon beakers. Ra separation was achieved using chromatographic techniques adapted from Cohen and O'Nions (1991) and Chabaux and Allègre (1994). Initial Ba-Ra pre-concentration was achieved by a double column pass using 2 ml cationic exchange resin eluted with HCl, H_2O and HNO_3. Ra was then purified using a single column pass through either 1 ml or 150 µl Sr-Spec® resin with HNO_3 as elutant. Samples were loaded onto single Re filaments following the procedure of Cohen and O'Nions (1991), and this yielded ^{226}Ra beams of 200-300 cps that were stable over >½ h and limited interferences to less than 1%. Reproducibility of the internal Ra standard was better than 1% (2σ). Determinations of the Mt. Lassen Ra standard yielded $^{226}Ra = 1.080 \pm 0.026$ pg g^{-1} and $^{226}Ra = 1.065 \pm 0.010$ pg g^{-1}, and are within error of the values of Volpe and Hammond (1991). Blank contribution was below detection limit. The decay constant used in the calculation of ^{226}Ra activities was $\lambda^{226}Ra = 4.272 \times 10^{-4}$ (Goldstein et al., 1989).

4.5 Major and trace elements

Major and trace element variations have already been discussed in Chapter 3 and are briefly summarised here. Samples from the SEC span the entire range from low K basalts to high K rhyolites (Figure 4-2a) and follow a broadly calc-alkaline major element trend, typical of continental margin magmatism. Major element variations have been attributed to early crystal fractionation of olivine, calcic plagioclase and clinopyroxene, followed by plagioclase, orthopyroxene, titanomagnetite and late stage apatite (Nicholls, 1971; Huijsmans et al., 1988). However, compositionally banded pumices, hybrid andesites (Druitt, 1999) and complex zoning of plagioclase crystals (Stamatelopoulou-Seymour et

al., 1990) suggest mixing of mafic and silicic magmas and open system behaviour, particularly at more evolved compositions (cf. Chapter 3).

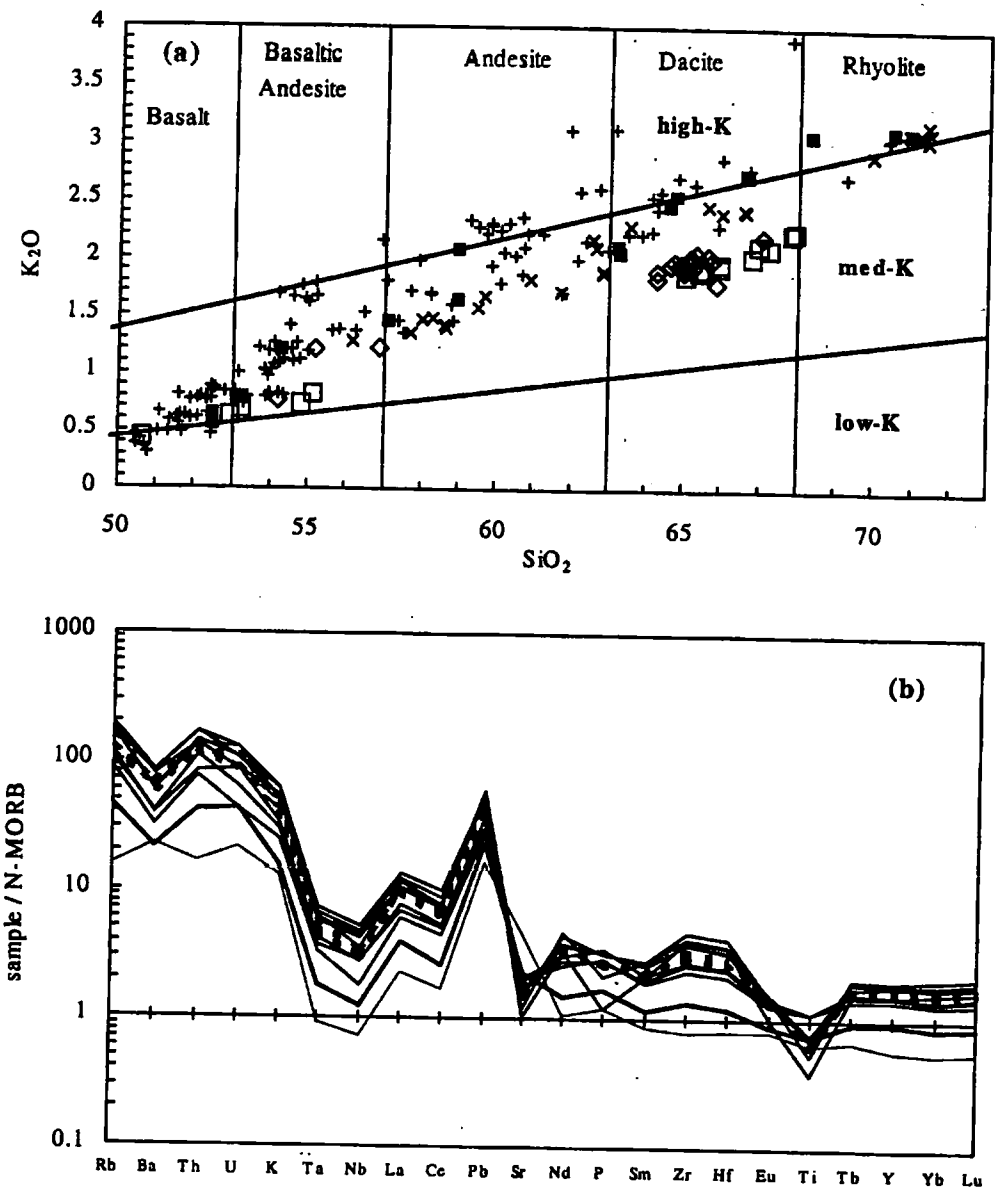

Figure 4-2: (a) K_2O versus SiO_2 variation. The SEC (+,■) ranges compositionally from low K basalts to high K rhyolites. The Kameni lavas (◇,□) are dominantly dacitic, with some mafic xenoliths. Data sources: (+,◇) Huijsmans (1985), (×) Edwards (1994), (■,□) this study. (b) N-MORB normalised incompatible rare earth element concentrations for selected samples from the second cycle (solid lines) and the Kameni dacites (dashed lines). The thick solid line is sample 'as2-Oia-1', used to constrain wedge and slab contributions to the source (see text for discussion). Note the low Ta, Nb, Sr and Ti concentrations and enrichment of LILE and LREE relative to N-MORB characteristic for island arc samples.

Trace element differentiation from basalts to andesites is consistent with fractional crystallisation models (Mann, 1983; Huijsmans et al., 1988), but open system behaviour is again indicated at more evolved compositions (cf. Chapter 3). The incompatible trace elements (Figure 4-2b) are enriched relative to N-MORB. There is a moderate enrichment of LREE over HREE and a considerable enrichment of LILE, Th and U relative to N-MORB. These trace element signatures are typical for island arcs (Pearce and Parkinson, 1993; Elliott et al., 1997; Turner et al., 1997). Negative Sr, Eu and Ti anomalies in the more evolved samples indicate extensive fractional crystallisation of plagioclase and magnetite, and negative P anomalies for two of the more evolved samples indicate limited apatite crystal fractionation.

Compared to the SEC, the Kameni island lavas are much more restricted in composition (Figure 4-2a): they are dacites that contain a few basaltic and andesitic enclaves. With respect to the SEC, the dacites are less enriched in incompatible elements. Huijsmans et al. (1988) suggested that this might be due to progressive depletion in the incompatible element budget of the parental magma with time. Recent work by Higgins (1996) used crystal size distribution (CSD) studies of plagioclase crystals from the Kameni island dacites to constrain magma residence times. Magma mixing was identified in each lava flow, and the magma residence times of the older magma was estimated at 43 to 96 years from plagioclase megacrysts, and for the younger magma it was estimated at 6 to 13 years from plagioclase microlites.

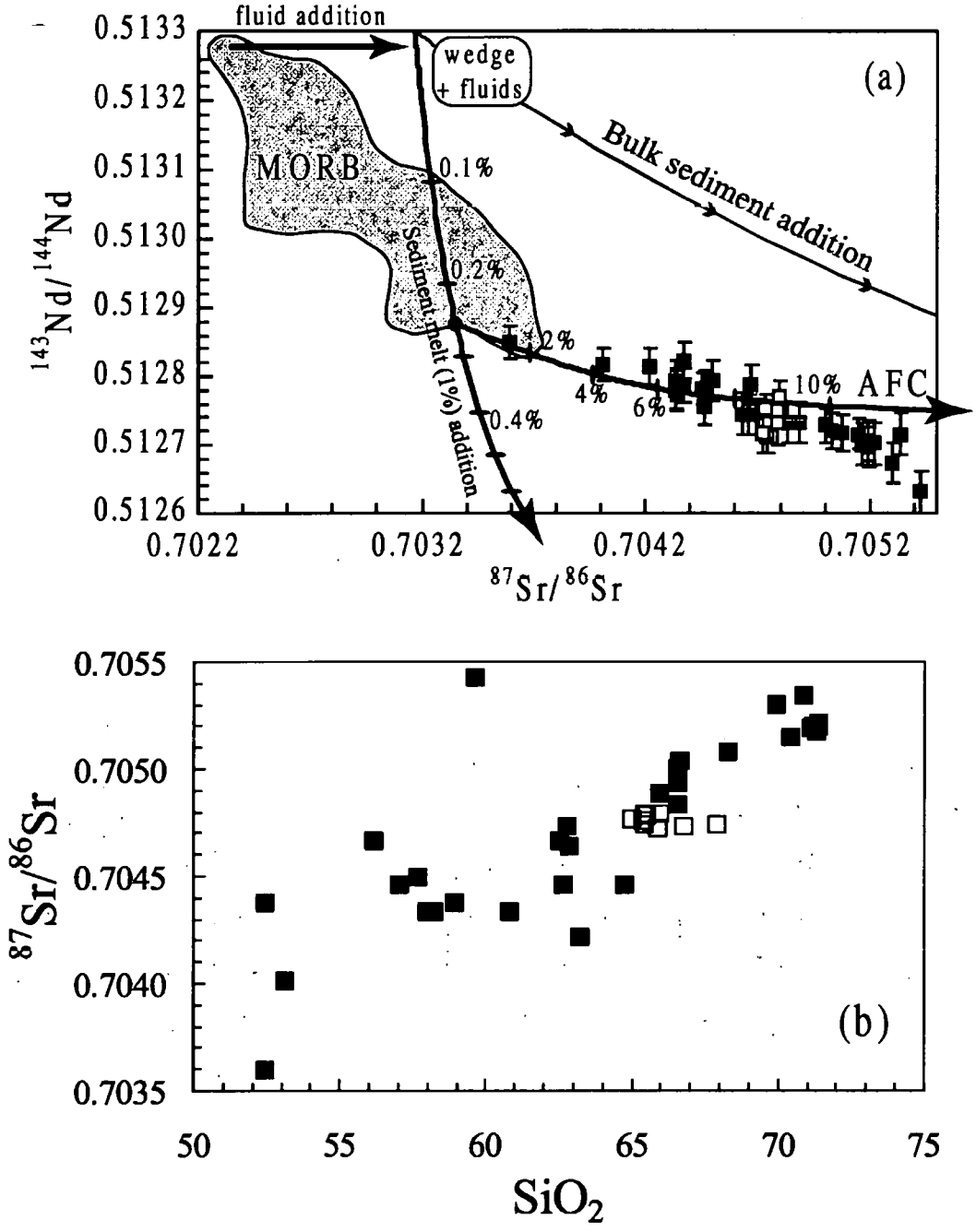

Figure 4-3: (a) $^{143}Nd/^{144}Nd$-$^{87}Sr/^{86}Sr$ variation. (■) SEC from Edwards (1994) and this study, (□) Kameni dacites, this study. Sr and Nd isotope ratios were determined statically in multi-collector mode on Finnigan MAT 261 and 262 thermal ionisation mass spectrometers. Sr was fractionation corrected to $^{86}Sr/^{88}Sr = 0.1194$ and Nd to $^{144}Nd/^{146}Nd = 0.7219$ and the isotope ratios were normalised with respect to internally determined values for NBS 987 = 0.71022, and Johnson and Matthey Nd = 0.511836. The standard deviation of the running mean of the NBS 987 and the J&M standards was ±0.00003 (2σ). Blanks were typically <2 ng and 500 pg for Sr and Nd respectively. See text and Figure 4-10 for a discussion of the petrogenesis as

constrained by incompatible trace elements. (b) Symbols as in (a). Reproducibility (2σ) is smaller than symbol size. $^{87}Sr/^{86}Sr$ increases with SiO_2, suggesting that the variation in Sr isotopes reflects crustal assimilation.

4.6 Isotope results

4.6.1 Sr and Nd isotopes

Samples from the SEC preserve good linear isotope-isotope correlations with $^{87}Sr/^{86}Sr = 0.7035\text{-}0.7054$ and $^{143}Nd/^{144}Nd = 0.51285\text{-}0.51263$ and are enriched relative to MORB (Figure 4-3a). In contrast, the Kameni dacites have constant $^{87}Sr/^{86}Sr$ and $^{143}Nd/^{144}Nd$ ratios of ~0.70475 and ~0.51274, respectively, but they plot within the Sr-Nd isotope trend defined by the SEC. For the SEC, the marked increase in $^{87}Sr/^{86}Sr$ with increasing SiO_2 (Figure 4-3b) is accompanied by a general increase in oxygen isotope ratios from $\delta^{18}O = 5.81$ to $\delta^{18}O = 11.22$ (Edwards, 1994).

4.6.2 U-Th-Ra isotopes

While the U and Th concentrations increase with SiO_2 content, the range in $(^{238}U/^{232}Th)$ is small, and the activity ratios bear no relationship to the degree of differentiation (Figure 4-4b). The $(^{234}U/^{238}U)$ ratios lie within error of unity for all samples (see Appendix D for details), suggesting that the U-Th systematics have not been disturbed by secondary alteration.

On a $(^{230}Th/^{232}Th)$ versus $(^{238}U/^{232}Th)$ equiline diagram (Figure 4-4a), samples from the SEC lie on the equiline, and activity ratios range from ~0.88 to ~0.97. A WR-plagioclase-magnetite isochron (Figure 4-4c) yields an age of 85 (+22/-19) ka (1σ) for a dacite from the base of the Skaros lava shield (sample 'ds1'), analytically indistinguishable from its eruption age of 67±9 ka (^{39}Ar-^{40}Ar).

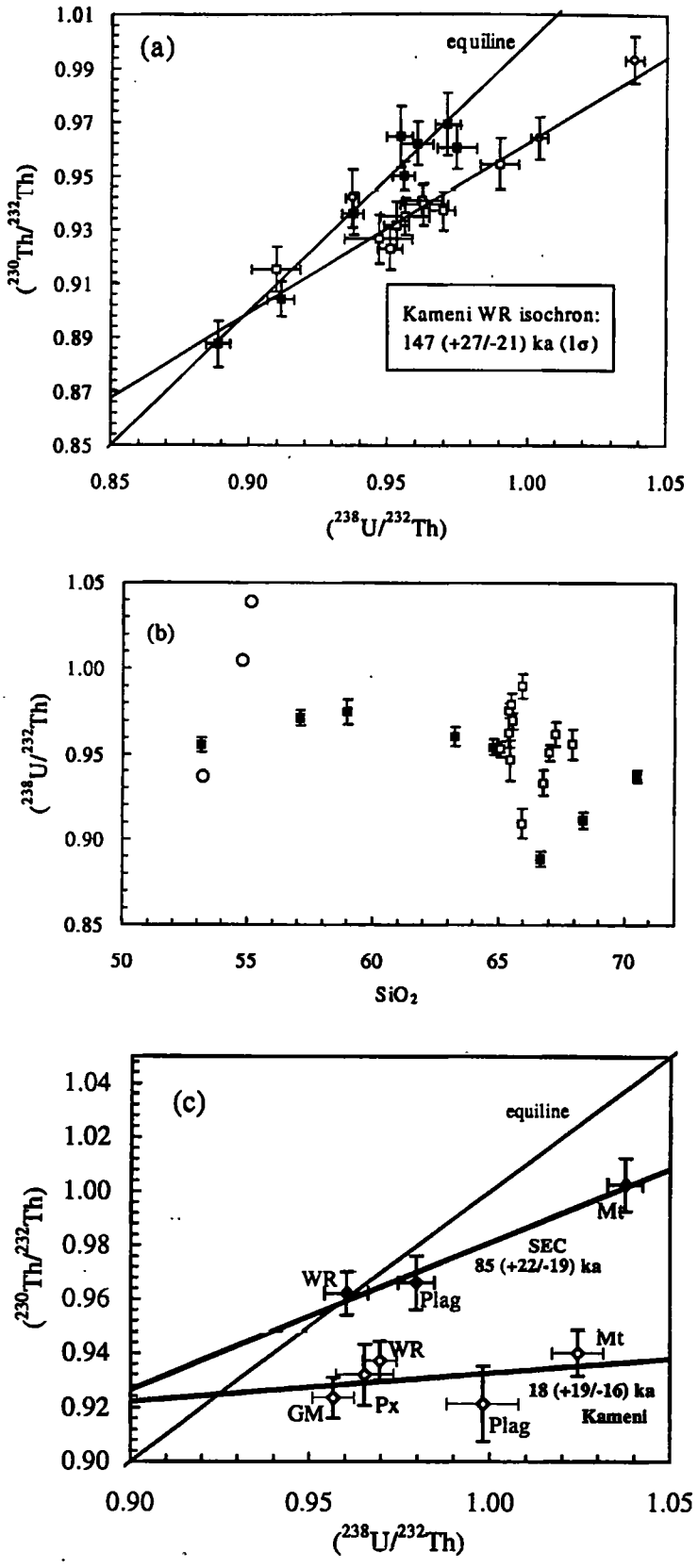

Figure 4-4: (a) ($^{230}Th/^{232}Th$)-($^{238}U/^{232}Th$) equiline diagram. Th and U concentrations and $^{230}Th/^{232}Th$ isotope ratios were determined by thermal ionisation mass spectrometry on a high abundance sensitivity Finnigan MAT

262 equipped with an RPQ-II energy filter. Samples were spiked with a mixed ^{229}Th-^{236}U tracer and the dissolution and chemical separation procedures employed were the same as those described by Turner et al. (1996). Mass spectrometric procedures follow those described in van Calsteren and Schwieters (1995), with an external reproducibility of this system (<0.6%, 1σ) which was monitored using the Th'u'Std. Total procedural blanks for U and Th were typically 100 pg which is negligible compared to the ~500 ng of sample usually loaded and the error on U/Th ratios is ~1%. Decay constants used in the calculation of activity ratios were the same as those compiled by Goldstein et al. (1989): $\lambda^{230}Th = 9.195 \times 10^{-6}$; $\lambda^{232}Th = 4.948 \times 10^{-11}$; $\lambda^{238}U = 1.551 \times 10^{-10}$. Determinations of the AThO and Mt. Lassen Th standards yielded ($^{230}Th/^{232}Th$) = 1.026 ± 0.014 (n=11) and ($^{230}Th/^{232}Th$) = 1.0655 ± 0.0168 (n=5) during this period. Samples from the SEC (■) are in radioactive equilibrium, indicating transfer times of more than 350 ka. The Kameni dacites (□) display U excesses typical for many young arc lavas. A whole rock isochron gives an age of 86 (+21/-17) ka (1σ). (○) are mafic enclaves in the Kameni dacites. (b) ($^{238}U/^{232}Th$)-SiO_2 variation diagram. Symbols as in Figure 4-4a. There is no consistent correlation, suggesting that AFC processes cannot account for variations in activity ratios. (c) Mineral isochrons for the 67±9 ka SEC dacite (◆) and the 1940 Kameni dacite (◇) give crystallisation ages indistinguishable from eruption ages.

All but one Kameni dacite lie to the right of the equiline, and ($^{230}Th/^{232}Th$) and ($^{238}U/^{232}Th$) activity ratios are well correlated (Figure 4-4a). Three andesitic enclaves (samples k35-dkt, k78-dkf and k107-dkl) in the 46AD, 1939 and 1950 Kameni dacites were analysed for U and Th isotopes. The 46AD enclave lies on the equiline above the array of the Kameni dacites and would appear to be part of an older magmatic system. However, the 1939 and 1950 enclaves extend the correlation defined by the dacites and display the highest disequilibrium of all whole rock (WR) samples. A WR isochron through the Kameni samples which display U excesses yields an age of 147 (+27/-21) ka (1σ), with a mean square weighted deviation (MSWD) of 0.50. Mineral separates from

the dkr-1940 Kameni dacite (Figure 4-4c) plot to the right of the equiline, and they define a mineral age of 18 (+19/-16) ka (1σ), with an MSWD of 3.06.

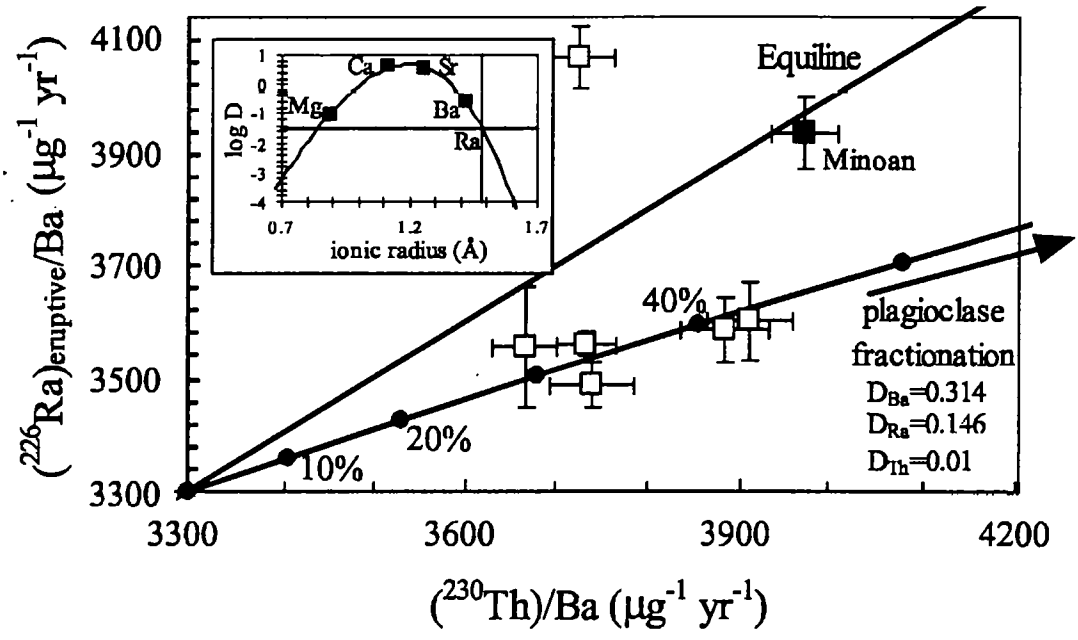

Figure 4-5: Ra-Th equiline diagram for the Minoan eruption (■) and selected Kameni dacites (□). The Kameni dacites were age corrected based on historic eruption ages. The Minoan pumice lies within error of the equiline and thus was not age corrected. Most Kameni dacites show Ra depletion. This can be modelled by plagioclase crystal fractionation. Plagioclase Th and Ba concentrations were determined for mineral separates from the dkr-1940 and the dkg-1866 Kameni dacite, respectively. Effective relative partitioning of Ra and Ba into plagioclase was calculated for the 726AD Kameni dacite, following the technique outlined by Blundy and Wood (1994) (inset) and taking into account ~10% fluid inclusions within the Kameni plagioclase crystals. The data indicate that plagioclase fractionation took place less than ~1000 years prior to eruption.

The Minoan pumice and selected Kameni dacites have been analysed for ^{226}Ra concentrations. Figure 4-5 is an (^{226}Ra)/Ba versus (^{230}Th)/Ba equiline diagram at the time of eruption, which shows the ^{226}Ra-^{230}Th disequilibria of selected Kameni dacites and the Minoan pumice. The Minoan pumice has not been age-corrected as it plots within error of the equiline. Most Kameni dacites are depleted in ^{226}Ra relative to ^{230}Th and have constant (^{226}Ra)/Ba ratios within error of 5.9 fmol g^{-1} a^{-1}.

4.7 Petrogenesis

In the following sections we use the major, trace element and Sr-Nd isotope data to constrain the petrogenesis of the Santorini lavas before turning to the U-Th-Ra data for information on the timescales involved. Firstly, the data are used to identify and quantify the effects of shallow-level fractional crystallisation and assimilation. Secondly, the relative contributions from the mantle wedge, sediments and fluids derived from the subducted slab are assessed.

4.7.1 Effects of shallow-level fractional crystallisation and assimilation

Volcanic arc lavas rarely have primary compositions implying that significant fractional crystallisation takes place during magma ascent and storage. Crustal contamination is also likely to occur during ascent and/or storage, and this is particularly well documented for arc lavas erupted through thickened crust (Davidson, 1985; Davidson, 1986; Davidson and Harmon, 1989).

Samples from the SEC show a range in Sr and Nd isotope ratios (Figure 4-3a), and particularly for the more evolved samples there is a fair positive correlation of $^{87}Sr/^{86}Sr$ ratios and oxygen isotope ratios (Edwards, 1994; cf. Figure 3-16c) with indices of differentiation, e. g. SiO_2 content (Figure 4-3b). This suggests that contamination occurs during differentiation, i. e. as crustal assimilation, and that the observed range in isotopic compositions is not a source feature (cf. Barton et al., 1983; Briqueu et al., 1986; Edwards, 1994). AFC modelling (cf. Chapter 3) suggests that the range of Sr isotopes for the SEC may be explained by up to ~12% assimilation of upper continental crust (Figure 4-3a). Modelling parameters of the primary magma were 165 ppm Sr, $^{87}Sr/^{86}Sr = 0.70335$, 5.4 ppm Nd, $^{143}Nd/^{144}Nd = 0.512878$, as constrained by incompatible trace element modelling (Section 4.7.2). The contaminant had 350 ppm Sr (UCC), $^{87}Sr/^{86}Sr = 0.7122$ (as in Chapter 3), 26 ppm Nd (UCC) and

$^{143}Nd/^{144}Nd = 0.51232$ (modelled parameter). The amount of contamination to generate the highest $^{87}Sr/^{86}Sr$ ratios is 4-5% larger than estimated in Chapter 3 that used sample 'as2-Oia-1' as starting composition. The petrogenesis of this sample, however, is modelled by ~4% assimilation of the calculated primary magma used here.

In contrast to the SEC, the Kameni dacites have constant Sr and Nd isotope ratios and would appear to have been contaminated to very similar degrees (8-10%).

4.7.2 Contributions from the mantle wedge and subducted slab

The petrogenesis at Santorini has been assessed in terms of a three component model for melt generation at destructive plate margins: the mantle wedge, subducted sediments, and slab fluids. Details of partition coefficients and source component compositions are given in the caption to Figure 4-10, and in Appendix B8.

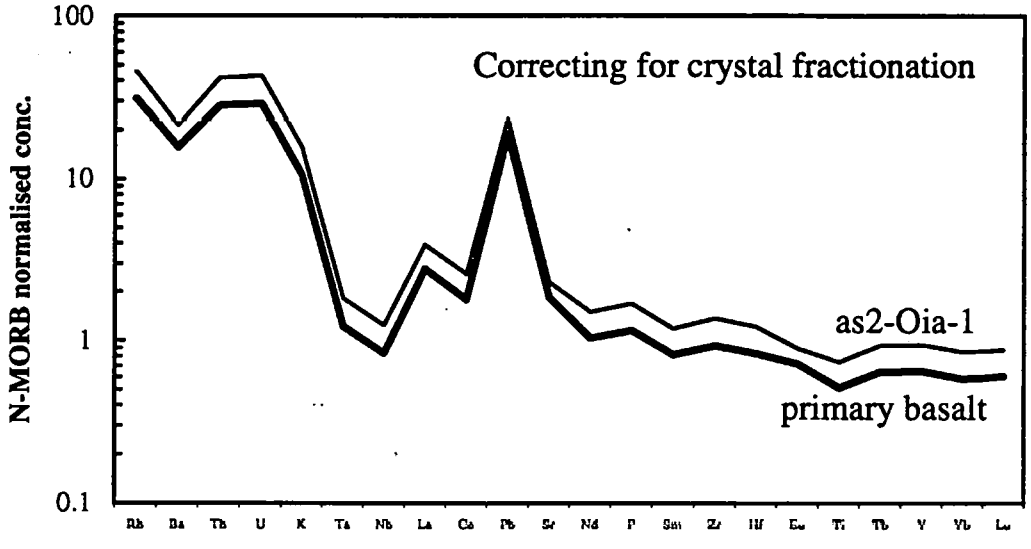

Figure 4-6: N-MORB normalised incompatible element diagram, illustrating the effect of correcting for crystal fractionation. See text for discussion.

4.7.2.1 Correcting for crustal level fractionation

Low Mg numbers of even the less evolved samples (e. g. sample 'as2-Oia-1', Mg# = 54) compared to primary magmas (Mg# ≈ 75) in equilibrium with the mantle (Mg# ≈ 90) required correcting for crustal level fractionation. A fractionating assemblage of olivine

(58%), clinopyroxene (6.5%) and plagioclase (35.5%) was assumed on the basis of least square modelling results for the early fractionating assemblage, taken from Mann (1983). The relation $(FeO/MgO)_{ol}/(FeO/MgO)_{lq} = 0.33$ (Roeder and Emslie, 1970) was used for the ferromagnesian phases and required correction for 33% crystal fractionation to obtain a "primary basalt". This composition has lower incompatible element abundances than sample 'as2-Oia-1', but fractional crystallisation does not significantly affect incompatible element ratios, and the general pattern of the N-MORB normalised element diagram is preserved Figure 4-6.

4.7.2.2 Constraining the degree of mantle melting

To constrain the degree of mantle melting, an estimate of residual mantle mineralogy is required. Flat HREE ratios of the primary basalt require that garnet is not a residual phase, and a mantle mineralogy similar to that of Class et al.'s (1994) spinel lherzolite was chosen, although some amphibole was included into the assemblage. The phase proportions were ol:opx:cpx:amph = 55:30:8:7. Incompatible element abundances of the MORB source were taken from Stolper and Newman (1994), and extrapolation with HREE was guided by depleted earth estimates from McKenzie and O'Nions (1991). The MORB source composition is given in Appendix B8. In the absence of other constraints, simple batch melting was used in the modelling.

The degree of mantle melting was constrained by the HREE abundances of the primary basalt. Because sediment addition contributes little to the HREE budget (see below), the heavy REE are initially assumed to be derived entirely from the mantle wedge. The best fit was achieved by 17% melting (Figure 4-7), but given both analytical and modelling uncertainties, 15-20% melting is a more conservative estimate.

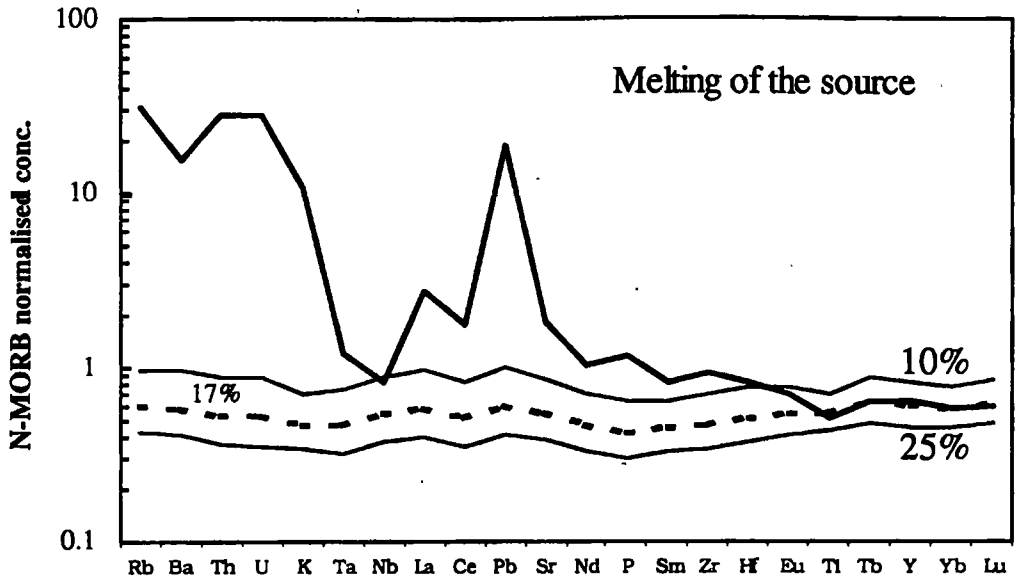

Figure 4-7: N-MORB normalised incompatible element diagram, illustrating the effect of variable degree of modal batch melting of the source. Small degrees of melting result in high incompatible element concentrations. In bold the calculated composition of the primary basalt. See text for modelling parameters and discussion.

4.7.2.3 Sediment addition

Enrichment in LREE over HREE and LILE over HFSE of the primary basalt, with negative Ta and Nb anomalies, was interpreted to be due to sediment addition to the source, as subducting sediments show a similar incompatible element pattern, albeit at much higher concentrations. Initially, bulk sediment addition to the source prior to melting was modelled. Figure 4-8 shows the incompatible element pattern after 17% melting of a source enriched with 4% and 8% sediments (GLOSS, see Appendix B8 for details), respectively. 4% bulk sediment addition, to match Nd abundances, results in too low LREE/HREE ratios and cannot account for the LILE pattern of the primary basalt. 8% bulk sediment addition, to match Th abundances as slab fluids carry essentially no Th (Bailey and Ragnarsdottir, 1994; Brenan et al., 1995), generally results in too high concentrations of the other incompatible elements.

To achieve lower Nd/Th ratios, and low Nd isotopic compositions of even the less evolved samples (Figure 4-3a), sediment melting is required.

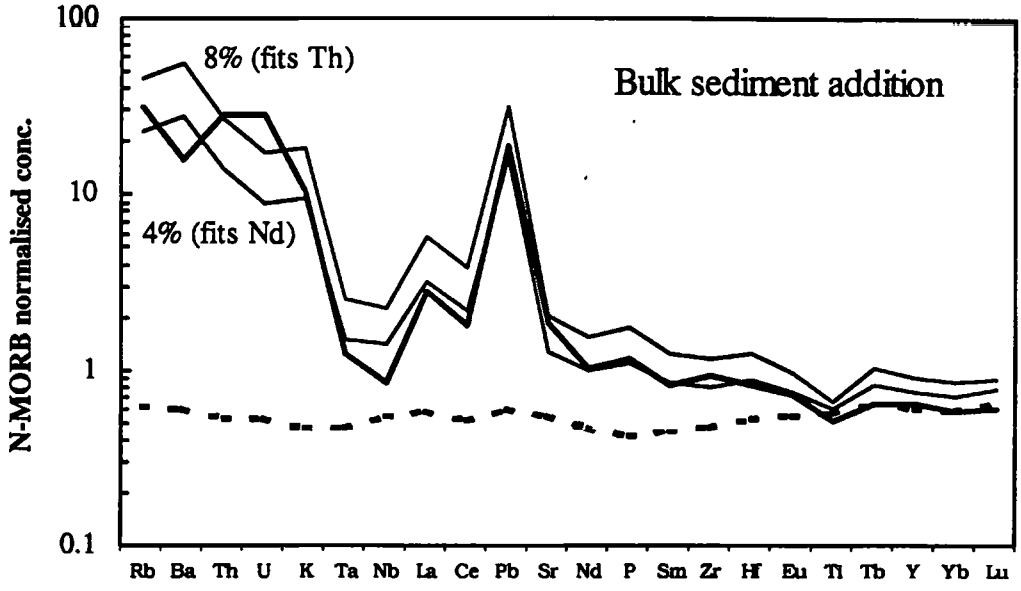

Figure 4-8: N-MORB normalised incompatible element diagram, illustrating the effect of variable GLOSS addition to the source before melting it. See text for discussion.

To constrain the degree of sediment melting, an estimate of residual mineralogy is required but not well constrained. Experiments on melting of pelagic sediments (Nichols et al., 1994) indicate that below ~13 kbar, the subsolidus assemblage is quartz, mica, hornblende and plagioclase, and that at ~13 kbar, plagioclase is replaced by kyanite, garnet and clinopyroxene. However, to achieve low Nd/Th ratios in combination with high Nd/Sr ratios required to model the low Nd isotopic ratios displayed by the less evolved samples, quartz and mica cannot be major constituents of the residual mineralogy. Garnet or clinopyroxene as residual phases may generate low Nd/Th ratios in the sediment melt. Plagioclase is required to achieve low Nd/Sr ratios and to prevent too strong Pb enrichments. This implies that sediment melting may take place in both the plagioclase and the garnet stability fields. Low Ta and Nb abundances suggest that rutile might be a residual phase. Simple batch melting was assumed. The trade-off between the

degree of melting and the amount of sediment addition required was resolved using Sr and Nd isotopes (Figure 4-3a).

Residual phases in Figure 4-9 were plagioclase (28%), garnet (46%), amphibole (26%), and less than 0.1% rutile. Modelling indicates that ~0.25% addition of a 1% sedimentary melt is required to match the Th concentration of the primary basalt. This also results in a match of HREE abundances. LREE abundances in the primary basalt are slightly higher than the modelled composition. In addition, modelled fluid mobile LILE abundances are significantly lower than in the primary basalt. Similar results were obtained when clinopyroxene (46%) was used instead of garnet, with the best results for ~0.4% addition of a 3% sedimentary melt. Due to the lack of adequate constraints on residual mineralogy these results cannot be considered quantitatively robust. They nevertheless indicate that both the degree of sediment melting and the amount of sediment addition are low, consistent with similar estimates from the Tonga-Kermadec island arc (Turner et al., 1997)

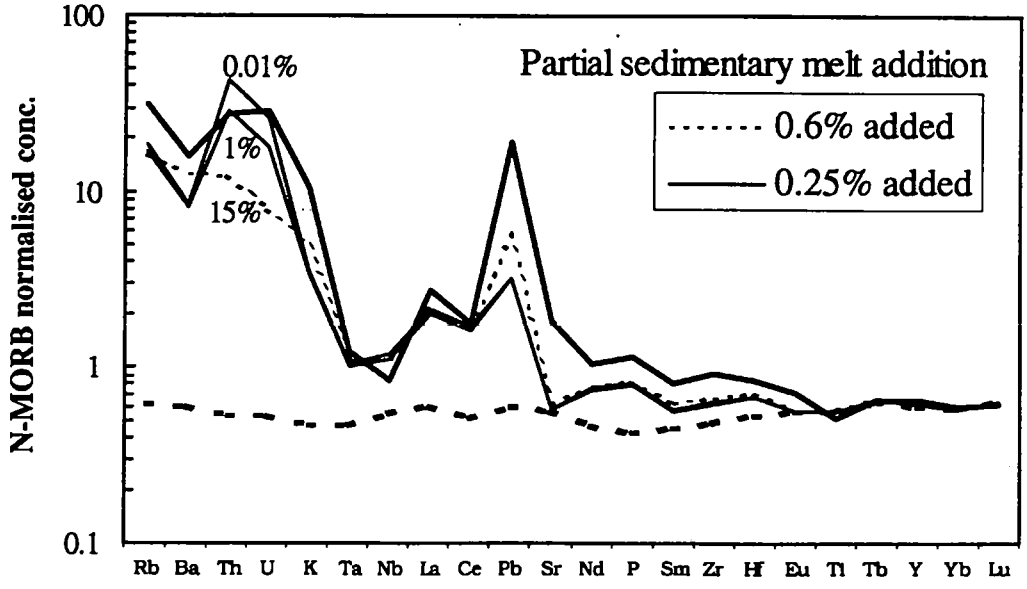

Figure 4-9: N-MORB normalised incompatible element diagram illustrating the effect of sediment melting. See text for modelling parameters and discussion.

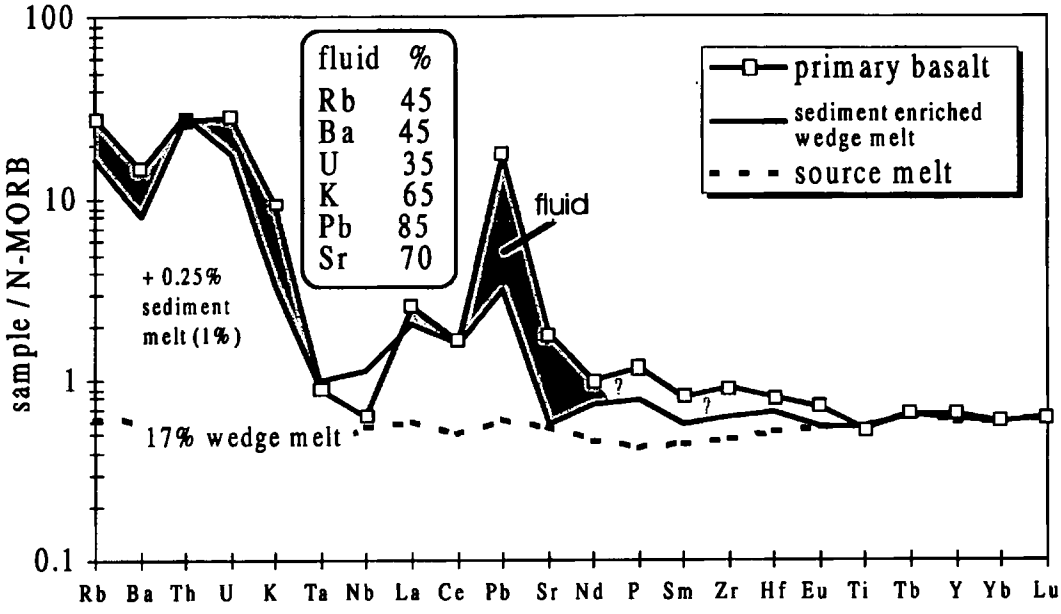

Figure 4-10: Melt generation model for the incompatible elements. Sample as2-Oia1 (c. f. Figure 4-2b) was corrected for olivine fractionation to give a Mg number of 73 for the "primary basalt". The wedge component is modelled as a 17% mantle melt to match the HREE profile. Addition of a partial sedimentary melt is modelled to match Th concentration as Th is considered to be fluid immobile and cannot be added by slab fluids (see text for discussion). Fluids are taken to account for additional enrichment in LILE and U. Note that while the U/Th ratio is similar to that of N-MORB, ca. 35% of the total U budget is attributed to result from slab fluid addition. Partition coefficients are from Jenner et al. (1993), Halliday et al. (1995), LaTourrette et al. (1995), Mahood and Hildreth (1983), and Nash and Crecroft (1985). MORB source is from Stolper and Newman (1994), with HREE extrapolation guided by McKenzie and O'Nions' (1991) depleted earth estimates. The sediment component is GLOSS from Plank and Langmuir (1998).

4.7.2.4 Slab fluid addition

Compared to a melt of the sediment-enriched wedge, the primary magma shows considerable enrichment in fluid mobile LILE and uranium (Figure 4-10), and these elements are taken to be added to the enriched mantle wedge by slab fluids from dehydration reactions. Note that slab fluids are inferred to have an $^{87}Sr/^{86}Sr$ ratio of

~0.7035 (Turner et al., 1996) and thus modify the Sr isotope ratio of the mantle wedge (cf. Figure 4-3a, where 70% of all Sr is fluid derived, see below). The amount of slab fluid addition cannot be estimated from this simple model, as the concentration of LILE in the fluid cannot be constrained. However, the percentage of LILE contributed by the fluid phase to the total LILE budget of the primary basalt may be estimated. Using the garnet bearing residual mineralogy from the previous section, slab fluids need to contribute 45% of the Rb and Ba budgets, 35% of the U budget, 65% of the K budget, 85% of the Pb budget and 70% of the Sr budget to match the LILE abundances of the primary basalt. Hence, while the U/Th ratio of the resulting primary magma is similar to that of MORB, a significant amount of the total U budget is derived from the slab fluid component, and so the fluid enrichment characteristic of many arc magmas results in a significant increase in U/Th ratio.

Trace element modelling is summarised in Figure 4-10. More complicated models that include mineral-fluid partitioning (Ayers, 1998) estimate the mass fraction of fluid released from the slab to be ~20%. The relatively poor match of the LREE may be due to limited fluid mobility of LREE (You et al., 1996).

4.8 U-series isotope constraints on the timescales of petrogenesis

4.8.1 The Second Eruptive Cycle

The petrogenesis of WR samples from the SEC involves addition of ~35% uranium by slab fluids to the mantle wedge (see Section 0, and Figure 4-10). As no correlation is observed between ($^{238}U/^{232}Th$) and the degree of differentiation (Figure 4-4b), the range in U/Th ratios cannot be attributed to variable degrees of late stage crustal assimilation, and samples were expected to show variable ^{238}U excesses over ^{230}Th. However, the WR samples from the SEC lie on the equiline (Figure 4-4a), implying that any initial U-Th disequilibria have decayed back to equilibrium. We

conclude that slab-derived fluid addition to the mantle wedge occurred more than ~350 ka ago for these rocks.

A U-Th mineral-WR age of 85 (+22/-19) ka (1σ) for the basal dacite of the Skaros lava shield is within error of the age of formation of the shield, dated to 67±9 ka by ^{39}Ar-^{40}Ar. This suggests that crystallisation of the separated phases within the magma may have occurred any time between 50 ka and 0 ka prior to eruption, but it could have occurred immediately prior to it. If U-Th mineral isochrons date the onset of crystallisation, and hence the crustal residence times of the magma (e. g. Heath et al., 1998), this would imply that for the SEC, combined fluid and magma transfer times through the mantle wedge beneath Santorini are in excess of ~300 ka. If, however, U-Th mineral isochrons are dominated by the latest period of crystallisation and thus represent minimum rather than absolute magma residence times, fluid and magma transfer through the mantle wedge could be considerably faster (e. g. Turner et al., 1996; Elliott et al., 1997), and total transfer times may be dominated by crustal residence times. Using the available data from Santorini alone does not allow us to distinguish between these alternatives.

4.8.2 The Kameni lavas

On Figure 4-4a the Kameni WR samples that display U excesses yield an age of 147 (+27/-21) ka (1σ), with an MSWD of 0.50. To assess its significance, it is necessary to consider whether processes other than differential uranium addition from slab fluids to the mantle wedge might have produced the linear relationship of the Kameni WR samples. Such processes include U-Th differentiation due to fractionation of accessory phases such as apatite or zircon; magma mixing; and crustal assimilation. These are considered in turn below.

Firstly, fractional crystallisation and partial melting processes that involve apatite or zircon would result in progressive decreases in P_2O_5 and Zr with increasing fractionation.

However, Zr remains incompatible over the entire SiO_2 range, and P_2O_5 abundances within the Kameni dacites are approximately constant (Huijsmans et al., 1988) and only decrease slightly for the 726AD lava (see also Figure 4-2b). Thus, neither zircon nor (to a significant degree) apatite fractionation is observed, and U-Th differentiation does not involve either of these phases.

Magma mixing has previously been identified by CSD studies (Higgins, 1996) as an important factor in the petrogenesis of the Kameni dacites. On a diagram of ($^{230}Th/^{232}Th$) activity ratios versus reciprocal Th concentration (Figure 4-11a), simple mixing between two endmembers would produce linear correlations. Similarly, linear correlations would also be expected on a diagram of Hf/Yb versus Tb/Yb (Figure 4-11b). However, no such correlations are observed, suggesting that magma mixing cannot account for the linear relationship of the Kameni WR samples on an U-Th equiline diagram.

Continental crust has a Th isotope ratio of 0.8-0.85. In addition to the trace element evidence above, the possibility of differential crustal assimilation generating the isochronous relationship of the Kameni lavas may be assessed using variations in Sr isotopic composition. As the Kameni dacites have constant $^{87}Sr/^{86}Sr$ ratios (Figure 4-3a), differential crustal assimilation to produce the observed range in U/Th ratios can be ruled out. The mafic enclaves may have suffered differential crustal assimilation. However, crustal assimilation is unlikely to have generated the observed linear trend of the dacites and their mafic enclaves, and thus it is argued that this linearity is a feature independent of crustal assimilation.

It is thus inferred that differential excesses of U over Th in the Kameni lavas are a source feature, and that the Kameni isochron of 147 (+27/-21) ka (1σ) represents the time since U-Th differentiation in the mantle. In addition, the collinear relationship between the

dacites and their mafic enclaves suggests that U-Th differentiation in their sources occurred at approximately the same time.

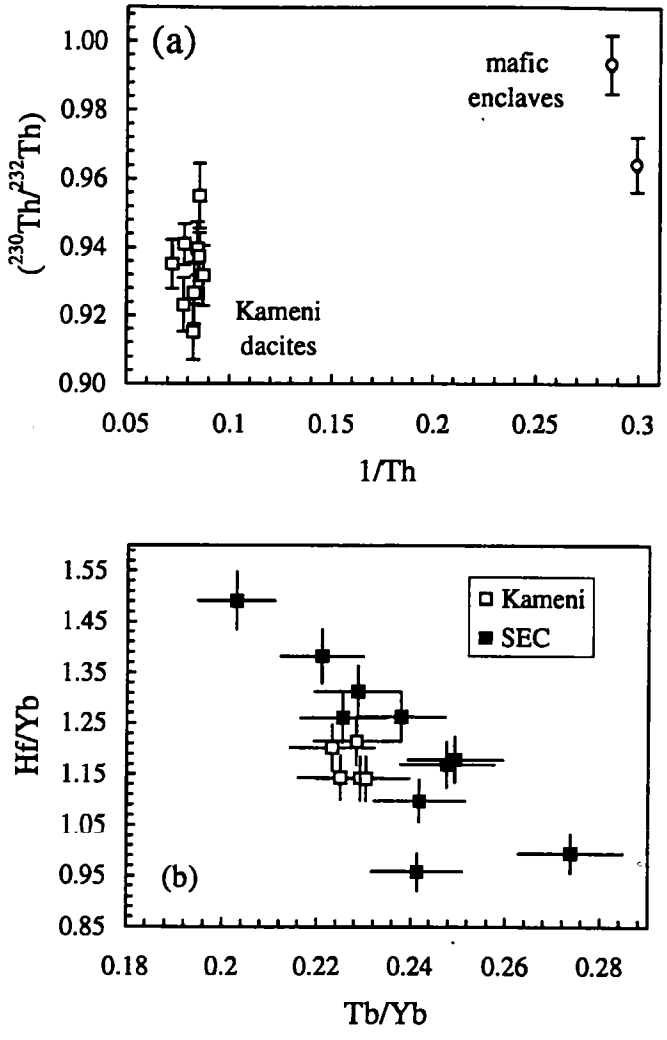

Figure 4-11: Symbols as in Figure 4-4a. (a) ($^{230}Th/^{232}Th$) versus 1/Th for samples that form the Kameni isochron. There is no evidence for a mixing relationship between the dacites and the mafic enclaves. (b) Hf/Yb versus Tb/Yb: while open system processes are evident for the SEC, the Kameni dacites have constant HREE ratios.

4.8.3 Shallow level differentiation

The U-Th mineral isochron for the 'dkr-1940' Kameni dacite (Figure 4-4c) is essentially indistinguishable from zero age, thus suggesting that crystallisation occurred recently. ^{226}Ra-^{230}Th disequilibrium data were used to constrain further the timescales of shallow level fractional crystallisation of the Kameni dacites. While present day (^{226}Ra)/Ba ratios

vary, eruptive (^{226}Ra)/Ba ratios are relatively constant within error of 5.9 fmol g^{-1} a^{-1}. Most dacites are variably depleted in ^{226}Ra with respect to ^{230}Th (Figure 4-5), and this trend can be modelled by up to ~40% plagioclase crystal fractionation with $D_{Ra} > D_{Th}$ from a source magma in Ra-Th equilibrium with an initial (^{226}Ra)/Ba ratio of ~5.5 fmol g^{-1} a^{-1}. For details on the effective relative partitioning of Th, Ra and Ba into plagioclase, see the caption to Figure 4-5. Fractionation is inferred to have occurred less than 1 ka prior to each individual eruption, as longer timescales would result in significant subsequent ^{226}Ra ingrowth, which is not observed. Even shorter crystal residence times are suggested by CSD studies (Higgins, 1996) that constrain residence times to less than 100 years, and by a recent study of Sr diffusion within individual plagioclase crystals (Zellmer et al., 1998, see Chapter 5).

Evidence for extensive recent crystallisation in conjunction with very long total transfer times elucidates the problem associated with taking U-Th mineral isochrons to be indicative for crustal residence times. If they are, then the data indicate that the fluid and magma transfer time through the mantle wedge below Santorini is long and, in addition, that it varies by more than 100 ka between eruptive cycles. Alternatively, if U-Th mineral isochrons only date the last of a series of crystallisation events within the crust, then wedge transfer times may be much shorter and relatively invariable (Turner et al., 1997). To distinguish between these alternatives, the data need to be evaluated within a global context.

4.8.4 Discussion within a global context

The time since U-Th differentiation derived in section 4.8.2 may be compared with estimates from other arc systems. Reference lines of 30-50 ka through high (^{238}U/^{230}Th) samples anchored at low (^{230}Th/^{232}Th) activities on the equiline have been obtained for the Marianas and Tonga-Kermadec (Elliott et al., 1997; Turner et al., 1997), where

crustal thickness is significantly less than 20 km. For the Kermadecs, zero age U-Th isochrons of gabbroic xenoliths and their host magmas are taken to indicate minimal crustal residence times (Turner et al., 1997). In contrast, transfer times of ~90 ka were obtained for the Lesser Antilles (Turner et al., 1996), situated on ~30 km thick crust. There, a U-Th mineral isochron study from St. Vincent was taken to imply crustal residence times of up to 78 (+8/-7) ka (1σ), MSWD 1.97 (Heath et al., 1998). These data suggest that fluid transfer time through the wedge may typically be ~15-30 ka, and that crustal thickness may affect the time between U-Th differentiation and eruption by controlling magma storage time in the crust.

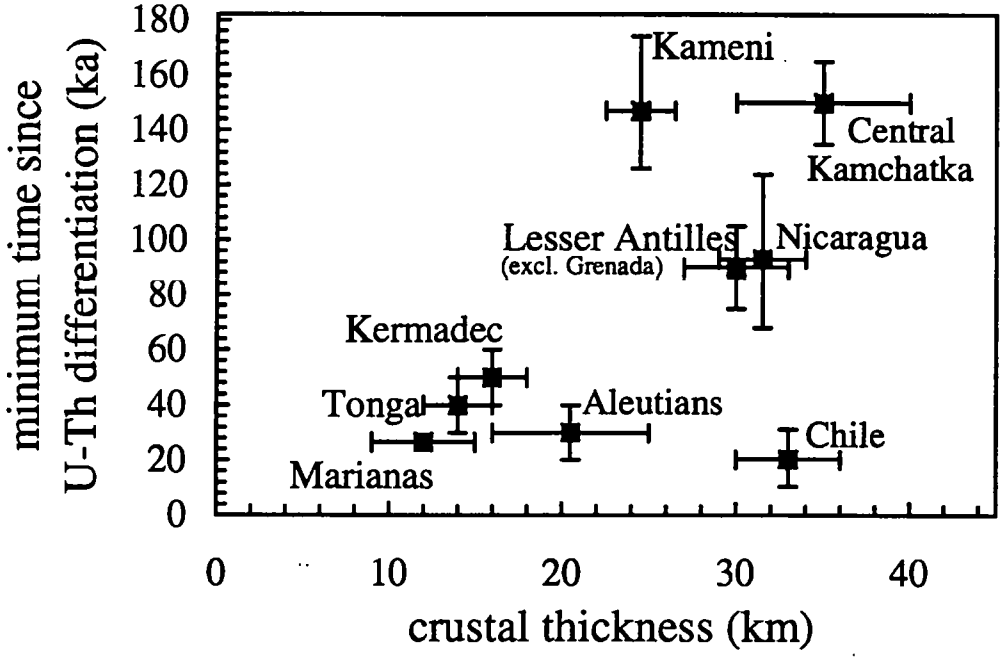

Figure 4-12: The minimum time between U-Th differentiation by slab fluid addition and eruption versus crustal thickness, for selected volcanic arcs. Timescales are from Elliott et al. (1997), Reagan et al. (1994), Sigmarsson et al. (1990), Sigmarsson et al. (1998), Turner et al. (1996), Turner et al. (1997), Turner et al. (1998), and this work. Crustal thickness data are from Carr (1984), Ewart et al. (1977), Fryer (1996), Geist et al. (1994), Harmon et al. (1984), Helmberger (1977), Makris (1978) and Turner et al. (1996). See text for discussion.

To illustrate this hypothesis, we have plotted the time since U-Th differentiation (as obtained by reference lines through the samples with lowest ($^{230}Th/^{232}Th$) activity ratios) against crustal thickness for a range of arcs (Figure 4-12). It is immediately apparent that volcanic arcs situated on thin crust (less than ~20 km in thickness) generally display total fluid and magma transfer times less than ~60 ka. In contrast, volcanic arcs situated on thicker crust (>20 km in thickness) show a much wider range in transfer times which in addition are generally well in excess of 60 ka, with the exception of data from the Southern Volcanic Zone in Chile (Sigmarsson et al., 1990; Sigmarsson et al., 1998).

The significantly greater variability of total fluid and magma transfer times in volcanic arcs situated on thick crust indicates that crustal thickness may indeed affect total transfer times. An interconnected network of magma chambers, as expected within thick arc crust, would introduce variabilities in magma transfer times. In contrast, total transfer times in arcs situated on thinner crust range from 25 to 50 ka and are much less variable. If it is indeed the crust that introduces variability into the total transfer times, and if wedge transfer times are thus taken to be relatively constant and less than ~30 ka, then this work indicates that U-Th mineral isochrons may not represent absolute but rather minimum crustal magma storage times. Furthermore, this then suggests that wedge transfer times may be much shorter than ~30 ka, and that despite zero-age cumulate-WR U-Th isochrons crustal storage times may be significant even in the Marianas and Tonga-Kermadec. Very short wedge transfer times are conceivable if slab fluids are transferred by hydrofracture (Davies and Rowland, 1997), and if magma ascends by channelled flow through the mantle wedge.

4.9 Conclusions

The major and trace element, and Sr and Nd isotope variation of the second eruptive cycle at Santorini can be modelled using a combination of fractional crystallisation and

up to ~12% crustal assimilation, although there is evidence for magma mixing. The range of Sr and Nd isotopes is produced at upper crustal level and is not a source feature. The incompatible trace element budget of the least evolved sample places constraints on the relative contributions of subducted sediments (carrying LREE and LILE) and slab fluids (carrying fluid mobile LILE) to the mantle wedge, and on the proportion of mantle melting (15-20%). Sediment melting (1-3%) is required to account for low Nd/Th ratios and the relatively radiogenic Nd isotopic composition of the even the less evolved samples, but as little as 0.2-0.4% sediment melt addition is required.

U-Th isotope systematics constrain the time since U-Th differentiation to >350 ka for the SEC and to 147 (+27/-21) ka (1σ) for the Kameni dacites. These timescales are much longer than those observed in the Mariana and Tonga-Kermadec island arcs (30-50 ka). However, comparison of total fluid and magma transfer times at volcanic arcs globally suggests that crustal thickness strongly influences transfer times, with longer and more variable timescales at volcanic arcs situated on thicker crust. This indicates that fluid and magma transfer times through the mantle wedge are approximately constant and about 30 ka, and that magma storage time within the crust far exceeds wedge transfer time below Santorini. U-Th mineral isochron data from both the SEC and the Kameni dacites that yield crystallisation ages indistinguishable from eruption ages are thus taken to record the youngest period of crystallisation of magmas with a much longer crustal residence times.

Finally, recent crystallisation is also evidenced by Ra-Th disequilibria in the Kameni dacites. These indicate that each eruption was preceded by a short (less than a few hundred years) period of plagioclase fractionation from a parent magma with approximately constant composition, pointing to very short crystal residence times in the subvolcanic plumbing system. This is consistent with CSD and Sr-diffusion data for the Kameni dacite plagioclase crystals.

CHAPTER 5

Petrogenetic processes and their timescales in the present day subvolcanic magma chamber

5.1 Chapter outline

In this chapter the results of an ion microprobe study of trace element zonations within selected crystals from the Kameni islands and Soufriere, St. Vincent, are presented. The chapter is in two parts: the first part investigates whether fluids may have had an influence on the Ra-Th budget of the Kameni dacites and Ra excesses observed in Soufriere, whilst the second part is a paper submitted to Contributions to Mineralogy and Petrology, October 1998, on "Short plagioclase residence times at two island arc volcanoes (Kameni islands, Santorini, and Soufriere, St. Vincent) determined by Sr diffusion systematics". The paper describes a new method for calculating plagioclase crystal residence times and allows us to investigate processes that operate on very short timescales. It thus serves as a supplement to crystal size distribution and U-series isotope studies and gives additional insights into the timescales of crystallisation in the subvolcanic magma chamber.

Part I

Magmatic fluids as a source of Ra-Th disequilibria?

5.2 Introduction

In Chapter 4, Ra depletion in the Kameni dacites was modelled by plagioclase fractionation within the subvolcanic magma chamber. However, as Ra is a fluid mobile element, fluids may also significantly influence the magmatic Ra budget. Thus, an alternative interpretation may be depletion of Ra by fluid transport out of the magma chamber, although such fluids would have to be reducing in order to leave the magmatic U budget unaffected. To test this hypothesis, an ion microprobe study of trace element zonations within selected crystals from the Kameni islands was undertaken in order to see if Ba (as a proxy for Ra) significantly varies from crystal cores to crystal rims. If interaction of magma with hydrothermal fluids at a late crystallisation stage is the dominant reason for Ra depletion, a systematic drop in Ba concentration at the crystal rim of each crystal would be observed.

In addition, recent U-Th mineral isochrons of arc magmas from Soufriere, St. Vincent, suggest magma residence times between ~46 ka and ~77 ka (Heath et al., 1998b). These ages are in disagreement with Ra excesses that have been measured for the Lesser Antilles (Soufriere andesite, Chabaux and Allègre, 1994) and that would require magma residence times of much less than 8 ka if Ra excesses resulted from Ra-Th differentiation during mantle melting. Thus it seems that the U-Th and Ra-Th systems are decoupled, and that Ra excesses may reflect upper crustal processes subsequent to both fluid addition to the mantle wedge and the majority of crustal residence time. An ion microprobe study across selected crystals from the 1979 Soufriere andesite of Heath et

al. (1998b) was thus undertaken to see if late stage Ra addition by hydrothermal fluids may be an explanation for Ra excesses in Soufriere.

5.3 Results

Of the fluid mobile trace elements, Sr, Ba and Rb were analysed along traverses across selected plagioclase and pyroxene crystals (Figure 5-1). Uranium was too low in concentration to allow intra-crystal variations to be detected, but U crystal rim - groundmass partitioning data were obtained along with partitioning data for a number of other trace elements (Appendix E). No systematic differences were detected between fluid mobile trace element profiles and profiles of other trace elements. While some plagioclase crystals show systematic co-variation of anorthite content with the concentrations of some trace elements (dka-fsp-1, dkr-fsp-2, STV-fsp-1), most traverses reveal relatively constant trace element concentrations, and there is generally no indication for sudden changes of fluid mobile trace element concentrations towards the crystal rim.

An exception may be STV-fsp-2 from Soufriere, where Ba concentration increases by a factor of 2 within the outer 200 μm of the crystal. This may be attributed to Ba addition to the magmatic system at the late stages of crystal growth, for example by hydrothermal fluids. However, this interpretation is neither supported by variations of the other fluid mobile trace elements within STV-fsp-2, nor by trace element variations within the other crystals of this sample. In addition, although the major element traverse of STV-fsp-2 defines the composition of its rim only, changes in Ba concentration may in principle reflect changes in major element composition of the magma, as for example observed in crystal STV-fsp-1, where Ba increases with decreasing anorthite content but Sr and Rb trace element pattern seem unaffected.

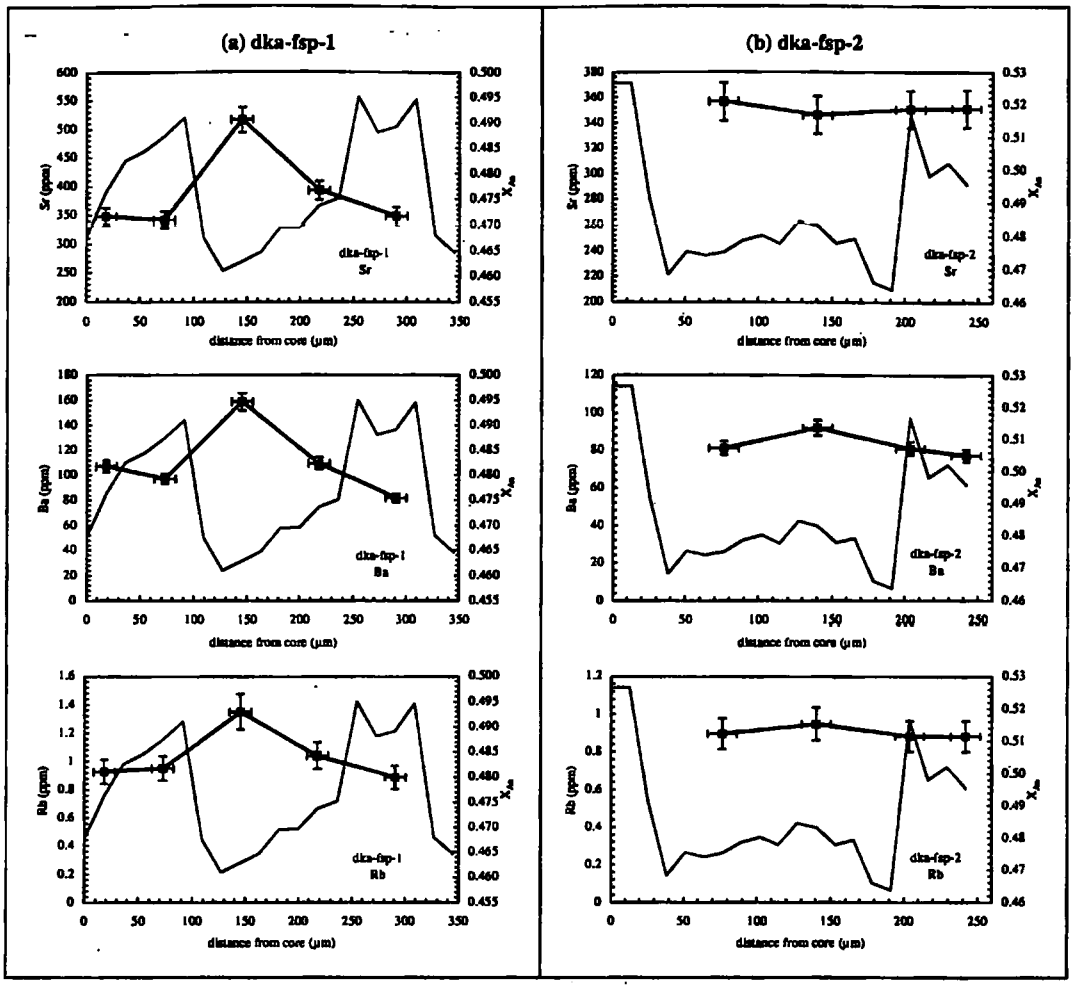

Figure 5-1: Fluid mobile trace element traverses through selected crystals.

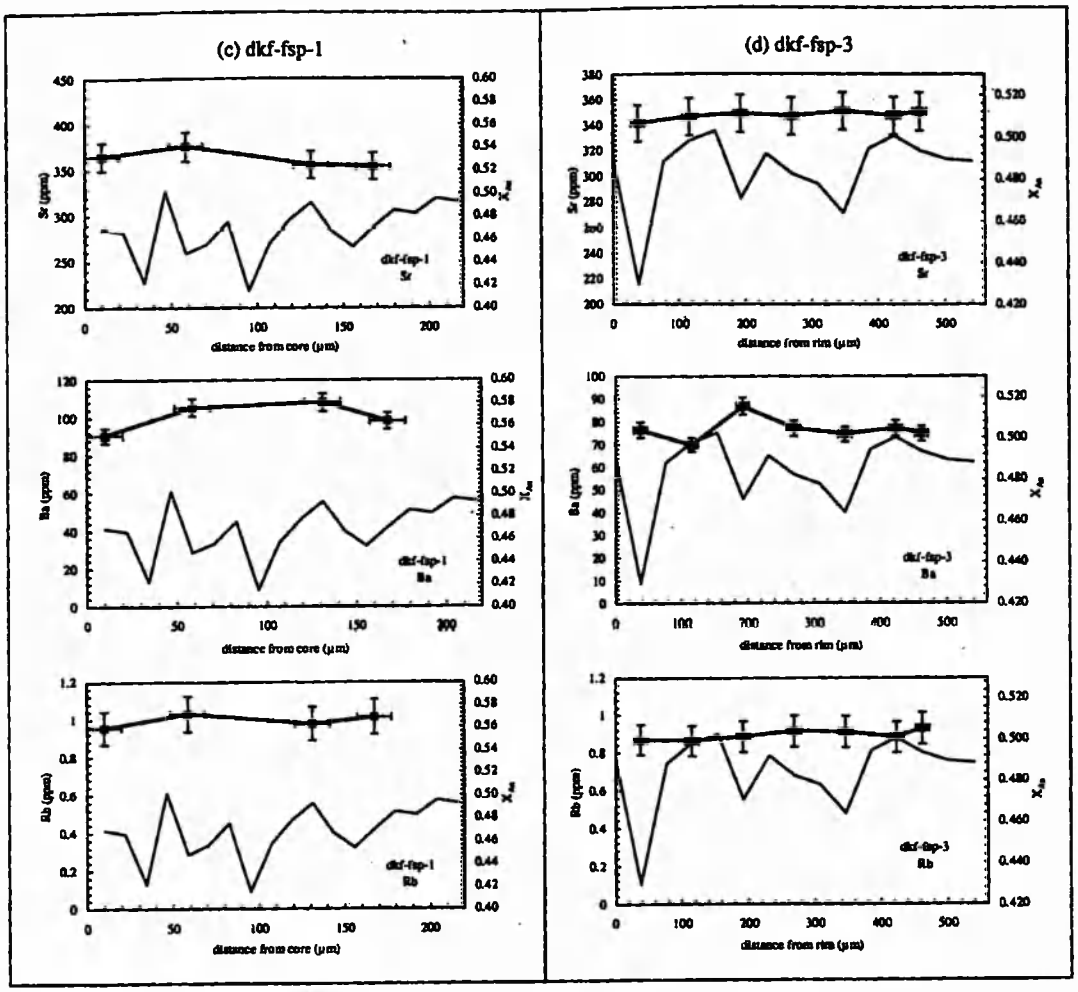

Figure 5-1 (continued)

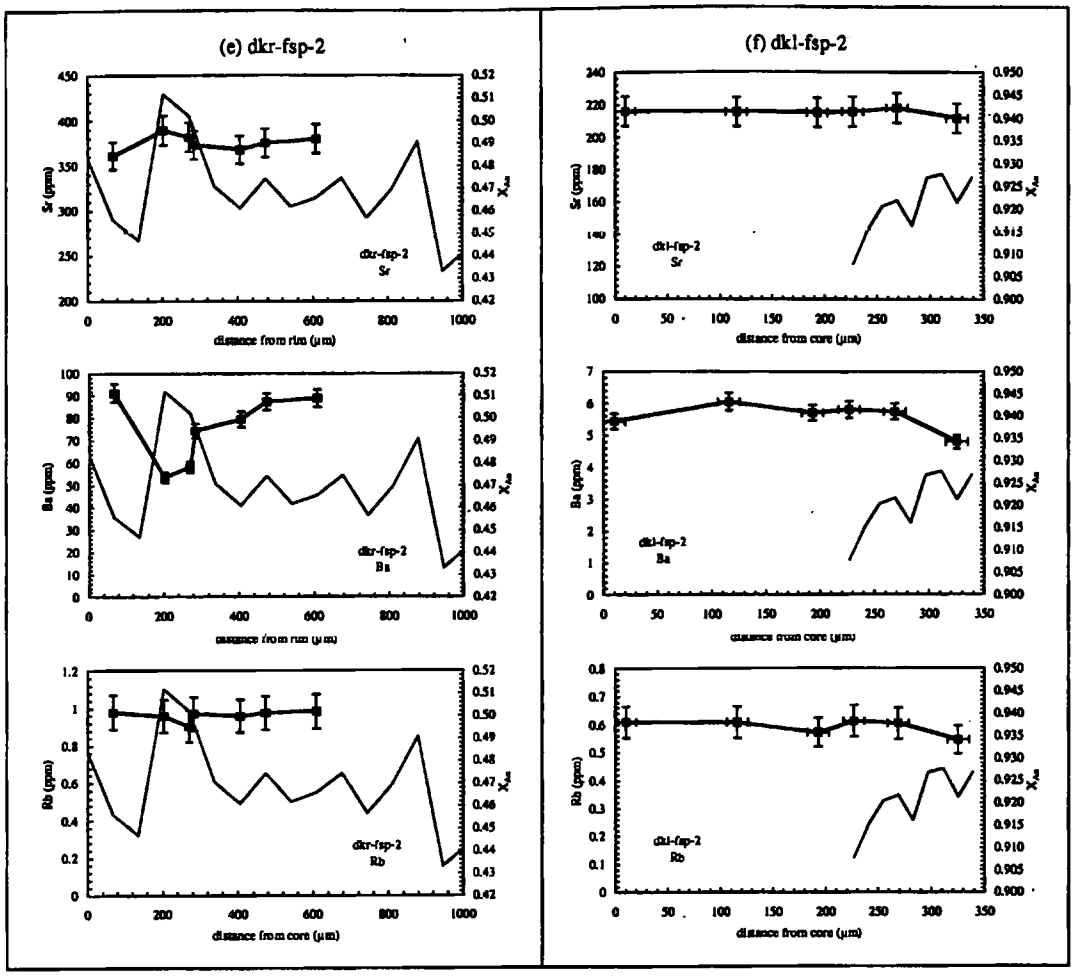

Figure 5-1 (continued)

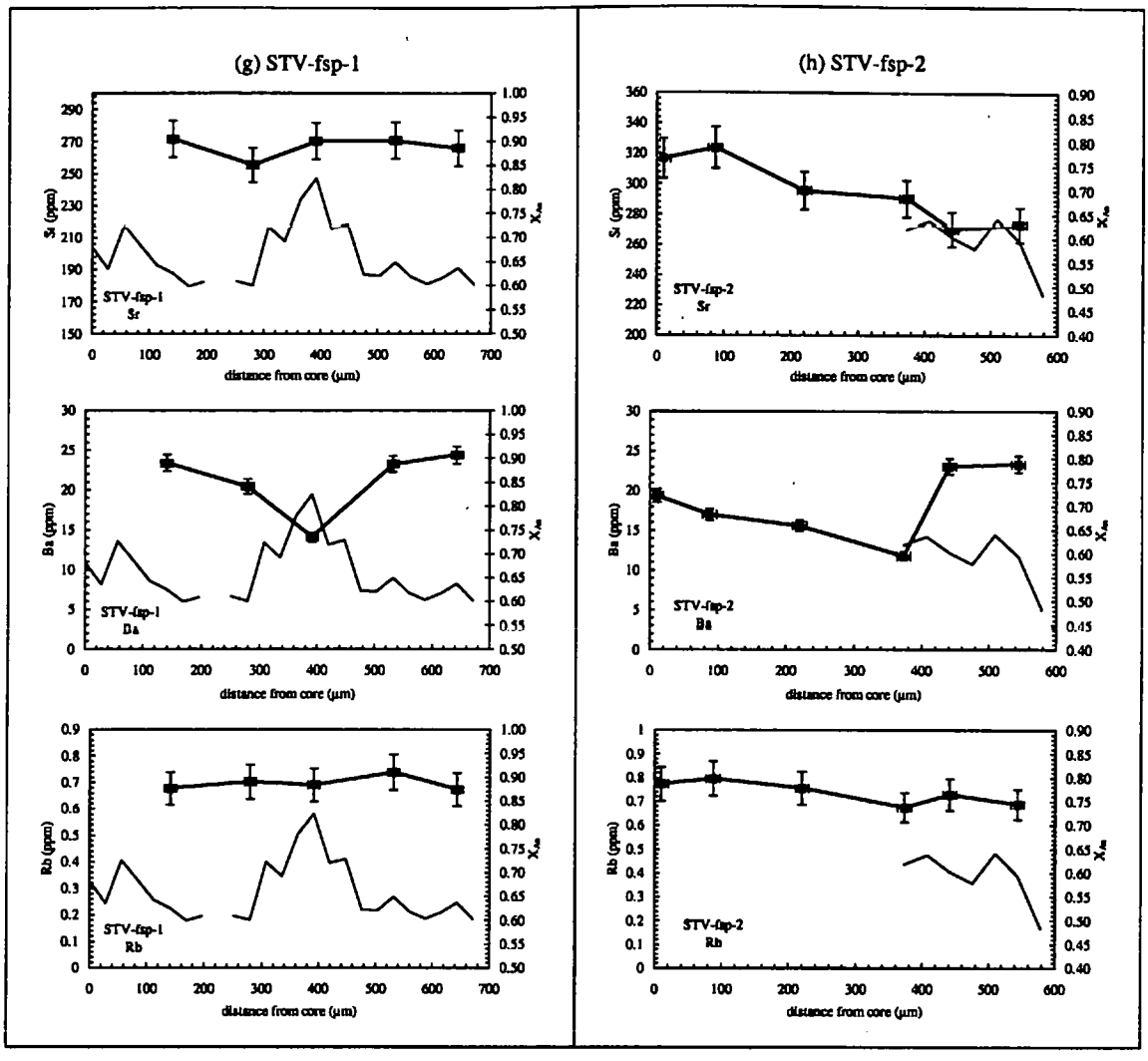

Figure 5-1 (continued)

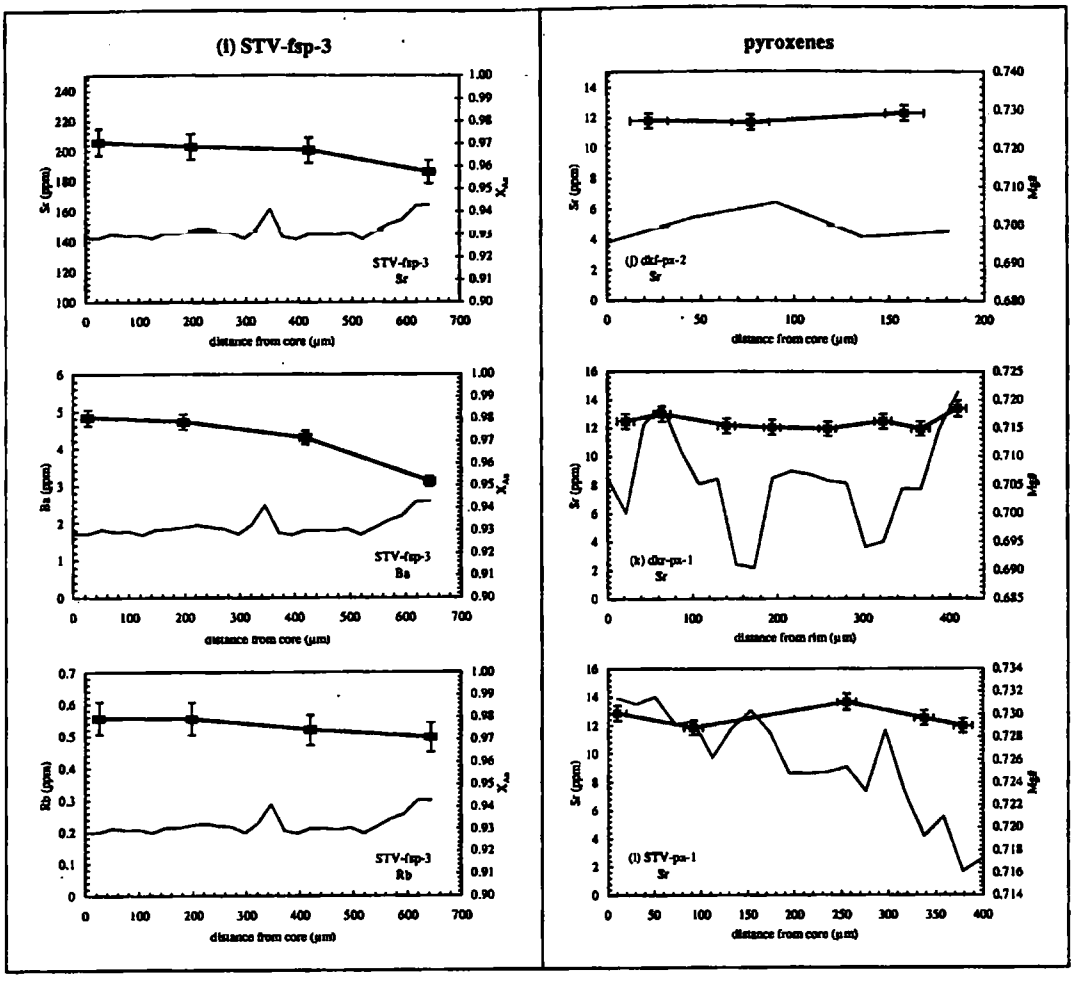

Figure 5-1 (continued)

5.4 Conclusions

In conclusion, for the Kameni dacites there is no evidence that the source of Ra depletion is pre-eruptive removal of fluid mobile trace elements by hydrothermal fluids. Thus, Ra-Th differentiation within the present day magma chamber is not governed by open system processes, and plagioclase crystal fractionation prior to eruption is a plausible explanation for the observed Ra depletion.

Similarly, for the 1979 Soufriere andesite there is no unequivocal evidence for fluid influx into the magma chamber as an explanation for the observed Ra excess (Chabaux and Allègre, 1994). If the crustal residence time of the andesite was greater than 40 ka (Heath et al., 1998b), then Ra was differentiated from Th within the crust. Whilst accumulation of young plagioclase may in principle lead to Ra excess within a magma, and there is evidence for very recent plagioclase crystal growth within the 1979 Soufriere andesite (see Part II of this chapter), there is as yet no unequivocal explanation for the origin of Ra disequilibrium within the sample studied by Chabaux and Allègre (1994).

Part II

Short plagioclase residence times at two island arc volcanoes (Kameni islands, Santorini, and Soufriere, St. Vincent) determined by Sr diffusion systematics

A paper submitted to Contributions to Mineralogy and Petrology, October 1998

5.5 Abstract

The diffusive relaxation of trace element profiles in plagioclase phenocrysts may provide important constraints on crystal residence times in crustal magma chambers. Initial trace element profiles in plagioclase phenocrysts are governed by variations in the concentration of a trace element in the melt and by the plagioclase - melt partition coefficient. Trace element diffusion will subsequently act to modify this initial profile, and given enough time it will produce a profile that is in equilibrium with the anorthite variations *within* the crystal. We argue that the trace element partition coefficient $D^{a/b}$ between two parts a and b of a plagioclase crystal of variable anorthite content is equal to the ratio of their crystal-liquid partition coefficients, and that the equilibrium profile of the crystal can be calculated. The time required to establish diffusive equilibrium is dependent on the wavelength and amplitude of the initial trace element concentration range and on the diffusivity of the trace element in plagioclase. Sr plagioclase - melt partition coefficients and diffusivities are calculated for a range of magmatic temperatures and plagioclase compositions. A one-dimensional diffusion model is developed that describes the diffusive destruction of oscillatory trace element zoning with time and allows the calculation of upper limits for plagioclase crystal residence times in a crystallising magma reservoir.

The model is tested using major and trace element concentrations measured along crystal traverses of plagioclase phenocrysts from the Kameni island dacites, Santorini, and from the 1979 Soufriere andesite, St. Vincent. Three out of eight plagioclase phenocrysts have Sr concentration profiles that are not in diffusive equilibrium. For these, the diffusion model is employed to calculate maximum crystal residence times from incomplete diffusive equilibration of trace element zoning in plagioclase. Maximum crystal residence times range from 100 to 450 years. This is in good agreement with estimates from crystal size distribution and from Ra-Th disequilibrium studies for the Kameni islands. For Soufriere, however, such short residence times are incompatible with U-Th mineral isochron data that suggest residence times of >40 ka in a thermally buffered magma reservoir. To reconcile these apparently different ages, we invoke a more complicated magmatic history for Soufriere where an initially buffered magma reservoir is disturbed by magma mixing and suffers limited additional crystal fractionation prior to eruption.

5.6 Introduction

A wide variety of processes operate in subvolcanic magma chambers. These include cooling, fractional crystallisation, crystal resorption, convection, magma mixing, assimilation and degassing and result in the large compositional range observed in erupted volcanic rocks (Bacon, 1986; Bacon et al., 1989; Marsh, 1989). To improve our understanding of these processes, it is necessary to establish the timescales over which they operate. Various techniques have been employed to determine magma residence times and crystal residence times in upper crustal magma chambers:

Models of steady state, crystallising magma reservoirs in conjunction with short-lived isotope studies were employed to obtain very short magma residence times of the order of tens to hundreds of years for a number of basaltic and andesitic volcanoes (Pyle, 1992; Condomines, 1994; Pyle, 1994). Assumptions included uniform magma output rate and

approximately constant magma composition. Such results are supported by crystal size distribution (CSD) studies (Marsh, 1988) that date the onset of crystallisation of a crystal population from a magma (Cashman and Marsh, 1988). Again magma residence times of the order of tens to hundreds of years were derived for some andesitic and dacitic lavas using plagioclase CSD studies (Higgins, 1996b; Higgins, 1996a), although this technique requires a good knowledge of crystal growth rates which are not usually well constrained. Short crystal residence times are also suggested by recent Th-Ra data that yield plagioclase crystal residence times of hundreds of years or less (Thomas et al., 1998; Zellmer et al., 1998).

In contrast, U-Th isotope analysis of mineral separates, employed to date short periods of crystallisation, yield much longer magma residence times of the order of thousands to tens of thousands of years (Allègre and Condomines, 1976; Pyle et al., 1988; Volpe and Hammond, 1991; Heath et al., 1998b). This technique assumes that the period of crystallisation was very short compared to the timescale of magma residence. Even longer magma residence times of the order of a million years have been suggested for rhyolitic systems on basis of Rb-Sr isotope disequilibria of mineral-groundmass pairs (Halliday et al., 1989; Halliday, 1990; Mahood, 1990; Christensen and DePaolo, 1993).

Here we describe a new approach to constraining crystal residence times in magmatic systems using trace element variations in plagioclase and their diffusive re-equilibration. The approach is similar to those previously used to constrain olivine residence times using Fe-Mg interdiffusion (Gerlach and Grove, 1982) and Ni diffusion (Humler and Whitechurch, 1988), and magnetite residence times using Ti diffusion (Nakamura, 1995). Plagioclase is one of the major rock-forming minerals, and the diffusion model we present here thus provides a technique to investigate crystal residence times for a wide range of rock samples.

In the first part of the paper we develop a model that describes the nature of the zoning expected for Sr concentrations in plagioclase together with a mathematical model that relates the process of diffusive re-equilibration with time. In the second part of the paper, we present selected ion probe data for plagioclase phenocrysts from two island arc volcanoes (the Kameni islands, Santorini, Aegean Volcanic Arc and Soufriere, St. Vincent, in the Lesser Antilles), and apply our theoretical model to these data. We show that the diffusion model can be applied to some of the probed plagioclase crystals, and that their maximum residence times are of the order of tens to hundreds of years. We then discuss these results in terms of the discrepancies between the inferred plagioclase crystal residence timescales and U-Th mineral isochron data.

5.7 Theory and approach

5.7.1 Introduction

A plagioclase phenocryst can develop zoning in major element (notably mole fraction anorthite, X_{An}) and trace element content in response to changes in the pressure, water pressure, temperature and melt composition during its growth. The resulting zonation in a particular crystal reflects the magmatic processes involved and the order in which they occurred. Over time, however, the zonation in the crystal can be degraded by diffusion. We therefore distinguish two extreme types of compositional zonation. The first is the *initial concentration profile*, the profile produced during crystal growth. Secondly, the *equilibrium concentration profile* is the profile that would be produced by complete diffusive equilibration of the initial concentration profile of the crystal. The observed concentration profile will lie between these two extremes depending on the diffusivity of the chemical element being considered and the amount of time elapsed. Thus, the initial concentration profile of the anorthite content is likely to be preserved because interdiffusion of CaAl and NaSi is extremely slow (Grove et al., 1984; Morse, 1984).

The diffusivity of Sr is considerably faster (Giletti and Casserly, 1994) such that the observed Sr concentration profile may lie between the initial and equilibrium profiles. Given a known or estimated initial concentration profile, a mathematical model of diffusion can be used to calculate the time required to attain the observed concentration profile. This supposes that equilibrium has not been reached, so we start by deriving a test for equilibrium and describe how the equilibrium concentration profile may be calculated.

5.7.2 Equilibrium concentration profiles

The equilibrium concentration profile, in the case of plagioclase, is not necessarily a flat profile but rather it depends on the variation in anorthite content across the crystal. Following Blundy and Wood (1991), the equilibrium partition coefficient D_{Sr} for Sr between plagioclase and liquid depends on temperature and the anorthite content of the plagioclase:

$$RT \ln D_{Sr} = 26{,}800 - 26{,}700\, X_{An}, \qquad (1)$$

where R is the universal gas constant (8.31451 J mol^{-1} K^{-1}). The effect of major element liquid composition is insignificant because the entry of Sr into plagioclase is largely controlled by the crystal chemical controls of the plagioclase, and not by the melt structure. It follows that the partitioning of Sr between two plagioclase compositions a and b, $D_{Sr}^{a/b}$, is given by

$$D_{Sr}^{a/b} = C_{Sr}^{a} / C_{Sr}^{b} = D_{Sr}^{a/lq} / D_{Sr}^{b/lq}, \qquad (2)$$

where C denotes concentration and lq is the liquid. Thus, while the initial concentration profile of Sr is dependent on both $D_{Sr}^{crystal/lq}$ and C_{Sr}^{lq}, any initial variation in $C_{Sr}^{crystal}$ introduced by variation of C_{Sr}^{lq} alone will diffuse with time to establish the equilibrium concentration profile that obeys equation (2).

Substituting (1) into (2), we obtain the Sr equilibrium partition coefficient between two plagioclase compositions a and b:

$$D_{Sr}^{a/b} = \exp\left(\frac{-26700\left(X_{An}^{a} - X_{An}^{b}\right)}{RT}\right). \qquad (3)$$

Figure 5-2 is a graphic representation of $D_{Sr}^{a/b}$ between two parts a and b of a plagioclase crystal with different anorthite contents. Clearly the relative partitioning is only a weak function of temperature.

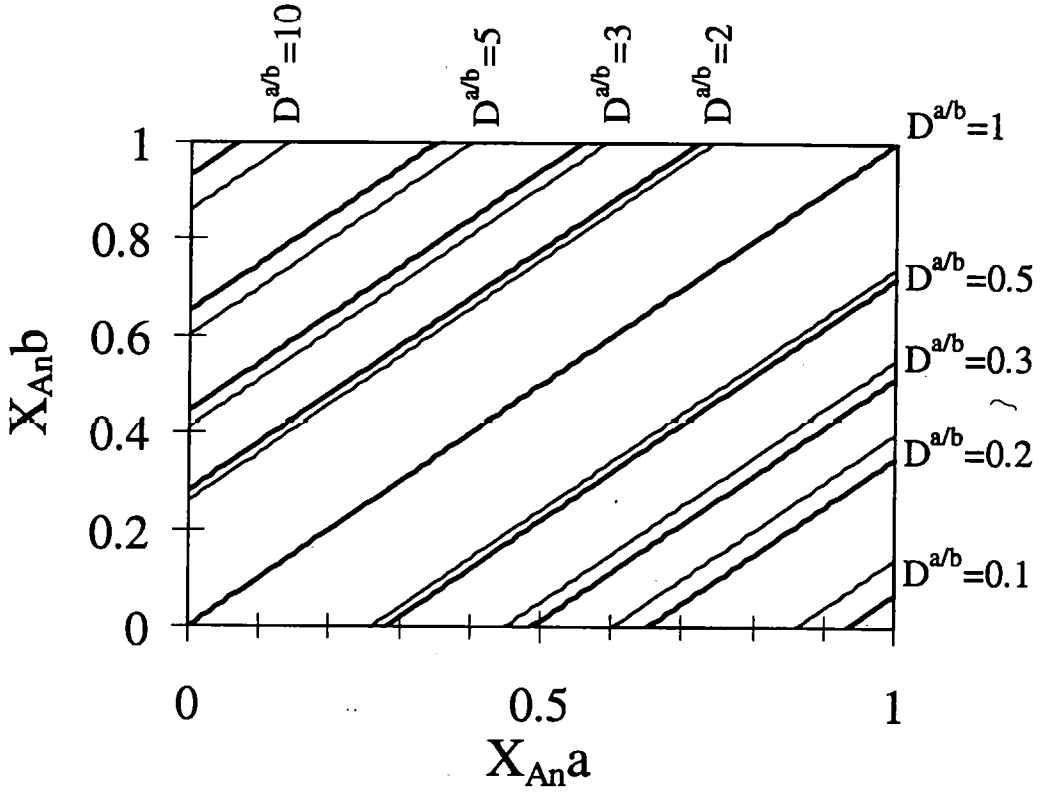

Figure 5-2: Relative partitioning between two parts a and b of a plagioclase of variable X_{An} content for temperatures of 1200 (thin lines) and 1300 K (thick lines).

Equation (3) provides a test for equilibrium between any pair of points within a plagioclase crystal. In cases where the observed concentrations are in equilibrium, the crystal may either have grown from a liquid with constant Sr content during the period of crystal growth, or any initial disequilibrium may have diffused with time. The former is

unlikely, because crystal growth will itself induce changes in the Sr concentration of the liquid for $D_{Sr} \neq 1$. In addition, any sudden changes in X_{An} indicate magmatic events that are likely to be associated with changes in the trace element concentrations in the melt (e. g. recharge or assimilation). Hence equilibrium trace element zonation in association with significant X_{An} zonation indicates that trace element diffusion has taken place. In contrast, a crystal that shows trace element concentration profiles that are not in equilibrium presumably cooled to temperatures below which diffusion is insignificant before it reached equilibrium.

It is useful to determine the absolute equilibrium Sr concentration at any point of the crystal by integrating the observed Sr concentration over the entire crystal, thus conserving the total Sr content. For a crystal zoned in direction x,

$$\frac{1}{X}\int_{rim1}^{rim2} C_{Sr}^{crystal}\, dx = k_{Sr}, \qquad (4)$$

where X is the distance between the rims of the crystal and k_{Sr} is the total amount of Sr in the crystal and is constant.

5.7.3 Diffusive modification of Sr concentration profiles

Diffusion is described by the Arrhenius equation:

$$Đ = Đ_0\, e^{(-Q/RT)}, \qquad (5)$$

where Đ is diffusivity, $Đ_0$ is a pre-exponential factor and Q is activation energy.

Giletti and Casserly (1994) measured the diffusion rate of Sr in albite ($Ab_{98}Or_1An_{0.6}$), oligoclase (An_{25}), labradorite (An_{60}) and anorthite (An_{96}), and determined $Đ_0$ and Q for each mineral over a wide range of magmatic temperatures. The activation energies were 277±26 (albite), 261±46 (oligoclase), 295±31 (labradorite) and 267±58 kJ mol^{-1}

(anorthite). The data are adequately described by a single activation energy of 276 kJ mol^{-1}, and a $Ð_0$ (in m^2s^{-1}) that is a function of X_{An}:

$$\log_{10}(Ð_0) = -4.08 - 4.1\ X_{An} \quad (6)$$

Thus,

$$Ð_{Sr} = 10^{-(4.1X_{An}+4.08)} \exp(-3.32\times10^4/T). \quad (7)$$

Hence, the Sr diffusivities in plagioclase can be calculated from known values of X_{An} and T. (For a discussion of errors associated with calculated Sr diffusion rates, see section 2.5.)

To constrain the diffusion process further, we consider a model of diffusive destruction of oscillatory trace element zoning in a crystal with constant diffusivity $Ð_{Sr}$ but variable partitioning (Figure 5-3). For simplicity, we model two zones a and b of equal width, 2w, and initial Sr concentrations $C^a_{Sr,0}$ and $C^b_{Sr,0}$. While diffusion does not significantly change their anorthite contents because of the extremely slow diffusion of CaAl and NaSi (Grove et al., 1984; Morse, 1984), the initial Sr zonation diffuses towards the equilibrium distribution of Sr defined by mass conservation

$$C^a_{Sr,0} + C^b_{Sr,0} = C^a_{Sr,equil} + C^b_{Sr,equil} \quad (8)$$

and equilibrium partitioning

$$D^{a/b}_{Sr} = C^a_{Sr,equil} / C^b_{Sr,equil}. \quad (9)$$

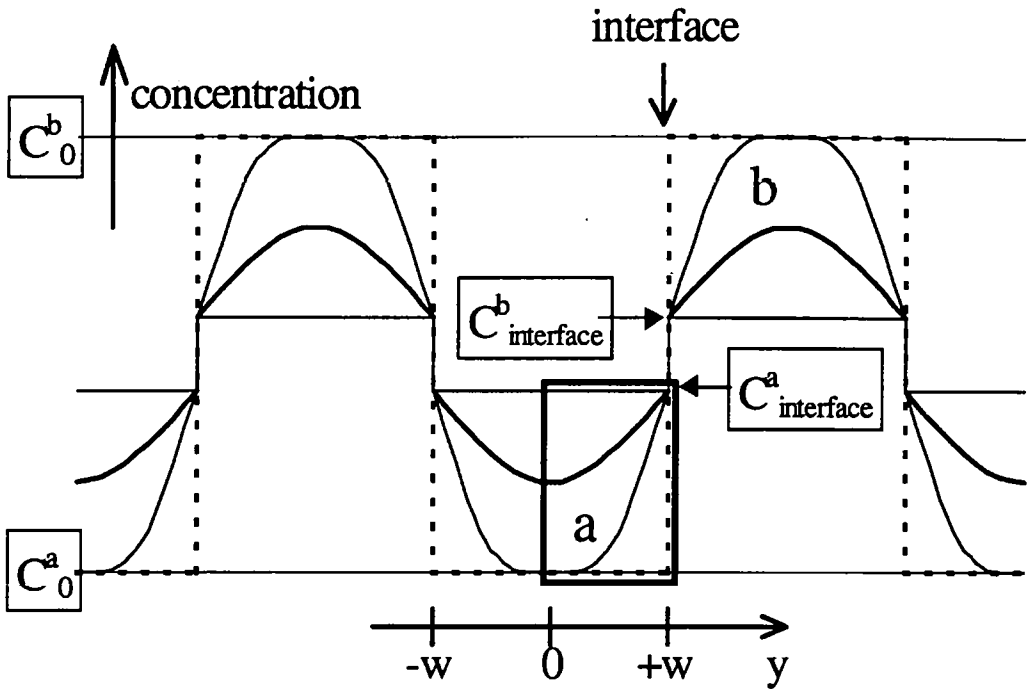

Figure 5-3: Model of diffusive destruction of oscillatory zoning. Initially, the crystal has alternating bands of width 2w and trace element concentrations C^a_0 and C^b_0. As diffusion proceeds, the contact compositions between bands are $C^a_{interface}$ and $C^b_{interface}$. The composition - time - position relationship in a given band is the same as that for a slab of width 2w and of initial composition C_0 with the surface composition fixed at $C_{interface}$ (black box). In the beginning, the amplitudes of the zoning remain constant as diffusion affects only the edges of the bands. Subsequently, zoning amplitudes decrease as chemical equilibration proceeds towards equilibrium.

At the onset of diffusion, the equilibrium concentrations are reached at the interface between the two zones a and b:

$$C^a_{Sr,interface} = C^a_{Sr,equil} = \left(C^a_{Sr,0} + C^b_{Sr,0}\right) D^{a/b}_{Sr} / \left(1 + D^{a/b}_{Sr}\right) \tag{10}$$

$$C^b_{Sr,interface} = C^b_{Sr,equil} = \left(C^a_{Sr,0} + C^b_{Sr,0}\right) / \left(1 + D^{a/b}_{Sr}\right) \tag{11}$$

The diffusion in each zone of the crystal can then be modelled using the solution for diffusion in a layer of half-width w with its edge (y = +w) at the constant interface concentration (e. g. Bird et al., 1963, their equation 11.1-31, black box in Figure 5-3),

where the Sr concentration C_{Sr} is a function of time t and distance y from the centre of a band:

$$\frac{C_{Sr} - C_{Sr,equil}}{C_{Sr,0} - C_{Sr,equil}} = 2\sum_{n=0}^{\infty} \frac{(-1)^n}{(n+\frac{1}{2})\pi} e^{-(n+\frac{1}{2})^2 \pi^2 D_{Sr} t/w^2} \cos\left((n+\frac{1}{2})\frac{\pi y}{w}\right). \quad (12)$$

In cases where the zones are not of equal width or where the diffusivities of Sr are not equal, diffusive equilibration will take a different path. As a first approximation appropriate to our purposes, we use equation (12) in conjunction with the highest X_{An} (i. e. slowest diffusivity) of a crystal to model the timescales of equilibration.

It is useful to define a parameter δ as the undiffused fraction of the initial concentration profile (i. e. Equation 12 evaluated at y = 0):

$$\delta = \left[\frac{C_{Sr} - C_{Sr,equil}}{C_{Sr,0} - C_{Sr,equil}}\right]_{y=0}. \quad (13)$$

Figure 5-4a to c show the diffusive destruction of square wave concentration signals with time for different plagioclase compositions, temperatures and bandwidths, in terms of the evolution of δ. Initially (up to $t \approx 0.1\ w^2/D_{Sr}$), the amplitudes of the signals remain constant as diffusion affects their edges only. On Figure 5-4 this is represented by initial zero slopes and is most pronounced for slow diffusion rates (i. e. large X_{An} values) or wide band widths. Subsequently, however, the amplitudes of the signals decrease to 10% of their initial value after a total time $t \approx w^2/D_{Sr}$, which for the examples in Figure 5-4 is within tens to hundreds of years. The most rapid equilibration is achieved for plagioclase of low X_{An} with narrow bands held at high temperature. Plagioclase crystals of the type modelled in Figure 5-4 must experience magmatic temperatures for much less than ~500 years if they are to retain any significant non-equilibrium Sr zonation.

For crystals that show disequilibrium trace element profiles, we can calculate how much longer they would have had to reside in their magma reservoir to equilibrate. It is

impossible, however, to determine the amount of time the crystals resided in the chamber precisely unless their initial trace element concentration profiles at the time of crystallisation are known.

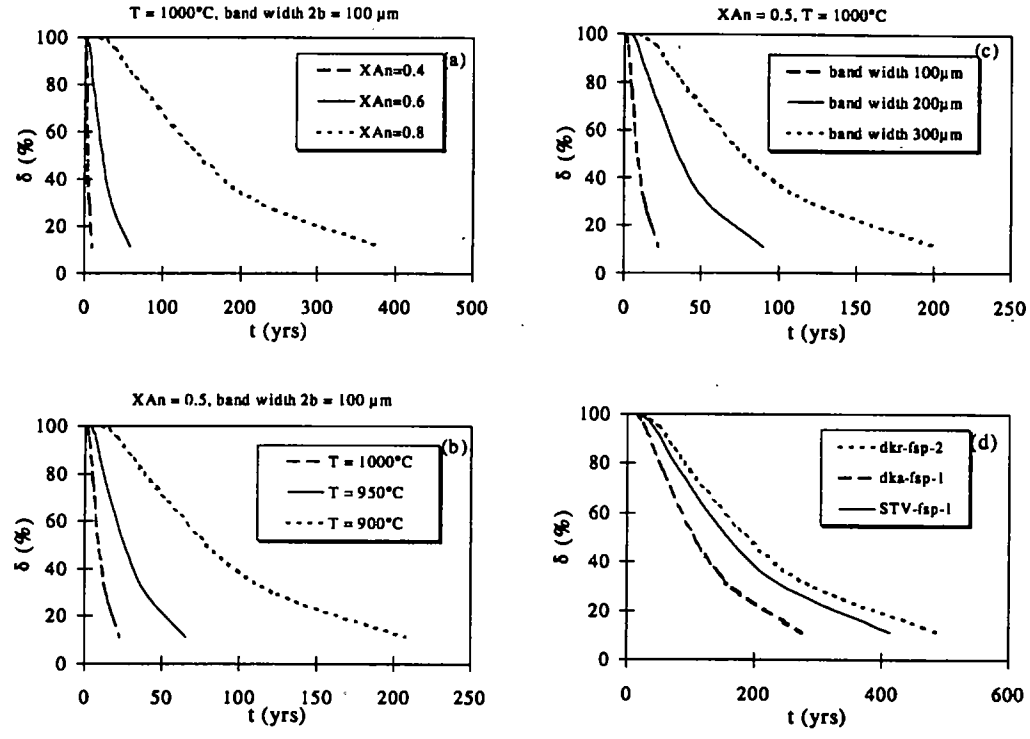

Figure 5-4: Diffusive destruction of square wave Sr concentration signals with time for (a) different plagioclase compositions, (b) temperatures and (c) bandwidths. δ is the undiffused fraction of an initial square wave concentration profile (Equation 13). (d) Application of the model to plagioclase crystals from the Kameni dacites, Santorini (Section 5.8) and the 1979 Soufriere andesite (Section 5.9).

5.7.4 Initial Sr concentration profiles

One way to assess the initial trace element profiles is to use published data on trace element variations in plagioclase phenocrysts to constrain the maximum petrologically conceivable range in initial trace element concentration. Along with the observed profile and a calculated equilibrium profile, this can then be used to obtain a maximum residence time of a crystal in its magma reservoir. Previous ion microprobe studies of trace element variations across plagioclase crystals from the Tatara-San Petro volcanic complex, Chile

(Singer et al., 1995), the Val Fredda Complex, Italy (Blundy and Shimizu, 1991), and Ngauruhoe and Taupo, New Zealand (Rogan, 1996), have investigated a wide range of compositions from $X_{An} < 0.3$ to $X_{An} > 0.9$ and trace element concentrations ranging from less than 170 ppm to more than 2100 ppm Sr. The Sr concentrations within single plagioclase crystals studied by these authors varied by no more than a factor of ~2.5. In addition, plagioclase core - rim pairs from rhyodacite lavas from Crater Lake, Oregon, analysed by electron microprobe (Nakada et al., 1994), contain 0.09 wt% to 0.23 wt% SrO, with a maximum range of a factor ~2.5.

We argue that a factor of ~2.5 is a petrologically reasonable estimate for the maximum range in the Sr concentration in any one crystal. Based on this upper estimate, *maximum range initial concentration profiles* can thus be constructed assuming an initial square wave variation, again using equation (4) as a boundary condition. Equations (12) and (13) can then be used to model their diffusive destruction towards final equilibrium profiles given by equations (1) to (4). The extent to which they attain equilibrium provides a maximum constraint on the residence time of the crystal in the magma.

5.7.5 Sources of errors

Errors associated with calculating the maximum crystal residence times in this way may be conveniently divided as follows: (a) those associated with calculation of the equilibrium profile; (b) those relating to imprecision in the diffusion data; (c) errors associated with departures from the assumed initial profile, variable anorthite contents and uncertainties in magmatic temperatures. These are discussed in turn below.

(a) When calculating the equilibrium concentration profile, an error is associated with the semi-empirical equation (1). Blundy and Wood (1991) estimated the 2σ error on the slope of $RT \ln D_{Sr}$ versus X_{An} to be almost 10%, and on the intercept almost 5%. This results in errors on D_{Sr} that may be of the order of a factor 2 or more. However, these

errors are based on a literature compilation of both experimental and volcanic plagioclase-melt partitioning data. In the technique presented here, we are concerned with the relative distribution coefficients between different parts of the same crystal. We propose that the error on relative partitioning between adjacent parts of a crystal with a small range in X_{An} may be negligible.

(b) Diffusivities measured at a given temperature are taken to have a 2σ uncertainty of less than factor of 2 on the basis of the statistics of the measurements (Cherniak and Watson, 1994; Giletti and Casserly, 1994). We are confident that the error on the diffusivity measurement is not larger than that for two reasons. Firstly, as the diffusion measurements were made in the temperature range appropriate for magmatic systems (550°C-1300°C), there are no errors involved in extrapolation using the Arrhenius relationship. Secondly, the results from two independent sets of experiments of Giletti and Casserly (1994) and Cherniak and Watson (1994) coincide almost exactly, except for the albitic end of the spectrum. Furthermore, activation energies could not be measured to better than 10 to 20% accuracy, which transposes to an insignificant contribution to the error in Đ of around ±1%. The linear regression of $Đ_0$ values (equation 6) carries an error on $Đ_0$ and thus on Đ of up to a factor of 2, similar to the error of the measurement. Finally, we assume that Sr diffusion in plagioclase is isotropic within error of the measurement (Giletti and Casserly, 1994; LaTourette and Wasserburg, 1998), although there is some evidence of slight anisotropy (Cherniak and Watson, 1994), with diffusion of Sr normal to (010) being somewhat slower (by <0.7 log units) than diffusion perpendicular to (001). As diffusional anisotropy in plagioclase has not been studied in sufficient detail, we are unable to correct for its effects and consider a one-dimensional diffusion model as an adequate first approximation. In conclusion, the error on calculated diffusivities may be of the order of a factor of 2.

(c) Further errors are introduced in the process of calculating crystal residence times. First, the model is based on a simple step function and does not account for more subtle variations in the initial concentration profile. Second, the variability of X_{An} is not included into equation (12). Finally, it is often impossible to constrain magma temperatures to better than ± 50 - 100°C. However, these errors can be accounted for by restricting oneself to estimates of the *maximum*, rather than the exact crystal residence times. The simple step function of the maximum range initial concentration profile diffuses within a time $t^* \approx 0.1\ w^2 / Đ$ to a smooth profile that has a signal of the same amplitude. Thus, using a simple step function will result in an overestimate of the residence time of the crystal if the initial concentration profile was in fact smooth. Figure 5-4 shows that this would only be an overestimate of 5-10% even in the most unfavorable cases. Secondly, diffusion is controlled by that part of the crystal with the slowest diffusivity, i. e. with the highest anorthite content. Using the highest anorthite content as an overall anorthite content in the model again ensures that estimated residence times are maximum residence times. Using the lower end of the range of temperature estimates may accommodate poor knowledge of magma temperatures.

In summary, diffusion modeling is clearly very sensitive to changes in anorthite content (Figure 5-4a), temperature (Figure 5-4b), bandwidth (Figure 5-4c) and concentration range. At this stage of our knowledge it seems difficult to calculate exact crystal residence times on the basis of the diffusion model, particularly in the light of uncertainty of the employed parameters. However, the technique appears robust when *maximum* residence times are calculated. When all of the parameters used in the modeling are chosen to give the lowest conceivable estimates on diffusivity, and thus maximum residence times, it is probable that these residence times are, if anything, overestimates of the actual residence times.

5.8 Case study 1: Santorini, Aegean Volcanic Arc, Greece

We have chosen to apply the diffusion model to plagioclase crystals from the Kameni island dacites, Santorini. Plagioclase crystal size distribution studies in these lavas (Higgins, 1996) imply plagioclase crystal residence times of less than 100 years. Such short residence times are also consistent with preliminary results from Ra-Th isotope disequilibria (Zellmer et al., 1998). The object of this study is to obtain another independent estimate of the timing of the crystal fractionation events, and to compare the results with those from crystal size distribution studies as a test of the diffusion model.

5.8.1 Geological setting

The Aegean Volcanic arc, Greece, is a 450 km long chain of late Pliocene – Quaternary volcanoes formed by northward subduction of the African plate beneath the continental Aegean microplate. Volcanic activity at Santorini in the central part of the arc began ~700 ka ago and continues to the present day. For a detailed summary of the geological evolution of Santorini, see Druitt et al. (1996).

Magma residence times at Santorini were first investigated by Pyle et al. (1988), using U-Th mineral isochron dating. Two crystal populations were identified with statistically indistinguishable crystallisation ages of 79 (+14/-12) ka and 93 (+29/-22) ka and with different initial Th isotope ratios. These were attributed to physical intermingling of magma with an older crystal mush prior to eruption, and as the eruption age of their sample is not well established, these ages are maximum crystal residence times. Because the ages overlap, only an approximate residence time (0-55 ka) of the crystal mush before mingling with the new magma can be derived.

More recent work by Higgins (1996b) used crystal size distribution (CSD) studies of plagioclase crystals to infer crystal residence times in the 46AD – 1950 Kameni dacites, the youngest volcanic products of Santorini. Magma mixing was identified for each lava

flow, with magma chamber residence times of 43 to 96 years for the older magma derived from plagioclase megacrysts, and residence times of 6 to 13 years for the younger magma derived from plagioclase microlites. Short plagioclase crystal residence times of the order of 10s to 100s of years are consistent with Ra-Th isotope disequilibria of Kameni whole rock samples (Zellmer et al., 1998). Depletion of ^{226}Ra with respect to ^{230}Th was attributed to plagioclase crystal fractionation with $D_{Ra} > D_{Th}$ shortly prior to the eruption of each Kameni dacite.

5.8.2 Analytical results

Four dacitic rock samples from the Kameni islands (Agios Nicolaos lava "dka", 726AD; Fouqué lava "dkf", 1939-40; Reck and Smith lava "dkr", 1940; and Liatsikis lava "dkl", 1950) were selected for ion probe analysis of selected plagioclase crystals. Trace element traverses were undertaken on six plagioclase phenocrysts to obtain Sr zonation profiles (see caption to Figure 5-5 for analytical details). Sr equilibrium profiles were calculated using equations (1) to (4) in order to assess the degree of diffusive equilibration. Results are given in Table 5-1 and are divided into equilibrium profiles (Figure 5-5) and disequilibrium profiles (Figure 5-6).

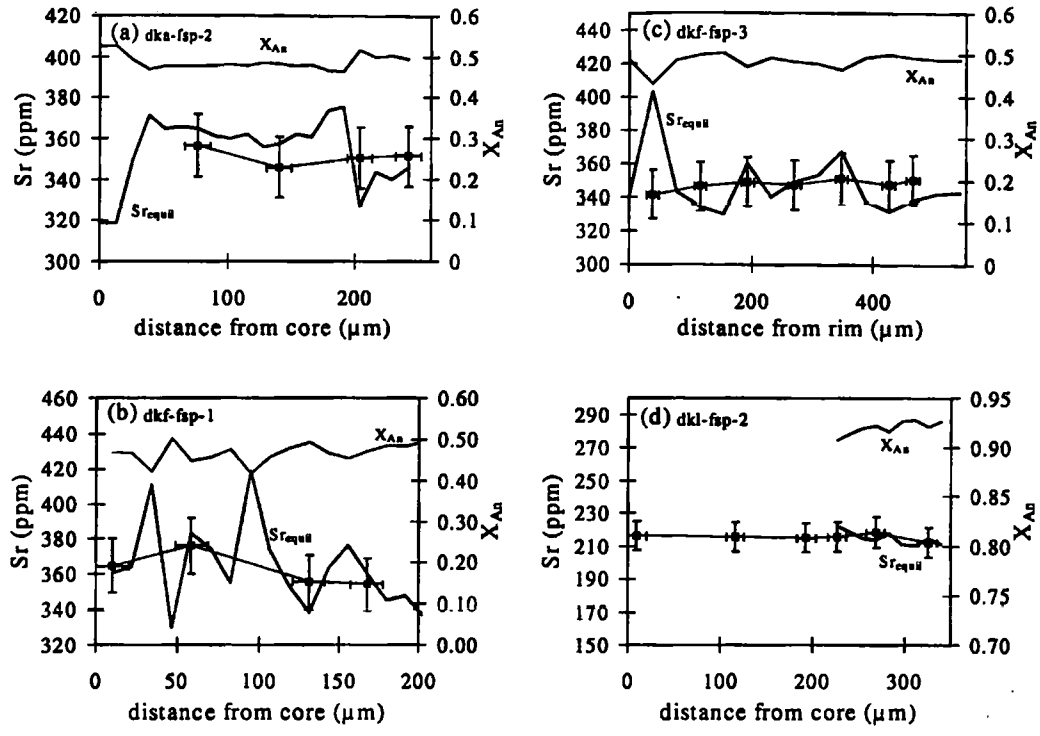

Figure 5-5: X_{An} and Sr profiles of plagioclase phenocrysts from the Kameni dacites. Sr error bars (4.2%, 2σ) are based on repeated analyses of standards (Hinton, pers. comm.). Note that relative errors between points may be much smaller than these because of similarity in the matrix. Samples were analysed for major elements by electron microprobe at the Earth Science department of the Open University, using standard techniques. Ion microprobe analyses were performed on the Cameca ims-4f ion microprobe at the Department of Geology and Geophysics, University of Edinburgh, using a 10 kV primary O^--ion beam. To eliminate molecular species, only the high-energy portion of the dispersed secondary ion beam was selected by an energy window and allowed to pass into the mass analyser. An electron multiplier was used as secondary ion detector. Typical background count rates were much lower then 0.03 cps, whereas the signal was of the order of 10000 cps for Sr. Sr equilibrium profiles were calculated using equations (1)-(4). Observed Sr concentration profiles mirror equilibrium profiles.

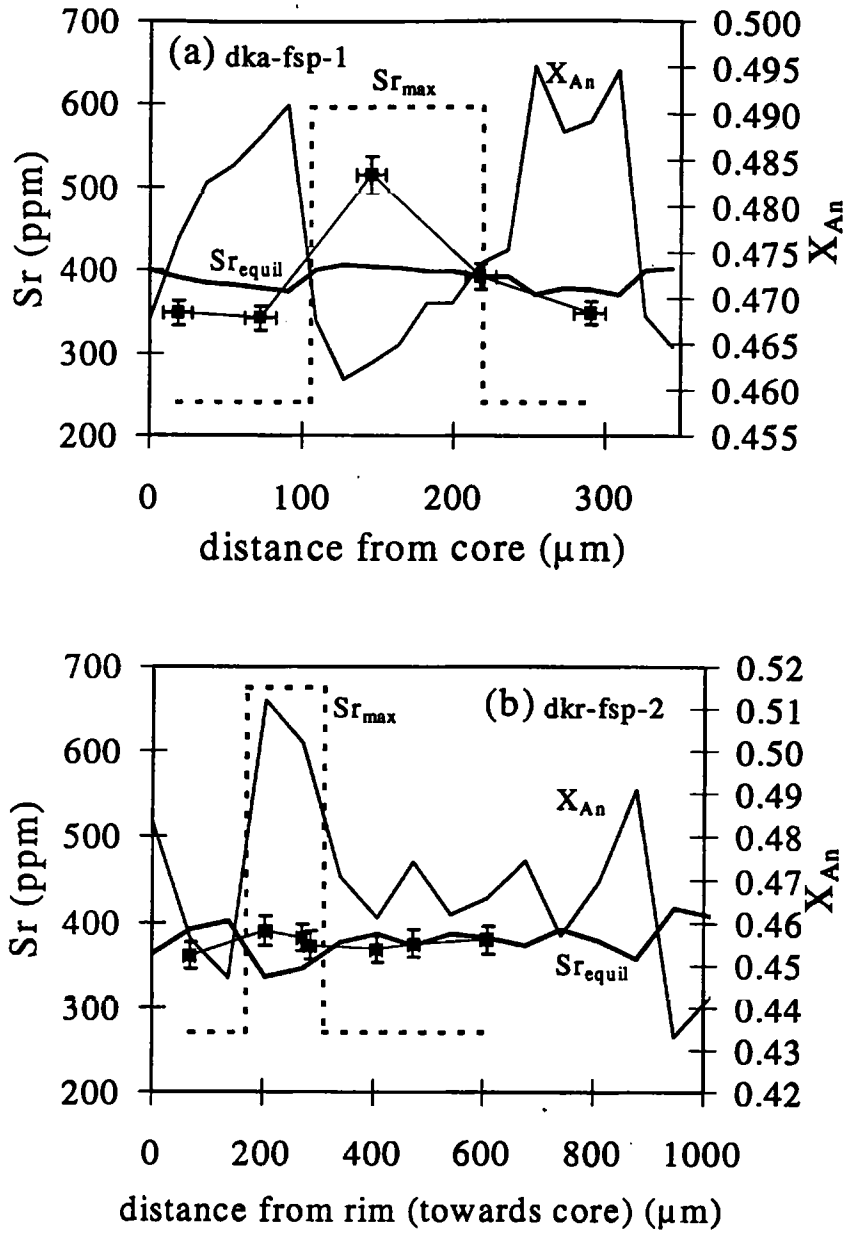

Figure 5-6: X_{An} and Sr profiles of plagioclase phenocrysts from the Kameni dacites. Analytical techniques as in Figure 4. Sr equilibrium profiles were calculated using equations (1)-(4). Observed Sr concentration profiles are not in diffusive equilibrium. Maximum range initial profiles were determined as described in the text. Note that while dka-fsp-1 shows a large variation in Sr content and is grossly out of equilibrium, dkr-fsp-2 shows a much smaller range and is much closer to equilibrium.

Eruptive unit	age	crystal	length (μm) and type of traverse		X_{An}	Sr (ppm)	Figure	equilibrium
Kameni island equilibrium profiles:								
Agios Nicolaos	726AD	dka-fsp-2	250	rim only	0.46-0.53	346-356	4a	yes
Fouque	1939-40	dkf-fsp-1	220	core to rim	0.41-0.50	354-376	4b	yes
Fouque	1939-40	dkf-fsp-3	550	rim to rim	0.43-0.50	341-351	4c	yes
Liatsikis	1950	dkl-fsp-2	350	rim only	0.92-0.93*	212-218	4d	yes
Kameni island disequilibrium profiles:								
Agios Nicolaos	726AD	dka-fsp-1	350	rim only	0.46-0.50	342-516	5a	no
Reck and Smith	1940	dkr-fsp-2	1000	core to rim	0.43-0.51	361-390	5b	no
Profiles from Soufriere, St. Vincent:								
Soufriere andesite	1979	STV-fsp-1	700	outer core to rim	0.60-0.82	255-272	6a	no
Soufriere andesite	1979	STV-fsp-3	650	core to rim	0.92-0.94	177-206	6b	yes

*Anorthite contents were only measured at the outer 100μm of the traverse.

Table 5-1 Summary of plagioclase crystal traverses

5.8.3 Modelling

Two out of six crystals from the Kameni dacites (dka-fsp-1 and dkr-fsp-2, Figure 5-6) show Sr concentration profiles that are not in diffusive equilibrium and thus could be modelled using the technique outlined above.

5.8.3.1 Plagioclase crystal dka-fsp-1, Palea Kameni, Santorini

Crystal dka-fsp-1 (Figure 5-6a) was the object of a rim traverse only. Barton and Huijsmans (1986) reported magma temperatures of 900°C to 1012°C for all Kameni island dacites, based on two-pyroxene geothermometry, depending on the method of calculation. Their lower estimate of 900°C was used here to calculate maximum residence times.

A mean Sr concentration of 390 ppm was calculated for the modelled profile width of 273 μm. The equilibrium concentration profile was calculated from equations (3) and (4), conserving the mean Sr concentration over the modelled profile width. The maximum range initial concentration profile was calculated on the basis of a square wave concentration signal of 115 μm width, with a concentration step of factor 2.5, centred on the low X_{An} band of the crystal, again using equation (4) as the boundary condition. The

remaining proportion $\delta = \sim 60\%$ of the maximum initial range concentration was then calculated using equation (13).

For diffusion modeling, an anorthite content of $X_{An} = 0.50$ was used since the maximum anorthite content of the crystal is the limiting parameter for diffusive destruction of trace element zoning. A Sr diffusivity of $D_{Sr} = 3.81 \times 10^{-19}$ $m^2 s^{-1}$ was therefore calculated using equation (7), and diffusion curves for the initial range concentration maximum were then constructed using equation (12). From $\delta = 60\%$, a maximum crystal residence time of ~100 years was derived for the modelled rim of the crystal at 900°C (Figure 5-4d). The actual crystal residence time is likely to have been much shorter than this.

5.8.3.2 Plagioclase crystal dkr-fsp-2, Nea Kameni, Santorini

dkr-fsp-2 (Figure 5-6b) was probed from core to rim, and a magma temperature of 900°C was again used as a lower estimate based on two-pyroxene geothermometry.

A mean Sr concentration of 376 ppm was calculated for the modelled profile width of 540 μm, and the equilibrium concentration profile was calculated using the method described above. The maximum range initial concentration profile was calculated on the basis of a square wave concentration signal of 140 μm width, and a concentration step with a factor of 2.5, centred on the high X_{An} band of the crystal, again using equation (4) as boundary condition. We find that $\delta = \sim 15\%$.

For diffusion modeling, an anorthite content of $X_{An} = 0.52$ was used. This yielded a Sr diffusivity of $D_{Sr} = 1.25 \times 10^{-18}$ $m^2 s^{-1}$, and again diffusion curves were constructed. From $\delta = 15\%$, the maximum crystal residence time is 450 years at 900°C (Figure 5-4d), but again the actual residence time is likely to have been much shorter than this.

5.8.4 Implications

The Sr concentration profiles of plagioclase crystals dka-fsp-2, dkf-fsp-1, dkf-fsp-3 and dkl-fsp-2 (Figure 5-5a to d) are in diffusive equilibrium and thus they do not carry any information about crystal residence times. It is possible that these crystals crystallised from a magma with constant Sr content. However, sudden changes in X_{An} across the profiles of dka-fsp-2, dkf-fsp-3 and dkl-fsp-2 indicate that their growth histories were more complex, and suggest that the Sr concentrations may have been more variable and have been homogenised by diffusion. However, while these crystals may be old, the diffusion model cannot be used to estimate their minimum age, since minimum range initial concentration profiles are not available.

For dka-fsp-1, a maximum residence time of ~100 years was obtained for the crystal rim. This is consistent with the megacryst residence times of 70 years derived from crystal size distribution studies of the dka726AD Kameni dacite (Higgins, 1996). For dkr-fsp-2, the maximum crystal residence time of 450 years derived from diffusion modeling may be compared with a megacryst residence time of 63 years determined by the combined crystal size distribution study of the 1939-1941 Kameni dacite flows (Higgins, 1996). The consistency of residence timescales derived by these two very different approaches gives us confidence that results based on diffusion modeling contain meaningful time information. In addition, short crystal residence times are also in agreement with Ra-Th whole rock disequilibria measured for the Kameni dacites (Zellmer et al., 1998) which constrain plagioclase crystal residence times to less than a few hundred years. Unfortunately, the Ra-Th dating technique cannot give more accurate time information on such short timescales.

Plagioclase crystal dkl-fsp-2 is highly calcic ($X_{An} > 0.9$), and thus it is not in equilibrium with its dacitic host magma. We suggest that this crystal is a xenocryst derived from a

more mafic magma. Although we cannot deduce any information about the residence time of this crystal from diffusion modeling, it is important to note that the Kameni island dacites contain plagioclase xenocrysts that are likely to be old. Depending on their abundance, they may introduce an error into crystal residence time estimates derived from CSD studies. In this respect, maximum residence times calculated from Sr diffusion in plagioclase crystals may be more robust, although the two techniques are not strictly comparable. While CSD studies use a range of phenocrysts to estimate the time of onset of crystallisation of this phenocryst population, Sr diffusion modeling is restricted to the residence time of single crystals and so it can yield different results.

5.9 Case study 2: St. Vincent, Lesser Antilles island arc, West Indies

U-Th mineral isochrons from Soufriere, St. Vincent (Heath et al., 1998b), point to crystal residence times of tens of thousands of years, in striking contrast to much shorter plagioclase residence timescales for the Kameni islands, Santorini. In addition, such long crystal residence times would appear to be inconsistent with a whole rock Th-Ra disequilibrium result from Soufriere (Chabaux and Allègre, 1994). To elucidate these discrepancies, we have applied the diffusion model to one of the Soufriere andesites to investigate the age of plagioclase crystals using a technique independent of the U-series decay system.

5.9.1 Geological setting

The Lesser Antilles intra oceanic arc is a 750 km long chain of volcanic islands resulting from the subduction of the American plate beneath the Caribbean plate. Volcanic activity at Soufriere volcano on St. Vincent at the southern end of the central islands of the arc began ~600 ka ago and it continues to the present day. For a detailed summary of the geological evolution of St. Vincent, see Heath et al. (1998a).

Magma residence times at Soufriere were studied by Heath et al. (1998b) using U-Th mineral isochron dating of separated phases from four historic eruptions, including the 1979 Soufriere andesite. Olivine, clinopyroxene, plagioclase, magnetite and groundmass were separated and analysed for U and Th isotopes. Plotted on U-Th equiline diagrams, these show positive correlations of ($^{230}Th/^{232}Th$) activity ratio with ($^{238}U/^{232}Th$) activity ratio. Lines of best fit give isochron ages ranging from 77 (+22/-19) ka (2σ) to 46 (+51/-35) ka (2σ) for the 1979 Soufriere andesite (STV354 of Heath et al., 1998b), with MSWDs ranging from 2.6 to 19.3. The ages are statistically indistinguishable, and an isochron through the combined data set yields an age of 58 (+12/-11) ka with an MSWD of 14. Heath et al. (1998b) argued that this age reflects the average age of both crystals and magma at the time of eruption. They concluded that crystallisation was essentially instantaneous, occurred >40 ka ago, and then stopped due to thermal buffering in the crustal magma chamber.

5.9.2 Analytical results

A rock sample from the 1979 Soufriere andesite (STV354 of Heath et al., 1998b), was selected for ion microprobe analysis. Ion microprobe traverses were undertaken on two plagioclase phenocrysts to obtain Sr zonation profiles (Figure 5-7). Sr equilibrium profiles were calculated using equations (1) to (4) in order to assess the degree of diffusive equilibration. In plagioclase phenocryst STV-fsp-1 diffusive equilibration of Sr is not complete, whereas phenocryst STV-fsp-3 is in diffusive equilibrium. The results are summarised in Table 5-1.

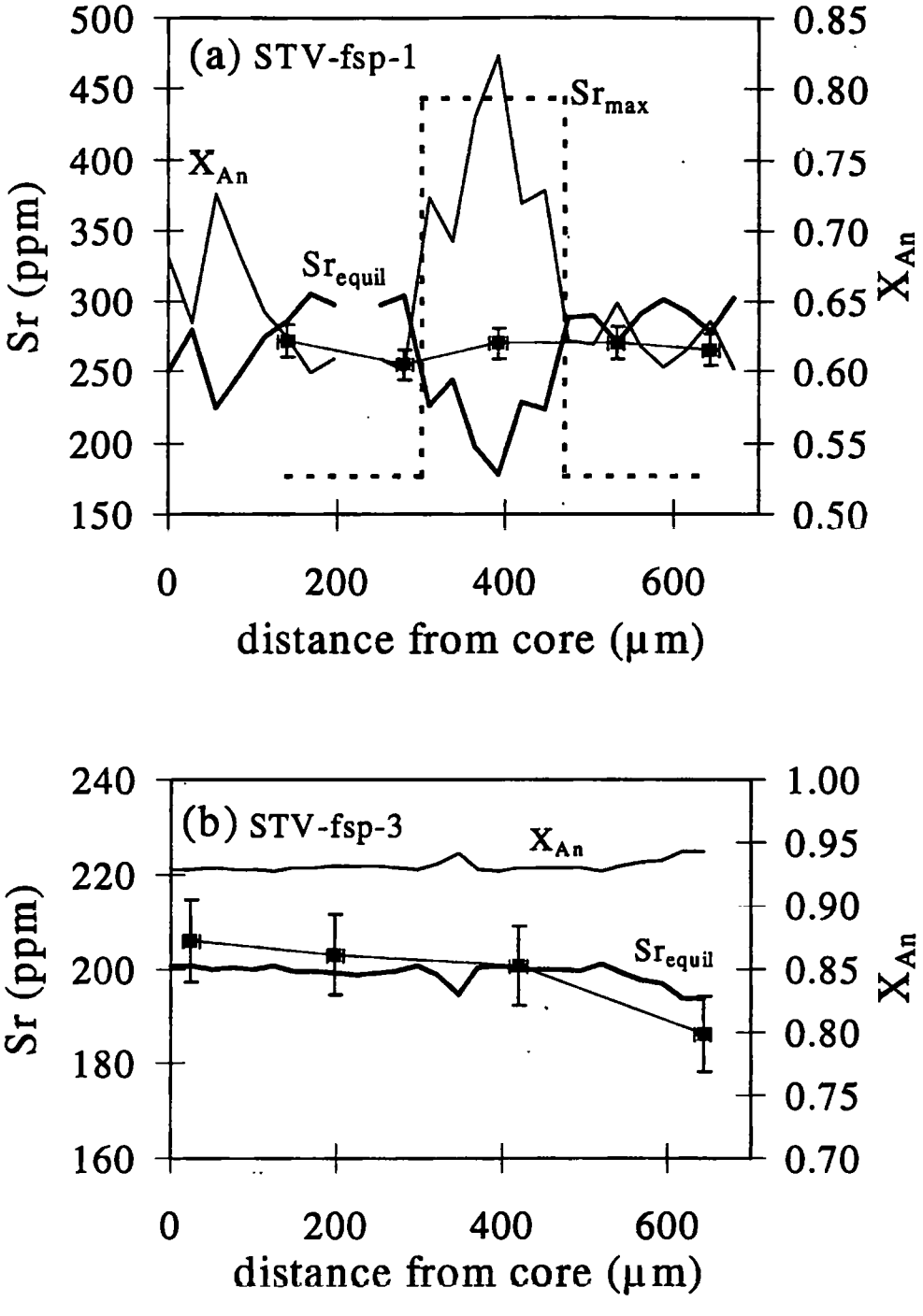

Figure 5-7: X_{An} and Sr profiles of plagioclase phenocrysts from the 1979 Soufriere andesite, St. Vincent. Sr equilibrium profiles were calculated using equations (1)-(4). (a) Observed Sr concentration profiles are not in diffusive equilibrium. Maximum range initial profiles were determined as described in the text. (b) The observed Sr concentration profiles mirror the equilibrium profile.

5.9.3 Modelling

The plagioclase phenocryst STV-fsp-1 preserves a Sr concentration profile that is not in diffusive equilibrium and thus could be modelled by the technique outlined above (Figure 5-7a). A magma temperature of 1060°C was used since this was the lowest estimate available from geothermometry (Heath et al., 1998a). A mean Sr concentration of 267 ppm was calculated for the modelled profile width of 503 µm, and the equilibrium concentration profile was calculated using equations 1 to 4. The maximum range initial concentration profile was calculated on the basis of a square wave concentration signal of 170 µm width, and a concentration step with a factor of 2.5, centred on the high X_{An} band of the crystal, again using equation (4) as the boundary condition. We find that $\delta = \sim 35\%$.

For diffusion modeling, the highest anorthite content ($X_{An} = 0.82$) of the crystal was used. A Sr diffusivity of $D_{Sr} = 5.55 \times 10^{-19}$ $m^2 s^{-1}$ was therefore calculated, and diffusion curves were constructed. From $\delta = 35\%$, a maximum residence time of ~150 years was obtained for the euhedral arm of the crystal at 1060°C (Figure 5-4d). The actual residence time is likely to have been much shorter than this.

5.9.4 Implications

For STV-fsp-1 from the 1979 Soufriere andesite, St. Vincent, a maximum residence time of ~150 years for a large part of this crystal is a result similar to those obtained for the Kameni islands. However, a timescale of less then 150 years is in striking contrast to the U-Th mineral isochron of 46 (+51/-35) ka (2σ) obtained by Heath et al. (1998b), which suggested that crystallisation was essentially instantaneous and stopped significantly more than 10 ka ago. Their mineral isochron included plagioclase separated by standard techniques, and the separates undoubtedly included young plagioclase crystals such as STV-fsp-1. The MSWD of 19.3 for the line of best fit through the separated phases of

the 1979 Soufriere andesite indicates a considerable scatter of the data. Thus each mineral phase may in fact represent a mixture of several crystal growth events under various crystallisation conditions. This suggestion is supported by the variability of X_{An} observed in STV-fsp-1, and by the presence of highly calcic plagioclase crystals (STV-fsp-3, $X_{An} > 90$) that are not in equilibrium with their host rock.

The positive correlation of ($^{230}Th/^{232}Th$) activity ratio and ($^{238}U/^{232}Th$) activity ratio for the separated phases in each sample analysed is well established, and the similarity of their slopes is striking. In addition, the isochron from one of the rocks has an MSWD of 2.6 and may indeed represent a true age of a magma that crystallised under the conditions suggested by Heath et al. (1998b). Thus, a large proportion of crystals may indeed be old, and magma storage in a thermally buffered reservoir is plausible. We suggest that the high X_{An} xenocryst STV-fsp-3 may have crystallised under such conditions, and that the available data do not preclude an age of tens of thousands of years for this crystal. However, the data indicate that either limited crystal fractionation continued until eruption, or there were several periods of plagioclase fractionation, the latest culminating in eruption. We conclude that old crystal ages of the order of tens of thousands of years are evident from the U-Th mineral isochron data, but that precise residence times cannot be derived for mineral isochrons with high MSWDs, where crystal fractionation shortly prior to eruption is evident.

5.10 Discussion

The time required for initial concentration profiles to diffuse to $\delta = 10\%$ of their amplitude may be used as a general guide to the timescale of diffusive equilibration. (When $\delta = 10\%$, using a maximum initial Sr concentration range with a factor of 2.5, and the equilibrium profile midway between initial Sr concentration minima and maxima, Sr will have diffused to the equilibrium concentration profile within error of the

measurement.) Figure 5-8 shows how this timescale $t_{\delta=10\%}$ varies with the zoning bandwidth 2w for different compositions and temperatures. For very small bandwidths, diffusive equilibration is rapid. We suggest that this may be the reason for the observed equilibrium Sr profiles in the majority of the Kameni dacite phenocrysts, e. g. dkf-fsp-1 where bandwidths are less than ~30 μm (Figure 5-5b). In addition, for bandwidths of less than 200 μm, and the compositions and temperatures modelled in sections 3 and 4, the maximum crystal residence time that may be investigated using diffusion modeling is of the order of 1 ka. In contrast, for bandwidths in excess of 2 mm, the timescale for complete diffusive equilibration is 10-100 ka or more, depending on the temperatures and compositions considered. Diffusion on this lengthscale is therefore negligible, and recent studies have used Sr isotope profiles obtained by microdrilling across large plagioclase phenocrysts to assess open and closed system crystallisation and magmatic interactions in mafic and intermediate volcanic systems (Davidson and Tepley, 1997; Tepley et al., 1998). Sr equilibration may however affect small scale zoning in such crystals, and chemical disequilibrium on lengthscales of 0.5 mm or less indicates that the crystals are unlikely to be older than ~1 ka.

It is also evident from Figure 5-8 that at very low temperatures, the timescales of diffusive equilibration are in excess of 10 ka even for bandwidths as small as 50 μm. For example, the Rb-Sr isotope systematics of phenocrysts and glass from the Bishop Tuff, Long Valley, California (Christensen and DePaolo, 1993), revealed very long magma residence times of greater than 300 ka. The large difference between these estimates and those obtained here are explicable in terms of Figure 5-8 and the exponential dependence of diffusivity on temperature. In the case of the Bishop Tuff, with estimated magmatic temperatures of ~725°C, and with sanidines of 2 mm diameter, the timescales of diffusive

equilibration of Sr are very long. Complete equilibration under such conditions would require crystal residence times in excess of 10 Ma.

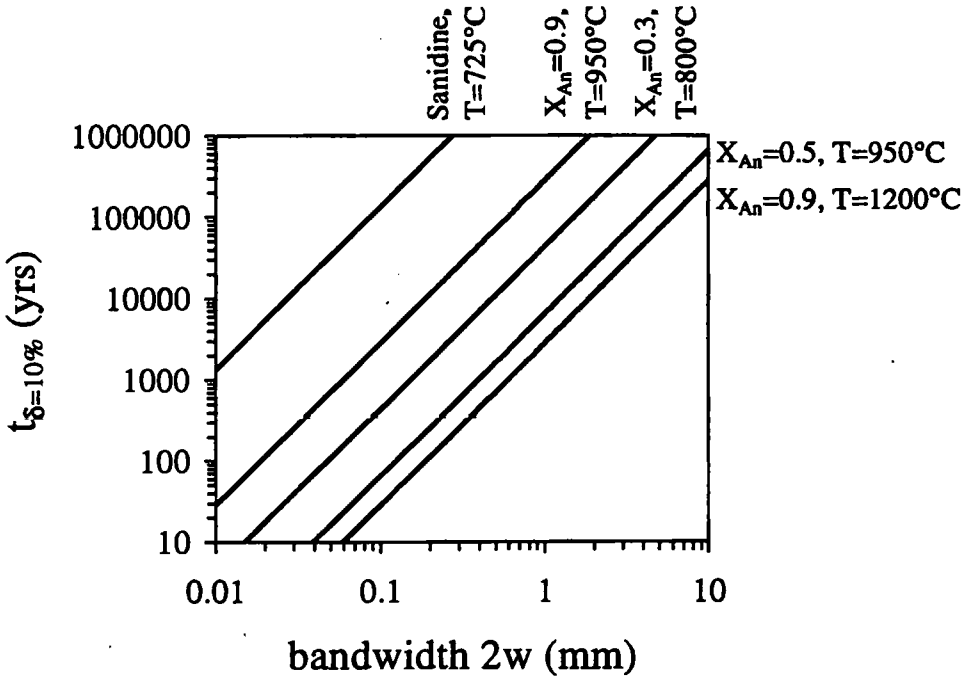

Figure 5-8: Timescales of diffusive equilibration as a function of zoning bandwidth for temperatures and anorthite contents typical for magmatic plagioclase crystals. See text for a detailed discussion.

5.11 Conclusions

We have developed a technique to constrain plagioclase crystal residence times in magmatic systems using incomplete diffusive destruction of Sr zonation towards an equilibrium Sr profile constrained by crystal-liquid partitioning data.

We have applied the diffusion model to trace element profiles across plagioclase phenocrysts from young lavas from the Kameni island dacites, Santorini, and from Soufriere, St. Vincent. For Sr, most crystals have equilibrium concentration profiles. However, two plagioclase phenocrysts from the Kameni islands, Santorini, and one from Soufriere, St. Vincent, have Sr concentration profiles that have not equilibrated by

diffusion. For these, maximum crystal residence times of 100 to 450 years have been obtained.

For the Kameni island dacites this is in good agreement with crystal size distribution studies and supported by Ra-Th isotope disequilibrium data. For Soufriere, St. Vincent, however, such a short time between crystallisation and eruption is in striking contrast to a U-Th mineral isochron age of 46 (+51/-35) ka (2σ) derived for the studied sample. The high MSWD of the U-Th isochron suggests that considerable scatter was introduced into the U-Th system, and our calculations suggest that more recent crystal fractionation is responsible for this scatter. Thus, while the average crustal residence times of the Soufriere magmas and crystals may have been of the order of tens of thousands of years, a more exact estimate is hindered by a complex petrogenetic history of continued or periodic crystal fractionation and magma mixing.

Plagioclase partitioning and diffusion data for trace elements other than Sr are required to put further constraints on crystal residence times and to use diffusion modeling to its full potential. In addition, initial trace element concentration profiles may be derived from melt inclusion studies, and this would greatly improve the estimates of crystal residence times.

CHAPTER 6

Synthesis and conclusions

6.1 Chapter outline

The aim of this thesis was to constrain the petrogenetic processes that lead to melt generation and subsequent differentiation at Santorini as a typical continental margin volcano, with emphasis on the associated rates of fluid transfer and timescales of melt generation, transfer, and storage. In this chapter, the results of this study are summarised, beginning with the seismicity within the subducting slab and its implications for slab fluid transfer through the mantle wedge. After a summary of the relative contributions of slab fluids, sediments and wedge peridotite to the primary magma, the differentiation processes within the crust are discussed. The second part of this synthesis focusses on the timescales of fluid and magma transfer and magma storage in an attempt to distinguish between different models of destructive plate margin petrogenesis. The implications of U-Th isotope studies for magma transfer times through the wedge and magma storage times within the crust are summarised, and the implications of Ra-Th disequilibria and Sr diffusion studies for the timescales of magmatic differentiation in the subvolcanic magma chamber are discussed. This synthesis concludes with some suggestions for further studies highlighted by this work.

6.2 Slab seismicity, fluid transfer processes, and mantle melting

Shallow seismicity at the Hellenic Trench predominantly occurs due to segmentation of the subducting slab in response to stresses imposed by the geometry of the plate margin. Intermediate depth seismicity is confined to the slab segment boundaries where the slab has presumably fractured and been structurally weakened. The coincidence of

intermediate depth seismicity and volcanic activity implies that processes within the slab control melt generation in the wedge. It is inferred that fluids from dehydration reactions within the slab are channelled towards the slab-wedge interface by faulting along the slab segment boundaries. Subsequently, focussed slab fluid release into hotter regions of the mantle wedge occurs via hydraulic fracturing. This results in increased melt generation in those parts of the mantle wedge that overlie the fracture zones, and determines the location of recent volcanic activity in the South Aegean. Thus, the distribution of volcanism in the Aegean Arc is not random, but rather controlled by tectonic processes within the subducting slab, which in turn depend on the curvature and the geometry of the plate boundary.

Uranium excesses in the Kameni lavas provide further evidence for a mechanism that allows rapid slab fluid transfer into hotter regions of the mantle, such as hydraulic fracturing. Gradual lateral migration of slab fluids by slab-parallel wedge flow and amphibole breakdown as envisaged by Davies and Stevenson (1992) is unable to generate the observed disequilibria as the time between slab fluid release and mantle melting is too long. Taking the Aegean subduction zone as an example, the volcanic arc is situated ~130 km above the Benioff zone. Using a slab dip angle of 38° (Papazachos et al., 1991) and a convergence rate of 50 mm a^{-1} (Taymaz et al., 1990), slab fluids need to migrate more than 40 km laterally into the mantle wedge if slab dehydration is taken to occur at 100 km depth (Liu et al., 1996). Using a lateral migration velocity of ~40 mm a^{-1} as calculated from the convergence rate and the slab dip angle above, this would require ~1 Ma, and initial U-Th disequilibria would have decayed. In contrast, the biggest hydraulic fractures may continue over tens of kilometres and may induce large amounts of melting directly and quickly (Davies and Rowland, 1997), so that the slab fluid transfer time into the melting region may be negligible.

However, MELTS modelling indicates that the primary basalts had low H_2O contents of less than ~0.7 wt%. This implies that the amount of water flux into the melting region beneath the Aegean arc is also too low to generate more than a few percent of mantle melting (cf. Davies and Bickle, 1991). In consequence, hydrous fluxing of the mantle wedge alone cannot account for the relatively large degrees of mantle melting (15-20%) indicated by trace element constraints (Section 6.3). Hence, unless other volatiles such as CO_2 are released from the slab and increase melt production, melting beneath Santorini may at least in part be due to decompression by mantle diapirism, although U series disequilibria indicate that magma transport through the wedge is relatively fast and probably occurs via channelled flow through the mantle wedge.

6.3 Magma source components and sediment transfer

The incompatible trace element budget of recent eruptive products from Santorini places constraints on the degree of mantle melting and the relative contributions of subducted sediments (carrying LREE and LILE) and slab fluids (carrying fluid mobile LILE) to the mantle wedge beneath the Aegean. HREE abundances in the least evolved samples are similar to N-MORB and can be modelled by 15-20% batch melting of a MORB source mantle wedge. Low Nd/Th ratios and relatively unradiogenic Nd isotopic compositions of even the less evolved samples indicate that low degree (less than 5%) partial sedimentary melts infiltrate the wedge. Very low degree partial melting of subducting sediments has also been suggested as a mechanism to produce high silica melt inclusions in mantle xenoliths from the Philippines (Schiano et al., 1995). As little as 0.2-0.4% sediment melt addition is required to account for the elevated LREE abundances in the least evolved samples. However, this contribution from subducting sediments is not sufficient to generate the observed enrichment of fluid mobile LILE, and slab fluids are inferred to contribute of the order of 35-85% of the LILE budget to the primary magma.

6.4 Upper crustal differentiation processes

MELTS major element modelling and trace element constraints indicate that simple isobaric (1.5 kbar) crystal fractionation from a basaltic parent can produce the basaltic andesites and andesites of the second eruptive cycle. However, magma mixing and assimilation processes become significant in the generation of more felsic members of the sample suite, and the range of Sr and Nd isotopes is produced at upper crustal levels, hence is not a source feature.

In addition, trace element evidence further suggests that the mafic enclaves within the Kameni dacites are not the mafic endmembers of a coeval suite of samples but are geochemically unrelated to their host. Due to constant La/Yb, Tb/Yb, Hf/Yb, Zr/Th and Y/Th ratios of the Kameni dacites, their range in U/Th ratios is unlikely to result from magma mixing and is interpreted to reflect differential slab fluid uranium addition to their source.

6.5 U-Th isotope constraints on fluid and magma transfer times

The time since U-Th differentiation, inferred to represent the age of slab fluid addition to the mantle wedge beneath Santorini, was shown to be >350 ka for the SEC and 147 (+27/-21) ka (1σ) for the Kameni dacites. Such timescales are long compared to those observed in the Mariana and Tonga-Kermadec intra-oceanic island arcs (25-50 ka). In addition, they are very different from the U-Th mineral isochron data from samples of the SEC and the Kameni dacites that yield ages of 85 (+22/-19) ka (1σ) and 18 (+19/-16) ka (1σ), respectively, indistinguishable from their eruption ages.

Comparison of total fluid and magma transfer times at volcanic arcs globally suggests that crustal thickness strongly influences transfer times, with longer and more variable timescales at volcanic arcs situated on thicker crust. The global dataset indicates that the

combined fluid and magma transfer times through the mantle wedge beneath island arcs may generally be about 30 ka, with any additional time representing magma storage within the crust. According to this model, magma storage time far exceeds wedge transfer time below Santorini, and U-Th mineral isochron data from the SEC and the Kameni dacites are not indicative of the timescale of crustal magma storage. Instead, they are taken to record the youngest period of a longer history of crystallisation. The occurrence of some very calcic plagioclases which have anorthite contents that are not in equilibrium with the groundmass provides evidence for separate periods of crystallisation during a prolonged history of crustal residence.

In addition, variable crustal magma storage times at Santorini are apparent between different eruptive cycles. Results from along-arc studies that use a limited number of samples from each volcano hence may not be very reliable unless they are backed up by more detailed work on a single volcanic site, at least in the continental margin environment.

6.6 Timescales of subvolcanic differentiation processes

In this study, two techniques have been employed to place constraints on the timescales of plagioclase crystallisation within the subvolcanic magma chamber. These are Ra-Th isotope studies, pointing to plagioclase fractionation less than ~1 ka prior to the eruption of the Kameni dacites, and Sr diffusion studies within single plagioclase crystals. The latter demonstrates that some of the Kameni plagioclase crystals have crystallised less than 100 years before eruption, in agreement with CSD studies (Higgins, 1996b). Similar results have been obtained for Soufriere, St. Vincent, in the Lesser Antilles island arc. In conclusion, while crustal magma storage times may be of the order of tens to hundreds of thousands of years, crystal residence times within the uppermost subvolcanic plumbing system may be comparatively short, with timescales of tens to hundreds of years.

6.7 Implications for further studies

Global teleseismic earthquake relocation has improved the precision of the global earthquake dataset significantly, and in this study it has been demonstrated that earthquake data may be useful in constraining fluid transfer and melt generation processes at subduction zones. This suggests that earthquake data should also be studied in detail at other subduction zones with complicated tectonic settings, such as the Aleutians and Sumatra, where fracture zone subduction is evident, or in Central America, where the concave geometry of the plate margin requires the slab to break up at depth and separate.

U-series isotope results at Santorini have indicated the necessity to study selected volcanoes from other arcs in more detail to verify transfer time estimates based on along arc studies. So far, the only example of a convincing along-arc whole rock isochron comes from the Mariana oceanic arc (Elliott et al., 1997). Most other along-arc studies employed reference lines through high ($^{238}U/^{230}Th$) samples anchored at low ($^{230}Th/^{232}Th$) activities on the equiline to yield the timescales of U-Th differentiation. Strictly, these at best are minimum slab fluid transfer times, and in addition such estimates will be very dependent on the number of samples analysed.

The Sr diffusion studies presented in this thesis provided some interesting initial results, indicating variable plagioclase crystal residence times in crustal magma reservoirs. However, more stringent criteria should be used in future when choosing samples for such studies. In the case of Santorini, the number of data points along each traverse was very limited by the relatively small size of even the largest crystals (~1 mm across), and by abundant inclusions that hindered a closer spacing of probe points. If this technique is to be developed further, larger phenocrysts with less complicated magmatic histories may be more suitable and may even allow constraining the timescales of crystal growth of

different parts of the crystal. In addition, better constraints on diffusivities of other trace elements such as Ba would significantly improve this approach.

More work is also required to establish the significance of U-Th mineral isochron data. Such data will have little significance if it is not clear which episode of crystallisation is being dated, or if the mineral separates are in fact a mixture of crystals formed during various episodes of crystallisation. In particular, the MSWD of errorchrons through mineral separate analyses may be indicative of the effects that late stage crystallisation events may have had on an older mineral assemblage (c. f. Heath et al., 1998).

Finally, many arc magmas show Ra excesses over Th, and these have commonly been attributed to Ra-Th differentiation during partial melting within the mantle wedge, followed by rapid magma ascent. However, Ra excesses observed on a sample from Soufriere, St. Vincent (Chabaux and Allègre, 1994), where U-Th mineral isochron data suggest long crustal residence times (Heath et al., 1998b), cannot be explained by Ra-Th fractionation processes within the mantle. Such inconsistencies cannot be resolved unless more Ra data on a well-characterised set of samples becomes available, as only then we will begin to better understand the petrogenetic processes that govern the Ra budget at destructive plate margins.

REFERENCES

Allègre C. J. and Condomines M. (1976) Fine chronology of volcanic processes using ^{238}U-^{230}Th systematics. *Earth and Planetary Science Letters* **28**, 395-406.

Allègre C. J. and Condomines M. (1982) Basalt genesis and mantle structure studied through Th-isotopic geochemistry. *Nature* **299**, 21-24.

Anderson R. N., Uyeda S., and Miyashiro A. (1976) Geophysical and geochemical constraints at converging plate boundaries, I: Dehydration in the down-going slab. *Geophysical Journal of the Royal Astronomical Society* **44**, 333-357.

Andrews D. J. and Sleep N. H. (1974) Numerical modeling of tectonic flow behind island arcs. *Journal of the Royal Astronomical Society* **38**, 237-251.

Andriessen P. A. M., Boelrijk N. A. I. M., Hebeda E. H., Priem H. N. A., Verdurmen E. A. T., and Verschure R. H. (1979) Dating the events of metamorphism and granitic magmatism in the Alpine orogen of Naxos (Cyclades, Greece). *Contributions to Mineralogy and Petrology* **69**, 215-232.

Armstrong R. L. (1971) Isotopic and chemical constraints on models of magma genesis in volcanic arcs. *Earth and Planetary Science Letters* **12**, 137-142.

Avigad D. and Garfunkel Z. (1991) Uplift and exhumation of high-pressure metamorphic terrains: The example of the Cycladic blueschist belt (Aegean Sea). *Tectonophysics* **188**, 357-372.

Ayers J. (1998) Trace element modelling of aqueous fluid - peridotite interaction in the mantle wedge of subduction zones. *Contributions to Mineralogy and Petrology* **132**, 390-404.

Bacon C. R. (1986) Magmatic inclusions in silicic and intermediate volcanic rocks. *Journal of Geophysical Research* **91**, 6091-6112.

Bacon C. R., Adami L. H., and Lanphere M. A. (1989) Direct evidence for the origin of low 18O silicic magmas: Quenched samples of a magma chamber's partially-fused granitoid walls, Crater Lake, Oregon. *Earth and Planetary Science Letters* **96**, 199-208.

Bailey E. H. and Ragnarsdottir K. V. (1994) Uranium and thorium solubilities in subduction zone fluids. *Earth and Planetary Science Letters* **124**, 119-129.

Banno S., Sakai C., and Higashino T. (1986) Pressure-temperature trajectory of the Sanbagawa metamorphism deduced from garnet zoning. *Lithos* **19**, 51-63.

Barreiro B. (1983) Lead isotopic compositions of South Sandwich Island volcanic rocks and their bearing on magmagenesis in intra-oceanic island arcs. *Geochimica et Cosmochimica Acta* **47**, 817-822.

Barton M. and Huijsmans J. P. P. (1986) Post-caldera dacites from the Santorini volcanic complex, Aegean Sea, Greece: an example of the eruption of lavas of near-constant composition over a 2,200 year period. *Contributions to Mineralogy and Petrology* **94**, 472-495.

Barton M., Salters V. J. M., and Huijsmans J. P. P. (1983) Sr isotope and trace element evidence for the role of continental crust in calc-alkaline volcanism on Santorini and Milos, Aegean Sea, Greece. *Earth and Planetary Science Letters* **63**, 273-291.

Beattie P., Drake M., Jones J., Leeman W., Longhi J., McKay G., Nielsen R., Palme H., Shaw D., Takahashi E., and Watson B. (1993) Terminology for trace-element partitioning. *Geochimica et Cosmochimica Acta* **57**, 1605-1606.

Ben Othman D., White W. M., and Patchett J. (1989) The geochemistry of marine sediments, island arc magma genesis and crust-mantle recycling. *Earth and Planetary Science Letters* **94**, 1-21.

Besenecker H. and Otte O. (1977) Late Cenozoic development of Kos, Aegean Sea. *Alps, Appennines, Hellenides. H. Cloos et al. (Eds.). Inter-Union Commission on Geodynamics, 38. Schweizerbart, Stuttgart.*, 506-509.

Biju-Duval B., Letouzey J., and Montadert L. (1978) Structure and evolution of the Mediterranean basins. *Initial Reports of the Deep Sea Drilling Project* **42**, 951-984.

Birck J. L. (1986) K, Rb, Sr isotope analysis: application to Rb-Sr chronology. *Chemical Geology* **56**, 73-83.

Bird A. B., Stewart W. E., and Lightfoot E. N. (1963) *Transport Phenomena.* Wiley.

Blundy J. D., Robinson J. A. C., and Wood B. J. (1998) Heavy REE are compatible in clinopyroxene on the spinel lherzolite solidus. *Earth and Planetary Science Letters* **160**(3-4), 493-504.

Blundy J. D. and Shimizu N. (1991) Trace element evidence for plagioclase recycling in calc-alkaline magmas. *Earth and Planetary Science Letters* **102**, 178-197.

Blundy J. D. and Wood B. J. (1991) Crystal-chemical controls on the partitioning of Sr and Ba between plagioclase feldspar, silicate melts, and hydrothermal solutions. *Geochimica et Cosmochimica Acta* **55**, 193-209.

Blundy J. and Wood B. (1994) Prediction of crystal-melt partition coefficients from elastic moduli. *Nature* **372**, 452-454.

Brenan J. M., Shaw H. F., Ryerson F. J., and Phinney D. L. (1995) Mineral-aqueous fluid partitioning of trace elements at 900°C and 2.0 GPa: constraints on the trace element chemistry of mantle and deep crustal fluids. *Geochimica et Cosmochimica Acta* **59**, 3331-3350.

Briqueu L., Javoy M., and Lancelot J. R. (1986) Isotope geochemistry of recent magmatism in the Aegean arc: Sr, Nd, Hf, and O isotopic ratios in the lavas of Milos and Santorini - geodynamic implications. *Earth and Planetary Science Letters* **80**, 41-54.

Brophy J. G. and Marsh B. D. (1986) On the origin of high-alumina arc basalt and the mechanics of melt extraction. *Journal of Petrology* **27**, 763-789.

Carr M. J. (1984) Symmetrical and segmented variation of physical and geochemical characteristics of the Central American volcanic front. *Journal of Volcanology and Geothermal Research* **20**, 231-252.

Cashman K. V. and Marsh B. D. (1988) Crystal size distribution (CSD) in rocks and the kinetics and dynamics of crystallisation. II: Makaopuhi lava lake. *Contributions to Mineralogy and Petrology* **99**, 292-305.

Chabaux F. and Allègre C. J. (1994) ^{238}U-^{230}Th-^{226}Ra disequilibria in volcanics: A new insight into melting conditions. *Earth and Planetary Science Letters* **126**, 61-74.

Chabaux F., Ben Othman D., and Birck J. L. (1994) A new Ra-Ba chromatographic separation and its application to Ra mass-spectrometric measurement in volcanic rocks. *Chemical Geology* **114**, 191-197.

Chen J. H., Edwards L. R., and Wasserburg G. J. (1986) ^{238}U, ^{234}U and ^{232}Th in seawater. *Earth and Planetary Science Letters* **80**, 241-251.

Cherniak D. J. and Watson E. B. (1994) A study of strontium diffusion in plagioclase using Rutherford backscattering spectroscopy. *Geochimica et Cosmochimica Acta* **58**(23), 5179-5190.

Christensen J. N. and DePaolo D. J. (1993) Time scales of large volume silicic magma systems: Sr isotopic systematics of phenocrysts and glass from the Bishop Tuff, Long Valley, California. *Contributions to Mineralogy and Petrology* **113**, 100-114.

Class C., Altherr R., Volker F., Eberz G., and McCulloch M. T. (1994) Geochemistry of Pliocene to Quaternery alkali basalts from the Huri Hills, northern Kenya. *Chemical Geology* **113**, 1-22.

Cohen A. S. and O'Nions R. K. (1991) Precise determination of femtogram quantities of radium by thermal ionisation mass spectrometry. *Analytical Chemistry* **61**, 2705-2706.

Condomines M. (1994) Comment on: The volume and residence time of magma beneath active volcanoes determined by decay series disequilibria methods. *Earth and Planetary Science Letters* **122**, 251-255.

Condomines M. (1997) Dating recent volcanic rocks through ^{230}Th-^{238}U disequilibrium in accessory minerals: Example of the Buy de Dome (French Massif Central). *Geology* **25**(4), 375-378.

Condomines M., Hemond C., and Allègre C. J. (1988) U-Th-Ra radioactive disequilibria and magmatic processes. *Earth and Planetary Science Letters* **90**, 243-262.

Conrey R. M. (1997) The Bowen-Fenner debate resolved: a review of basalt crystal fractionation and the generation of andesite. *in preparation.*

Cox K. G., Bell J. D., and Pankhurst R. J. (1979) *The interpretation of igneous rocks.* Chapman and Hall.

Davidson J. P. (1985) Mechanisms of contamination in Lesser Antilles island arc magmas from radiogenic and oxygen isotope relationships. *Earth and Planetary Science Letters* **72**, 163-174.

Davidson J. P. (1986) Isotopic and trace element constraints on the petrogenesis of subduction-related lavas from Martinique, Lesser Antilles. *Journal of Geophysical Research* **91**(B6), 5943-5962.

Davidson J. P. (1996) Deciphering Mantle and Crustal Signatures in Subduction Zone Magmatism. *Geophysical Monograph 96*, 251-262.

Davidson J. P. and Harmon R. S. (1989) Oxygen isotope constraints on the petrogenesis of volcanic arc magmas from Martinique, Lesser Antilles. *Earth and Planetary Science Letters* **95**, 255-270.

Davidson J. P. and Tepley F. J. (1997) Recharge in Volcanic Systems: Evidence from Isotope Profiles of Phenocrysts. *Science* **275**, 826-829.

Davies E. N. and Bastas C. (1978) Petrology and geochemistry of the metamorphic system of Santorini. *Thera and the Aegean World I*, 61-79.

Davies J. H. and Bickle M. J. (1991) A physical model for the volume and composition of melt produced by hydrous fluxing above subduction zones. *Philosophical Transactions of the Royal Society of London* **A335**, 355-364.

Davies G. R., Halliday A. N., Mahood G. A., and Hall C. M. (1994) Isotopic constraints on the production rates, crystallisation histories and residence times of pre-caldera silicic magmas, Long Valley, California. *Earth and Planetary Science Letters* **125**(1-4), 17-37.

Davies J. H. and Rowland A. (1997) Importance of temperature dependent viscosity and hydraulic fracture on physical models of subduction zone magmatism. *Geological Society of Australia Abstracts* **45**, 17-20.

Davies J. H. and Stevenson D. J. (1992) Physical model of the source region of subduction zone volcanics. *Journal of Geophysical Research* **97**, 2037-2070.

de Bremond d'Ars J., Jaupard C., and Sparks R. S. J. (1995) Distribution of volcanoes in active margins. *Journal of Geophysical Research* **100**(B10), 20421-20432.

Defant M. J. and Drummond M. S. (1990) Derivation of some modern arc magmas by melting of young subducted lithosphere. *Nature* **347**, 662-665.

Delany J. M. and Helgeson H. C. (1978) Calculation of thermodynamic consequences of dehydration in subducting oceanic crust to 100 kb and >800°C. *American Journal of Science* **278**, 636-686.

DePaolo D. (1981) Trace element and isotopic effects of combined wallrock assimilation and fractional crystallisation. *Earth and Planetary Science Letters* **53**, 189-202.

di Paola G. M. (1974) Volcanology and petrology of Nisyros island (Dodecanese, Greece). *Bulletin of Volcanology* **38**, 944-987.

Dickin A. P. (1997) *Radiogenic isotope geology*. Cambridge University Press.

Druitt T., et al. (1999) Santorini Memoir. *Journal of the Geological Society of London Special Publications*, in press.

Druitt T. and Davies M. (1999) Geological map of Santorini. in press.

Druitt T., Lanphere M., and Vougioukalakis G. (1996) Field workshop Santorini, 8.-15.9.1996, Guide and Excursions. *IAVCEI, Commission on Explosive Volcanism.*

Druitt T. H., Mellors R. A., Pyle D. M., and Sparks R. S. J. (1989) Explosive volcanism on Santorini, Greece. *Geological Magazine* **126**(2), 95-213.

Dun T. and Sen C. (1994) Mineral/matrix partition coefficients for orthopyroxene, plagioclase, and olivine in basaltic to andesitic systems: A combined analytical and experimental study. *Geochimica et Cosmochimica Acta* **58**(2), 717-733.

Edwards L. (1994) Magma cyclicity and isotopic variation on Santorini volcano, Aegean Sea, Greece. PhD thesis, University of Bristol.

Edwards R. L., Chen J. H., and Wasserburg G. J. (1986/87) ^{238}U-^{234}U-^{230}Th-^{232}Th systematics and the precise measurement of time over the past 500000 years. *Earth and Planetary Science Letters* **81**, 175-192.

Eiler M., McInnes B., Valley J. W., Graham C. M., and Stolper E. M. (1998) Oxygen isotope evidence for slab-derived fluids in the sub-arc mantle. *Nature* **393**, 777-781.

Elliott T., Plank T., Zindler A., White W., and Bourdon B. (1997) Element transport from slab to volcanic front at the Mariana arc. *Journal of Geophysical Research* **102**(B7), 14991-15019.

Engdahl E. R., van der Hilst R., and Buland R. (1998) Global teleseismic earthquake relocation with improved travel times and procedures for depth determination. *Bulletin of the Seismological Society of America* **88**, 722-743.

Ewart A., Brothers R. N., and Mateen A. (1977) An outline of the geology and geochemistry and the possible petrogenetic evolution of the volcanic rocks of the Tonga-Kermadec-New Zealand island arc. *Journal of Volcanology and Geothermal Research* **2**, 205-250.

Ewart A. and Hawkesworth C. J. (1987) The Pleistocene-Recent Tonga-Kermadec arc lavas: interpretation of new isotopic and rare earth data in terms of a depleted mantle source model. *Journal of Petrology* **28**, 495-530.

Fauzi, McCaffrey R., Wark D., Sunaryo, and Prih Haryadi P. Y. (1996) Lateral variation in slab orientation beneath Toba caldera, northern Sumatra. *Geophysical Research Letters* **23**, 443-446.

Francalanci L., Varekamp J. C., Vougioukalakis G., Defant M. J., Innocenti F., and Manetti P. (1995) Crystal retention, fractionation and crustal assimilation in a convecting magma chamber, Nisyros Volcano, Greece. *Bulletin of Volcanology* **56**, 601-620.

Fryer P. (1996) Evolution of the Mariana convergent plate margin system. *Reviews of Geophysics* **34**(1), 89-125.

Fukao Y., Hori S., and Ukawa M. (1983) A seismological constraint on the depth of basalt-eclogite transition in a subducting oceanic crust. *Nature* **303**, 413-415.

Fyticas M., Giuliani O., Innocenti F., Marinelli G., and Mazzuoli R. (1976) Geochronological data on Recent magmatism of the Aegean Sea. *Tectonophysics* **31**, T29-T34.

Fytikas M., Kolios N., and Vougioukalakis G. (1989) Post-Minoan volcanic activity of the Santorini volcano. Volcanic hazard and risk, forecasting possibilities. *Thera and the Aegean World III*, 183-198.

Geist E. L., Vallier T. L., and Scholl D. W. (1994) Large-scale deformation related to the collision of the Aleutian arc with Kamchatka. *Tectonics* **13**, 538-560.

Gerlach D. C. and Grove T. L. (1982) Petrology of Medicine Lake Highland volcanics: characterisation of endmembers of magma mixing. *Contributions to Mineralogy and Petrology* **80**, 147-159.

Ghiorso M. and Carmichael I. S. E. (1980) A regular solution model for met-aluminous silicate liquids: Applications to geothermometry, immiscibility and the source region of basic magmas. *Contributions to Mineralogy and Petrology* **71**, 323-342.

Ghiorso M. S. and Sack R. O. (1995) Chemical mass transfer in magmatic processes IV. A revised and internally consistent thermodynamic model for the interpolation and extrapolation of liquid-solid equilibria in magmatic systems at elevated temperatures and pressures. *Contributions to Mineralogy and Petrology* **119**, 197-212.

Giletti B. J. and Casserly J. E. D. (1994) Strontium diffusion kinetics in plagioclase feldspars. *Geochimica et Cosmochimica Acta* **58**(18), 3785-3793.

Gill J. B. (1981) *Orogenic andesites and plate tectonics.* Springer.

Gill J. B. and Williams R. W. (1990) Th isotope and U-series studies of subduction-related volcanic rocks. *Geochimica et Cosmochimica Acta* **54**, 1427-1442.

Gill J. B., Williams R. W., and Pyle D. M. (1991) Igneous Rocks. In *Short course handbook on applications of radiogenic isotope systems to problems in geology* (ed. L. Heaman and J. N. Ludden), pp. 287-335. Mineralogical Association of Canada.

Goldstein S. J., Murrel M. T., and Janecky D. R. (1989) Th and U isotopic systematics of basalts from the Juan de Fuca and Gorda Ridges by mass spectrometry. *Earth and Planetary Science Letters* **96**, 134-146.

Green D. H. (1973) Experimental melting studies on a model upper mantle composition at high pressure under water-saturated and water-undersaturated conditions. *Tectonophysics* **17**, 285-297.

Green H. W. and Houston H. (1995) The mechanics of deep earthquakes. *Annual Reviews of Earth and Planetary Sciences* **23**, 169-213.

Green T. H. and Ringwood A. E. (1968) Genesis of the calc-alkaline igneous rock suite. *Contributions to Mineralogy and Petrology* **18**, 105-162.

Greenough J. D. (1988) Minor phases in the Earth's mantle: evidence from trace- and minor-element patterns in primitive alkaline magmas. *Chemical Geology* **69**, 177-192.

Grove T. L. and Baker M. B. (1984) Phase equilibrium controls on the tholeiitic versus calc-alkaline differentiation trends. *Journal of Geophysical Research* **89**, 3253-3274.

Grove T. L., Baker M. B., and Kinzler R. J. (1984) Coupled CaAl-NaSi diffusion in plagioclase feldspar: experiments and applications to cooling rate speedometry. *Geochimica et Cosmochimica Acta* **48**, 2113-2121.

Halliday A. N. (1990) Reply to comment of R.S.J. Sparks, H.E. Huppert and C.J.N. Wilson on Evidence for long residence times of rhyolitic magma in the Long Valley magmatic system: the isotope record in precaldera lavas of Glass Mountain. *Earth and Planetary Science Letters* **99**, 390-394.

Halliday A. N., Lee D. C., Tommasini S., Davies G. R., Paslick C. R., Fitton J. G., and James D. E. (1995) Incompatible trace elements in OIB and MORB and source enrichment in the sub-oceanic mantle. *Earth and Planetary Science Letters* **133**, 379-395.

Halliday A. N., Mahood G. A., Holden P., Metz J. M., Dempster T. J., and Davidson J. P. (1989) Evidence for long residence times of rhyolitic magma in the Long Valley magmatic system: the isotope record in precaldera lavas of Glass Mountain. *Earth and Planetary Science Letters* **94**, 274-290.

Hardiman J. (1996) Quarternary volcanism on Nisyros, Greece. PhD thesis, Cambridge University.

Harmon R. S., Barreiro B. A., Moorbath S., Hoefs J., Francis P. W., Thorpe R. S., Duruelle B., McHugh J., and Viglino J. A. (1984) Regional O-, Sr-, and Pb-isotope relationships in the late Cenozoic calc-alkaline lavas of the Andean Cordillera. *Journal of the Geological Society of London* **141**, 803-822.

Hashida T., Stavrakakis G., and Shimazaki K. (1987) Three-dimensional seismic attenuation structure beneath the Aegean region and its tectonic implication. *Tectonophysics* **145**, 43-54.

Hatzfeld D. (1994) On the shape of the subducting slab beneath the Peloponnese, Greece. *Geophysical Research Letters* **21**, 173-176.

Hatzfeld D., Besnard M., Makropoulos K., Voulgaris N., Kouskouna V., Hatzidimitriou P., Panagiotopoulos D., Karakaisis G., Deschamps A., and Lyon-Caen H. (1993) Subcrustal microearthquake seismicity and fault plane solutions beneath the Hellenic Arc. *Journal of Geophysical Research* **98**(B6), 9861-9870.

Hatzfeld D. and Martin C. (1992) Intermediate depth seismicity in the Aegean defined by teleseismic data. *Earth and Planetary Science Letters* **113**, 267-275.

Hawkesworth C. J. (1982) Isotope characteristics of magmas erupted along destructive plate margins. In *Andesites: orogenic andesites and related rocks* (ed. R. S. Thorpe), pp. 549-571. Wiley.

Hawkesworth C. J., Gallagher K., Hergt J. M., and McDermott F. (1993) Mantle and slab contributions in arc magmas. *Annu. Rev. Earth Planet. Sci.* **21**, 175-204.

Hawkesworth C. J., Turner S. P., McDermott F., Peate D. W., and van Calsteren P. (1997b) U-Th isotopes in arc magmas: implications for element transfer from the subducted crust. *Science* **276**, 551-555.

Hawkesworth C., Turner S., Peate D., McDermott F., and van Calsteren P. (1997a) Elemental U and Th variations in island arc rocks: implications for U-series isotopes. *Chemical Geology* **139**, 207-221.

Heath E., Macdonald R., Belkin H., Hawkesworth C., and Sigurdsson H. (1998a) Magmagenesis at Soufriere Volcano, St. Vincent, Lesser Antilles Arc. *Journal of Petrology* **39**(10), 1721-1764.

Heath E., Turner S., Macdonald R., Hawkesworth C. J., and van Calsteren P. (1998b) Long magma residence times at an island arc volcano (Soufriere, St. Vincent) in the Lesser Antilles: evidence from ^{238}U-^{230}Th isochron dating. *Earth and Planetary Science Letters* **160**, 49-63.

Helmberger D. V. (1977) Fine structure of an Aleutian crustal section. *Geophysical Journal of the Royal Astronomical Society* **48**, 81-90.

Higgins M. D. (1996a) Crystal size distributions and other quantitative textural measurements in lavas and tuff from Egmont volcano (Mt. Taranaki), New Zealand. *Bulletin of Volcanology* **58**, 194-204.

Higgins M. D. (1996b) Magma dynamics beneath Kameni volcano, Thera, Greece, as revealed by crystal size and shape measurements. *Journal of Volcanology and Geothermal Research* **70**, 37-48.

Hofmann H. J., Beer J., Bonani G., von Gunten H. R., Raman S., Suter M., Walker R. L., Wolfli W., and Zimmermann D. (1987) 10Be half-life and AMS-standards. *Nuclear Instrumental Methods in Physical Research* **B29**, 32-36.

Hsü K. J. and Bernoulli D. (1978) Genesis of the Tethys and the Mediterranean. *Initial Reports of the Deep Sea Drilling Project, Washington (U. S. Government Printing Office)* **42**(1), 943-949.

Huijsmans J. P. P. (1985) Calc-alkaline lavas from the volcanic complex of Santorini, Aegean Sea, Greece. A petrological, geochemical and stratigraphic study. PhD, Rijksuniversiteit te Utrecht.

Huijsmans J. P. P., Barton M., and Salters V. J. M. (1988) Geochemistry and evolution of the calc-alkaline volcanic complex of Santorini, Aegean Sea, Greece. *Journal of Volcanology and Geothermal Research* **34**, 283-306.

Humler E. and Whitechurch H. (1988) Petrology of basalts from the Central Indian Ridge (lat. 25°23'S, long. 70°04'E): estimates of frequencies and fractional volumes of magma injections in a two-layered reservoir. *Earth and Planetary Science Letters* **88**, 169-181.

Innocenti F., Manetti P., Peccerillo A., and Poli G. (1981) South Aegean Volcanic Arc: Geochemical Variations and Geotectonic Implications. *Bulletin of Volcanology* **44**(3), 377-391.

Irvine T. N. and Baragar W. R. A. (1971) A guide to the chemical classification of common rocks. *Canadian Journal of Earth Sciences* **8**, 523-548.

Jenner G. A., Foley S. F., Jackson S. E., Green T. H., Fryer B. J., and Longerich H. P. (1993) Determination of partition-coefficients for trace elements in high pressure temperature experimental run products by laser-ablation microprobe inductively-coupled plasma-mass spectrometry (LAM-ICP-MS). *Geochimica et Cosmochimica Acta* **57**(23-24), 5099-5103.

Jongsma D. (1977) Bathymetry and shallow structure of the Pliny and Strabo trenches south of the Hellenic Arc. *Geological Society of America Bulletin* **88**, 797-805.

Kastens K. (1991) Rate of outward growth of the Mediterranean Ridge accretionary complex. *Tectonophysics* **199**, 25-50.

Kay R. W. (1978) Aleutian magnesian andesites: melts from subducted pacific ocean crust. *Journal of Volcanology and Geothermal Research* **4**, 117-132.

Kay S. M., Kay R. W., and Citron G. P. (1982) Tectonic controls on tholeiitic and calc-alkaline magmatism in the Aleutian arc. *Journal of Geophysical Research* **87**(4051-4072).

Keller J. (1982) Mediterranean Island Arcs. In *Andesites: Orogenic andesites and related rocks* (ed. R. S. Thorpe), pp. 307-325. Wiley.

Keller J., Rehren T., and Stadlbauer E. (1989) Explosive Volcanism in the Hellenic Arc: a Summary and Review. *Thera and the Aegean World III*, 13-26.

Kincaid C. and Sacks I. S. (1997) Thermal and dynamical evolution of the upper mantle in subduction zones. *Journal of Geophysical Research* **102**(B6), 12295-12315.

Kissel C. and Lay C. (1987) The Tertiary geodynamical evolution of the Aegean arc: a palaeomagnetic reconstruction. *Tectonophysics* **146**, 183-201.

Kitahara S., Takenouchi S., and Kennedy G. C. (1966) Phase relations in the szstem MgO-SiO2-H2O at high temperatures and pressures. *American Journal of Science* **264**, 223-233.

Kornprobst J., Kienast J.-R., and Vilminot J.-C. (1979) The high-pressure assemblages at Milos, Greece. *Contributions to Mineralogy and Petrology* **69**, 49-63.

Kuno H. (1968) Differentiation of basalt magmas. In *Basalts: the Poldervaart treatise on rocks of basaltic composition*, Vol. 2 (ed. H. H. Hess and A. Poldervaart), pp. 623-688. Interscience.

Langseth M. G. and Moore J. C. (1990) Introduction to special section on the role of fluids in sediment accretion, deformation, diagenesis, and metamorphism in subduction zones. *Journal of Geophysical Research* **95**, 8737-8741.

LaTourrette T., Hervig R. L., and Holloway J. R. (1995) Trace element partitioning between amphibole, phlogopite, and basanite melt. *Earth and Planetary Science Letters* **135**, 13-30.

LaTourette T. and Wasserburg J. (1998) Mg diffusion in anorthite: implications for the formation of early solar system planetesimals. *Earth and Planetary Science Letters* **158**, 91-108.

Le Fort P., Cuney M., Deniel C., France-Lanord C., Sheppard S. M. F., Upreti B. N., and Vidal P. (1987) Crustal generation of the Himalayan leucogranites. *Tectonophysics* **134**, 39-57.

Le Pichon X. and Angelier J. (1979) The Hellenic arc and trench system: a key to the neotectonic evolution of the eastern Mediterranean area. *Tectonophysics* **60**, 1-42.

Le Pichon X., Angelier J., Aubouin J., Lyberis N., Monti S., Renard V., Got H., Hsü K., Mart Y., Mascle J., Matthews D., Mitropoulos D., Tsoflias P., and Chronis G. (1979) From subduction to transform motion: a seabeam survey of the Hellenic trench system. *Earth and Planetary Science Letters* **44**, 441-450.

Leeman W. P., Carr M. J., and Morris J. D. (1994) Boron geochemistry of the Central American volcanic arc: constraints on the genesis of subduction-related magmas. *Geochimica et Cosmochimica Acta* **58**, 149-168.

Lister G. S., Banga G., and Feestra A. (1984) Metamorphic core complexes of Cordilleran type in the Cyclades, Aegean Sea, Greece. *Geology* **12**, 221-225.

Livermore R. A. and Smith A. G. (1985) Some boundary conditions for the evolution of the Mediterranean region. In *Geological evolution of the Mediterranean region* (ed. D. J. Stanley and F.-C. Wenzel), pp. 83-98. Springer.

Loughnan F. C. (1969) *Chemical weathering of the silicate minerals.* American Elsevier.

Mahood G. and Hildreth W. (1983) Large partition coefficients for trace elements in high-silica rhyolites. *Geochimica et Cosmochimica Acta* **47**, 11-30.

Mahood G. A. (1990) Second reply to comment of R.S.J. Sparks, H.E. Huppert and C.J.N. Wilson on Evidence for long residence times of rhyolitic magma in the Long Valley magmatic system: the isotope record in precaldera lavas of Glass Mountain. *Earth and Planetary Science Letters* **99**, 395-399.

Makris J. (1977) Geophysical Investigations of the Hellenides. *Hamburger Geophysikalische Einzelschriften* **33**, 126 pp.

Makris J. (1978) The crust and upper mantle of the Aegean region from deep seismic soundings. *Tectonophysics* **46**, 269-284.

Mann A. C. (1983) Trace Element Geochemistry of High Alumina Basalt - Andesite - Dacite - Rhyodacite Lavas of the Main Volcanic Series of Santorini Volcano, Greece. *Contributions to Mineralogy and Petrology* **84**, 43-57.

Marsh B. D. (1979) Island arc development: some observations, experiments and speculations. *Journal of Geology* **87**, 687-713.

Marsh B. D. (1988) Crystal size distribution (CSD) in rocks and the kinetics and dynamics of crystallisation. I: Theory. *Contributions to Mineralogy and Petrology* **99**, 277-291.

Marsh B. D. (1989) Magma chambers. *Annual Reviews of Earth and Planetary Science* **17**, 439-474.

McDermott F. and Hawkesworth C. J. (1991) Th, Pb, and Sr isotope variations in young island arc vlcanics and oceanic sediments. *Earth and Planetary Science Letters* **104**(1), 1-15.

McKenzie D. P. (1969) Speculations on the consequences and causes of plate motions. *Geophysical Journal of the Royal Astronomical Society* **18**, 1-32.

McKenzie D. P. and O'Nions R. K. (1991) Partial melt distributions from inversion of rare earth element concentrations. *Journal of Petrology* **32**, 1021-1091.

Mercier J. L., Sorel D., Vergely P., and Simeakis K. (1989) Extensional tectonic regimes in the Aegean basins during the Cenozoic. *Basin Research* **2**, 49-71.

Meulenkamp J. E. (1985) Aspects of the Late Cenozoic evolution of the Aegean region. *Geological Evolution of the Mediterranean Basin, D. J. Stanley and F.-C. Wezel (Eds.), Springer, New York*, 307-321.

Meulenkamp J. E., Wortel M. J. R., van Wamel W. A., Spakman W., and Hoogerduyn Strating E. (1988) On the Hellenic subduction zone and the geodynamic evolution of Crete since the late Middle Miocene. *Tectonophysics* **146**, 203-215.

Mitropoulos P., Tarney J., Saunders A. D., and Marsh N. G. (1987) Petrogenesis of Cenozoic volcanic rocks from the Aegean island arc. *Journal of Volcanology and Geothermal Research* **32**, 177-193.

Miyashiro A. (1974) Volcanic rock series in island arcs and active continental margins. *American Journal of Science* **274**, 321-355.

Molnar P. and England P. (1995) Temperatures in zones of steady state underthrusting of young oceanic lithosphere. *Earth and Planetary Science Letters* **131**, 57-70.

Monaghan M. C., Klein J., and Measures C. I. (1988) The Origin of 10Be in island-arc volcanic rocks. *Earth and Planetary Science Letters* **89**, 288-298.

Moore J. C. and Vrolijk P. (1992) Fluids in accretionary prisms. *Reviews of Geophysics* **30**, 113-135.

Morris J. D., Leeman W. P., and Tera F. (1990) The subducted component in island-arc lavas - constraints from Be isotopes and B-Be systematics. *Nature* **344**(6261), 31-36.

Morse S. A. (1984) Cation diffusion in plagioclase feldspar. *Science* **225**, 504-505.

Nakada S., Bacon C. R., and Gartner A. E. (1994) Origin of phenocrysts and compositional diversity in pre-Mazama rhyodacite lavas, Crater Lake, Oregon. *Journal of Petrology* **35**(1), 127-162.

Nakamura M. (1995) Continuous mixing of crystal mush and replenished magma in the ongoing Unzen eruption. *Geology* **23**(9), 807-810.

Nash W. P. and Crecroft H. R. (1985) Partition coefficients for trace elements in silicic magmas. *Geochimica et Cosmochimica Acta* **49**, 2309-2322.

Nicholls I. A. (1971) Petrology of Santorini Volcano, Cyclades, Greece. *Journal of Petrology* **12**(1), 67-119.

Nicholls I. A. and Ringwood A. E. (1973) Effect of water on olivine stability in tholeiites and the production of silica-saturated magmas in the island-arc environment. *Journal of Geology* **81**, 285-300.

Nichols G. T., Wyllie P. J., and Stern C. R. (1994) Subduction zone melting of pelagic sediments constrained by melting experiments. *Nature* **371**, 785-788.

Ninkovich D. and Hays J. D. (1972) Mediterranean island arcs and origin of the high potash volcanoes. *Earth and Planetary Science Letters* **16**(3), 331-345.

Osborn E. F. (1959) Role of oxygen pressure in the crystallization and differentiation of basaltic magma. *American Journal of Science* **257**, 609-647.

Page B. G. N., Bennet J. D., Cameron N. R., Bridge D. M., Jeffery D. II., Keats W., and Thaib J. (1979) A review of the main structural and magmatic features of northern Sumatra. *Journal of the Geological Society of London* **136**, 569-579.

Panjasawatwong Y., Danyushevsky L. V., Crawford A., and Harris K. L. (1995) An experimental study of the effects of melt composition on plagioclase - melt equilibria at 5 and 10 kbar: implications for the origin of magmatic high-An plagioclase. *Contributions to Mineralogy and Petrology* **118**, 420-432.

Papazachos B. C. and Hoogerduyn-Strating E. (1973) Distribution of seismic foci in the Mediterranean and surrounding area and its tectonic implication. *Geophysical Journal of the Royal Astronomical Society* **33**, 421-430.

Papazachos B. C., Kiratzi A., and Papadimitriou E. (1991) Regional focal mechanisms for earthquakes in the Aegean area. *Pure and Applied Geophysics* **136**(4), 405-420.

Papazachos B. C. and Panagiotopoulos D. G. (1993) Normal faults associated with volcanic activity and deep rupture zones in the southern Aegean volcanic arc. *Tectonophysics* **220**, 301-308.

Patiño Douce A. E. and Harris N. (1998) Experimental constraints on Himalayan anatexis. *Journal of Petrology* **39**(4), 689-710.

Pe G. G. (1973) Petrology and Geochemistry of Volcanic Rocks of Aegina, Greece. *Bulletin of Volcanology* **37**, 491-514.

Pe G. G. (1975) Strontium isotope ratios in volcanic rocks from the northwestern part of the Hellenic Arc. *Chemical Geology* **15**, 53-60.

Peacock S. M. (1993) Large-scale hydration of the lithosphere above subduction slabs. *Chemical Geology* **1993**, 49-49.

Peacock S. M., Rushmer T., and Thompson A. B. (1994) Partial melting of subducting oceanic crust. *Earth and Planetary Science Letters* **121**, 227-244.

Pearce J. A. (1982) Trace element characteristics of lavas from destructive plate boundaries. In *Andesites: orogenic andesites and related rocks* (ed. R. S. Thorpe), pp. 230-249. Wiley.

Pearce J. A. and Parkinson I. J. (1993) Trace element models for mantle melting: application to volcanic arc petrogenesis. In *Magmatic Processes and Plate Tectonics*, Vol. 76 (ed. H. M. Prichard, T. Alabaster, N. B. W. Harris, and C. R. Neary), pp. 373-403. Geological Society Special Publication.

Pe-Piper G., Kotopouli C. N., and Piper D. J. W. (1997) Granitoid rocks of Naxos, Greece: regional geology and petrology. *Geological Journal* **32**(2), 153-171.

Plank T. and Langmuir C. H. (1988) An evaluation of the global variations in the major element chemistry of arc basalts. *Earth and Planetary Science Letters* **90**, 349-370.

Plank T. and Langmuir C. H. (1993) Tracing trace elements from sediment input to volcanic output at subduction zones. *Nature* **362**, 739-743.

Plank T. and Langmuir C. H. (1998) The geochemical composition of subducting sediments and its consequence for the crust and mantle. *Chemical Geology* **145**(3-4), 325-394.

Potts P. J., Thorpe O. W., Isaacs M. C., and Wright D. W. (1985) High precision neutron activation analysis of geological samples employing simultaneous counting with both planar and coaxial detectors. *Chemical Geology* **48**, 145-155.

Pouchou J. L. and Pichoir F. (1985) "PAP" procedure for improved quantitative analysis. *Microbeam Analysis* **20**, 104-105.

Pyle D. M. (1992) The volume and residence time of magma beneath active volcanoes determined by decay-series disequilibria methods. *Earth and Planetary Science Letters* **112**, 61-73.

Pyle D. M. (1994) Reply to comment by M. Condomines on The volume and residence time of magma beneath active volcanoes determined by decay-series disequilibria methods. *Earth and Planetary Science Letters* **122**, 257-258.

Pyle D. M., Ivanovich M., and Sparks R. S. J. (1988) Magma cumulate mixing identified by U-Th disequilibrium dating. *Nature* **331**, 157-159.

Ramsey M. H., Potts P. J., Webb P. C., Watson J. S., and Coles B. J. (1995) An objective assessment of analytical method precision: comparison of ICP-AES and XRF for the analysis of silicate rocks. *Chemical Geology* **124**, 1-19.

Reagan M. K., Morris J. D., Herrstrom E. A., and Murrell M. T. (1994) Uranium series and beryllium isotope evidence for an extended history of subduction modification of the mantle below Nicaragua. *Geochimica et Cosmochimica Acta* **58**(19), 4199-4212.

Regelous M., Collerson K. D., Ewart A., and Wendt J. I. (1997) Trace element transport rates in subduction zones: evidence from Th, Sr and Pb isotope data for Tonga-Kermadec arc lavas. *Earth and Planetary Science Letters* **150**, 291-302.

Robbins J. W., Dunn P. J., Torrence M. H., and Smith D. E. (1995) Deformation in the eastern Mediterranean. *First Turkish International Symposium on Deformations*, 738-745.

Robertson A. H. F. and Grasso M. (1995) Overview of the late Tertiary to Recent tectonic and palaeo-environmental development of the Mediterranean region. *Terra Nova* **7**, 114-127.

Roeder P. L. and Emslie R. F. (1970) Olivine-liquid equilibrium. *Contributions to Mineralogy and Petrology* **29**, 275-289.

Rogan W. (1996) New insights on magmatic processes from trace element zonation in phenocrysts. PhD thesis, The Open University.

Ryan J. G., Morris J., Tera F., Leeman W. P., and Tsvetkov A. (1995) Cross-arc geochemical variations in the Kurile arc as a function of slab depth. *Science* **270**, 625-627.

Sakuyama M. (1983) Petrology of arc volcanic rocks and their origin by mantle diapirs. *Journal of Volcanology and Geothermal Research* **18**, 297-320.

Schiano P., Clochiatti R., Shimizu N., Mauri R. C., Jochum K. P., and Hofmann A. W. (1995) Hydrous, silica-rich melts in the subarc mantle and their relationship with erupted lavas. *Nature* **377**, 595-600.

Shock E. L., Sassani D. C., and Betz H. (1997) Uranium in geologic fluids: estimates of standard partial molal properties, oxidation potentials, and hydrolysis constants at high temperatures and pressures. *Geochimica et Cosmochimica Acta* **61**(20), 4245-4266.

Sigmarsson O., Condomines M., Morris J. D., and Harmon R. S. (1990) Uranium and 10Be enrichments by fluids in Andean arc magmas. *Nature* **346**, 163-165.

Sigmarsson O., Martin H., and Knowles J. (1998) Melting of a subducting oceanic crust from U-Th disequilibria in austral Andean lavas. *Nature* **394**, 566-569.

Singer B. S., Dungan M. A., and Layne G. D. (1995) Textures and Sr, Ba, Mg, Fe, K, and Ti compositional profiles in volcanic plagioclase: Clues to the dynamics of calc-alkaline magma chambers. *American Mineralogist* **80**, 776-798.

Singer B. S., Leeman W. P., Thirlwall M. F., and Rogers N. W. (1996) Does fracture zone subduction increase sediment flux and mantle melting in subduction zones? Trace element evidence from Aleutian arc basalt. *Geophysical Monograph 96*, 285-291.

Sisson T. W. and Bronto S. (1998) Evidence for pressure-release melting beneath magmatic arcs from basalt at Galunggung, Indonesia. *Nature* **391**, 883-886.

Sisson T. W. and Grove T. L. (1993) Experimental investigations of the role of H2O in calc-alkaline differentiation and subduction zone magmatism. *Contributions to Mineralogy and Petrology* **113**, 143-166.

Smith I. E. M., Worthington T. J., Price R. C., and Gamble J. A. (1997) Primitive magmas in arc-type volcanic associations: examples from the southwest Pacific. *The Canadian Mineralogist* **35**, 257-273.

Spakman W., Wortel M. J. R., and Vlaar N. J. (1988) The Hellenic subduction zone: a tomographic image and its geodynamic implications. *Geophysical Research Letters* **15**(1), 60-63.

Stamatelopoulou-Seymour K., Vlassopoulos D., Pearce T. H., and Rice C. (1990) The record of magma chamber processes in plagioclase phenocrysts at Thera Volcano, Aegean Volcanic Arc, Greece. *Contributions to Mineralogy and Petrology* **104**, 73-84.

Stern C. R. and Kilian R. (1996) Role of the subducted slab, mantle wedge and continental crust in the generation of adakites from the Andean Austral Volcanic Zone. *Contributions to Mineralogy and Petrology* **123**, 263-281.

Stolper E. and Newman S. (1994) The role of water in the petrogenesis of Mariana trough magmas. *Earth and Planetary Science Letters* **121**, 293-325.

Strelow F. W. E. (1960) An ion exchange selectivity scale of cations based on equilibrium distribution coefficients. *Analytical Chemistry* **32**(9), 1185-1188.

Strelow F. W. E., Rethemeyer R., and Bothma C. J. C. (1965) Ion exchange selectivity scales for cations in nitric acid and sulphuric acid media with a sulfonated polystyrene resin. *Analytical Chemistry* **37**(1), 106-111.

Sutton A. (1995) Evolution of a large silicic magma system: Taupo volcanic centre, New Zealand. PhD thesis, The Open University.

Takahashi E. (1990) Speculations on the Archean mantle: Missing link between komatiite and depleted garnet peridotite. *Journal of Geophysical Research* **95**, 15941-15954.

Tatsumi Y. (1986) Formation of the volcanic front in subduction zones. *Geophysical Research Letters* **13**, 717-720.

Tatsumi Y. (1989) Migration of fluid phases and genesis of basalt magmas in subduction zones. *Journal of Geophysical Research* **94**, 4697-4707.

Taylor S. R. and McLennan S. M. (1995) The geochemical evolution of the continental crust. *Reviews of Geophysics* **33**(2), 241-265.

Taymaz T., Jackson J., and McKenzie D. (1991) Active tectonics of the north and central Aegean Sea. *Geophysical Journal International* **106**, 433-490.

Taymaz T., Jackson J., and Westaway R. (1990) Earthquake mechanisms in the Hellenic Trench near Crete. *Geophysical Journal International* **102**, 695-731.

Tepley F. J., Davidson J. P., and Clynne M. A. (1998) Magmatic interactions as recorded in plagioclase phenocrysts of Chaos Crags, Lassen Volcanic Center, California. *Journal of Petrology*, in press.

Tera F., Brown L., Morris J., and Sacks I. S. (1986) Sediment incorporation in island-arc magmas: inferences from 10Be. *Geochimica et Cosmochimica Acta* **50**, 535-550.

Thomas L. E. (1998) Uranium series, major and trace element geochemistry of lavas from Tenerife and Lanzarote, Canary Islands. PhD thesis, The Open University.

Thomas L., Hawkesworth C. J., van Calsteren P., and Ablay G. (1998) Rates and timescales of melt generation and differentiation in the Teide-Pico Viejo Complex, Tenerife, inferred from U-series isotopes. *Mineralogical Magazine* **62A**(3), 1513-1514.

Toksoz M. N. and Hsui A. T. (1978) Numerical studies of back-arc convection and the formation of marginal basins. *Tectonophysics* **50**, 177-196.

Turner S. P. and Hawkesworth C. J. (1997) Constraints on flux rates and mantle dynamics beneath island arcs from Tonga-Kermadec lava geochemistry. *Nature* **389**, 568-573.

Turner S. P. and Hawkesworth C. J. (1998) Using geochemistry to map mantle flow beneath the Lau Basin. *Geology* **26**(11), 1019-1022.

Turner S., Hawkesworth C., Rogers N., Bartlett J., Worthington T., Hergt J., Pearce J., and Smith I. (1997a) ^{238}U-^{230}Th disequilibria, magma petrogenesis, and flux rates beneath the depleted Tonga-Kermadec island arc. *Geochimica et Cosmochimica Acta* **61**(22), 4855-4884.

Turner S., Hawkesworth C., Rogers N., and King P. (1997b) U-Th isotope disequilibria and ocean island basalt generation in the Azores. *Chemical Geology* **139**, 145-164.

Turner S., Hawkesworth C., van Calsteren P., Heath E., Macdonald R., and Black S. (1996) U-series isotopes and destructive plate margin magma genesis in the Lesser Antilles. *Earth and Planetary Science Letters* **142**(1-2), 191-207.

Turner S. P., McDermott F., Hawkesworth C. J., and Kepezhinskas P. (1998) A U-series study of lavas from Kamchatka and the Aleutians: constraints on source composition and melting processes. *Contribution to Mineralogy and Petrology*, in press.

van Calsteren P. and Schwieters J. B. (1995) Performance of a thermal ionisation mass spectrometer with a deceleration lens system and post-deceleration detector selection. *International Journal of Mass Spectrometry and Ion Processes* **146/147**, 119-129.

van der Hilst R. D. (1998) Seismological constraints on the fate of slabs and the scale of mantle convection. *Mineralogical Magazine* **62A**(3), 1571-1572.

Volpe A. M. and Hammond P. E. (1991) ^{238}U-^{230}Th-^{226}Ra disequilibria in young Mount St. Helens rocks: time constraint for magma formation and crystallisation. *Earth and Planetary Science Letters* **107**, 475-486.

Volpe A. M., Olivares J. A., and Murrel M. T. (1991) Determination of radium isotope ratios and abundances in geologic samples by thermal ionization mass spectrometry. *Analytical Chemistry* **63**, 913-916.

Watson J. (1996) Fast, simple method of powder pellet preparation for x-ray fluorescence analysis. *X-ray Spectrometry* **25**, 173-174.

White W. M. and Dupre B. (1986) Sediment subduction and magma genesis in the Lesser Antilles - isotopic and trace-element constraints. *Journal of Geophysical Research* **91**(B6), 5927-5941.

Woodhead J. D. (1989) Geochemistry of the Mariana arc (western Pacific): source composition and processes. *Chemical Geology* **76**, 1-24.

Wortel R. (1982) Seismicity and rheology of subducted slabs. *Nature* **296**, 553-556.

Wyllie P. J. (1979) Magmas and volatile components. *American Mineralogist* **64**, 469-500.

Wyllie P. J. (1984) Constraints imposed by experimental petrology on possible and impossible magma sources and products. *Philosophical Transactions of the Royal Society of London* **A310**, 439-456.

Yogodzinski G. M., Kay R. W., Volynets O. N., Koloskov A. V., and Kay S. M. (1995) Magnesian andesite in the western Aleutian Komandorsky region: Implications for slab melting and processes in the mantle wedge. *Geological Society of America Bulletin* **107**(5), 505-519.

You C.-F., Castillo P. R., Gieskes J. M., Chan L. H., and Spivack A. J. (1996) Trace element behaviour in hydrothermal experiments: Implications for fluid processes at shallow depths in subduction zones. *Earth and Planetary Science Letters* **140**(1-4), 41-52.

You C.-F., Morris J. D., Gieskes J. M., Rosenbauer R., Zheng S. H., Xu X., Ku T. L., and Bischoff J. L. (1994) Mobilization of berillium in the sedimentary column at convergent margins. *Geochimica et Cosmochimica Acta* **58**(22), 4887-4897.

Zellmer G. F., Blake S., Vance D., Hawkesworth C., and Turner S. (1998a) Short plagioclase residence times at two island arc volcanoes (Kameni islands, Santorini, and Soufriere, St. Vincent) determined by Sr diffusion systematics. *Contributions to Mineralogy and Petrology*, in press.

Zellmer G. F., Hawkesworth C. J., and Turner S. P. (1998b) U-Th-Ra isotope evidence for rates of fluid transport and magmatic processes beneath Santorini, Aegean Volcanic Arc, Greece. *Mineralogical Magazine* **62A**(3), 1685-1686.

APPENDIX A

Analytical Techniques

A1 Preliminary sample preparation

A1.1 Crushing and milling

After removal of weathered surfaces using an electrical diamond grinder, rock samples were split by hand into pieces ~5 cm across and subsequently jaw-crushed to fragments <5 mm in size. For mineral separation, the crushate was put through the jaw crusher again to obtain a finer crushate and to ensure efficient breakup of crystals. For whole rock analysis, the crushate was ground to a grain size of <60 μm using an agate ball mill.

A1.2 Mineral Separation

The crushate was then sieved through a set of metal sieves to separate size fractions. The size fraction used for separation was chosen according to the size of phenocrysts in the sample. Usually, fragments between 64 μm and 125 μm were most useful for separation, as the number of compound grains increased rapidly for grains greater than 125 μm, while grains smaller than 64μm were difficult to separate efficiently.

Initially, the heavy liquid sodiumpolytungstate with a density of ~2.8×10^3 kg m^{-3} was used to separate the heavy fraction (magnetite and pyroxene) from the light fraction (plagioclase and groundmass) in a separating funnel.

Subsequently, the light fraction was passed through a Frantz magnetic separator to separate plagioclase from groundmass. For the heavy fraction, a hand magnet was used to extract magnetite. The residual was passed through the magnetic separator several times to obtain a clean fraction of pyroxene.

A1.3 Contamination

Splitter and jaw crusher may release fragments of steel, resulting in a contamination of ~0.05% Fe. To avoid cross contamination, all devices were thoroughly cleaned between samples, using compressed air and water.

Agate mills contaminate the sample with SiO_2. Between each sample, the milling devices were either cleaned by crushing pure quartz followed by washing with hot water, or by washing with hot water followed by pre-contamination with crushate of the next sample.

A2 X-ray Fluorescence Analysis (XRF)

A2.1 Instrumental specifications and setup

All XRF major and trace element analyses were carried out at the Open University on an ARL 8420+ dual goniometer wavelength dispersive XRF spectrometer, equipped with a 3 kW Rh anode end-window X-ray tube, fully collimated flow proportional and scintillation counters, and diffraction crystals AX06 (multilayer), PET (penta-erythrytol), Ge111, LiF200 and LiF220.

Experimental intensities were corrected for background and known peak overlap interferences. Instrumental intensity drift was taken into account using a drift monitor. Machine calibration was checked by a number of standard reference material covering a range of compositions (ca. 60 for major elements and 35 for trace elements). Major element matrix corrections were carried out using the Traill-Lachance procedure, whilst trace element corrections involved ratioing with the Compton scattered tube lines. Count times for trace elements were selected to achieve an analytical precision for trace elements of <2% (2σ) at the 100 ppm level.

A2.2 Sample preparation

For major element analysis, glass discs were produced by a 15 min. fusion of one part rock powder dried at 110°C with five parts of dried lithium metaborate/tetraborate flux (Johnson Matthey Spectroflux 100B) in Pt-5%Au alloy crucibles at 1100°C. The melt was swirled repeatedly to ensure complete dissolution and homogenisation, then poured into a brass mould and pressed on a hot plate to form a 1.5 mm thick glass disc of a diameter of 36 mm.

For trace element analysis, 3.5 mm thick powder pellets were produced by mixing ca. 10 g dried rock powder with 9 ml polyvinylpyrollidone (PVP)-methyl cellulose binder and subsequent compression of the mixture at ~18 MPa. The pellets were then dried overnight at 105°C. See Watson (1996) for details.

A2.3 LOI determination

Ca 1.2 g of dried rock powder was ignited in alumina crucibles at 1000°C for 1 hour. Subsequently the percentage weight loss was obtained.

A3 Instrumental Neutron Activation Analysis (INAA)

INAA was performed to determine the abundances of selected REE, and Sc, Co, Cs, Hf, Ta, Th and U. Full details of the analytical procedure are described in Potts et al., (1985). The following summary is modified from Sutton (1995).

Dried rock powder samples (0.3000 g) were sealed inside polyethylene capsules and then stacked into a polyethylene casing tube to be irradiated. Nine sample capsules were placed into each tube, along with two capsules containing standart powders, the calibration standard AC-2 (Ailsa Craig microgranite) and the internal standard WS (Whin Sill dolerite). A weighed lacquered disc of pure iron foil was placed between each capsule to monitor the neutron flux along the tube. Samples were irradiated at the

Imperial College Reactor Centre near Ascot in a thermal neutron flux of 10^{12} n cm^{-2} s^{-1} for 7 hours. After 'cooling' to allow the shortlived radio-nucleides to decay, samples were counted at the Open University. Two detectors were used in tandem: a coaxial Ge(Li) detector and a planar low-energy photon spectrometer (LEPS). Two sets of counting were performed on each sample over a period of approximately one month. The first stage ('short counts') lasted for 8000 seconds. A second stage, employed to increase precision on the longer-lived isotopes took place two to four weeks after irradiation and lasted 6-10 hours ('long counts'). The iron foils were 'counted' using the coaxial detector for 1000 seconds each, to assess variations in the neutron flux and to correct photopeak data.

Precision for the REE is generally better than ±3% (see Appendix D for details).

A4 Sample preparation for Sr, Nd, Th and U analysis by TIMS

All isotopic analyses were carried out in clean chemistry laboratories of the Department of Earth Sciences at the Open University. Samples were analysed for Sr, Nd, U, Th, Ra and Ba. All acids used were either twice-quartz (QD) or twice-Teflon (TD) distilled. Milli-Q reverse osmosis purified water (RO water) was used.

A4.1 Beaker Cleaning

Teflon beakers were used for sample dissolution.

The beakers were initially rinsed with RO water. Then 10-15 ml QD 1.5M HNO_3 were added and the beakers were left overnight on a hotplate, in order to dissolve any residue of previous sample. Following another rinse with RO water, the beakers were then transferred into hot Analar conc. HNO_3 where they were left for a minimum of 24 hours. Subsequently, the beakers were again rinsed with RO water and transferred into a 5 liter beaker of hot RO water. After a minimum of another 24 hours, the beakers were rinsed

again, filled with ca. 10 ml of QD 6M HCl and left sealed under the evaporating hoods for about 30 minutes. Then, the beakers were rinsed once more with RO water and left to dry upside down on a clean Kimwipe™ tissue.

A4.2 Strontium extraction

Approximately 150 mg of rock powder was weighed into clean Teflon Salivex™ beakers. A few drops of TD 15M HNO_3 was added to wet the powder prior to addition of <4 ml TD HF (48%). The sealed beakers were left on a hotplate overnight in order to completely dissolve the sample.

The HF solution was then evaporated off under evaporating hoods until only a small amount of viscous fluid was left, to which 2-3 ml TD 15M HNO_3 was added, diminishing the chance of fluoride formation. The beakers were then once again left on a hotplate overnight. After subsequent evaporation to total dryness, ca. 6 ml TD 6M HCl was added, and the sealed beakers were left to heat up under the evaporating hoods to ensure complete dissolution of any fluorides that may have formed. The samples were then evaporated to dryness and dissolved in about 2 ml QD 2.5M HCl, transferred to a centrifuge tube rinsed with QD 2.5M HCl and centrifuged at 4000 rpm for 5 minutes to give a clear solution.

One millilitre of the sample solution was then loaded onto a 10 ml preconditioned ion-exchange resin column for Sr separation. Once absorbed by the resin, the sample was washed twice with 1 ml QD 2.5M HCl, followed by elution of 36 ml QD 2.5M HCl to remove the Rb fraction. 14 ml of QD 2.5M HCl were then collected through the columns into the Teflon beakers that had been rinsed with RO water, cleaned with QD 6M HCl under the evaporating hoods and rinsed again with RO water. The collected fraction was then evaporated to dryness, the residue ready for loading onto MAT261 single Ta filaments for analysis.

For Sr isotope analysis, 1 µl 10% H_3PO_4 was loaded onto a single Ta filament (outgassed for 5 minutes at 4 A). The sample, taken up in 2 µl TD H_2O, was then added, and the drop was dried down at 1.5 V, 1.2 A. Subsequently the current was turned up to 2 A for ~3 s to burn off excess phosphoric acid.

A4.3 Neodymium extraction

After the Sr fraction had been collected, the Sr columns were washed with 18 ml QD 3M HNO_3, followed by addition of another 18 ml QD 3M HNO_3 to the columns and subsequent collection into a clean Teflon beaker. This solution was then evaporated to dryness, and the residue was dissolved in 0.5 ml QD 0.25M HNO_3, with this passed through a second set of ion exchange columns.

Once the sample had been loaded onto the resin bed, it was washed twice with 1 ml QD 0.25M HNO_3, followed by elution of 15 ml QD 0.25M HNO_3 to remove the Sm fraction. 9 ml of the same acid were then collected through the columns into the Teflon beakers that had been cleaned as described above. The collected Nd fraction was then evaporated to dryness, the residue ready for loading onto MAT 261 double Ta filaments for analysis.

For Nd isotope analysis, the samples was loaded in 2 µl TD H_2O onto a double Ta filament (outgassed for 5 minutes at 4 A) and dried down at 1.5 V, 0.8 A. Nd samples were run with Re double ionisation filaments (outgassed for 5 minutes at 4 A).

A4.4 Thorium and Uranium extraction

Rock powder was weighed into clean Teflon Salivex™ beakers aiming for 500 ng of Th in the beaker. They were then spiked with a mixed ^{236}U-^{229}Th spike, aiming for a $^{232}Th/^{229}Th$ ratio of ~3000. Samples younger than 8 ka were also spiked with Ra-spike, aiming for equal amounts of ^{226}Ra and ^{228}Ra, and Ba-spike, for Ra-Ba chemistry.

A few drops of TD 7M HNO_3 were added to wet the powder prior to addition of 3 ml TD HF (48%) and 1 ml TD 6M HCl. The sealed beakers were left on a hotplate overnight in order to completely dissolve the sample.

The sample was evaporated to dryness and redissolved in TD 6M HCl, evaporated again, redissolved again in TD 6M HCl, and again evaporated to dryness. Then it was dissolved in equal amounts of TD 6M HCl and H_3BO_4 and left on a hotplate overnight, before it was once again dried down. HCl addition was repeated until a clear solution was obtained.

For conversion to nitrates, the sample was then redissolved in TD 15M HNO_3 and left on a hotplate overnight, dried down and redissolved in ~3 ml TD 7M HNO_3, again overnight on a hotplate. A light yellow clear solution was obtained which was centrifuged at 4000 rpm for 5 minutes to obtain a clear solution free of boric acid crystals.

For column separation of U and Th, 4 ml of 1-x8 200-400 biorad anionic exchange resin were preconditioned with 12 ml TD 7M HNO_3. Then, the sample was loaded in 7M HNO_3 and washed on with 2×1 ml TD 7M HNO_3, followed by an elution of 8-18 ml TD 7M HNO_3. All nitric acid was collected Ra-Ba chemistry (see Section A5).

Then, 4 ml TD 6M HCL were eluted and Th was collected in 4 ml TD 6M HCl. 3 ml TD 1M HBr were eluted, and U was collected in 5 ml TD 1M HBr.

The collected fractions were evaporated to dryness, the U- and Th-residue ready for loading onto MAT 262 Re-filaments for analysis.

For U isotope analysis, 1 µl of AQUADAG suspended graphite solution was loaded onto a Re single filament (outgassed for 5 minutes at 4 A) and dried down at 1.5 V, 0.6 A.

The sample was then loaded onto the graphite in 2 µl 0.1M HNO3 and dried down at 1.5 V, 0.7 A.

For Th isotope analysis, 2 µl of Th loading solution (6 ml 0.2M HNO_3 + 25 drops 10% H_3PO_4) were put onto the sample ~1 hour before loading to dissolve Th salts. Subsequently, the samples was loaded onto a double Re filament (outgassed for 5 minutes at 4 A) and dried down at 1.5 V, 0.6 A. Any sample left in the beaker was taken up in a second drop of Th loading solution and added during drying down.

A5 Radium Analysis

A5.1 Initial separation technique

A5.1.1 Introduction

Initially, radium separation chemistry followed a procedure that Thomas (pers. comm.) had modified from Cohen and O'Nions (1991), Volpe et al. (1991) and Cohen (pers. comm.).

Ra separation requires two stages: Ba-Ra preconcentration using cation exchange chromatography, followed by Ra purification to separate Ra and Ba. Here, Ra purification was achieved by extraction chromatography with Sr-Spec® resin.

A5.1.2 Initial Ba-Ra preconcentration procedure

The Ra enrichment was conducted using two successive elutions on a cation-exchange resin. The first elution was performed on a 10 ml BioRad chromatographic column packed with 2 ml cation-exchange resin (Biorad, 200-400 mesh, 0.8 g ml^{-1} dry resin), preconditioned with 3 × 2 ml 3M HCl. Samples were loaded in 3 ml 3M HCl and washed on with 2 × 1 ml 3M HCl. Subsequently, 8 ml 3M HCl followed by 2 × 1 ml H_2O were eluted. Then, the Ra-enriched fraction was collected in 2 × 1 ml 3.75M HNO_3 followed

by 10 ml 3.75M HNO_3. The collected fraction was evaporated to dryness, converted to chlorite with 2 × 3 ml 6M HCl, again evaporated to dryness and taken up in 0.2 ml 3M HCl.

Then a second elution was performed on an 10 ml cleanup column packed with 0.6 ml of the same resin, preconditioned with 3 × 0.6 ml 3M HCl. Samples were loaded in 0.2 ml 3M HCl and washed on with 4 × 0.6 ml 3M HCl. Subsequently, 8 ml 3M HCl followed by 3 × 0.6 ml H_2O were eluted. Then, the Ra-enriched fraction was collected in 2 × 0.2 ml 3.75M HNO_3 followed by 4 ml 3.75M HNO_3. The collected fraction is evaporated to dryness and taken up in 50 µl 3M HNO_3.

A5.1.3 Initial Ra purification procedure

Ra purification was performed using a 150 µl polyprep column packed with Sr-Spec® resin of the ElChrom Company. This resin is composed of an inert substrate onto which a solution of bis-t-butyl-cis-Dicyclohexano-18-crown-6 in 1-octanol is adsorbed. Following a procedure modified from Chabaux et al. (1994), the resin was washed with 300 µl 0.5M HNO_3 and preconditioned with 4 × 150 µl 3M HNO_3. The preconcentrated fraction was then loaded in 50 µl 3M HNO_3 and eluted in 3 × 50 µl 3M HNO_3. Ra was then collected in 300 µl 3M HNO_3.

A5.1.4 Results

Thomas (pers. comm.) achieved ~50% success in analysing her samples for Ra by TIMS. Problems included insufficient Ra purification, resulting in high Ba count rates and suppressed Ra ionisation, and too low and rapidly dying Ra beams, suggesting that some Ra was lost during separation and that column yields were variable and very low at times. Of the Kameni dacite samples run using the above procedure, only one sample out of 20 could be analysed.

A5.2 Preliminary modification of the Ra separation procedure

A5.2.1 Possible causes of insufficient Ra-Ba separation and Ra count rates

Insufficient Ra-Ba separation during the Ra purification stage was thought to be the major reason for unsuccessful analyses. Also, the possibility of column capacities too low for more evolved rocks like the Kameni dacites was anticipated. Thus, two modifications were undertaken: Firstly, the second cationic column was scaled up from 0.6 ml to 2 ml. Secondly, the Sr-Spec® column was scaled up to 1 ml, using a 2 ml quartz column, and was recalibrated, starting from the elution procedure outlined by Chabaux et al. (1994).

A5.2.2 Scaling up the second cationic column

2 ml cationic resin was used during the second preconcentration step. After preconditioning with 3 × 2ml 3M HCl, the sample was loaded in 2 ml 3M HCl. Subsequently, 33 ml 3M HCl were eluted before the Ra-bearing fraction was collected in 15 ml 3.75M HNO_3. Using a larger resin volume also meant that small perturbations of the resin-acid boundary had less effects on separation efficiency.

A5.2.3 Setting up and calibrating the 1 ml Sr-Spec® column

The 1 ml Sr-Spec® column had a considerably larger diameter than the 150 µl polyprep column. To prevent the resin from being disturbed during acid additions, it was topped with ~100 µl of inert Biorad biobeads.

Following Chabaux et al. (1994), the column was preconditioned with 20 ml 3M HNO_3. 150 µl unspiked sample solution of known ^{226}Ra concentration was then loaded onto the column and washed on with 0.85 ml 3M HNO_3. Subsequently, six 1 ml elutions were collected separately and each was spiked with ^{228}Ra spike and analysed by TIMS. It was found that all ^{226}Ra had been extracted with the first 2 ml eluted immediately after loading the sample. This result differed from the elution systematics of Chabaux et al.

(1994) who suggested the sample should be washed on with ca. 3 ml 3M HNO_3 before Ra collection. Clearly, using their procedure all Ra would have been lost.

This was very surprising, and the calibration was repeated: First, the 1 ml Sr-Spec® column was cleaned by ample washing with 3M HNO_3 and 0.5M HNO_3 to ensure complete elution of the Ba and Sr peaks. Cleaning the column was preferred to setting up a new 1 ml column for economical reasons. During the second calibration, which was undertaken using a Ra standard solution to which some Ba spike was added, no Ra was eluted in the first 2 ml, but almost all in the following 2 ml. While this result was still incompatible with observations by Chabaux et al. (1994), it was even more surprising that this second calibration differred so much from the first.

It was concluded that the Sr-Spec® resin changed its adsorption properties during elution of 3M HNO_3. This conclusion was supported by another observation: When the first column calibration was commenced by ample preconditioning with 3M HNO_3, it was noticed that the resin became light green in colour. Starting from the Sr-Spec® - biobeads interface, the colour slowly migrated downwards through the column and became fainter and fainter throughout the separation procedure, until it was not noticeable any more close to the end of the column cleaning stage. While an immediate explanation of this colour change is not at hand, it may be that the crown ether of the Sr-Spec® resin was modified during HNO_3 elution, resulting in changes of its adsorption properties.

All 1 ml Sr-Spec® columns set up subsequently were preconditioned with 3M HNO_3 until the green tint of the resin disappeared, and then the second column calibration was used.

A5.2.4 Results

Using the modified separation procedure, analyses of Ra by TIMS were slightly more successful as interferences observed on mass numbers 225, 227 and 229 almost always

dropped to well below 10% of Ra peaks on mass numbers 226 and 228. However, results were still not satisfactory as beams were dying rapidly and it was impossible to determine ^{226}Ra concentrations to sufficient accuracy.

A5.3 Further modifications to the Ba-Ra preconcentration

A5.3.1 Checking the calibration of the cationic columns

Rapidly dying beams suggested that an appreciable amount of Ra was still lost during chromatographic separation. As the previous Sr-Spec® calibration suggested that the yield of the Sr-spec column was greater than 90%, the yield of both cationic columns was checked. Samples of known ^{226}Ra concentration were spiked with ^{228}Ra spike after passing through the first and after passing through the second cationic column, respectively, and then were passed through the Sr-Spec® column. Mass-spectrometric analyses indicated that while the yield of the first cationic column was ~95%, the yield of the second column was less than 3%. This result was verified by Thomas (pers. comm.) and was surprising as a very similar cationic column procedure was used successfully by Cohen and O'Nions (1991) and Volpe et al. (1991). Furthermore, both Peate (pers. comm.) and Thomas (1998) had calibrated the elution procedure previously. It is suspected that the batch of cationic exchange resin used by these workers had considerably different Ra-adsorption properties. Indeed, changes of adsorption properties for different batches of the same resin are such that elution volume changes of ±10% or more are frequently observed (Cohen, pers. comm.). To achieve better yields for the second cationic column, the elution procedure was revised on basis of published distribution coefficients between exchange resin and solution.

A5.3.2 Distribution coefficients in cationic exchange chromatography

The distribution coefficient for the partitioning of cations between exchange resins and solution is defined as

$$D = \frac{\text{amount of cation / g of dry resin}}{\text{amount of cation / ml of solution}}.$$

This coefficient is dependent on the composition and concentrations of the reagents in the solution, the nature of the resin, the amount of cation to amount of resin ratio (q), and - to a lesser degree - temperature and pressure (Strelow, 1960). If the total amount of the cation is less than ~3% of the total column capacity, i. e. $q < 0.03$, it can be shown that

$$V = D \times m_r,$$

where V is the volume of the eluting agent which has to be passed through the column to elute the maximum of the elution peak, and m_r is the mass of dry resin in the column. For known values of D_i we can thus determine V for any element, i, for a given amount of resin.

Strelow (1960) and Strelow et al. (1965) determined D values at $q = 0.4$ for various acid concentrations of HCl and HNO_3, using AG 50 sulfonated polystyrene processed from Dowex 50 by Bio-Rad. They showed that for $D < 20$, the dependence of D values on q was negligible, but that D values increased with decreasing q for $D \gg 20$. Using column experiments, Strelow (1960) also showed that elution maxima were shifted forward to considerably lower elution volumes when q was increased from 0.005 to 0.1.

A5.3.3 Changing the elution procedure for the second cationic column

In the following, resin D coefficients determined by Strelow (1960) and Strelow et al. (1965) are used to discuss the elution of cations in the second Ba-Ra pre-concentration

stage. The relevant D values are given in Table A-1. Elements with $D^{3M\ HCl} < 6.8$, including most major elements, are not presented. D_{Ra} values are derived from Volpe et al. (1991). For 3.75M HNO_3, D values are not significantly higher than those for 4M HNO_3, which have been used.

Cation	$D^{3M\ HCl}$	$D^{4M\ HNO_3}$
Ra^{+2}	26.5	~3.6
La^{+3}	18.8	9.1
Ce^{+3}	18.8	8.2
Ba^{+2}	18.5	3.6
Y^{+3}	13.6	10.0
Sr^{+2}	10.0	4.7
Ca^{+2}	7.3	1.8
Pb^{+2}	6.8	4.5

Table A-1: Distribution coefficients for ion exchange chromatography, see text for details.

The density of the cationic resin used was 0.8 g ml^{-1} dry resin. Thus, the initial elution of 35 ml 3M HCl, using a 2 ml column, was equivalent to 21.9 ml g^{-1}. Using $D = V / m_r$, we find that the elution maxima of cations with $D^{3M\ HCl} < 21.9$ ml g^{-1} are eluted. From Table A-1 we find that only Ra and possibly the elution tails of Ba, Hg and the rare earth elements should remain on the column. These are subsequently collected using 15 ml 3.75M HNO_3. However, the low Ra yield of <3% suggests that most Ra was in fact lost during HCl elution. It is possible that q ratios higher then 0.005 resulted in a shift of V to lower elution volumes.

Thus, a different approach was taken: To ensure Ra remains on the column during the HCl stage, only 13 ml 3M HCl were eluted, equivalent to 8.125 ml g^{-1} dry resin. As a result, all major elements including Ca were eluted, while Ra, the rare earth elements, Y, Ba and some Sr remained on the column. These elements had moved down through the resin, and - using the above D values - each of them had to elute through the remaining resin amount of <1.07 g, ~0.9 g, 0.6 g, 0.9 g and 0.3 g, respectively.

Subsequently, 5.5 ml 3.75M HNO_3 were collected. This ensured that all of the above elements apart from Ra, Ba and Sr remained on the column. On the Sr-Spec® column Sr is eluted last. Thus, the fact that Sr is part of the Ba-Ra preconcentrated fraction does not represent a problem. In addition, it was checked and verified that all Ra was eluted using only 5.5 ml 3.75M HNO_3: No Ra was found in 3.75M HNO_3 eluted subsequently.

A5.3.4 Results and discussion

Sample analyses by TIMS were performed much more successfully. Typically, more that 80 $^{228}Ra/^{226}Ra$ ratios could be collected on sufficiently stable beams. Interferences typically decreased to less then 5%. Analytical errors decreased to much better than 2% (2σ).

It is suggested that the use of a 150 µl Sr-Spec® column is once more attempted. Using the new Ra-Ba preconcentration procedure, the amount of rare earth elements loaded onto the Sr-Spec® column may be negligible, thus allowing the collection of all of the first four eluted column volumes of 3M HNO_3, i. e. ~600 µl. This may result in a Ra purification procedure insensitive to the observed variations in position of Ra elution maxima due to possible changes in Ra-Ba peak separation properties of the Sr-Spec® resin during HNO_3 elution (section A5.2.3).

A5.4 Filament preparation

For Ra isotope analysis, samples were loaded in 2 µl Ta-HF-H_3PO_4 activator solution (Birck, 1986) onto single Re filaments (outgassed for 5 minutes at 4A) and dried down at 1.5 V, 0.6 A. Then, the current was increased to 1.0-1.5 A for ~3 s to remove excess phosphoric acid.

A6 Thermal Ionisation Mass Spectrometry

All samples were analyses on Finnegan MAT261 and MAT262 multi-collector thermal ionisation mass spectrometers. Instrumentation, technical details and performance of the MAT262 on Th and U isotopic measurements are outlined in van Calsteren and Schwieters (1995). The software for the mass spectrometers was developed by D. W. Wright and P. van Calsteren at the Open University.

A6.1 Standart variability and normalisation procedure

A6.1.1 Internal standards

Solution standards for Sr isotopes (NBS987), Nd isotopes (J&M), U isotopes (U456Std, U456Std2) and Th isotopes (Th'u'Std) were analysed during the periods of sample analysis. Results for the Th'u'Std are shown graphically in Figure A-1. Standards analysed as part of this study are highlighted. Standards with analytical errors greater than 1% or collected under conditions of unstable beam intensities or - for the Th'u'Std - SEM yields outside 95-100% were excluded.

The running mean of the NBS987 varies between $^{87}Sr/^{86}Sr = 0.710144$ and $^{87}Sr/^{86}Sr = 0.710232$, with 2σ standard deviations of the mean ranging from ± 0.000022 to ± 0.000036. Samples were normalised to NBS987 = 0.710220, using the running mean of the NBS987 standard of the period during which they were analysed.

The running mean of the J&M varies between $^{143}Nd/^{144}Nd = 0.511746$ and $^{143}Nd/^{144}Nd = 0.511778$, with 2σ standard deviations of the mean ranging from ± 0.000022 to ± 0.000030. Samples were normalised to J&M = 0.511836, using the running mean of the J&M standard of the period during which they were analysed.

For the entire period from June 1997 until December 1997, the running mean of the U456Std2 was $^{234}U/^{236}U = 0.097449$ and $^{235}U/^{236}U = 13.270492$, with 2σ standard

deviations of ±0.56% and ±0.18%, respectively. Standard deviations of the U456Std were of the same order. Normalisation of samples was not required.

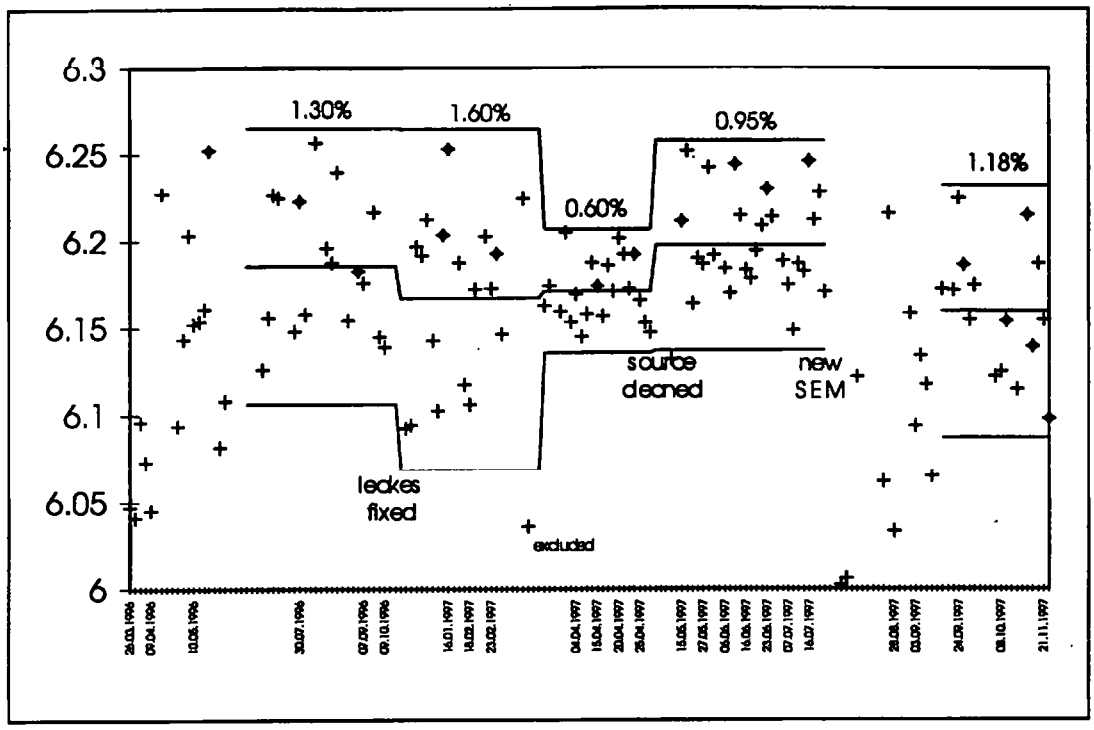

Figure A-1: Running means and their 2σ standard deviations for the Th'u'Std.

The running mean of the Th'u'Std varies between $^{230}Th/^{232}Th = 6.15933$ and $^{230}Th/^{232}Th = 6.19740$, with 2σ standard deviations of the mean ranging from 0.60% to 1.60%. However, for the entire period from May 1996 until July 1997, the running mean of the Th'u'Std is $^{230}Th/^{232}Th = 6.21702$, with a 2σ standard deviation of ±0.90%, when only standards analysed as part of this study are considered. Samples run after July 1997 were normalised to $^{230}Th/^{232}Th = 6.21702$, using the running mean of the Th'u'Std of the period during which they were analysed.

For Sr and Nd isotopes, analytical errors are much smaller than the standard deviations of the running mean of the standard. For U and Th isotopes, analytical errors are of the order of the standard deviation of the running mean of the standard. At any case, the standard deviation should be used when assessing precision of sample analyses.

The AN radium solution standart ([^{226}Ra] = 83.83 fg/g) was used to calibrate the AU radium spike (decay corrected [^{228}Ra] = 172.6±0.2 fg/g), and reproducibility of the spike ratio was better than 1% (2σ), with a weighted average value of ^{228}Ra/^{226}Ra = 5.17±0.01.

A6.1.2 External standards

Whole rock standards were analysed by members of the isotope geochemistry group, including the author, to allow comparison of U-Th data with results from other laboratories. Results are shown in Table A-2. 2σ standard deviations from the averages of a number of analyses, n, should not be taken as indicative for sample reproducibility

	U (ppm)	Th (ppm)	(^{238}U/^{232}Th)	(^{230}Th/^{232}Th)	(^{230}Th/^{238}U)
ATHO	2.2639	7.2554	0.9465	1.0260	1.0887
	±3.60%	±4.39%	±1.84%	±1.33%	±1.87%
TML	10.7806	29.3244	1.1161	1.1155	0.9991
	±0.94%	±2.96%	±3.46%	±10.2%	±6.75%
Mt. Lassen	2.7616	8.3768	1.0071	1.0655	1.0605
	±2.69%	±1.43%	±2.06%	±1.58%	±2.05

Table A-2 Averages of U-Th WR standards, and their 2σ standard deviations

within a range of samples, as the analyses compiled here were performed over a period of ~3 years, and have been analysed by not one but numerous researchers. Analyses presented in this thesis could generally be reproduced with a precision better than 1.5% (2σ). The TML standard is given for reference only as the number of analyses is too low to draw any significant conclusions.

The Mt. Lassen standard was analysed for radium abundancies and values of ^{226}Ra = 1.080±0.026 pg g^{-1} and ^{226}Ra = 1.065±0.010 pg g^{-1} were obtained. These values

are within error of the Mt. Lassen analyses by Volpe et al. (1991) who obtained $^{226}Ra = 1.063 \pm 0.010$ and $^{226}Ra = 1.068 \pm 0.011$.

A6.2 Total procedure blanks

To assess contamination levels of Sr and Nd, one total procedure blank (TP blank) was run with each batch of samples. TP blanks for U, Th and Ra were run at intervals.

TP blank levels were typically below 2 ng for Sr, 0.5 ng for Nd, and 100 pg for Th and U. Their contribution to both concentration and isotopic composition of sample analyses is thus negligible. Ra blank contributions were below detection limit and are negligible.

A7 Electron Microprobe Analysis

Electron microprobe analyses were made on polished thin sections of standart thickness (~30 µm), that were carbon-coated to provide a conductive layer and to minimise charge build-up under the electron beam. Analyses were performed at the Open University on a wavelength dispersive Cameca SX100 microprobe. The instrument is a fully computerised system which enables spectrometer angles, count times, crystal selection, speciment movement and on line PAP (Pouchou and Pichoir, 1985) corrections to be performed automatically. An accelerating potential of 20 kV and a beam current of 20 nA were used. The electron beam was defocussed to about 10 µm to reduce the possibility of sample decomposition. For glass analyses, the beam was defocussed still further, to about 25 µm, to reduce the risk of Na volatilisation.

Primary standarts used were feldspar (Si, K, Al), bustamite (Mn, Ca), willemite (Zn), hematite (Fe), forsterite (Mg), rutile (Ti), jadeite (Na), synthetic potassium chloride (Cl) and synthetic LiF (F). The calibration was checked against a secondary standart, KKA (a kaersutitic amphibole). If any element fell outside the expected range for KKA, then a recalibration of that element was attempted on the primary standard until a satisfactory

value was obtained. Reproducibility of KKA major element abundancies is generally better than 2% (2σ).

A8 Ion Microprobe Analysis

A8.1 Instrumental specifications and setup

The Cameca ims-4f ion microprobe at the Department of Geology and Geophysics, University of Edinburgh, was used to study trace element concentration variations within plagioclase and pyroxene crystals and to determine distribution coefficients experimentally. The following description of the instrument, based on a user guide by John Craven, has been limited to the instrument units relevant to this study.

A duoplasmatron source is used as ion source. Primary O^--ions are passed to the sample via the primary column, consisting of a mass filter and a series of apertures, electrostatic lenses and deflection plates. The primary beam mass filter removes OH, N, Fe and Ni and other components, and produces a beam of O^--ions. This beam is focussed and positioned within the primary column and accelerated from -10kV to ca. +4.5kV at the sample target. Where the primary ions hit the sample, charged particles are ejected from the sample surface. Of these secondary ions, all cations are immediately extracted by an electrostatic immersion lens at ground potential. Any off-axis ions are deflected back onto axis by a set of dynamic transfer lenses.

The secondary ion beam is then focussed by a set of electrostatic transfer lenses onto the entrance slit of the spectrometer. This consists of an ion energy analyser and a mass analyser. In the ion energy analyser, the beam is first passed through an electrostatic sector that consists of two spherical electrode surfaces of opposite polarities, deflecting lower energy ions more strongly then higher energy ions. To eliminate molecular species, only the high energy portion of the dispersed ion beam is selected by an energy window

and allowed to pass into the mass analyser. In practice, rejection of low energy ions is achieved by lowering the sample voltage and keeping the energy window centred. The energy filtered ion beam is subsequently aligned into the mass analyser by an electrostatic spectrometer lens. The mass analyser is an electromagnet that separates the ions according to their mass. During analyses, the magnetic field is adjusted so that only ions of the desired mass are allowed to pass through the spectrometer exit slit into the ion detection system. In combination with the energy analyser, high mass resolution is attained. An electron multiplier with a background count rate of less then 0.01 cps is used as one of the secondary ion detectors.

A8.2 Sample preparation and procedures

Carbon-coated electron probe sections were cut into discs of 1 inch diameter. Then, the carbon coat was removed and the sections were gold-coated to prevent charge build-up within the sample during analysis.

The analysis consisted of using an O^- primary beam accelerated to 12.5 kV, with a primary beam current of ~20 nA (~60 nA for uranium and thorium). The primary beam diameter varied with beam current but was ~20 µm at 20 nA, although the gold coating was affected within an area ~50 µm in diameter.

Standart interference corrections (FeSi, and element oxides) were applied, and data were normalised to the mean SiO_2 content of the probed crystals or groundmass, as determined by electron microprobe. 2σ errors stated are aproximate reproducibility, which is 2% plus the error based on counting statistics for masses smaller than 70 amu, and otherwise 4% plus the error based on counting statistics (Hinton, pers. comm.).

APPENDIX B

Mathematical background, constants and coefficients

B1 Calculating the Ce anomaly

Ce* has been calculated by interpolation of La and Nd, as Pr data was not available, assuming that REE form a straight line on a chondrite normalised REE diagram with logarithmic scale. Thus

$\log Ce_N^* = \frac{2\log La_N + \log Nd_N}{3}$, and the cerium anomaly is given by

$Ce/Ce^* = Ce_N / \sqrt[3]{La_N^2 * Nd_N}$.

B2 Batch melting

B2.1 Modal batch melting

$$X_L = \frac{X_O}{F + D - FD},$$

where X_L is the concentration of the element in the liquid, X_O is the concentration in the original, unmelted source, F is the weight proportion of melt formed, and D is the bulk distribution coefficient for the residual solids at the moment when the melt is removed from the system (e. g. Cox et al., 1979).

B2.2 Non-modal batch melting

$$X_L = \frac{X_O}{F + D - FP},$$

where P is the bulk distribution coefficient of the minerals which make up the melt.

B3 Derivation of the Rayleigh fractionation equation

The derivation of the Rayleigh fractionation equation is summarised following Wood and Fraser (1976). We consider a finite magma reservoir containing a total of n moles of various components including y moles of a trace element Tr. The mole fraction of Tr in the system is X_{Tr} = y/n. After a short time of fractional crystallisation,

$$X_{Tr}^{crystal} = \frac{dy}{dn},$$

$$X_{Tr}^{melt} = \frac{y - dy}{n - dn} \equiv \frac{y}{n}.$$

Tr is a component obeying Henry's law, hence

$$X_{Tr}^{crystal} = D_{Tr}^{crystal/melt} X_{Tr}^{melt}.$$

Differentiating $y = nX_{Tr}^{melt}$ with respect to n, we obtain

$$\frac{dy}{dn} = n\frac{d\left(X_{Tr}^{melt}\right)}{dn} + X_{Tr}^{melt}.$$

Substituting for dy/dn and rearranging gives

$$\frac{1}{n}dn = \frac{1}{X_{Tr}^{melt}\left(D_{Tr}^{crystal/melt} - 1\right)} d\left(X_{Tr}^{melt}\right).$$

The total changes in concentration during crystallisation can now be obtained by integration between X_{Tr}^{0} andX_{Tr} and between the initial and final amounts of melt n^0 and n. We obtain

$$\ln\left(\frac{n}{n^0}\right) = \frac{1}{D_{Tr}^{crystal/melt} - 1} \ln\left(\frac{X_{Tr}^{melt}}{X_{Tr}^{0,melt}}\right).$$

(n/n^0) is the fraction of melt remaining, F. Hence we obtain the Rayleigh fractionation equation

$$X_{Tr}^{melt} = X_{Tr}^{0,melt} \times F^{\left(D_{Tr}^{crystal/melt} - 1\right)}.$$

B4 Mixing

B4.1 Major and trace elements

$X_L = f X_C + (1\text{-}f) X_O,$

where X denotes concentrations, and subscripts L, C and O denote the mixed magma, the contaminant and the uncontaminated magma, respectively, and f is the fraction of contaminant.

B4.2 Isotopes

Using Sr isotopes as an example, the Sr concentration of the parental magma is

$[Sr]_p = [^{86}Sr]_p + [^{87}Sr]_p$

Equally, for a contaminant,

$[Sr]_c = [^{86}Sr]_c + [^{87}Sr]_c$

Thus, the Sr isotopic ratio of a mixed magma is given by

$$\left(\frac{^{87}Sr}{^{86}Sr}\right)_m = \frac{f\left[^{87}Sr\right]_c + (1-f)\left[^{87}Sr\right]_p}{f\left[^{86}Sr\right]_c + (1-f)\left[^{86}Sr\right]_p},$$

where f is the fraction of the contaminating magma. If we know the ($^{87}Sr/^{86}Sr$) ratio of the contaminant, we can write

$$\left(\frac{^{87}Sr}{^{86}Sr}\right)_c = \frac{\left[^{87}Sr\right]_c}{\left[^{86}Sr\right]_c} = \frac{\left[^{87}Sr\right]_c}{[Sr]_c - \left[^{87}Sr\right]_c}.$$

Rearranging, we find that

$$\left[^{87}Sr\right]_c = \frac{[Sr]_c}{\left(\frac{^{86}Sr}{^{87}Sr}\right)+1}.$$

Similar expressions can be derived for $[^{87}Sr]_p$, $[^{86}Sr]_c$ and $[^{86}Sr]_p$. The isotope mixing equation is then obtained by substitution:

$$\left(\frac{^{87}Sr}{^{86}Sr}\right)_m = \frac{f[Sr]_c / \left(1+\left(^{86}Sr/^{87}Sr\right)_c\right) + (1-f)[Sr]_p / \left(1+\left(^{86}Sr/^{87}Sr\right)_p\right)}{f[Sr]_c / \left(1+\left(^{87}Sr/^{86}Sr\right)_c\right) + (1-f)[Sr]_p / \left(1+\left(^{87}Sr/^{86}Sr\right)_p\right)}.$$

B5 Assimilation and fractional crystallisation (AFC)

For the derivation of the AFC equations, see DePaolo (1981). Symbols used are:

X_L = concentration of the trace element in the contaminated liquid

X_O = concentration of the trace element in the original magma

X_C = concentration of the trace element in the assimilant

R_L = isotope ratio of the contaminated liquid

R_O = isotope ratio of the original magma

R_C = isotope ratio of the assimilant

r = ratio (rate of assimilation)/(rate of fractional crystallisation)

D = bulk distribution coefficient of the fractionating assemblage

F = fraction of magma remaining

$$K = \frac{r-1+D}{r-1}$$

B5.1 Trace elements

$$X_L = X_O F^{-K} + \frac{r}{r-1+D} X_C \left(1 - F^{-K}\right),$$

B5.2 Radiogenic isotopes

$$R_L = R_O + \left(R_C - R_O\right)\left(1 - \frac{X_O}{X_L} F^{-K}\right)$$

B6 Principles and applications of radioactive decay

B6.1 The decay equation

The rate of change in abundance of a radioactive element is proportional to its abundance:

$$\frac{dn}{dt} = -\lambda n.$$

Integrating:

$$\int_{n_0}^{n} \frac{dn}{dt} = -\lambda \int_{t=0}^{t} dt.$$

$$\ln\left(\frac{n}{n_0}\right) = -\lambda t.$$

$$n = n_0 e^{-\lambda t}.$$

The number of radioactive daughters produced after time t is

$D^* = n_0 - n = ne^{\lambda t} - n = n\left(e^{\lambda t} - 1\right)$. Hence, the total number of daughters is

$$D = D_0 + D^* = D_0 + n\left(e^{\lambda t} - 1\right).$$

B6.2 The Bateman equation

However, as the daughter decays itself,

$\frac{dn_2}{dt} = n_1\lambda_1 - n_2\lambda_2$, where subscript 1 denotes the parent and subscript 2 the daughter.

It follows that

$$\frac{dn_2}{dt} = \left(n_{1,initial} e^{-\lambda_1 t}\right)\lambda_1 - n_2\lambda_2 .$$

This can be integrated choosing a set of initial conditions. For the case n_2=0 at t=0 (no daughters initially), we get the Bateman equation (after Bateman, 1910)

$$n_2 = \frac{\lambda_1}{\lambda_2 - \lambda_1} n_{1,initial}\left(e^{-\lambda_1 t} - e^{-\lambda_2 t}\right).$$

B6.3 Application to U-Th isotope systematics - the isochron equation

For ^{230}Th we have

$$n^{230}Th = \frac{\lambda_{238}}{\lambda_{230} - \lambda_{238}} n^{238}U_{initial}\left(e^{-\lambda_{238} t} - e^{-\lambda_{230} t}\right).$$

This can be expressed in terms of activities:

$$\frac{\left(^{230}Th\right)}{\lambda_{230}} = \frac{\lambda_{238}}{\lambda_{230} - \lambda_{238}} \frac{\left(^{238}U\right)_{initial}}{\lambda_{238}}\left(e^{-\lambda_{238} t} - e^{-\lambda_{230} t}\right).$$

$$\left(^{230}Th\right) = \frac{\lambda_{230}}{\lambda_{230} - \lambda_{238}}\left(^{238}U\right)_{initial}\left(e^{-\lambda_{238} t} - e^{-\lambda_{230} t}\right).$$

However, as the half-life of ^{238}U is very large, its activity can be considered constant, and $\lambda_{238} \approx 0$. Hence the equation simplifies to

$$\left(^{230}Th\right) = \left(^{238}U\right)\left(1 - e^{-\lambda_{230} t}\right).$$

For any inital Th left we get

$$\left(^{230}Th\right) = \left(^{230}Th\right)_{initial} e^{-\lambda_{230} t} + \left(^{238}U\right)\left(1 - e^{-\lambda_{230} t}\right)$$

and we obtain the U-Th isochron equation

$$\left(\frac{^{230}Th}{^{232}Th}\right) = \left(\frac{^{230}Th}{^{232}Th}\right)_{initial} e^{-\lambda_{230} t} + \left(\frac{^{238}U}{^{232}Th}\right)\left(1 - e^{-\lambda_{230} t}\right)$$ as (^{232}Th) is constant.

On an U-Th equiline diagram, this is the equation of a straight line with slope $\left(1 - e^{-\lambda_{230} t}\right)$ and intercept $\left(\frac{^{230}Th}{^{232}Th}\right)_{initial} e^{-\lambda_{230} t}$ and thus the basis of U-Th dating of silicates using mineral isochrons.

B6.4 Application to Th-Ra isotope systematics

For Ra, using the same arguments, we obtain

$$(^{226}Ra) = (^{226}Ra)_{initial}\, e^{-\lambda_{226} t} + (^{230}Th)(1 - e^{-\lambda_{226} t}),$$

using $\lambda_{230} \ll \lambda_{226}$ and $(^{230}\mathrm{Th})_{initial} \approx (^{230}\mathrm{Th})$ for small t. In this case, we normalise to [Ba] and obtain

$$\frac{(^{226}Ra)}{[Ba]} = \frac{(^{226}Ra)_{initial}}{[Ba]} e^{-\lambda_{226} t} + \frac{(^{230}Th)}{[Ba]}(1 - e^{-\lambda_{226} t})$$ and thus the basis of Th-Ra dating of silicates using mineral isochrons.

B6.5 Decay correction

Using U-Th systematics as an example, we obtain the Th isotopic signature of a rock at the time of eruption by substituting $\left(\frac{^{230}Th}{^{232}Th}\right)_{initial}$ with $\left(\frac{^{230}Th}{^{232}Th}\right)_{eruptive}$ and t with Δt, where Δt is the age of the sample. Then, rearranging the isochron equation, we obtain

$$\left(\frac{^{230}Th}{^{232}Th}\right)_{eruptive} = \left(\frac{^{230}Th}{^{232}Th}\right) e^{\lambda_{230}\Delta t} - \left(\frac{^{238}U}{^{232}Th}\right)(e^{\lambda_{230}\Delta t} - 1).$$

For Ra, following the same argument, we have

$$\frac{(^{226}Ra)_{eruptive}}{[Ba]} = \frac{(^{226}Ra)}{[Ba]} e^{\lambda_{226}\Delta t} - \frac{(^{230}Th)}{[Ba]}(e^{\lambda_{226}\Delta t} - 1).$$

B6.6 Error Systematics

If Z = Z (A, B, ...) (with A, B, etc. independent), then

$$(\sigma_Z)^2 = \left(\frac{\partial Z}{\partial A}\sigma_A\right)^2 + \left(\frac{\partial Z}{\partial B}\sigma_B\right)^2 + \ldots.$$

We hence find that

$$\sigma\left(\frac{^{230}Th}{^{232}Th}\right)_{eruptive} = \sqrt{\left[\sigma\left(\frac{^{230}Th}{^{232}Th}\right)e^{\lambda_{230}\Delta t}\right]^2 + \left[\sigma\left(\frac{^{238}U}{^{232}Th}\right)(1 - e^{\lambda_{230}\Delta t})\right]^2 + \left\{\lambda e^{\lambda_{230}\Delta t}\sigma(\Delta t)\left[\left(\frac{^{230}Th}{^{232}Th}\right) - \left(\frac{^{238}U}{^{232}Th}\right)\right]\right\}^2}$$

For Ra, following the same argument, we have

$$\sigma\left(\frac{(^{226}Ra)_{eruptive}}{[Ba]}\right)=\sqrt{\left[\sigma\left(\frac{(^{226}Ra)}{[Ba]}\right)e^{\lambda_{226}\Delta t}\right]^2+\left[\sigma\left(\frac{(^{230}Th)}{[Ba]}\right)(1-e^{\lambda_{226}\Delta t})\right]^2+\left\{\lambda e^{\lambda_{226}\Delta t}\sigma(\Delta t)\left[\left(\frac{(^{226}Ra)}{[Ba]}\right)-\left(\frac{(^{230}Th)}{[Ba]}\right)\right]\right\}^2},$$

where $\sigma\left(\frac{(^{226}Ra)}{[Ba]}\right)=\left(\frac{(^{226}Ra)}{[Ba]}\right)\sqrt{\left(\frac{\sigma(^{226}Ra)}{(^{226}Ra)}\right)^2+\left(\frac{\sigma[Ba]}{[Ba]}\right)^2}$.

B7 Decay constants

Decay constants are taken from Goldstein et al. (1989).

$\lambda_{226} = 4.272\times10^{-4}$

$\lambda_{230} = 9.1952\times10^{-6}$

$\lambda_{232} = 4.9475\times10^{-11}$

$\lambda_{234} = 2.83495\times10^{-6}$

$\lambda_{238} = 1.55125\times10^{-10}$

B8 Partition coefficients and source compositions

Partition coefficients are taken from Halliday et al. (1995), Jenner et al. (1993), LaTourrette et al. (1995), Mahood and Hildreth (1983), McKay et al. (1994) and Nash and Crecroft (1985).

MORB source composition is taken from Stolper and Newman (1994), with the extrapolation to the heavy REE guided by depleted earth estimates of McKenzie and O'Nions (1991).

The composition of global subducting sediments (GLOSS) is taken from Plank and Langmuir (1998), with Tb extrapolated from Plank and Ludden (1992).

	MORB source	Partition coefficients					
	concentration (ppm)	olivine	orthopyroxene	clinopyroxene	garnet	amphibole	rutile
Rb	0.062	3.0E-4	2.0E-4	4.0E-4	2.0E-4	0.2	0
Ba	0.67	5.0E-6	6.0E-6	3.0E-4	7.0E-5	0.16	0
Th	0.011	7.0E-6	2.0E-5	2.1E-3	2.1E-3	3.9E-2	0
U	0.0042	9.0E-6	4.0E-5	1.0E-3	1.1E-2	4.1E-3	0
K	57.3	2.0E-5	1.0E-4	1.0E-3	1.3E-2	0.58	0
Ta	0.011	5.0E-5	3.0E-4	8.9E-3	1.0E-2	0.159	99.5
Nb	0.23	5.0E-5	3.0E-4	8.9E-3	1.0E-2	0.159	52.6
La	0.26	2.0E-4	3.1E-3	5.4E-2	7.0E-4	5.5E-2	0
Ce	0.7	7.0E-5	2.1E-3	8.6E-2	2.6E-3	9.6E-2	0.73
Pb	0.031	3.0E-4	1.4E-3	7.5E-3	3.0E-4	1.9E-2	0
Sr	9.6	4.0E-5	7.0E-4	9.1E-2	7.0E-4	0.298	0.518
Nd	0.67	3.0E-4	2.3E-3	0.19	2.7E-2	0.25	0
P	43	9.0E-4	2.3E-3	0.19	2.7E-2	0.25	0
Sm	0.25	1.0E-2	3.7E-3	0.27	0.22	0.32	0
Zr	6.9	1.0E-3	1.2E-2	0.26	0.2	0.127	4.76
Hf	0.22	2.9E-3	1.9E-2	0.33	0.23	0.13	0
Eu	0.13	5.0E-4	9.0E-3	0.43	0.61	0.52	0
Ti	1193	1.5E-2	8.6E-2	0.4	0.6	1	0
Tb	0.1	2.0E-3	8.5E-3	0.44	1.7	0.52	0
Y	4	8.2E-3	1.5E-2	0.47	2	0.52	0
Yb	0.44	2.4E-2	3.8E-2	0.43	6.4	0.5	0
Lu	0.07	2.4E-2	3.8E-2	0.43	6.4	0.43	0

	GLOSS	Partition coefficients						
	concentration (ppm)	biotite	ilmenite	plagioclase	garnet	amphibole	rutile	quartz
Rb	0.062	3	0	9.0E-2	2.0E-4	0.2	0	1.6E-2
Ba	0.67	5.4	0	0.63	7.0E-5	0.16	0	4.0E-3
Th	0.011	1.43	5	3.0E-2	2.1E-3	3.9E-2	0	9.0E-3
U	0.0042	0.18	6.3E-2	5.0E-2	1.1E-2	4.1E-3	0	2.8E-2
K	57.3	1.5	0	9.0E-2	1.3E-2	0.58	0	1.4E-2
Ta	0.011	1.36	106	2.0E-2	1.0E-2	0.159	99.5	8.0E-3
Nb	0.23	1.36	106	2.0E-2	1.0E-2	0.159	52.6	8.0E-3
La	0.26	2.59	1.31	0.022* / 0.32	7.0E-4	5.5E-2	0	1.8E-2
Ce	0.7	2.15	1.19	0.21	2.6E-3	9.6E-2	0.73	1.4E-2
Pb	0.031	4.0E-3	0	1.3	3.0E-4	1.9E-2	0	1.0E-2
Sr	9.6	4.4E-2	0.518	6.8	7.0E-4	0.298	0.518	1.0E-2
Nd	0.67	1.8	0.96	0.14	2.7E-2	0.25	0	1.6E-2
P	43	1.7	0	0.1	2.7E-2	0.25	0	1.0E-2
Sm	0.25	1.61	0.68	0.11	0.22	0.32	0	1.7E-2
Zr	6.9	0.47	0.65	4.0E-2	0.2	0.127	4.76	2.3E-2
Hf	0.22	0.47	0.65	6.0E-2	0.23	0.13	0	2.3E-2
Eu	0.13	1	0.4	3.8	0.61	0.52	0	8.0E-2
Ti	1193	0.98	0	9.0E-2	0.6	1	0	1.9E-2
Tb	0.81	1.3	0.36	9.0E-2	1.7	0.52	0	1.9E-2
Y	4	0.6	0.55	4.0E-2	2	0.52	0	1.7E-2
Yb	0.44	0.6	0.55	4.0E-2	6.4	0.5	0	1.7E-2
Lu	0.07	0.65	0.74	6.0E-2	6.4	0.43	0	1.1E-2

*McKay et al. (1994), used in fractionation modelling.

B9 Modelling trace element partitioning

The following equation (Blundy and Wood, 1994) describes the partition coefficient $D_i(P, T, X)$ between an element i and the coexisting melt at a given pressure P, temperature T and composition X as a function of $D_0(P, T, X)$, E, r_0, r_i and T. E is Young's Modulus of the crystal, r_0 is the optimum radius of the lattice site, r_i is the radius of the substituent cation, and $D_0(P, T, X)$ is the strain-compensated partition coefficient, that describes strain-free cation substitution ($r_i = r_0$):

$$D_i(P,T,X) = D_0(P,T,X) \times \exp\left[\frac{-4\pi E N_A\left[\frac{r_0}{2}(r_i - r_0)^2 + \frac{1}{3}(r_i - r_0)^3\right]}{RT}\right]$$

APPENDIX C

Sample localities and key to the units

C1 Santorini.

Sample localities are indicated of Figure 3-1. The following key to the stratigraphic units is adapted from Druitt and Davies (1999), see also Figure 3-2.

C1.1 Kameni Islands

Dacite lava domes and flows of the Kameni islands:

dkl Liatsikis lava, 1950. These contain andesitic xenoliths, e. g. samples "k101dkl xa" and "k107dkl xa", sampled by Nicholls (1971).

dki Niki lavas, 1940-1941

dkr Reck and Smith lavas, 1940

dkf Fouqué lavas, 1939-1940. These contain basaltic xenoliths, e. g. sample "k78dkf xb", sampled by Nicholls (1971).

dkk Ktenas lavas, 1939

dkd Dafni lavas, 1925-1926. These contain gabbroic xenoliths, e. g. sample "k97dkd xg", sampled and by Nicholls (1971).

dkg Georgios lavas, 1866-1870

dko Afroessa lavas, 1866

dkn Nea Kameni lavas, 1707. These contain basaltic xenoliths, e. g. sample "k103dkn xb", sampled by Nicholls (1971).

dkm Mikri Kameni lavas, 1570

dka Agios Nikoloas lavas, 726AD

dkt Thira lavas, 46-47AD. These contain andesitic xenoliths, e. g. sample "k35dkt xa", sampled by Nicholls (1971).

Second eruptive cycle

rp7 Rhyodacitic pyroclastic deposits of the Minoan eruption.

rp6 Ryodacitic pyroclastic deposits of the Cape Riva eruption (not sampled in this study).

ao Andesitic lavas of Oia.

rt Rhyodacitic domes of Therasia and Thera.

ap5 Andesitic pyroclastic deposits of the Upper Scoriae 2 eruption. Red welded agglomerates and lithic brechias.

as2 Andesitic and basaltic lavas of the Skaros lava shield. Approximately 25 stacked flows.

ds1 Dacitic lava domes forming the base of the Skaros lava shield

ap4 Andesitic to dacitic pyroclastic deposits of the Cape Thera, Middle Pumice, Vourvoulos, and Upper Scoriae 1 eruptions.

as Andesites and basalts of Cape Simandiri forming the remnants of a lava shield, the ancient summit of which lay within the present caldera.

C1.2 First eruptive cycle and earlier deposits

rp1 Andesitic tuffs and scoria-flow deposits of the Cape Therma 1 eruption.

av3 Bedded andesitic-basaltic lavas and tuffs of the youngest parts of Peristeria Volcano.

apa Andesitic and basaltic cinder cones of the Akrotiri Peninsula.

C2 Nisyros

Sample localities are indicated on Figure C-1, and the key to sample numbers is included in the stratigraphic column (Figure C-2). The geological map and the stratigraphy of Nisyros are adapted from Francalanci et al. (1995) and Hardiman (1996).

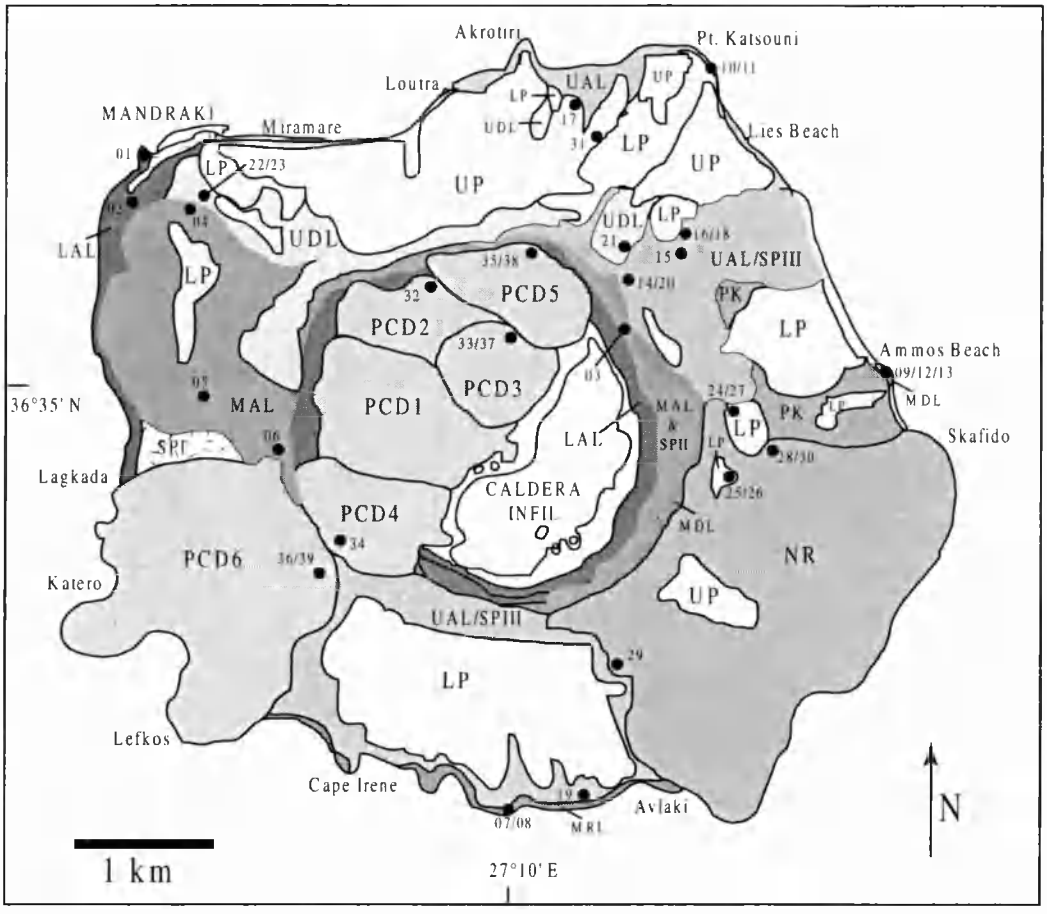

Figure C-1: Geological map of Nisyros, and sample locations.

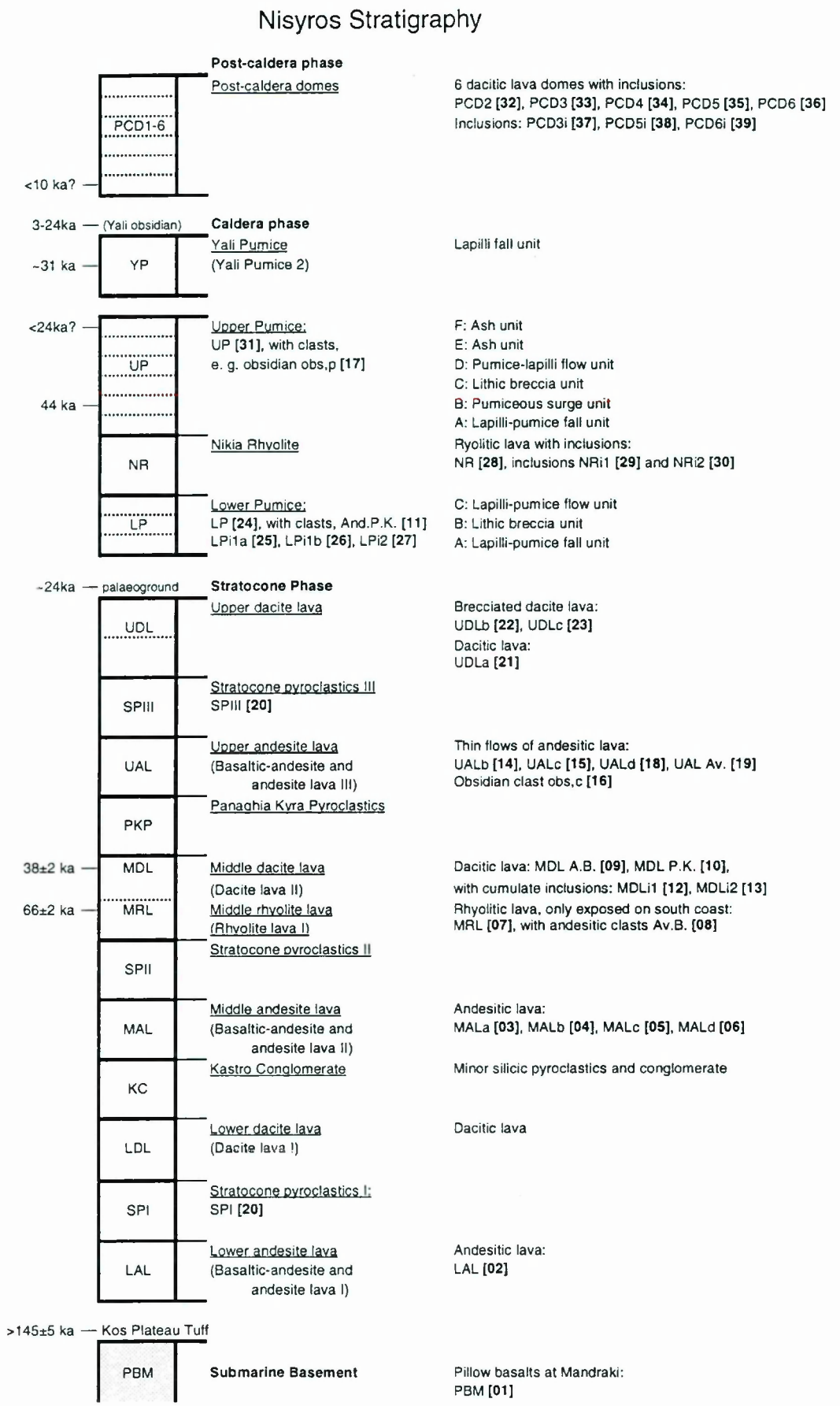

Figure C-2: Stratigraphy of Nisyros, and key to the samples.

APPENDIX D

Data tables

D1 Major element oxide data determined by XRF

All major element oxide abundancies are quoted in wt%. $Fe_2O_3^T$ denotes the total Fe content expressed as Fe_2O_3. Data have been normalised to 100%. Loss on ignition (LOI) weight percentages are quoted for additional information. 2σ errors are based on reproducibility, after Sutton (1995).

D2 Trace element data determined by XRF

All trace element abundancies are quoted in parts per million (ppm). 2σ errors stated are instrumental errors in ppm. Results of XRF analyses of repeated preparations of the same sample powder by Sutton (1995) show similar or even less variation irrespective of composition, suggesting that errors due to sample preparation or inhomogeneity are insignificant. Data in brackets are below detection limit and should be taken as indicative only.

D3 Trace element data (including REE) determined by INAA

All trace element data are quoted in parts per million (ppm). 2σ errors stated are based on repeat analyses of whole rock standards during a period of 1 year. All data are well above detection limit.

D4 Thermal ionisation mass spectrometry (TIMS) data

Units are quoted where applicable. Sr and Nd isotopes were normalised to an NBS987 Sr standard value of 0.710220 and an J&M Nd standard value of 0.511836, respectively. Analytical errors are quoted as subscripts and refer to the last figures of a given value. Thus, 0.704569±10 is to be read 0.704569 ± 0.000010. For Sr and Nd isotopes, 1σ errors are quoted, all other errors are quoted as 2σ. For U, Th and Ba abundancies, errors are always much better then 1% (2σ). For U and Th isotopes, analytical errors are generally better than 1% (2σ). For Radium data, analytical errors are generally between 1% and 1.5% (2σ). All errors quoted are analytical errors and do not include reproducibility. Reproducibility is generally better then 1.5% (2σ), see Appendix A for details.

D5 Electron microprobe data

All major element oxide abundancies are quoted in wt%. For details on the precision and reproducibility of the analyses, see Appendix A.

D6 Ion microprobe data

All trace element data are quoted in parts per million (ppm). For details on the reproducibility of the analyses, see Appendix A.

Santorini

Major, trace and isotope data

Group		Nea Kameni	Nea Kameni	Nea Kameni	Nea Kameni	Nea Kameni
Age		49 a	58-59 a	59 a	59-60 a	60 a
Sample		dkl-1950	dki-1940	dkr-1940	dkf-1939	dkk-1939
XRF	2σ					
SiO_2	±0.5%	65.04	65.92	65.53	65.38	65.49
TiO_2	±2.5%	0.798	0.745	0.788	0.785	0.798
Al_2O_3	±0.7%	15.57	15.59	15.49	15.56	15.54
$Fe_2O_3^T$	±1.7%	5.86	5.32	5.68	5.71	5.66
MnO	±8%	0.150	0.143	0.148	0.148	0.146
MgO	±3.3%	1.54	1.28	1.39	1.40	1.37
CaO	±2.5%	4.10	3.79	3.90	3.95	3.91
Na_2O	±3.6%	4.90	5.05	4.98	4.98	4.97
K_2O	±4.5%	1.87	1.96	1.92	1.90	1.93
P_2O_5	±20%	0.181	0.185	0.182	0.179	0.184
LOI		0.11	0.12	0.05	0.11	0.06
XRF						
Rb	±1.5	63.1	67.2	65.3	65.7	64.6
Sr	±3	164	153	158	163	160
Y	±2.0	45.8	48.3	45.9	47.0	46.8
Zr	±3	215	228	220	222	217
Nb	±1.1	7.1	7.3	7.4	8.0	8.3
Ba	±15	371	373	362	368	361
Pb	±3	10	14	12	15	11
Th	±3	14	15	12	15	13
U	±2	4	4	4	4	6
Sc	±5	18	11	13	14	13
V	±8	60	40	49	53	48
Cr	±2	7	7	7	12	6
Co	±2	9	8	7	8	7
Ni	±3	4	2	[1]	3	2
Cu	±3	17	15	15	18	18
Zn	±3	80	84	76	78	76
Ga	±2	17	17	17	17	17
INAA						
La	±1.1	23.2				
Ce	±2.2	46.5				
Nd	±3.6	23.3				
Sm	±2.1	5.68				
Eu	±2.6	1.43				
Tb	±2.7	1.09				
Yb	±2.9	4.73				
Lu	±3.3	0.74				
Th	±2.4	11.4				
U	±17	3.5				
Ta	±5.6	0.57				
Hf	±2.5	5.40				
Cs	±7.6	1.68				
Rb						
Zn		84				
Co		7.6				
Cr		4				
Sc		15.8				

Group	Nea Kameni	Nea Kameni	Nea Kameni	Nea Kameni	Nea Kameni
Age	49 a	58-59 a	59 a	59-60 a	60 a
Sample	dkl-1950	dki-1940	dkr-1940	dkf-1939	dkk-1939
I.D.					
Ba	367.5	382.7	377.6	363.8	
Th	11.48	11.75	11.75	11.86	11.81
U	3.61	3.83	3.76	3.76	3.81
Isotopes					
$^{87}Sr/^{86}Sr$	0.704765	0.704721	0.704782	0.704754	0.704788
1σ	±10	±6	±10	±7	±5
$^{143}Nd/^{144}Nd$		0.512718	0.512750	0.512732	0.512731
1σ		±4	±4	±6	±6
$(^{234}U/^{238}U)$	1.006	1.004	1.006	1.004	1.006
2σ	±3	±3	±3	±2	±3
$(^{238}U/^{232}Th)$	0.953	0.990	0.970	0.963	0.979
2σ	±4	±7	±5	±9	±7
$(^{230}Th/^{232}Th)$	0.932	0.955	0.937	0.931	0.927
2σ	±9	±9	±7	±8	±11
$(^{230}Th/^{232}Th)_0$	0.932	0.955	0.937	0.931	0.927
2σ	±9	±9	±7	±8	±11
^{226}Ra	1.317	1.180	1.187	1.153	1.209
[ppt] 2σ	±17	±13	±7	±17	±19
$(^{230}Th)/Ba$	3737	3751	3746	3897	
[×1/μg/yr] 2σ	±39	±45	±33	±48	
$(^{226}Ra)/Ba$	4077	3508	3579	3607	
[×1/μg/yr] 2σ	±53	±38	±22	±54	
$(^{226}Ra)_0/Ba$	4084	3502	3575	3599	
[×1/μg/yr] 2σ	±54	±39	±22	±55	

Group		Nea Kameni	Nea Kameni	Nea Kameni	Nea Kameni	Nea Kameni
Age		73-74 a	129-133 a	133 a	289-292 a	429 a
Sample		dkd-1925	dkg-1866	dko-1866	dkn-1707	dkm-1570
XRF	2σ					
SiO_2	±0.5%	65.38	65.95	65.45	66.77	67.26
TiO_2	±2.5%	0.786	0.776	0.790	0.741	0.710
Al_2O_3	±0.7%	15.60	15.49	15.57	15.36	15.27
$Fe_2O_3^T$	±1.7%	5.68	5.47	5.68	5.08	4.88
MnO	±8%	0.149	0.149	0.149	0.146	0.139
MgO	±3.3%	1.40	1.28	1.38	1.10	1.01
CaO	±2.5%	3.91	3.73	3.92	3.40	3.24
Na_2O	±3.6%	4.99	5.04	4.97	5.19	5.21
K_2O	±4.5%	1.92	1.94	1.91	2.03	2.10
P_2O_5	±20%	0.180	0.183	0.179	0.187	0.183
LOI		0.10	0.15	0.08	0.12	0.23
XRF						
Rb	±1.5	63.3	66.0	65.0	68.4	69.3
Sr	±3	160	156	161	149	145
Y	±2.0	45.6	46.7	46.7	47.4	48.8
Zr	±3	218	225	220	234	240
Nb	±1.1	7.0	7.5	7.0	7.3	7.5
Ba	±15	365	363	367	402	399
Pb	±3	11	13	12	12	15
Th	±3	14	15	12	15	16
U	±2	5	4	[3]	5	[3]
Sc	±5	14	15	14	12	12
V	±8	47	41	48	21	28
Cr	±2	6	5	7	7	4
Co	±2	7	4	8	5	5
Ni	±3	2	2	4	[1]	3
Cu	±3	14	14	15	9	12
Zn	±3	79	77	77	78	77
Ga	±2	16	18	16	16	20
INAA						
La	±1.1		23.7		23.7	
Ce	±2.2		48.2		51.0	
Nd	±3.6		23.8		24.8	
Sm	±2.1		5.67		5.86	
Eu	±2.6		1.47		1.50	
Tb	±2.7		1.13		1.15	
Yb	±2.9		4.93		5.11	
Lu	±3.3		0.77		0.79	
Th	±2.4		12.0		12.5	
U	±17		3.7		3.9	
Ta	±5.6		0.60		0.63	
Hf	±2.5		5.63		5.84	
Cs	±7.6		1.81		1.83	
Rb					70	
Zn			82		74	
Co			5.8		4.5	
Cr			3		5	
Sc			14.4		13.5	

Group	Nea Kameni	Nea Kameni	Nea Kameni	Nea Kameni	Nea Kameni
Age	73-74 a	129-133 a	133 a	289-292 a	429 a
Sample	dkd-1925	dkg-1866	dko-1866	dkn-1707	dkm-1570
I.D.					
Ba		358.8			
Th	11.62	12.13	12.09	12.83	12.83
U	3.73	3.64	3.77	3.95	4.07
Isotopes					
$^{87}Sr/^{86}Sr$		0.704792	0.704735	0.704731	
1σ		±7	±10	±9	
$^{143}Nd/^{144}Nd$		0.512771	0.512752	0.512730	
1σ		±6	±5	±4	
$(^{234}U/^{238}U)$	1.003	1.006	1.003	1.007	1.005
2σ	±2	±3	±5	±4	±3
$(^{238}U/^{232}Th)$	0.975	0.909	0.946	0.933	0.962
2σ	±4	±9	±12	±7	±7
$(^{230}Th/^{232}Th)$	0.927	0.907	0.927	0.935	0.932
2σ	±8	±8	±9	±6	±6
$(^{230}Th/^{232}Th)_0$	0.927	0.907	0.927	0.935	0.932
2σ	±8	±8	±9	±6	±6
^{226}Ra	1.155				
[ppt] 2σ	±18				
$(^{230}Th)/Ba$					
[×1/μg/yr] 2σ					
$(^{226}Ra)/Ba$	3601				
[×1/μg/yr] 2σ	±57				
$(^{226}Ra)_0/Ba$					
[×1/μg/yr] 2σ					

Group		Palea Kameni	Palea Kameni	Palea Kameni	Kameni enclave
Age		1273 a	1273 a	1952-1953 a	49 a
Sample		dka-726AD	dka-A	dkt-46AD	k101dkl xa
XRF	2σ				
SiO_2	±0.5%	67.92	67.81	66.99	
TiO_2	±2.5%	0.671	0.674	0.709	
Al_2O_3	±0.7%	15.11	15.19	15.46	
$Fe_2O_3^T$	±1.7%	4.68	4.69	4.87	
MnO	±8%	0.133	0.131	0.137	
MgO	±3.3%	0.92	0.91	1.07	
CaO	±2.5%	3.01	3.06	3.38	
Na_2O	±3.6%	5.14	5.13	5.08	
K_2O	±4.5%	2.25	2.23	2.13	
P_2O_5	±20%	0.167	0.168	0.187	
LOI		0.23	0.13	0.07	
XRF					
Rb	±1.5	77.0	76.7	73.0	36.3
Sr	±3	134	137	148	219.2
Y	±2.0	49.9	50.0	47.2	36.2
Zr	±3	256	256	242	145
Nb	±1.1	8.2	8.1	8.2	5.3
Ba	±15	426	421	416	253
Pb	±3	15	14	13	7
Th	±3	16	16	13	8
U	±2	4	4	5	1
Sc	±5	9	9	12	19
V	±8	23	26	25	199
Cr	±2	5	9	4	10
Co	±2	4	3	5	19
Ni	±3	[1]	3	2	3
Cu	±3	18	20	12	31
Zn	±3	76	76	75	81
Ga	±2	17	17	17	20
INAA					
La	±1.1	26.4		25.2	
Ce	±2.2	55.1		52.0	
Nd	±3.6	26.9		25.8	
Sm	±2.1	6.30		5.98	
Eu	±2.6	1.50		1.46	
Tb	±2.7	1.19		1.14	
Yb	±2.9	5.33		4.99	
Lu	±3.3	0.82		0.78	
Th	±2.4	14.3		13.3	
U	±17	4.4		4.3	
Ta	±5.6	0.72		0.67	
Hf	±2.5	6.41		6.06	
Cs	±7.6	2.07		1.79	
Rb		81		74	
Zn		75		82	
Co		4.6		4.6	
Cr		6		6	
Sc		12.6		13.2	

Group	Palea Kameni	Palea Kameni	Palea Kameni	Kameni enclave
Age	1273 a	1273 a	1952-1953 a	49 a
Sample	dka-726AD	dka-A	dkt-46AD	k101dkl xa
I.D.				
Ba	420.9		415.8	
Th	13.88		12.90	
U	4.37		4.04	
Isotopes				
$^{87}Sr/^{86}Sr$	0.704738			
1σ *	±7			
$^{143}Nd/^{144}Nd$	0.512717		0.512747	
1σ	±5		±5	
$(^{234}U/^{238}U)$	1.005		1.002	
2σ	±3		±3	
$(^{238}U/^{232}Th)$	0.956		0.951	
2σ	±9		±4	
$(^{230}Th/^{232}Th)$	0.927		0.924	
2σ	±7		±8	
$(^{230}Th/^{232}Th)_0$	0.926		0.923	
2σ	±7		±8	
^{226}Ra	1.385		1.326	
[ppt] 2σ	±14		±16	
$(^{230}Th)/Ba$	3924		3678	
[x1/μg/yr] 2σ	±47		±35	
$(^{226}Ra)/Ba$	3745		3631	
[x1/μg/yr] 2σ	±36		±43	
$(^{226}Ra)_0/Ba$	3615		3569	
[x1/μg/yr] 2σ	±69		±108	

Group		Kameni enclave	Kameni enclave	Kameni enclave	Kameni enclave	Kameni enclave
Age		49 a	59-60 a	73-74 a	289-292 a	1952-1953 a
Sample		k107dkl xa	k78dkf xb	k97dkd xg	k103dkn xb	k35dkt xa
XRF	2σ					
SiO_2	±0.5%	54.79	55.15	50.63	52.93	53.24
TiO_2	±2.5%	1.239	1.076	0.995	0.955	1.004
Al_2O_3	±0.7%	16.68	16.85	19.68	18.27	17.01
$Fe_2O_3^T$	±1.7%	10.57	9.89	9.87	9.43	9.88
MnO	±8%	0.188	0.182	0.160	0.167	0.178
MgO	±3.3%	3.84	4.15	4.34	4.74	5.01
CaO	±2.5%	8.27	8.61	11.33	10.04	9.99
Na_2O	±3.6%	3.74	3.59	2.78	3.05	3.10
K_2O	±4.5%	0.74	0.83	0.44	0.63	0.69
P_2O_5	±20%	0.125	0.123	0.079	0.098	0.104
LOI		-0.19	-0.45	-0.31	-0.31	-0.21
XRF						
Rb	±1.5	21.5	23.8	11.8	17.1	18.7
Sr	±3	238	223	259	230	222.9
Y	±2.0	32.3	31.4	21.9	26.2	27.0
Zr	±3	106	104	62	87	83
Nb	±1.1	4.2	4.0	3.0	3.3	3.5
Ba	±15	186	189	112	151	143
Pb	±3	4	3	4	4	2
Th	±3	4	5	2	3	3
U	±2	2	2	1	2	0
Sc	±5	30	28	31	31	36
V	±8	307	273	323	261	295
Cr	±2	11	17	22	25	22
Co	±2	25	27	28	29	29
Ni	±3	8	12	10	14	13
Cu	±3	71	35	59	58	16
Zn	±3	76	74	60	65	70
Ga	±2	20	19	19	18	16
iNAA						
La	±1.1					
Ce	±2.2					
Nd	±3.6					
Sm	±2.1					
Eu	±2.6					
Tb	±2.7					
Yb	±2.9					
Lu	±3.3					
Th	±2.4					
U	±17					
Ta	±5.6					
Hf	±2.5					
Cs	±7.6					
Rb						
Zn						
Co						
Cr						
Sc						

Group	Kameni enclave	Kameni enclave	Kameni enclave	Kameni enclave	Kameni enclave
Age	49 a	59-60 a	73-74 a	289-292 a	1952-1953 a
Sample	k107dkl xa	k78dkf xb	k97dkd xg	k103dkn xb	k35dkt xa
I.D.					
Ba					
Th	3.34	3.49			2.51
U	1.11	1.19			0.774
Isotopes					
$^{87}Sr/^{86}Sr$ 1σ					
$^{143}Nd/^{144}Nd$ 1σ					
$(^{234}U/^{238}U)$ 2σ	1.004 ±6	1.004 ±5			1.007 ±5
$(^{238}U/^{232}Th)$ 2σ	1.004 ±3	1.038 ±4			0.937 ±3
$(^{230}Th/^{232}Th)$ 2σ	0.964 ±8	0.993 ±9			0.942 ±11
$(^{230}Th/^{232}Th)_0$ 2σ	0.964 ±8	0.993 ±9			0.942 ±11
^{226}Ra [ppt] 2σ					
$(^{230}Th)/Ba$ [×1/μg/yr] 2σ					
$(^{226}Ra)/Ba$ [×1/μg/yr] 2σ					
$(^{226}Ra)_0/Ba$ [×1/μg/yr] 2σ					

Group		SEC	SEC	SEC	SEC	SEC
Age		3.6 ka	3.6 ka	3.6 ka	>21 ka, <50 ka	>21 ka, <50 ka
Sample		rp7b	rp7a-2	rp7a-1	ao-Ola	rt
XRF	2σ					
SiO_2	±0.5%	64.59	70.47	70.92	57.09	68.34
TiO_2	±2.5%	0.836	0.410	0.404	1.223	0.584
Al_2O_3	±0.7%	15.66	14.73	14.54	15.70	15.03
$Fe_2O_3^T$	±1.7%	6.02	3.18	3.10	10.07	4.52
MnO	±8%	0.156	0.087	0.085	0.171	0.116
MgO	±3.3%	1.37	0.66	0.59	3.37	0.67
CaO	±2.5%	3.75	2.30	2.21	7.23	2.44
Na_2O	±3.6%	4.94	4.95	4.95	3.51	5.06
K_2O	±4.5%	2.47	3.13	3.12	1.45	3.09
P_2O_5	±20%	0.214	0.079	0.082	0.181	0.139
LOI		1.86	3.28	3.18	-0.26	0.11
XRF						
Rb	±1.5	94.0	98.4	103.4	57.1	108.7
Sr	±3	146	95	91	181	109
Y	±2.0	52.6	42.6	44.2	42.7	56.9
Zr	±3	282	301	314	195	352
Nb	±1.1	10.5	8.1	10.0	6.6	12.2
Ba	±15	366	511	531	250	524
Pb	±3	16	18	19	9	16
Th	±3	16	20	21	13	20
U	±2	6	6	6	[3]	5
Sc	±5	14	6	7	31	12
V	±8	37	16	15	307	9
Cr	±2	5	[3]	6	11	7
Co	±2	10	4	3	27	4
Ni	±3	4	[1]	2	10	2
Cu	±3	13	12	14	87	14
Zn	±3	94	47	48	96	73
Ga	±2	18	14	14	20	16
INAA						
La	±1.1	26.0	28.7		17.1	33.5
Ce	±2.2	55.6	58.6		37.4	72.9
Nd	±3.6	28.2	24.9		20.7	34.9
Sm	±2.1	6.84	5.67		5.40	7.47
Eu	±2.6	1.58	1.02		1.35	1.53
Tb	±2.7	1.33	1.02		1.06	1.39
Yb	±2.9	5.59	5.03		4.25	6.29
Lu	±3.3	0.86	0.76		0.68	0.98
Th	±2.4	15.9	18.0		9.9	17.8
U	±17	4.6	5.4		3.3	5.5
Ta	±5.6	0.80	0.83		0.49	0.97
Hf	±2.5	7.06	7.50		5.01	8.69
Cs	±7.6	2.92	2.69		1.43	2.95
Rb		97	99		70	105
Zn		88	48		94	71
Co		6.4	3.9		22.3	3.3
Cr		5	6		10	7
Sc		15.4	5.3		31.0	12.1

Group	SEC	SEC	SEC	SEC	SEC
Age	3.6 ka	3.6 ka	3.6 ka	>21 ka, <50 ka	>21 ka, <50 ka
Sample	rp7b	rp7a-2	rp7a-1	ao-Ola	rt
I.D.					
Ba					
Th		16.94		9.71	18.13
U		5.23		3.11	5.45
Isotopes					
$^{87}Sr/^{86}Sr$		0.705147		0.704457	0.705079
1σ		±10		±10	±9
$^{143}Nd/^{144}Nd$		0.512715		0.512756	0.512718
1σ		±6		±7	±7
$(^{234}U/^{238}U)$		1.005		1.011	1.006
2σ		±3		±5	±3
$(^{238}U/^{232}Th)$		0.937		0.971	0.911
2σ		±4		±5	±5
$(^{230}Th/^{232}Th)$		0.936		0.970	0.904
2σ		±8		±11	±6
$(^{230}Th/^{232}Th)_0$		0.936		0.969	0.901
2σ		±8		±15	±10
^{226}Ra		1.773			
[ppt] 2σ		±29			
$(^{230}Th)/Ba$		3983			
[x1/μg/yr] 2σ		±37			
$(^{226}Ra)/Ba$		3949			
[x1/μg/yr] 2σ		±64			
$(^{226}Ra)_0/Ba$					
[x1/μg/yr] 2σ					

Group		SEC	SEC	SEC	SEC	SEC
Age		54±3 ka	54±3 ka	54±3 ka	54±3 ka	67±9 ka
Sample		ap5-Nod-Ola	ap5-Sk	ap5-nip-B	ap5-nip-A	as2-up-Ola
XRF	2σ					
SiO_2	±0.5%	52.45	58.94	66.62	66.66	53.10
TiO_2	±2.5%	0.684	1.218	0.742	0.749	0.819
Al_2O_3	±0.7%	17.39	16.08	15.44	15.40	18.50
$Fe_2O_3^T$	±1.7%	8.69	8.90	5.04	5.08	8.35
MnO	±8%	0.146	0.166	0.127	0.128	0.148
MgO	±3.3%	6.56	2.61	0.97	0.97	5.07
CaO	±2.5%	10.82	6.13	3.03	3.03	10.29
Na_2O	±3.6%	2.54	4.08	5.07	5.04	2.83
K_2O	±4.5%	0.65	1.65	2.75	2.73	0.78
P_2O_5	±20%	0.077	0.223	0.204	0.206	0.110
LOI		-0.02	-0.12	0.15	0.15	-0.05
XRF						
Rb	±1.5	8.8	63.4	97.1	94.8	27.5
Sr	±3	407	187	134	133	205.1
Y	±2.0	16.3	45.1	56.0	55.4	26.6
Zr	±3	58	202	315	311	101
Nb	±1.1	1.7	6.4	11.4	11.0	3.0
Ba	±15	142	246	491	495	137
Pb	±3	5	11	17	17	3
Th	±3	[2]	10	20	16	7.
U	±2	[1]	4	5	4	[1]
Sc	±5	37	25	12	12	36
V	±8	244	191	21	21	226
Cr	±2	61	5	7	11	38
Co	±2	38	19	6	5	30
Ni	±3	38	4	3	3	25
Cu	±3	103	14	14	15	79
Zn	±3	69	100	77	75	70
Ga	±2	17	17	17	16	16
INAA						
La	±1.1	5.7	19.3		30.1	
Ce	±2.2	12.6	40.5		64.9	
Nd	±3.6	7.8	22.8		32.6	
Sm	±2.1	2.26	5.78		7.48	
Eu	±2.6	0.82	1.47		1.58	
Tb	±2.7	0.46	1.10		1.34	
Yb	±2.9	1.68	4.44		5.86	
Lu	±3.3	0.26	0.71		0.91	
Th	±2.4	1.3	10.9		15.6	
U	±17	0.6	3.6		4.6	
Ta	±5.6	0.12	0.56		0.88	
Hf	±2.5	1.67	5.19		7.69	
Cs	±7.6		1.21		2.80	
Rb						
Zn		71	95		72	
Co		32.7	14.5		4.4	
Cr		50	7		4	
Sc		35.9	23.8		13.7	

Group	SEC	SEC	SEC	SEC	SEC
Age	54±3 ka	54±3 ka	54±3 ka	54±3 ka	67±9 ka
Sample	ap5-Nod-Ola	ap5-Sk	ap5-nip-B	ap5-nip-A	as2-up-Ola
I.D.					
Ba					
Th	1.14				
U	0.48				
Isotopes					
$^{87}Sr/^{86}Sr$ 1σ	0.703595 ±10	0.704371 ±9	0.705003 ±8	0.705034 ±9	
$^{143}Nd/^{144}Nd$ 1σ	0.512849 ±6	0.512787 ±7	0.512728 ±7	0.512721 ±5	
$(^{234}U/^{238}U)$ 2σ				0.999 ±5	
$(^{238}U/^{232}Th)$ 2σ				0.889 ±4	
$(^{230}Th/^{232}Th)$ 2σ				0.888 ±9	
$(^{230}Th/^{232}Th)_0$ 2σ				0.887 ±14	
^{226}Ra [ppt] 2σ					
$(^{230}Th)/Ba$ [×1/μg/yr] 2σ					
$(^{226}Ra)/Ba$ [×1/μg/yr] 2σ					
$(^{226}Ra)_0/Ba$ [×1/μg/yr] 2σ					

Group		SEC	SEC	SEC	SEC	SEC
Age		67±9 ka	67±9 ka	67±9 ka	67±9 ka	85 (+22/-19) ka
Sample		as2-Sk	as2-Oia-3	as2-Oia-2	as2-Oia-1	ds1
XRF	2σ					
SiO_2	±0.5%	54.26	63.24	52.49	53.18	63.26
TiO_2	±2.5%	1.220	0.922	0.768	0.804	0.844
Al_2O_3	±0.7%	16.33	15.76	18.91	18.65	16.10
$Fe_2O_3^T$	±1.7%	9.76	6.84	8.35	8.31	6.46
MnO	±8%	0.162	0.166	0.154	0.148	0.134
MgO	±3.3%	4.81	1.53	4.83	4.94	1.70
CaO	±2.5%	8.95	4.38	10.87	10.36	4.61
Na_2O	±3.6%	3.10	4.81	2.97	2.73	4.62
K_2O	±4.5%	1.21	2.11	0.56	0.78	2.06
P_2O_5	±20%	0.188	0.245	0.098	0.109	0.210
LOI		0.03	0.55	0.20	-0.11	0.12
XRF						
Rb	±1.5	48.6	70.8	15.7	25.6	66.2
Sr	±3	183	198	228	207	175.9
Y	±2.0	40.1	50.7	24.2	26.5	47.1
Zr	±3	173	239	79	101	232
Nb	±1.1	4.2	8.1	2.9	2.9	9.5
Ba	±15	195	350	123	134	357
Pb	±3	8	14	7	7	11
Th	±3	9	15	4	5	11
U	±2	[2]	5	[0]	[2]	5
Sc	±5	33	18	32	35	16
V	±8	286	51	209	239	72
Cr	±2	90	8	32	42	12
Co	±2	29	8	26	26	11
Ni	±3	35	2	17	26	3
Cu	±3	119	25	64	82	37
Zn	±3	84	94	67	69	66
Ga	±2	17	17	16	18	18
INAA						
La	±1.1	15.2			9.8	
Ce	±2.2	33.7			19.3	
Nd	±3.6	18.6			11.0	
Sm	±2.1	5.02			3.13	
Eu	±2.6	1.32			0.91	
Tb	±2.7	0.97			0.63	
Yb	±2.9	4.01			2.61	
Lu	±3.3	0.63			0.40	
Th	±2.4	8.1			4.5	
U	±17	2.5			1.6	
Ta	±5.6	0.44			0.24	
Hf	±2.5	4.40			2.50	
Cs	±7.6	1.25			0.66	
Rb		59				
Zn		97			82	
Co		26.1			25.5	
Cr		93			44	
Sc		34.4			33.1	

Group	SEC	SEC	SEC	SEC	SEC
Age	67±9 ka	67±9 ka	67±9 ka	67±9 ka	85 (+22/-19) ka
Sample	as2-Sk	as2-Ola-3	as2-Ola-2	as2-Ola-1	ds1
I.D.					
Ba					
Th				4.51	12.26
U				1.42	3.88
Isotopes					
$^{87}Sr/^{86}Sr$ 1σ				0.704012 ±11	
$^{143}Nd/^{144}Nd$ 1σ				0.512817 ±8	
$(^{234}U/^{238}U)$ 2σ				0.990 ±3	1.007 ±5
$(^{238}U/^{232}Th)$ 2σ				0.955 ±4	0.960 ±6
$(^{230}Th/^{232}Th)$ 2σ				0.950 ±5	0.962 ±8
$(^{230}Th/^{232}Th)_0$ 2σ				0.946 ±10	0.964 ±16
^{226}Ra [ppt] 2σ					
$(^{230}Th)/Ba$ [×1/µg/yr] 2σ					
$(^{226}Ra)/Ba$ [×1/µg/yr] 2σ					
$(^{226}Ra)_0/Ba$ [×1/µg/yr] 2σ					

Group		SEC	SEC
Age		~100 ka	172±4 ka
Sample		ap4	as
XRF	2σ		
SiO_2	±0.5%	64.75	58.96
TiO_2	±2.5%	0.843	1.253
Al_2O_3	±0.7%	15.56	15.74
$Fe_2O_3^T$	±1.7%	6.02	8.82
MnO	±8%	0.154	0.152
MgO	±3.3%	1.35	2.76
CaO	±2.5%	3.70	6.02
Na_2O	±3.6%	4.84	3.95
K_2O	±4.5%	2.56	2.09
P_2O_5	±20%	0.215	0.242
LOI		2.46	0.29
XRF			
Rb	±1.5	94.3	74.6
Sr	±3	147	174
Y	±2.0	52.6	45.9
Zr	±3	283	233
Nb	±1.1	9.8	11.4
Ba	±15	369	313
Pb	±3	18	12
Th	±3	17	14
U	±2	5	6
Sc	±5	14	26
V	±8	40	211
Cr	±2	5	30
Co	±2	7	20
Ni	±3	2	12
Cu	±3	10	37
Zn	±3	93	89
Ga	±2	15	18
INAA			
La	±1.1	25.6	
Ce	±2.2	54.0	
Nd	±3.6	27.4	
Sm	±2.1	6.76	
Eu	±2.6	1.53	
Tb	±2.7	1.22	
Yb	±2.9	5.41	
Lu	±3.3	0.83	
Th	±2.4	15.5	
U	±17	4.8	
Ta	±5.6	0.76	
Hf	±2.5	6.82	
Cs	±7.6	2.89	
Rb		92	
Zn		88	
Co		5.5	
Cr		4	
Sc		15.1	

Group	SEC	SEC
Age	~100 ka	172±4 ka
Sample	ap4	as
I.D.		
Ba		
Th	15.50	12.63
U	4.87	4.06
Isotopes		
$^{87}Sr/^{86}Sr$ 1σ	0.704454 ±10	
$^{143}Nd/^{144}Nd$ 1σ	0.512783 ±6	
$(^{234}U/^{238}U)$ 2σ	1.009 ±5	1.002 ±3
$(^{238}U/^{232}Th)$ 2σ	0.954 ±5	0.974 ±7
$(^{230}Th/^{232}Th)$ 2σ	0.965 ±11	0.961 ±8
$(^{230}Th/^{232}Th)_0$ 2σ	0.981 ±29	0.909 ±48
^{226}Ra [ppt] 2σ		
$(^{230}Th)/Ba$ [×1/μg/yr] 2σ		
$(^{226}Ra)/Ba$ [×1/μg/yr] 2σ		
$(^{226}Ra)_0/Ba$ [×1/μg/yr] 2σ		

Group		FEC	Peristeria	Peristeria	Peristeria	Akrotiri
Age		>220 ka	>300 ka	>300 ka	>300 ka	>320 ka
Sample		rp1	av3-S	av3-Sk	av3-a	apa
XRF	2σ					
SiO_2	±0.5%	54.50	61.91	61.28	57.32	54.49
TiO_2	±2.5%	0.759	0.656	1.043	0.813	0.856
Al_2O_3	±0.7%	17.13	18.04	16.53	17.17	17.24
$Fe_2O_3^T$	±1.7%	7.92	5.28	7.10	7.20	8.17
MnO	±8%	0.139	0.104	0.162	0.129	0.148
MgO	±3.3%	5.51	1.47	1.71	3.90	5.67
CaO	±2.5%	9.93	5.29	4.32	7.54	9.07
Na_2O	±3.6%	2.75	4.26	4.84	3.49	2.98
K_2O	±4.5%	1.26	2.83	2.74	2.27	1.24
P_2O_5	±20%	0.107	0.165	0.279	0.158	0.133
LOI		0.63	0.19	1.29	0.04	0.15
XRF						
Rb	±1.5	46.3	101.7	89.5	79.2	44.7
Sr	±3	210	236	211	264	182.9
Y	±2.0	25.4	36.0	47.4	31.6	30.3
Zr	±3	125	232	283	207	141
Nb	±1.1	5.4	10.3	11.9	10.0	5.6
Ba	±15	246	532	508	426	225
Pb	±3	8	21	16	18	9
Th	±3	8	20	16	16	9
U	±2	[2]	5	4	4	3
Sc	±5	30	8	14	20	30
V	±8	214	64	54	155	204
Cr	±2	74	6	6	52	100
Co	±2	27	11	8	21	29
Ni	±3	34	7	3	22	44
Cu	±3	62	27	19	24	64
Zn	±3	68	56	91	68	74
Ga	±2	16	16	19	17	17
INAA						
La	±1.1		35.5		30.6	16.2
Ce	±2.2		70.6		59.3	32.9
Nd	±3.6		28.7		25.0	16.5
Sm	±2.1		5.88		5.25	3.96
Eu	±2.6		1.24		1.14	1.06
Tb	±2.7		0.93		0.84	0.79
Yb	±2.9		3.78		3.21	3.10
Lu	±3.3		0.57		0.49	0.47
Th	±2.4		17.2		13.4	7.4
U	±17		4.5		3.6	2.3
Ta	±5.6		0.85		0.73	0.43
Hf	±2.5		5.70		4.91	3.48
Cs	±7.6		1.59		2.52	1.38
Rb			96		83	49
Zn			60		75	76
Co			10.9		20.5	25.7
Cr			6		58	103
Sc			10.4		21.0	30.5

Group	FEC	Peristeria	Peristeria	Peristeria	Akrotiri
Age	>220 ka	>300 ka	>300 ka	>300 ka	>320 ka
Sample	rp1	av3-S	av3-Sk	av3-a	apa
I.D.					
Ba					
Th					
U					
Isotopes					
$^{87}Sr/^{86}Sr$ 1σ *		0.706341 ±10	0.704731 ±10		0.704569 ±10
$^{143}Nd/^{144}Nd$ 1σ		0.512578 ±7	0.512612 ±6		0.512702 ±8
$(^{234}U/^{238}U)$ 2σ					
$(^{238}U/^{232}Th)$ 2σ					
$(^{230}Th/^{232}Th)$ 2σ					
$(^{230}Th/^{232}Th)_0$ 2σ					
^{226}Ra [ppt] 2σ					
$(^{230}Th)/Ba$ [×1/μg/yr] 2σ					
$(^{226}Ra)/Ba$ [×1/μg/yr] 2σ					
$(^{226}Ra)_0/Ba$ [×1/μg/yr] 2σ					

Group	Nea Kameni	NK separate	NK separate	NK separate	NK separate
Age	59 a	59 a	59 a	59 a	59 a
Sample	dkr-WR	dkr-mt	dkr-px	dkr-plag	dkr-gm
I.D.					
Ba					
Th	11.75	1.97	0.775	0.102	13.48
U	3.76	0.666	0.247	0.034	4.25
Isotopes					
$^{87}Sr/^{86}Sr$					
1σ					
$^{143}Nd/^{144}Nd$					
1σ					
$(^{234}U/^{238}U)$	1.006	1.000	1.008	1.002	1.005
2σ	±3	±3	±4	±5	±3
$(^{238}U/^{232}Th)$	0.970	1.024	0.965	0.998	0.957
2σ	±5	±7	±8	±10	±6
$(^{230}Th/^{232}Th)$	0.937	0.940	0.932	0.921	0.924
2σ	±7	±9	±11	±14	±8

Group	NK separate	SEC	SEC separate	SEC separate
Age	129-133 a	85 (+22/-19) ka	85 (+22/-19) ka	85 (+22/-19) ka
Sample	dkg-plag	ds1-WR	ds1-plag	ds1-mt
I.D.				
Ba	112.8			
Th		12.26	0.257	1.42
U		3.88	0.083	0.486
Isotopes				
$^{87}Sr/^{86}Sr$				
1σ				
$^{143}Nd/^{144}Nd$				
1σ				
$(^{234}U/^{238}U)$		1.007	1.021	1.018
2σ		±5	±9	±8
$(^{238}U/^{232}Th)$		0.960	0.980	1.037
2σ		±6	±5	±5
$(^{230}Th/^{232}Th)$		0.962	0.966	1.003
2σ		±8	±10	±10

Nisyros

Major, trace and isotope data

Group		PCD inclusion	PCD inclusion	PCD inclusion	PCD	PCD
Age		<10 ka	<10 ka	<10 ka	<10 ka	<10 ka
Sample		PCD6-i	PCD5-i	PCD3-i	PCD6	PCD5
XRF	2σ					
SiO_2	±0.5%	54.75	54.19	55.63	68.29	67.03
TiO_2	±2.5%	0.747	0.745	0.716	0.406	0.413
Al_2O_3	±0.7%	18.83	19.71	19.38	15.71	16.23
$Fe_2O_3^T$	±1.7%	5.98	6.09	5.88	3.10	3.23
MnO	±8%	0.096	0.095	0.096	0.066	0.067
MgO	±3.3%	4.45	5.06	4.67	1.48	1.75
CaO	±2.5%	8.96	9.77	9.01	3.87	4.39
Na_2O	±3.6%	4.92	3.29	3.35	4.24	4.22
K_2O	±4.5%	1.08	0.89	1.09	2.73	2.57
P_2O_5	±20%	0.192	0.172	0.171	0.107	0.098
LOI		0.65	0.37	0.43	0.51	0.46
XRF						
Rb	±1.5	14.6	12.9	20.7	82.5	76.3
Sr	±3	966	984	913	416.9	457
Y	±2.0	18.7	16.8	16.9	15.3	14.7
Zr	±3	119	108	113	164	163
Nb	±1.1	7.8	6.8	7.3	12.7	11.4
Ba	±15	269	245	305	632	626
Pb	±3	6	3	13	10	11
Th	±3	[2]	3	3	11	10
U	±2	[2]	4	[2]	4	4
Sc	±5	11	18	14	6	5
V	±8	140	148	124	48	53
Cr	±2	13	16	16	8	9
Co	±2	21	24	21	6	7
Ni	±3	19	28	26	7	8
Cu	±3	21	21	17	12	12
Zn	±3	51	45	60	37	37
Ga	±2	18	18	18	14	13
INAA						
La	±1.1		14.0			27.1
Ce	±2.2		28.6			46.7
Nd	±3.6		15.1			16.1
Sm	±2.1		3.37			3.00
Eu	±2.6		1.10			0.75
Tb	±2.7		0.52			0.39
Yb	±2.9		1.60			1.67
Lu	±3.3		0.24			0.27
Th	±2.4		1.8			9.3
U	±17					2.6
Ta	±5.6		0.33			0.93
Hf	±2.5		2.72			3.81
Cs	±7.6		0.30			2.71
Rb			17			73
Zn			72			38
Co			20.6			7.6
Cr			19			6
Sc			17.2			6.8

Group		PCD	PCD	PCD	Caldera pyrocl.	CP inclusion
Age		<10 ka	<10 ka	<10 ka	?	?
Sample		PCD4	PCD3	PCD2	UP	NR-i-2
XRF	2σ					
SiO_2	±0.5%	70.63	70.34	66.28	72.04	71.86
TiO_2	±2.5%	0.368	0.369	0.429	0.333	0.333
Al_2O_3	±0.7%	14.75	14.98	16.54	14.38	14.62
$Fe_2O_3^T$	±1.7%	2.79	2.73	3.44	2.48	2.48
MnO	±8%	0.064	0.063	0.070	0.069	0.069
MgO	±3.3%	1.12	1.09	1.87	0.57	0.57
CaO	±2.5%	2.92	3.02	4.62	1.90	1.98
Na_2O	±3.6%	4.11	4.19	4.20	4.54	4.64
K_2O	±4.5%	3.14	3.11	2.45	3.60	3.36
P_2O_5	±20%	0.095	0.090	0.107	0.083	0.077
LOI		0.28	0.73	0.32	3.26	0.88
XRF						
Rb	±1.5	95.7	95.4	70.8	96.0	101.2
Sr	±3	309	319	491	199	213
Y	±2.0	15.5	15.5	13.8	18.8	17.9
Zr	±3	189	186	160	249	240
Nb	±1.1	14.0	14.2	11.9	16.6	17.1
Ba	±15	727	709	597	754	768
Pb	±3	13	12	13	15	15
Th	±3	11	11	9	12	12
U	±2	4	[3]	[3]	5	4
Sc	±5	[4]	[3]	6	[3]	[2]
V	±8	40	32	57	16	21
Cr	±2	8	5	12	4	7
Co	±2	6	6	10	3	3
Ni	±3	5	6	9	3	4
Cu	±3	7	11	14	6	4
Zn	±3	33	32	39	43	41
Ga	±2	14	14	16	14	14
INAA						
La	±1.1	30.2				
Ce	±2.2	52.2				
Nd	±3.6	17.0				
Sm	±2.1	3.14				
Eu	±2.6	0.61				
Tb	±2.7	0.40				
Yb	±2.9	1.85				
Lu	±3.3	0.29				
Th	±2.4	12.0				
U	±17	3.3				
Ta	±5.6	1.19				
Hf	±2.5	4.64				
Cs	±7.6	2.37				
Rb		92				
Zn		34				
Co		5.0				
Cr		6				
Sc		4.8				

Group		CP inclusion	Caldera pyrocl.	CP inclusion	CP inclusion	CP inclusion
Age		?	?	?	?	?
Sample		NR-i-1	NR	LP-i-2	LP-i-1b	LP-i-1a
XRF	2σ					
SiO_2	±0.5%	71.66	70.62	55.54	59.62	70.16
TiO_2	±2.5%	0.344	0.353	0.882	0.682	0.342
Al_2O_3	±0.7%	14.68	15.04	18.51	17.18	15.65
$Fe_2O_3^T$	±1.7%	2.57	2.74	7.73	2.98	1.24
MnO	±8%	0.075	0.072	0.132	0.049	0.018
MgO	±3.3%	0.64	0.80	3.98	3.07	0.94
CaO	±2.5%	2.07	2.50	7.70	10.36	5.70
Na_2O	±3.6%	4.58	4.61	3.73	5.55	5.51
K_2O	±4.5%	3.32	3.18	1.57	0.35	0.33
P_2O_5	±20%	0.062	0.078	0.219	0.159	0.097
LOI		1.51	1.85	0.82	0.12	0.15
XRF						
Rb	±1.5	96.4	91.8	32.2	2.0	2.0
Sr	±3	225	257	674	497	445.5
Y	±2.0	18.7	16.9	21.2	21.6	12.9
Zr	±3	235	222	130	118	195
Nb	±1.1	15.7	15.3	9.6	12.6	8.1
Ba	±15	808	751	434	193	217
Pb	±3	15	15	6	0	4
Th	±3	12	10	4	[2]	7
U	±2	[3]	4	[2]	[1]	[2]
Sc	±5	[2]	[1]	17	12	[1]
V	±8	20	25	163	87	33
Cr	±2	11	5	6	20	7
Co	±2	3	3	24	7	[2]
Ni	±3	4	3	8	8	3
Cu	±3	5	5	19	6	8
Zn	±3	39	39	55	14	11
Ga	±2	14	15	17	17	16
INAA						
La	±1.1					
Ce	±2.2					
Nd	±3.6					
Sm	±2.1					
Eu	±2.6					
Tb	±2.7					
Yb	±2.9					
Lu	±3.5					
Th	±2.4					
U	±17					
Ta	±5.6					
Hf	±2.5					
Cs	±7.6					
Rb						
Zn						
Co						
Cr						
Sc						

Group		Caldera pyrocl.	Upper lavas	Upper lavas	Upper lavas	Upper lavas
Age		?	>24 ka, <38 ka	>24 ka, <38 ka	>24 ka, <38 ka	>24 ka, <38 ka
Sample		LP	UDL-c	UDL-b	UDL-a	SP-III
XRF	2σ					
SiO_2	±0.5%	70.83	66.73	66.78	66.81	66.99
TiO_2	±2.5%	0.352	0.632	0.627	0.620	0.645
Al_2O_3	±0.7%	14.90	15.86	15.90	15.85	15.46
$Fe_2O_3^T$	±1.7%	2.62	4.23	4.15	4.18	4.22
MnO	±8%	0.064	0.089	0.089	0.090	0.086
MgO	±3.3%	0.80	1.26	1.24	1.24	1.53
CaO	±2.5%	2.61	3.48	3.43	3.37	3.71
Na_2O	±3.6%	4.43	4.50	4.48	4.49	4.31
K_2O	±4.5%	3.31	3.05	3.13	3.17	2.88
P_2O_5	±20%	0.084	0.183	0.175	0.176	0.160
LOI		2.34	-0.04	1.25	0.92	0.73
XRF						
Rb	±1.5	96.3	88.2	88.0	88.1	82.5
Sr	±3	258	311	308	302	286
Y	±2.0	16.9	25.6	24.1	23.7	19.9
Zr	±3	206	243	235	240	168
Nb	±1.1	15.0	18.3	17.8	17.5	15.1
Ba	±15	741	757	714	716	692
Pb	±3	15	8	12	12	9
Th	±3	13	12	12	9	12
U	±2	4	4	5	5	[3]
Sc	±5	[4]	6	7	7	6
V	±8	23	58	49	52	90
Cr	±2	5	9	8	8	14
Co	±2	4	7	6	5	10
Ni	±3	2	4	4	4	6
Cu	±3	5	9	8	9	15
Zn	±3	38	42	46	46	45
Ga	±2	13	17	16	16	15
INAA						
La	±1.1		35.3			
Ce	±2.2		62.1			
Nd	±3.6		23.7			
Sm	±2.1		4.57			
Eu	±2.6		1.02			
Tb	±2.7		0.68			
Yb	±2.9		2.71			
Lu	±3.3		0.42			
Th	±2.4		11.4			
U	±17		3.7			
Ta	±5.6		1.30			
Hf	±2.5		5.47			
Cs	±7.6		1.65			
Rb			83			
Zn			44			
Co			6.3			
Cr			6			
Sc			7.9			

Group		Upper lavas	Upper lavas	Obsidian	Obsidian	Upper lavas
Age		>24 ka, <38 ka	>24 ka, <38 ka	>24 ka, <38 ka	>24 ka, <38 ka	>24 ka, <38 ka
Sample		UAL-Av.	UAL-d	obs-p	obs-c	UAL-c
XRF	2σ					
SiO_2	±0.5%	54.94	57.99	58.69	57.78	58.73
TiO_2	±2.5%	0.922	1.067	1.113	1.055	1.112
Al_2O_3	±0.7%	18.50	17.21	17.32	17.55	17.41
$Fe_2O_3^T$	±1.7%	7.11	7.42	7.11	7.05	7.16
MnO	±8%	0.124	0.127	0.125	0.125	0.124
MgO	±3.3%	4.59	3.39	2.82	2.97	2.73
CaO	±2.5%	8.90	6.88	6.54	6.97	6.55
Na_2O	±3.6%	3.56	4.03	4.23	4.57	4.10
K_2O	±4.5%	1.14	1.65	1.80	1.70	1.82
P_2O_5	±20%	0.214	0.245	0.249	0.233	0.249
LOI		-0.2	-0.19	-0.2	-0.27	-0.01
XRF						
Rb	±1.5	28.3	43.2	52.4	48.8	48.7
Sr	±3	479.9	397	377	389	377.4
Y	±2.0	24.8	29.2	29.5	28.0	31.1
Zr	±3	141	175	187	176	182
Nb	±1.1	10.5	13.6	14.5	13.4	14.2
Ba	±15	311	421	431	418	473
Pb	±3	6	9	9	8	9
Th	±3	4	7	5	7	6
U	±2	[2]	[3]	[2]	[3]	[2]
Sc	±5	21	23	20	23	22
V	±8	187	213	211	216	222
Cr	±2	46	11	17	16	9
Co	±2	23	20	17	18	17
Ni	±3	31	9	8	7	8
Cu	±3	33	43	48	43	51
Zn	±3	68	68	75	73	73
Ga	±2	17	18	18	19	19
INAA						
La	±1.1	18.8				
Ce	±2.2	38.2				
Nd	±3.6	18.6				
Sm	±2.1	3.97				
Eu	±2.6	1.17				
Tb	±2.7	0.66				
Yb	±2.9	2.40				
Lu	±3.3	0.37				
Th	±2.4	3.6				
U	±17	1.1				
Ta	±5.6	0.66				
Hf	±2.5	3.26				
Cs	±7.6	1.00				
Rb		43				
Zn		67				
Co		20.6				
Cr		41				
Sc		21.0				

Group		Upper lavas	MDL inclusion	MDL inclusion	Middle lavas	Middle lavas
Age		>24 ka, <38 ka	38±2 ka	38±2 ka	?	38±2 ka
Sample		**UAL-b**	**MDL-i-2**	**MDL-i-1**	**And-PK**	**MDL-PK**
XRF	2σ					
SiO_2	±0.5%	58.85	46.86	64.60	58.71	58.54
TiO_2	±2.5%	1.107	0.678	0.505	1.111	1.084
Al_2O_3	±0.7%	17.35	15.20	16.80	17.36	17.36
$Fe_2O_3^T$	±1.7%	7.12	6.63	4.75	7.14	7.07
MnO	±8%	0.122	0.123	0.122	0.126	0.126
MgO	±3.3%	2.71	7.50	1.42	2.78	2.94
CaO	±2.5%	6.52	22.64	4.09	6.56	6.70
Na_2O	±3.6%	4.15	0.27	5.06	4.17	4.19
K_2O	±4.5%	1.82	0.01	2.47	1.79	1.74
P_2O_5	±20%	0.249	0.087	0.186	0.255	0.251
LOI		-0.02	0.12	1.47	-0.2	0.12
XRF						
Rb	±1.5	48.9	[0.5]	76.1	52.5	47.5
Sr	±3	378	271	377	380	382
Y	±2.0	30.9	16.4	23.6	30.3	28.7
Zr	±3	182	89	214	187	179
Nb	±1.1	14.1	3.9	14.2	13.9	13.4
Ba	±15	468	27	609	437	433
Pb	±3	9	[0]	13	9	8
Th	±3	6	[2]	8	7	6
U	±2	[1]	[3]	[2]	4	[1]
Sc	±5	17	22	5	19	22
V	±8	216	130	39	212	213
Cr	±2	11	54	14	12	14
Co	±2	17	19	7	17	17
Ni	±3	10	26	[1]	7	7
Cu	±3	52	5	6	44	39
Zn	±3	73	65	65	74	73
Ga	±2	19	13	17	18	18
INAA						
La	±1.1	27.2				
Ce	±2.2	50.6				
Nd	±3.6	23.8				
Sm	±2.1	4.97				
Eu	±2.6	1.32				
Tb	±2.7	0.81				
Yb	±2.9	3.10				
Lu	±3.3	0.46				
Th	±2.4	5.9				
U	±17	2.0				
Ta	±5.6	0.90				
Hf	±2.5	4.32				
Cs	±7.6	1.22				
Rb		51				
Zn		103				
Co		14.9				
Cr		11				
Sc		20.7				

Group		Middle lavas	Middle lavas	Middle lavas	Middle lavas	Middle lavas
Age		38±2 ka	?	66±2 ka	<145±5 ka	<145±5 ka
Sample		MDL-AB	Av-B	MRL	MAL-d	MAL-c
XRF	2σ					
SiO_2	±0.5%	64.80	71.23	71.12	55.45	59.57
TiO_2	±2.5%	0.501	0.361	0.364	0.952	1.133
Al_2O_3	±0.7%	16.76	14.64	14.61	18.15	16.89
$Fe_2O_3^T$	±1.7%	4.75	2.60	2.60	7.24	7.26
MnO	±8%	0.124	0.069	0.065	0.124	0.129
MgO	±3.3%	1.40	0.94	0.95	4.11	2.60
CaO	±2.5%	4.16	2.49	2.54	8.63	5.73
Na_2O	±3.6%	4.92	4.18	4.27	3.90	4.26
K_2O	±4.5%	2.40	3.40	3.37	1.20	2.16
P_2O_5	±20%	0.191	0.100	0.102	0.250	0.260
LOI		0.89	-0.53	0.01	-0.08	0.84
XRF						
Rb	±1.5	77.8	96.4	95.2	28.4	58.0
Sr	±3	380	263	267	515	388
Y	±2.0	23.2	16.0	15.0	22.7	29.4
Zr	±3	217	166	165	144	192
Nb	±1.1	14.3	16.4	15.7	9.9	15.5
Ba	±15	617	804	819	369	512
Pb	±3	15	13	12	5	9
Th	±3	9	15	16	4	8
U	±2	4	4	5	5	[1]
Sc	±5	5	[3]	[3]	22	18
V	±8	43	33	37	171	195
Cr	±2	6	13	10	49	9
Co	±2	6	5	4	19	16
Ni	±3	2	5	5	28	3
Cu	±3	6	6	6	42	26
Zn	±3	64	32	29	59	75
Ga	±2	17	14	15	18	18
INAA						
La	±1.1	31.1		36.0	20.0	
Ce	±2.2	56.8		59.4	40.6	
Nd	±3.6	21.7		18.3	18.8	
Sm	±2.1	4.15		3.29	3.81	
Eu	±2.6	1.05		0.67	1.12	
Tb	±2.7	0.60		0.39	0.62	
Yb	±2.9	2.72		1.81	2.35	
Lu	±3.3	0.42		0.29	0.35	
Th	±2.4	8.5		13.4	3.5	
U	±17	2.6		3.9	1.4	
Ta	±5.6	1.04		1.31	0.56	
Hf	±2.5	4.84		4.00	3.29	
Cs	±7.6	3.05		1.59	0.80	
Rb		80		98	37	
Zn		62		30	58	
Co		6.0		4.2	17.5	
Cr		5		10	47	
Sc		5.2		4.6	20.1	

Group		Middle lavas	Middle lavas	Lower lavas	Pillow basalts
Age		<145±5 ka	<145±5 ka	<145±5 ka	>145±5 ka
Sample		MAL-b	MAL-a	LAL	PBM
XRF	2σ				
SiO_2	±0.5%	59.60	59.92	55.73	54.51
TiO_2	±2.5%	1.128	1.118	0.816	0.929
Al_2O_3	±0.7%	16.92	16.89	18.07	17.92
$Fe_2O_3^T$	±1.7%	7.28	7.13	5.76	7.47
MnO	±8%	0.129	0.126	0.113	0.133
MgO	±3.3%	2.52	2.53	4.90	4.43
CaO	±2.5%	5.76	5.63	9.87	9.58
Na_2O	±3.6%	4.32	4.32	3.37	3.61
K_2O	±4.5%	2.08	2.09	1.15	1.23
P_2O_5	±20%	0.264	0.259	0.207	0.182
LOI		-0.27	-0.01	0.8	1.3
XRF					
Rb	±1.5	58.1	59.2	25.3	28.3
Sr	±1	395	389	595	515
Y	±2.0	30.2	30.4	20.4	22.7
Zr	±3	196	194	125	132
Nb	±1.1	15.6	15.4	11.7	11.0
Ba	±15	524	509	354	250
Pb	±3	11	6	7	5
Th	±3	7	7	7	4
U	±2	[1]	[2]	[1]	[3]
Sc	±5	19	17	25	20
V	±8	202	209	189	192
Cr	±2	14	10	86	24
Co	±2	16	16	21	34
Ni	±3	5	6	29	30
Cu	±3	24	23	23	18
Zn	±3	71	76	59	69
Ga	±2	18	18	16	17
INAA					
La	±1.1				
Ce	±2.2				
Nd	±3.6				
Sm	±2.1				
Eu	±2.6				
Tb	±2.7				
Yb	±2.9				
Lu	±3.3				
Th	±2.4				
U	±17				
Ta	±5.6				
Hf	±2.5				
Cs	±7.6				
Rb					
Zn					
Co					
Cr					
Sc					

Group	PCD inclusion	PCD inclusion	PCD inclusion	PCD
Age				
Sample	**PCD6-i**	**PCD5-i**	**PCD3-i**	**PCD5**
I.D.				
Th	1.95	1.74	2.57	8.88
U	0.664	0.594	0.779	2.56
Isotopes				
$(^{234}U/^{238}U)$	1.015	1.004	1.006	1.003
2σ	±5	±5	±4	±3
$(^{238}U/^{232}Th)$	1.034	1.036	0.919	0.873
2σ	±7	±9	±6	±6
$(^{230}Th/^{232}Th)$	0.987	0.937	0.894	0.861
2σ	±7	±9	±5	±8

Group	Upper lavas	MDL inclusion	Middle lavas
Age			
Sample	**UAL-b**	**MDL-i-2**	**MRL**
I.D.			
Th	5.40	2.29	12.50
U	1.64	1.73	3.62
Isotopes			
$(^{234}U/^{238}U)$	1.002	1.007	0.999
2σ	±4	±4	±5
$(^{238}U/^{232}Th)$	0.919	2.288	0.880
2σ	±4	±7	±5
$(^{230}Th/^{232}Th)$	0.915	2.657	0.898
2σ	±9	±24	±9

Santorini and Soufriere, St. Vincent

Electron microprobe data

Group:	Palea Kameni	Sample:	feldspar crystal (1) from dka-726AD
Age:	1273 a	Traverse:	from core to rim

Sample	point	SiO_2	TiO_2	Al_2O_3	CaO	FeO	BaO	Na_2O	K_2O	Total	X_{An}
dka-fsp-1	1	55.97	0.012	26.66	9.51	0.434	0.017	5.98	0.203	98.78	0.468
dka-fsp-1	2	55.64	0.030	26.73	9.69	0.435	0.049	5.89	0.180	98.65	0.476
dka-fsp-1	3	55.55	0.024	26.74	9.85	0.419	0.029	5.83	0.179	98.62	0.482
dka-fsp-1	4	55.22	0.036	26.82	9.87	0.426	0.003	5.81	0.165	98.35	0.485
dka-fsp-1	5	55.18	0.024	26.95	9.91	0.431	0.008	5.76	0.187	98.45	0.487
dka-fsp-1	6	55.35	0.027	26.97	10.01	0.434	0.004	5.74	0.179	98.72	0.491
dka-fsp-1	7	55.46	0.018	26.80	9.67	0.446	0.004	5.97	0.188	98.55	0.467
dka-fsp-1	8	56.01	0.028	26.58	9.45	0.477	0.032	5.97	0.193	98.73	0.461
dka-fsp-1	9	56.05	0.029	26.66	9.58	0.466	0.054	6.01	0.202	99.04	0.463
dka-fsp-1	10	55.77	0.044	26.73	9.57	0.444	0.017	5.97	0.184	98.73	0.465
dka-fsp-1	11	55.42	0.008	26.55	9.70	0.420	0.000	5.94	0.187	98.23	0.469
dka-fsp-1	12	55.56	0.026	26.50	9.74	0.456	0.020	5.95	0.203	98.46	0.470
dka-fsp-1	13	55.57	0.032	26.82	9.76	0.437	0.015	5.86	0.187	98.67	0.474
dka-fsp-1	14	55.60	0.040	26.93	9.81	0.417	0.000	5.86	0.189	98.84	0.475
dka-fsp-1	15	54.90	0.032	26.97	10.10	0.459	0.014	5.59	0.174	98.24	0.495
dka-fsp-1	16	55.25	0.028	26.87	10.05	0.427	0.019	5.71	0.168	98.53	0.488
dka-fsp-1	17	55.06	0.011	27.02	10.12	0.424	0.000	5.73	0.176	98.53	0.489
dka-fsp-1	18	54.75	0.044	27.06	10.16	0.456	0.000	5.64	0.160	98.28	0.495
dka-fsp-1	19	55.52	0.042	26.63	9.68	0.466	0.001	5.97	0.171	98.48	0.468
dka-fsp-1	20	55.94	0.045	26.61	9.53	0.454	0.029	5.95	0.197	98.76	0.465
	average:	55.49									

Group:	Palea Kameni	Sample:	feldspar crystal (2) from dka-726AD
Age:	1273 a	Traverse:	from core to rim

Sample	point	SiO_2	TiO_2	Al_2O_3	CaO	FeO	BaO	Na_2O	K_2O	Total	X_{An}
dka-fsp-2	1	54.36	0.03	27.48	10.90	0.48	0.03	5.32	0.15	98.75	0.527
dka-fsp-2	2	54.09	0.042	27.72	10.88	0.449	0.000	5.32	0.134	98.63	0.527
dka-fsp-2	3	55.05	0.034	27.17	10.25	0.409	0.015	5.74	0.165	98.84	0.492
dka-fsp-2	4	55.82	0.043	26.63	9.66	0.431	0.016	5.93	0.188	98.72	0.468
dka-fsp-2	5	55.64	0.032	26.90	9.85	0.424	0.024	5.89	0.189	98.94	0.475
dka-fsp-2	6	55.75	0.040	26.95	9.77	0.438	0.000	5.87	0.187	99.00	0.474
dka-fsp-2	7	55.58	0.027	26.84	9.77	0.450	0.012	5.86	0.166	98.70	0.475
dka-fsp-2	8	55.44	0.030	26.93	9.85	0.440	0.004	5.81	0.179	98.68	0.479
dka-fsp-2	9	55.47	0.025	26.81	9.93	0.428	0.031	5.83	0.180	98.70	0.480
dka-fsp-2	10	55.58	0.008	26.82	9.87	0.435	0.020	5.85	0.186	98.77	0.478
dka-fsp-2	11	55.35	0.041	27.07	9.96	0.417	0.000	5.73	0.187	98.76	0.485
dka-fsp-2	12	55.39	0.041	27.04	9.97	0.407	0.037	5.78	0.167	98.83	0.483
dka-fsp-2	13	55.21	0.028	26.82	9.89	0.424	0.032	5.85	0.176	98.44	0.478
dka-fsp-2	14	55.44	0.011	26.74	9.91	0.415	0.024	5.83	0.184	98.55	0.479
dka-fsp-2	15	55.88	0.030	26.86	9.68	0.421	0.011	6.00	0.189	99.07	0.466
dka-fsp-2	16	55.68	0.035	26.72	9.65	0.423	0.039	6.04	0.199	98.80	0.464
dka-fsp-2	17	54.30	0.039	27.40	10.69	0.458	0.025	5.42	0.150	98.49	0.517
dka-fsp-2	18	55.01	0.018	27.15	10.28	0.425	0.001	5.62	0.173	98.67	0.498
dka-fsp-2	19	54.71	0.017	27.25	10.38	0.450	0.025	5.59	0.158	98.57	0.502
dka-fsp-2	20	54.82	0.024	27.39	10.18	0.443	0.004	5.60	0.181	98.65	0.496
	average:	55.23									

Group:	Nea Kameni	Sample:	feldspar crystal (1) from dkf-1939
Age:	59-60 a	Traverse:	from core to rim

Sample	point	SiO_2	TiO_2	Al_2O_3	CaO	FeO	BaO	Na_2O	K_2O	Total	X_{An}
dkf-fsp-1	1	55.69	0.036	26.93	9.40	0.515	0.014	5.77	0.164	98.52	0.469
dkf-fsp-1	2	55.51	0.054	27.06	9.41	0.497	0.000	5.85	0.169	98.54	0.466
dkf-fsp-1	3	56.60	0.023	26.11	8.41	0.493	0.018	6.24	0.204	98.10	0.422
dkf-fsp-1	4	54.71	0.030	27.20	9.95	0.496	0.030	5.37	0.146	97.93	0.502
dkf-fsp-1	5	55.94	0.041	26.72	8.95	0.505	0.038	5.99	0.183	98.37	0.447
dkf-fsp-1	6	55.66	0.030	26.61	9.09	0.504	0.025	5.88	0.185	97.98	0.456
dkf-fsp-1	7	55.43	0.043	26.94	9.48	0.476	0.014	5.68	0.174	98.24	0.475
dkf-fsp-1	8	56.72	0.047	25.88	8.30	0.480	0.011	6.33	0.200	97.97	0.415
dkf-fsp-1	9	55.81	0.038	26.60	9.03	0.475	0.030	5.83	0.184	97.99	0.456
dkf-fsp-1	10	53.80	0.021	26.01	9.07	0.485	0.031	5.38	0.177	94.97	0.477
dkf-fsp-1	11	55.06	0.051	27.30	9.78	0.531	0.014	5.48	0.160	98.38	0.492
dkf-fsp-1	12	55.62	0.043	26.81	9.42	0.478	0.021	5.83	0.175	98.39	0.467
dkf-fsp-1	13	56.04	0.034	26.69	8.97	0.476	0.024	5.85	0.191	98.27	0.454
dkf-fsp-1	14	55.81	0.042	26.83	9.42	0.484	0.010	5.77	0.173	98.53	0.470
dkf-fsp-1	15	55.02	0.031	27.26	9.69	0.485	0.008	5.58	0.170	98.24	0.485
dkf-fsp-1	16	55.25	0.025	27.24	9.57	0.496	0.022	5.57	0.154	98.33	0.483
dkf-fsp-1	17	54.82	0.046	27.31	9.79	0.501	0.014	5.42	0.157	98.06	0.495
dkf-fsp-1	18	54.93	0.010	27.41	9.88	0.525	0.000	5.50	0.178	98.42	0.493
	average:	55.47									

Group:	Nea Kameni	Sample:	feldspar crystal (3) from dkf-1939
Age:	59-60 a	Traverse:	from rim to rim

Sample	point	SiO_2	TiO_2	Al_2O_3	CaO	FeO	BaO	Na_2O	K_2O	Total	X_{An}
dkf-fsp-3	1	55.12	0.026	27.18	9.81	0.519	0.000	5.50	0.187	98.35	0.490
dkf-fsp-3	2	56.69	0.053	26.10	8.61	0.486	0.016	6.19	0.195	98.34	0.430
dkf-fsp-3	3	55.21	0.047	27.28	9.75	0.484	0.000	5.52	0.172	98.46	0.488
dkf-fsp-3	4	54.74	0.040	27.49	9.96	0.507	0.000	5.43	0.165	98.33	0.498
dkf-fsp-3	5	54.87	0.032	27.49	10.01	0.487	0.000	5.37	0.156	98.42	0.503
dkf-fsp-3	6	55.81	0.042	26.94	9.47	0.488	0.000	5.78	0.170	98.71	0.471
dkf-fsp-3	7	54.99	0.035	27.24	9.82	0.437	0.000	5.50	0.156	98.17	0.492
dkf-fsp-3	8	55.14	0.022	27.05	9.65	0.469	0.030	5.62	0.159	98.14	0.482
dkf-fsp-3	9	55.41	0.041	26.92	9.67	0.467	0.000	5.73	0.166	98.40	0.478
dkf-fsp-3	10	55.59	0.045	26.89	9.28	0.468	0.000	5.81	0.186	98.27	0.464
dkf-fsp-3	11	54.85	0.034	27.31	9.89	0.504	0.003	5.49	0.155	98.23	0.494
dkf-fsp-3	12	54.60	0.037	27.30	9.95	0.489	0.000	5.38	0.147	97.90	0.501
dkf-fsp-3	13	54.88	0.040	27.34	9.88	0.450	0.025	5.49	0.163	98.26	0.493
dkf-fsp-3	14	55.35	0.059	27.13	9.83	0.492	0.001	5.56	0.155	98.58	0.489
dkf-fsp-3	15	55.02	0.033	27.21	9.85	0.568	0.013	5.59	0.169	98.45	0.488
	average:	55.22									

Group:	Nea Kameni	Sample:	feldspar crystal (1) from dkr-1940
Age:	59 a	Traverse:	from rim to rim

Sample	point	SiO_2	TiO_2	Al_2O_3	CaO	FeO	BaO	Na_2O	K_2O	Total	X_{An}
dkr-fsp-1	1	55.34	0.070	26.46	8.99	0.574	0.013	5.83	0.178	97.46	0.599
dkr-fsp-1	2	54.75	0.045	26.87	9.56	0.503	0.019	5.57	0.164	97.49	0.625
dkr-fsp-1	3	54.81	0.029	26.90	9.43	0.505	0.021	5.65	0.162	97.51	0.619
dkr-fsp-1	4	55.28	0.043	26.81	9.25	0.494	0.021	5.79	0.178	97.87	0.608
dkr-fsp-1	5	55.05	0.027	26.72	9.36	0.505	0.012	5.66	0.134	97.47	0.618
dkr-fsp-1	6	55.11	0.043	26.94	9.48	0.488	0.000	5.59	0.160	97.82	0.622
dkr-fsp-1	7	55.33	0.031	26.96	9.37	0.517	0.040	5.56	0.175	97.98	0.621
dkr-fsp-1	8	53.80	0.022	27.85	10.32	0.534	0.019	5.03	0.129	97.70	0.667
dkr-fsp-1	9	53.90	0.040	27.87	10.26	0.501	0.036	5.18	0.140	97.92	0.658
dkr-fsp-1	10	53.53	0.039	27.77	10.36	0.493	0.019	5.06	0.125	97.38	0.667
dkr-fsp-1	11	53.75	0.037	27.62	10.18	0.495	0.005	5.21	0.126	97.42	0.656
dkr-fsp-1	12	54.81	0.039	27.28	9.60	0.495	0.013	5.49	0.154	97.87	0.630
dkr-fsp-1	13	53.67	0.046	26.23	9.07	0.471	0.044	5.46	0.163	95.15	0.617
dkr-fsp-1	14	54.45	0.026	27.22	9.69	0.474	0.000	5.50	0.151	97.50	0.632
dkr-fsp-1	15	54.50	0.042	27.14	9.83	0.458	0.002	5.41	0.148	97.52	0.639
dkr-fsp-1	16	54.38	0.036	27.23	9.74	0.470	0.000	5.41	0.155	97.41	0.637
dkr-fsp-1	17	54.66	0.022	27.32	9.66	0.466	0.034	5.32	0.155	97.63	0.638
dkr-fsp-1	18	54.62	0.024	27.45	9.92	0.460	0.010	5.30	0.144	97.93	0.646
dkr-fsp-1	19	54.46	0.027	27.37	9.77	0.477	0.032	5.37	0.136	97.64	0.640
dkr-fsp-1	20	54.69	0.058	27.45	9.81	0.478	0.023	5.36	0.164	98.02	0.640
dkr-fsp-1	21	54.12	0.014	27.57	10.00	0.500	0.005	5.24	0.151	97.60	0.650
dkr-fsp-1	22	53.62	0.036	27.87	10.36	0.487	0.022	5.06	0.123	97.57	0.666
dkr-fsp-1	23	53.79	0.027	27.76	10.44	0.473	0.023	5.05	0.126	97.69	0.669
dkr-fsp-1	24	53.87	0.057	27.80	10.23	0.485	0.022	5.15	0.147	97.76	0.659
dkr-fsp-1	25	53.73	0.037	27.84	10.33	0.500	0.043	5.09	0.135	97.69	0.664
dkr-fsp-1	26	54.45	0.028	27.21	9.53	0.476	0.011	5.35	0.142	97.19	0.634
dkr-fsp-1	27	55.18	0.035	27.06	9.42	0.467	0.003	5.62	0.161	97.96	0.620
dkr-fsp-1	28	55.34	0.044	27.11	9.35	0.481	0.026	5.68	0.171	98.19	0.615
dkr-fsp-1	29	55.37	0.039	27.07	9.17	0.488	0.050	5.81	0.167	98.17	0.605
dkr-fsp-1	30	55.13	0.031	27.04	9.55	0.490	0.002	5.58	0.175	97.99	0.624
	average:	54.52									

Group:	Nea Kameni	Sample:	feldspar crystal (2) from dkr-1940
Age:	59 a	Traverse:	from rim to rim

Sample	point	SiO_2	TiO_2	Al_2O_3	CaO	FeO	BaO	Na_2O	K_2O	Total	X_{An}
dkr-fsp-2	1	55.01	0.035	27.28	9.48	0.558	0.024	5.49	0.178	98.06	0.626
dkr-fsp-2	2	55.98	0.042	26.65	9.10	0.467	0.023	5.88	0.172	98.31	0.601
dkr-fsp-2	3	56.17	0.055	26.63	8.85	0.424	0.029	5.93	0.184	98.27	0.592
dkr-fsp-2	4	54.51	0.037	27.58	10.09	0.546	0.014	5.23	0.141	98.15	0.653
dkr-fsp-2	5	54.54	0.039	27.54	9.84	0.477	0.000	5.30	0.135	97.87	0.644
dkr-fsp-2	6	55.48	0.049	27.06	9.33	0.418	0.004	5.70	0.133	98.17	0.615
dkr-fsp-2	7	55.85	0.049	26.85	9.04	0.450	0.017	5.75	0.145	98.15	0.605
dkr-fsp-2	8	55.40	0.044	27.05	9.34	0.452	0.000	5.65	0.133	98.06	0.618
dkr-fsp-2	9	55.64	0.056	26.86	9.14	0.506	0.003	5.78	0.152	98.13	0.607
dkr-fsp-2	10	55.66	0.039	26.90	9.27	0.470	0.038	5.79	0.137	98.31	0.610
dkr-fsp-2	11	55.68	0.015	27.04	9.49	0.463	0.026	5.72	0.134	98.58	0.618
dkr-fsp-2	12	56.10	0.017	26.63	9.05	0.468	0.000	5.85	0.155	98.27	0.601
dkr-fsp-2	13	55.65	0.043	26.85	9.27	0.449	0.000	5.70	0.131	98.10	0.614
dkr-fsp-2	14	55.09	0.053	27.31	9.74	0.496	0.011	5.49	0.152	98.35	0.633
dkr-fsp-2	15	56.76	0.037	26.42	8.56	0.391	0.021	6.06	0.187	98.44	0.578
dkr-fsp-2	16	56.53	0.037	26.46	8.76	0.422	0.000	5.97	0.192	98.37	0.587
	average:	55.63									

Group:	Nea Kameni	Sample:	feldspar crystal (1) from dkl-1950
Age:	49 a	Traverse:	from core to rim

Sample	point	SiO_2	TiO_2	Al_2O_3	CaO	FeO	BaO	Na_2O	K_2O	Total	X_{An}
dkl-fsp-1	1	56.15	0.020	27.19	9.98	0.457	0.014	5.73	0.196	99.74	0.485
dkl-fsp-1	2	55.41	0.049	27.28	10.32	0.460	0.004	5.62	0.177	99.31	0.499
dkl-fsp-1	3	55.40	0.007	27.31	10.32	0.441	0.002	5.51	0.177	99.16	0.504
dkl-fsp-1	4	55.24	0.018	27.30	10.38	0.455	0.006	5.54	0.180	99.12	0.503
dkl-fsp-1	5	55.91	0.035	26.52	9.63	0.497	0.004	5.97	0.195	98.75	0.466
dkl-fsp-1	6	54.98	0.046	27.01	10.33	0.536	0.039	5.58	0.186	98.70	0.500
dkl-fsp-1	7	56.96	0.061	25.20	8.41	0.622	0.031	6.40	0.362	98.06	0.412
	average:	55.72									

Group:	Nea Kameni	Sample:	feldspar crystal (2) from dkl-1950
Age:	49 a	Traverse:	from core to rim

Sample	point	SiO_2	TiO_2	Al_2O_3	CaO	FeO	BaO	Na_2O	K_2O	Total	X_{An}
dkl-fsp-2	1	44.33	0.000	33.69	18.49	0.536	0.000	1.03	0.014	98.09	0.908
dkl-fsp-2	2	44.25	0.009	33.91	18.34	0.538	0.015	0.93	0.010	98.00	0.915
dkl-fsp-2	3	44.22	0.006	34.00	18.58	0.537	0.000	0.88	0.010	98.23	0.921
dkl-fsp-2	4	43.99	0.002	34.23	18.68	0.530	0.000	0.87	0.003	98.31	0.922
dkl-fsp-2	5	44.16	0.000	33.86	18.58	0.518	0.000	0.93	0.019	98.08	0.916
dkl-fsp-2	6	43.75	0.006	34.22	18.74	0.521	0.016	0.82	0.000	98.08	0.927
dkl-fsp-2	7	43.70	0.000	34.26	18.74	0.522	0.000	0.81	0.004	98.03	0.928
dkl-fsp-2	8	44.14	0.007	34.19	18.57	0.540	0.000	0.87	0.013	98.32	0.921
dkl-fsp-2	9	43.98	0.042	34.36	18.62	0.553	0.003	0.81	0.006	98.37	0.927
dkl-fsp-2	10	55.40	0.036	25.93	9.29	0.741	0.012	6.00	0.239	97.65	0.455
	average:	44.06									

Group:	Soufriere	Sample:	feldspar crystal (1) from STV354 of Heath et al. (1998)
Age:	20 a	Traverse:	from core to rim

Sample	point	SiO_2	TiO_2	Al_2O_3	CaO	FeO	BaO	Na_2O	K_2O	Total	X_{An}
STV-fsp-1	1	49.83	0.027	30.34	14.14	0.550	0.000	3.63	0.053	98.56	0.681
STV-fsp-1	2	51.01	0.054	29.34	13.04	0.546	0.005	4.10	0.071	98.17	0.635
STV-fsp-1	3	48.90	0.017	30.82	14.85	0.563	0.005	3.08	0.054	98.28	0.725
STV-fsp-1	4	49.66	0.032	30.11	14.07	0.558	0.000	3.55	0.064	98.04	0.684
STV-fsp-1	5	50.89	0.029	29.63	13.27	0.559	0.024	4.04	0.065	98.51	0.643
STV-fsp-1	6	51.41	0.048	29.33	12.94	0.567	0.000	4.25	0.065	98.61	0.625
STV-fsp-1	7	52.25	0.026	28.75	12.42	0.557	0.002	4.53	0.083	98.60	0.599
STV-fsp-1	8	51.76	0.035	28.99	12.48	0.607	0.000	4.38	0.070	98.32	0.609
STV-fsp-1	9	49.53	0.029	30.59	14.38	0.593	0.000	3.37	0.051	98.53	0.700
STV-fsp-1	10	52.14	0.116	28.26	12.26	1.089	0.014	4.25	0.156	98.28	0.609
STV-fsp-1	11	52.50	0.038	28.87	12.53	0.593	0.011	4.57	0.068	99.18	0.600
STV-fsp-1	12	49.27	0.031	30.87	14.92	0.592	0.026	3.13	0.047	98.88	0.723
STV-fsp-1	13	50.01	0.030	30.40	14.27	0.603	0.030	3.49	0.042	98.87	0.692
STV-fsp-1	14	47.73	0.020	31.83	16.00	0.574	0.004	2.47	0.028	98.66	0.780
STV-fsp-1	15	46.71	0.016	32.49	16.74	0.573	0.017	1.97	0.020	98.55	0.823
STV-fsp-1	16	49.06	0.029	30.92	14.82	0.561	0.000	3.17	0.042	98.61	0.719
STV-fsp-1	17	48.94	0.043	30.99	14.94	0.592	0.014	3.06	0.046	98.62	0.728
STV-fsp-1	18	51.62	0.057	29.19	12.92	0.567	0.004	4.29	0.075	98.72	0.622
STV-fsp-1	19	51.81	0.039	29.27	12.81	0.544	0.009	4.30	0.060	98.83	0.620
STV-fsp-1	20	51.02	0.046	29.64	13.43	0.549	0.000	3.98	0.060	98.71	0.648
STV-fsp-1	21	52.07	0.037	29.01	12.79	0.552	0.000	4.33	0.067	98.85	0.618
STV-fsp-1	22	52.29	0.042	29.14	12.44	0.555	0.000	4.48	0.084	99.03	0.603
STV-fsp-1	23	52.25	0.028	29.15	12.73	0.568	0.000	4.33	0.071	99.13	0.616
STV-fsp-1	24	51.71	0.019	29.68	13.06	0.565	0.000	4.09	0.057	99.18	0.636
STV-fsp-1	25	52.55	0.049	29.11	12.44	0.573	0.000	4.50	0.082	99.30	0.602
	average:	50.68									

Group:	Soufriere	**Sample:**	feldspar crystal (2) from STV354 of Heath et al. (1998)
Age:	20 a	**Traverse:**	from core to rim

Sample	point	SiO_2	TiO_2	Al_2O_3	CaO	FeO	BaO	Na_2O	K_2O	Total	X_{An}
STV-fsp-2	1	52.57	0.049	29.36	12.64	0.574	0.012	4.27	0.071	99.54	0.619
STV-fsp-2	2	52.03	0.030	29.76	13.14	0.565	0.003	4.11	0.059	99.70	0.637
STV-fsp-2	3	52.70	0.032	29.00	12.40	0.590	0.000	4.47	0.078	99.27	0.603
STV-fsp-2	4	53.50	0.033	28.87	11.90	0.588	0.000	4.73	0.088	99.70	0.579
STV-fsp-2	5	51.67	0.024	29.58	13.04	0.579	0.000	3.99	0.065	98.95	0.641
STV-fsp-2	6	51.85	0.050	28.48	11.98	0.578	0.007	4.50	0.073	97.52	0.593
STV-fsp-2	7	58.70	0.436	23.05	8.98	2.817	0.004	4.97	0.496	99.45	0.483
	average:	52.39									

Group:	Soufriere	Sample:	feldspar crystal (3) from STV354 of Heath et al. (1998)
Age:	20 a	**Traverse:**	from core to rim

Sample	point	SiO_2	TiO_2	Al_2O_3	CaO	FeO	BaO	Na_2O	K_2O	Total	X_{An}
STV-fsp-3	1	43.82	0.000	34.31	18.75	0.529	0.000	0.79	0.014	98.20	0.929
STV-fsp-3	2	43.97	0.004	34.33	18.77	0.533	0.000	0.80	0.004	98.41	0.928
STV-fsp-3	3	43.93	0.012	34.57	18.80	0.546	0.000	0.78	0.006	98.64	0.930
STV-fsp-3	4	44.05	0.015	34.58	18.81	0.543	0.007	0.79	0.007	98.80	0.929
STV-fsp-3	5	44.08	0.000	34.52	18.91	0.539	0.000	0.79	0.000	98.84	0.930
STV-fsp-3	6	44.18	0.000	34.39	18.74	0.524	0.024	0.79	0.011	98.66	0.928
STV-fsp-3	7	44.19	0.008	34.49	18.92	0.549	0.000	0.77	0.013	98.94	0.930
STV-fsp-3	8	44.04	0.002	34.47	18.89	0.531	0.000	0.78	0.004	98.71	0.930
STV-fsp-3	9	44.01	0.000	34.49	18.93	0.516	0.000	0.77	0.001	98.72	0.932
STV-fsp-3	10	44.21	0.023	34.34	18.90	0.529	0.000	0.75	0.012	98.77	0.932
STV-fsp-3	11	43.92	0.018	34.33	18.83	0.511	0.000	0.77	0.006	98.37	0.931
STV-fsp-3	12	43.92	0.007	34.22	18.85	0.550	0.000	0.76	0.012	98.32	0.931
STV-fsp-3	13	43.27	0.005	33.84	18.44	0.531	0.000	0.78	0.022	96.89	0.928
STV-fsp-3	14	43.61	0.000	34.25	18.79	0.506	0.000	0.74	0.017	97.92	0.932
STV-fsp-3	15	43.63	0.000	34.51	19.01	0.524	0.005	0.65	0.009	98.33	0.941
STV-fsp-3	16	44.23	0.000	34.56	18.77	0.514	0.022	0.78	0.012	98.89	0.929
STV-fsp-3	17	44.31	0.000	34.35	19.01	0.525	0.000	0.81	0.000	99.01	0.928
STV-fsp-3	18	44.27	0.000	34.37	18.82	0.529	0.038	0.79	0.007	98.82	0.930
STV-fsp-3	19	44.23	0.000	34.72	18.89	0.521	0.000	0.78	0.010	99.14	0.930
STV-fsp-3	20	44.53	0.019	34.77	18.83	0.540	0.000	0.77	0.015	99.47	0.930
STV-fsp-3	21	44.24	0.027	34.50	18.98	0.545	0.001	0.77	0.011	99.08	0.931
STV-fsp-3	22	44.42	0.007	34.49	18.76	0.521	0.009	0.79	0.012	99.01	0.928
STV-fsp-3	23	44.31	0.018	34.76	18.97	0.554	0.008	0.76	0.011	99.39	0.931
STV-fsp-3	24	44.33	0.006	34.64	19.12	0.497	0.011	0.74	0.000	99.34	0.934
STV-fsp-3	25	44.01	0.006	34.74	19.09	0.521	0.000	0.71	0.016	99.09	0.936
STV-fsp-3	26	44.17	0.000	34.93	19.10	0.489	0.014	0.63	0.020	99.35	0.943
STV-fsp-3	27	44.21	0.000	34.98	19.20	0.501	0.008	0.65	0.005	99.54	0.943
STV-fsp-3	28	46.25	0.026	33.70	17.69	0.596	0.015	1.48	0.016	99.77	0.867
STV-fsp-3	29	45.85	0.012	33.31	17.46	0.601	0.000	1.47	0.020	98.72	0.867
STV-fsp-3	30	48.60	0.031	32.20	16.01	0.683	0.004	2.44	0.046	100.02	0.782
	average:	44.21									

Group:	Palea Kameni	Sample:	orthopyroxene crystal (1) from dka-726AD
Age:	1273 a	Traverse:	from rim to rim

Sample	point	SiO_2	TiO_2	Al_2O_3	MgO	CaO	MnO	FeO	Total	Mg#
dka-px-1	1	51.50	0.27	0.74	21.22	1.56	1.05	23.43	99.77	0.617
dka-px-1	2	51.62	0.26	0.71	21.02	1.49	1.07	23.36	99.52	0.616
dka-px-1	3	51.62	0.24	0.63	21.16	1.48	1.08	23.66	99.86	0.614
dka-px-1	4	51.06	0.27	0.75	20.22	1.81	1.11	24.23	99.44	0.598
dka-px-1	5	51.18	0.31	0.76	20.34	1.78	1.14	24.64	100.14	0.595
dka-px-1	6	50.94	0.24	0.68	20.48	1.55	1.09	24.00	98.97	0.603
dka-px-1	7	49.41	0.24	0.54	19.96	3.92	1.05	23.48	98.60	0.603
dka-px-1	8	51.79	0.26	0.61	20.53	1.54	1.08	24.58	100.39	0.598
dka-px-1	9	51.23	0.24	0.72	20.23	1.50	1.09	24.66	99.67	0.594
dka-px-1	10	51.66	0.26	0.71	20.10	1.52	1.12	25.02	100.39	0.589
dka-px-1	11	50.98	0.25	0.87	19.79	1.51	1.14	24.65	99.19	0.589
dka-px-1	12	51.98	0.26	0.73	20.62	1.59	1.10	23.95	100.23	0.605
dka-px-1	13	52.18	0.23	0.63	21.18	1.49	1.06	23.59	100.36	0.616
dka-px-1	14	52.25	0.24	0.64	21.24	1.46	1.09	23.42	100.33	0.618
dka-px-1	15	52.92	0.25	0.70	21.33	1.49	1.01	22.96	100.65	0.624
	average:	51.49								

Group:	Nea Kameni	Sample:	pyroxene crystal (1) from dkf-1939
Age:	59-60 a	Traverse:	from rim to rim

Sample	point	SiO_2	TiO_2	Al_2O_3	MgO	CaO	MnO	FeO	Na_2O	Total	Mg#
dkf-opx-1	1	52.27	0.52	1.43	14.49	17.83	0.60	11.59	0.285	99.00	0.690
dkf-opx-1	2	52.34	0.47	1.38	14.56	18.17	0.59	11.13	0.295	98.93	0.700
dkf-opx-1	3	52.33	0.47	1.27	14.49	18.24	0.58	10.98	0.293	98.66	0.702
dkf-opx-1	4	52.23	0.49	1.38	14.60	18.40	0.53	10.64	0.296	98.56	0.710
dkf-opx-1	5	51.74	0.55	1.87	14.70	18.15	0.51	10.53	0.294	98.34	0.713
dkf-opx-1	6	52.35	0.45	1.38	14.98	18.32	0.52	10.21	0.268	98.46	0.724
dkf-opx-1	7	52.23	0.46	1.46	14.83	18.32	0.52	10.37	0.298	98.49	0.719
dkf-opx-1	8	51.89	0.47	1.73	14.81	18.24	0.53	10.60	0.301	98.57	0.713
dkf-opx-1	9	51.83	0.60	1.91	14.82	17.90	0.56	11.00	0.309	98.94	0.706
dkf-opx-1	10	52.03	0.50	1.81	14.93	18.07	0.50	11.05	0.299	99.18	0.707
dkf-cpx-1	11	52.43	0.35	1.57	23.09	1.60	0.84	20.55	0.030	100.46	0.667
dkf-cpx-1	12	52.51	0.38	1.55	22.83	2.30	0.80	19.93	0.021	100.31	0.671
dkf-cpx-1	13	52.65	0.36	1.38	22.94	1.97	0.84	20.33	0.045	100.50	0.668
dkf-cpx-1	14	52.99	0.36	1.14	23.76	1.50	0.82	20.11	0.044	100.71	0.678
dkf-cpx-1	15	52.75	0.32	1.24	23.76	1.70	0.81	19.70	0.017	100.30	0.683
dkf-cpx-1	16	53.13	0.27	0.96	23.64	1.42	0.89	20.36	0.025	100.70	0.674
dkf-cpx-1	17	52.99	0.31	1.03	23.07	1.56	0.89	20.96	0.036	100.84	0.662
dkf-cpx-1	18	52.56	0.32	1.07	22.12	1.84	0.96	21.51	0.024	100.41	0.647
dkf-cpx-1	19	52.80	0.29	0.73	22.29	1.52	1.01	21.81	0.043	100.50	0.646
dkf-cpx-1	20	52.92	0.30	0.73	22.63	1.46	0.96	21.34	0.033	100.37	0.654
	average:	52.45									

Group:	Nea Kameni	Sample:	clinopyroxene crystal (2) from dkf-1939
Age:	59-60 a	Traverse:	from rim to rim

Sample	point	SiO_2	TiO_2	Al_2O_3	MgO	CaO	MnO	FeO	Na_2O	Total	Mg#
dkf-px-2	1	52.16	0.47	1.44	14.38	18.34	0.60	11.24	0.310	98.93	0.695
dkf-px-2	2	52.13	0.45	1.47	14.61	18.38	0.58	11.07	0.322	99.01	0.702
dkf-px-2	3	52.30	0.45	1.36	14.60	18.71	0.56	10.86	0.292	99.13	0.706
dkf-px-2	4	52.04	0.41	1.35	14.26	18.94	0.59	11.08	0.310	98.99	0.697
dkf-px-2	5	51.69	0.50	1.48	14.35	18.56	0.55	11.05	0.311	98.48	0.698
	average:	52.06									

Group:	Nea Kameni	Sample:	clinopyroxene crystal (1) from dkr-1940
Age:	59-60 a	Traverse:	from rim to rim

Sample	point	SiO_2	TiO_2	Al_2O_3	MgO	CaO	MnO	FeO	Na_2O	Total	Mg#
dkr-px-1	1	51.55	0.50	1.47	14.47	18.43	0.55	10.75	0.312	98.02	0.706
dkr-px-1	2	51.60	0.50	1.47	14.40	18.38	0.55	10.98	0.344	98.22	0.700
dkr-px-1	3	51.19	0.54	1.91	14.59	18.62	0.49	10.32	0.324	97.99	0.716
dkr-px-1	4	51.84	0.50	1.71	14.68	18.51	0.48	10.24	0.320	98.27	0.719
dkr-px-1	5	50.16	0.50	1.68	14.04	18.24	0.49	10.18	0.308	95.61	0.711
dkr-px-1	6	49.18	0.50	1.63	13.85	18.03	0.54	10.32	0.318	94.36	0.705
dkr-px-1	7	51.39	0.48	1.48	14.49	18.40	0.57	10.74	0.308	97.85	0.706
dkr-px-1	8	51.21	0.57	1.75	14.18	18.45	0.56	11.32	0.325	98.36	0.691
dkr-px-1	9	51.25	0.56	1.88	14.33	18.07	0.58	11.45	0.315	98.43	0.690
dkr-px-1	10	51.83	0.47	1.47	14.55	18.58	0.57	10.80	0.337	98.60	0.706
dkr-px-1	11	51.61	0.45	1.43	14.66	18.24	0.56	10.81	0.298	98.05	0.707
dkr-px-1	12	51.59	0.47	1.48	14.58	18.38	0.55	10.77	0.312	98.13	0.707
dkr-px-1	13	51.74	0.47	1.49	14.50	18.63	0.54	10.78	0.306	98.44	0.706
dkr-px-1	14	51.60	0.51	1.51	14.62	18.31	0.58	10.88	0.314	98.31	0.705
dkr-px-1	15	51.25	0.53	1.78	14.42	17.98	0.59	11.35	0.331	98.22	0.694
dkr-px-1	16	51.30	0.49	1.61	14.37	18.09	0.60	11.24	0.298	97.99	0.695
dkr-px-1	17	49.78	0.44	1.44	14.05	17.98	0.53	10.51	0.303	95.04	0.704
dkr-px-1	18	51.66	0.51	1.62	14.44	18.55	0.55	10.81	0.310	98.46	0.704
dkr-px-1	19	50.19	0.48	1.74	14.33	18.35	0.51	10.20	0.305	96.09	0.715
dkr-px-1	20	51.49	0.51	1.70	14.79	18.88	0.49	10.19	0.312	98.36	0.721
	average:	51.17									

Group:	Nea Kameni	Sample:	clinopyroxene crystal (2) from dkr-1940
Age:	59-60 a	Traverse:	from rim to rim

Sample	point	SiO_2	TiO_2	Al_2O_3	MgO	CaO	MnO	FeO	Na_2O	Total	Mg#
dkr-px-2	1	51.73	0.47	1.54	14.60	18.03	0.55	11.03	0.323	98.26	0.702
dkr-px-2	2	51.73	0.47	1.49	14.60	18.19	0.58	11.06	0.320	98.45	0.702
dkr-px-2	3	51.76	0.53	1.72	14.78	18.62	0.52	10.48	0.295	98.72	0.715
dkr-px-2	4	51.72	0.49	1.67	14.71	18.32	0.53	10.46	0.315	98.21	0.715
dkr-px-2	5	51.49	0.54	1.66	14.50	18.08	0.57	10.99	0.287	98.11	0.702
dkr-px-2	6	51.54	0.56	1.84	14.63	18.23	0.57	10.93	0.320	98.61	0.705
dkr-px-2	7	51.48	0.52	1.68	14.47	18.41	0.56	10.70	0.290	98.09	0.706
dkr-px-2	8	52.17	0.47	1.61	14.74	18.69	0.51	10.23	0.311	98.73	0.720
dkr-px-2	9	51.62	0.52	1.81	14.65	18.65	0.49	10.18	0.311	98.23	0.719
	average:	51.69									

Group:	Nea Kameni	Sample:	clinopyroxene crystal (1) from dkl-1950
Age:	49 a	Traverse:	from core to rim

Sample	point	SiO_2	TiO_2	Al_2O_3	MgO	CaO	MnO	FeO	Na_2O	Total	Mg#
dkl-px-1	1	51.43	0.52	1.57	14.16	19.54	0.59	11.52	0.298	99.63	0.686
dkl-px-1	2	51.71	0.47	1.47	14.50	19.67	0.60	11.26	0.306	99.99	0.697
dkl-px-1	3	51.79	0.52	1.50	14.51	19.90	0.58	10.83	0.310	99.93	0.705
dkl-px-1	4	51.84	0.47	1.45	14.56	19.94	0.54	10.75	0.281	99.83	0.707
dkl-px-1	5	51.50	0.47	1.47	14.65	19.97	0.54	10.59	0.327	99.51	0.711
dkl-px-1	6	51.85	0.47	1.58	14.69	19.91	0.53	10.55	0.301	99.89	0.713
dkl-px-1	7	51.45	0.53	1.74	14.76	19.81	0.52	10.61	0.305	99.71	0.712
dkl-px-1	8	51.66	0.55	1.75	14.98	19.84	0.51	10.34	0.301	99.92	0.721
dkl-px-1	9	51.42	0.55	1.88	14.90	19.57	0.54	10.58	0.304	99.75	0.715
dkl-px-1	10	51.57	0.51	1.73	14.62	19.76	0.50	10.51	0.312	99.53	0.712
	average:	51.62									

Group:	Nea Kameni	Sample:	clinopyroxene crystal (2) from dkl-1950
Age:	49 a	Traverse:	from rim to rim

Sample	point	SiO_2	TiO_2	Al_2O_3	MgO	CaO	MnO	FeO	Na_2O	Total	Mg#
dkl-px-2	1	52.31	0.42	1.42	15.01	18.20	0.56	10.80	0.297	99.03	0.712
dkl-px-2	2	51.64	0.51	1.65	14.84	17.94	0.54	11.25	0.270	98.63	0.702
dkl-px-2	3	52.04	0.47	1.62	14.85	18.20	0.50	10.47	0.311	98.47	0.717
dkl-px-2	4	51.86	0.45	1.37	14.91	18.46	0.53	10.56	0.285	98.42	0.715
dkl-px-2	5	52.01	0.45	1.35	14.68	18.44	0.58	10.74	0.280	98.51	0.709
dkl-px-2	6	52.04	0.43	1.39	14.83	18.55	0.56	10.80	0.293	98.89	0.710
dkl-px-2	7	51.78	0.48	1.85	15.02	18.83	0.47	10.17	0.271	98.87	0.725
dkl-px-2	8	51.81	0.47	1.53	14.68	18.81	0.51	10.52	0.297	98.63	0.713
dkl-px-2	9	51.69	0.46	1.45	14.55	18.76	0.53	10.57	0.297	98.30	0.710
dkl-px-2	10	51.86	0.43	1.39	14.69	18.64	0.52	10.60	0.298	98.43	0.712
dkl-px-2	11	52.01	0.46	1.42	14.69	18.84	0.54	10.53	0.291	98.78	0.713
dkl-px-2	12	51.07	0.55	2.56	14.78	19.37	0.35	9.32	0.293	98.30	0.738
dkl-px-2	13	51.47	0.52	2.22	15.18	19.42	0.33	9.17	0.307	98.61	0.747
dkl-px-2	14	51.47	0.52	2.27	15.03	19.40	0.33	9.19	0.288	98.50	0.744
dkl-px-2	15	51.73	0.48	1.70	14.78	18.93	0.45	9.96	0.303	98.33	0.726
dkl-px-2	16	51.94	0.44	1.49	14.82	18.74	0.52	10.56	0.301	98.80	0.715
dkl-px-2	17	51.77	0.46	1.40	14.80	18.49	0.53	10.73	0.306	98.47	0.711
dkl-px-2	18	51.87	0.43	1.35	14.51	18.72	0.54	10.70	0.307	98.44	0.708
dkl-px-2	19	51.73	0.47	1.40	14.70	18.39	0.54	10.67	0.296	98.20	0.711
dkl-px-2	20	51.90	0.44	1.32	14.62	18.53	0.52	10.54	0.277	98.15	0.712
	average:	51.80									

Group:	Soufriere	Sample:	clinopyroxene crystal (1) from STV354 of Heath et al. (1998)
Age:	20 a	Traverse:	from core to rim

Sample	point	SiO_2	TiO_2	Al_2O_3	MgO	CaO	MnO	FeO	Na_2O	Total	Mg#
STV-px-1	1	52.24	0.43	1.56	14.89	21.06	0.37	9.75	0.300	100.60	0.731
STV-px-1	2	52.29	0.46	1.59	14.85	20.97	0.35	9.74	0.310	100.55	0.731
STV-px-1	3	52.50	0.29	1.25	14.78	21.32	0.40	9.69	0.282	100.51	0.731
STV-px-1	4	52.74	0.18	0.90	14.64	21.59	0.42	9.68	0.253	100.41	0.729
STV-px-1	5	52.51	0.20	0.93	14.56	21.60	0.43	9.62	0.268	100.11	0.729
STV-px-1	6	52.63	0.24	1.10	14.61	21.68	0.45	9.82	0.272	100.80	0.726
STV-px-1	7	52.78	0.18	0.97	14.65	21.43	0.41	9.72	0.243	100.38	0.729
STV-px-1	8	51.86	0.22	1.03	14.73	21.49	0.38	9.69	0.251	99.65	0.730
STV-px-1	9	52.81	0.24	1.09	14.56	21.47	0.38	9.68	0.276	100.51	0.728
STV-px-1	10	52.40	0.34	1.30	14.69	21.34	0.48	9.92	0.294	100.75	0.725
STV-px-1	11	52.29	0.33	1.34	14.73	20.98	0.47	9.98	0.273	100.39	0.725
STV-px-1	12	51.78	0.51	1.71	14.76	20.75	0.41	10.00	0.301	100.22	0.725
STV-px-1	13	52.13	0.44	1.52	14.83	20.72	0.38	10.00	0.291	100.29	0.725
STV-px-1	14	50.94	0.86	2.81	14.54	20.41	0.33	9.92	0.329	100.14	0.723
STV-px-1	15	51.76	0.59	1.79	14.97	20.62	0.35	9.94	0.304	100.33	0.729
STV-px-1	16	51.89	0.66	2.14	15.24	19.91	0.39	10.41	0.344	100.97	0.723
STV-px-1	17	51.41	0.64	2.27	14.94	20.03	0.40	10.37	0.328	100.39	0.719
STV-px-1	18	51.51	0.59	2.02	14.95	20.17	0.41	10.32	0.291	100.25	0.721
STV-px 1	19	51.43	0.60	2.12	14.93	20.21	0.42	10.55	0.298	100.54	0.716
STV-px-1	20	51.38	0.61	2.32	14.86	20.03	0.41	10.45	0.301	100.35	0.717
	average:	52.06									

Group:	Palea Kameni	Samples:	groundmass of dka-726AD							
Age:	1273 a									

Sample	SiO_2	TiO_2	Al_2O_3	MgO	CaO	MnO	FeO	BaO	Na_2O	K_2O	Total
dka-gm-1	67.92	0.452	14.45	0.436	2.30	0.088	3.35	0.055	5.14	2.34	96.54
dka-gm-2	68.15	1.049	14.77	0.395	2.47	0.106	4.68	0.061	5.17	2.23	99.07
dka-gm-4	70.18	0.679	14.16	0.724	2.29	0.157	4.04	0.034	5.04	2.56	99.86
dka-gm-5	68.57	0.556	14.54	0.876	2.34	0.145	2.92	0.074	5.06	2.35	97.43
dka-gm-6	69.63	0.390	16.39	0.277	2.94	0.069	2.17	0.037	5.77	2.15	99.82
dka-gm-7	68.40	0.396	15.92	0.594	3.33	0.084	2.91	0.068	5.59	2.18	99.47
dka-gm-9	69.96	0.383	15.93	0.261	2.85	0.070	2.18	0.043	5.68	2.23	99.58
dka-gm-10	71.75	0.571	14.05	0.301	1.92	0.082	2.93	0.077	5.10	2.72	99.50
dka-gm-11	67.64	0.577	15.12	1.020	2.86	0.154	4.36	0.041	5.46	2.07	99.30
dka-gm-13	68.05	0.494	16.11	0.637	3.10	0.092	3.31	0.084	5.78	2.05	99.71
average:	69.02			0.552							

Group:	Nea Kameni	Samples:	groundmass of dkf-1939							
Age:	59-60 a									

Sample	SiO_2	TiO_2	Al_2O_3	MgO	CaO	MnO	FeO	BaO	Na_2O	K_2O	Total
dkf-gm-1	70.30	0.833	13.31	1.105	1.94	0.167	4.74	0.065	5.10	2.49	100.05
dkf-gm-2	67.14	0.447	16.82	0.449	3.69	0.086	2.48	0.047	5.77	1.87	98.80
dkf-gm-3	71.16	0.624	13.39	0.377	1.80	0.115	3.07	0.048	5.10	2.78	98.47
dkf-gm-5	68.21	0.537	14.67	0.945	2.84	0.158	3.66	0.012	5.33	2.25	98.61
dkf-gm-6	67.48	0.408	15.94	0.621	3.32	0.112	2.76	0.042	5.63	2.06	98.36
dkf-gm-7	65.51	0.343	16.95	0.556	4.28	0.099	2.44	0.071	5.96	1.67	97.88
dkf-gm-9	63.74	0.340	18.27	0.710	4.74	0.100	2.59	0.054	5.93	1.46	97.93
dkf-gm-10	71.23	0.655	12.43	0.894	1.68	0.148	3.88	0.053	4.80	2.85	98.61
dkf-gm-11	67.06	0.495	14.45	1.130	3.10	0.138	3.73	0.061	5.18	2.20	97.54
dkf-gm-12	69.52	0.565	14.81	0.373	2.55	0.082	2.71	0.064	5.44	2.34	98.46
dkf-gm-13	71.65	0.693	11.36	0.931	1.19	0.144	4.10	0.062	4.49	3.09	97.71
dkf-gm-14	67.13	0.465	14.92	0.722	3.18	0.131	3.26	0.047	5.47	2.23	97.55
dkf-gm-15	70.63	0.630	13.15	0.483	1.91	0.107	3.30	0.049	5.00	2.73	98.00
average:	68.5198			0.715							

Group:	Nea Kameni	Samples:	groundmass of dkr-1940							
Age:	59 a									

Sample	SiO_2	TiO_2	Al_2O_3	MgO	CaO	MnO	FeO	BaO	Na_2O	K_2O	Total
dkr-gm-2	67.38	0.390	16.58	0.707	4.06	0.105	2.93	0.033	5.62	1.84	99.65
dkr-gm-3	71.58	0.576	13.24	0.653	1.81	0.113	3.25	0.053	4.76	2.68	98.71
dkr-gm-4	67.64	0.585	16.30	0.433	3.25	0.076	2.89	0.071	5.58	2.06	98.89
dkr-gm-5	65.03	0.344	18.49	0.293	4.09	0.056	2.21	0.028	6.31	1.48	98.33
dkr-gm-6	67.59	0.447	16.36	0.293	3.38	0.086	2.46	0.046	5.52	2.05	98.23
dkr-gm-7	65.87	1.661	15.02	0.258	2.58	0.138	6.92	0.046	5.43	2.04	99.96
dkr-gm-8	68.15	0.394	17.34	0.201	3.71	0.06	1.88	0.054	5.68	1.95	99.41
dkr-gm-9	69.90	0.498	15.04	0.437	2.72	0.09	2.78	0.047	5.25	2.30	99.06
dkr-gm-11	72.00	0.643	13.38	0.662	1.89	0.125	3.72	0.034	4.99	2.65	100.08
dkr-gm-12	70.73	0.482	14.83	0.340	2.53	0.097	2.63	0.043	5.28	2.42	99.38
dkr-gm-13	71.43	0.524	13.34	0.855	2.34	0.138	3.59	0.068	4.78	2.54	99.60
dkr-gm-14	66.79	0.459	17.19	0.432	3.72	0.097	2.70	0.051	5.90	1.78	99.12
dkr-gm-15	72.08	0.589	12.67	0.613	2.04	0.143	3.46	0.065	4.75	2.84	99.23
average:	68.94			0.475							

Group:	Nea Kameni	Samples:	groundmass of dkl-1950							
Age:	49 a									
Sample	SiO_2	TiO_2	Al_2O_3	MgO	CaO	MnO	FeO	BaO	Na_2O	K_2O	Total
dkl-gm-1	73.21	0.658	12.52	0.436	1.50	0.107	3.61	0.039	4.64	2.96	99.67
dkl-gm-2	67.98	0.468	17.19	0.225	3.77	0.074	2.32	0.046	5.42	1.98	99.47
dkl-gm-3	68.54	0.550	15.73	0.463	3.45	0.114	3.31	0.008	5.62	1.82	99.60
dkl-gm-4	70.88	0.611	14.02	0.602	2.36	0.134	3.48	0.049	4.83	2.57	99.52
dkl-gm-6	71.33	0.557	14.58	0.430	2.18	0.104	2.87	0.060	5.43	2.46	100.00
dkl-gm-7	73.15	0.680	12.34	0.389	1.18	0.106	3.26	0.046	4.60	3.04	98.79
dkl-gm-8	72.24	1.162	11.84	0.741	1.21	0.146	5.84	0.064	4.44	2.94	100.63
dkl-gm-10	70.44	0.709	13.57	0.525	2.49	0.126	3.76	0.030	5.02	2.62	99.28
dkl-gm-11	68.92	0.511	15.86	0.260	3.03	0.063	2.49	0.067	5.66	2.21	99.07
dkl-gm-13	71.56	0.643	13.14	0.521	1.84	0.119	3.26	0.064	4.83	2.79	98.76
dkl-gm-14	68.83	0.483	15.69	0.558	3.33	0.095	2.83	0.061	5.68	2.08	99.65
dkl-gm-15	71.98	0.717	11.97	0.225	1.15	0.095	3.09	0.066	4.37	3.15	96.82
average:	70.75			0.448							

Group:	Soufriere	Sample:	groundmass of STV354 of Heath et al. (1998)							
Age:	20 a									
Sample	SiO_2	TiO_2	Al_2O_3	MgO	CaO	MnO	FeO	BaO	Na_2O	K_2O	Total
STV-gm-1	51.49	0.042	29.77	0.059	13.16	0.006	0.676	0	4.13	0.062	99.39

Group:	Kameni	Samples:	rims of Kameni plagioclases to determine D_{Mg}							
Sample	SiO_2	TiO_2	Al_2O_3	MgO	CaO	MnO	FeO	BaO	Na_2O	K_2O	Total
dka-fsp-#1	55.82	0.027	27.42	0.039	10.09		0.402	0.024	5.60	0.168	99.58
dka-fsp-#2	57.35	0.017	26.50	0.034	9.12		0.393	0.015	6.20	0.212	99.84
dka-fsp-#5	55.58	0.042	27.36	0.049	10.20		0.432	0.022	5.62	0.179	99.48
dkl-fsp-#2	55.29	0.034	27.06	0.060	10.17		0.524	0.007	5.57	0.170	98.89
dkl-fsp-#3	56.05	0.038	26.74	0.052	9.86		0.488	0.027	5.80	0.175	99.22
dkl-fsp-#4	56.17	0.037	26.69	0.053	9.54		0.459	0.027	5.85	0.191	99.02
dkl-fsp-#5	54.66	0.027	27.29	0.057	10.48		0.482	0.034	5.47	0.166	98.67
dkr-fsp-#2	56.65	0.034	26.29	0.054	9.30		0.518	0.009	6.13	0.211	99.19
dkr-fsp-#3	56.48	0.033	26.62	0.046	9.39		0.497	0.043	6.02	0.194	99.32
dkr-fsp-#4	54.13	0.043	26.95	0.044	10.39		0.527	0.008	5.54	0.157	97.78
dkf-fsp-#1	54.48	0.039	26.82	0.041	10.11		0.544	0.000	5.68	0.171	97.89
dkf-fsp-#2	55.91	0.026	25.68	0.059	9.13		0.643	0.011	6.20	0.265	97.92
			average:	0.049							

Santorini and Soufriere, St. Vincent

Ion microprobe data

Group:	Palea Kameni		Sample:	feldspar crystal (1) from dka-726AD
Age:	1273 a		Traverse:	from core to rim
EMP point	2	5	9	13	17
µm	18	73	145	218	291
Li	16.25	16.68	21.85	14.16	10.47
Be	0.92	0.85	1.33	1.01	0.87
Mg	9.62	9.83	12.51	9.64	9.05
K	1147	1094	1688	1162	967
Ca	54212	55444	79337	63722	58562
Fe	1864	2133	2837	2238	1834
Rb	0.93	0.95	1.35	1.04	0.89
Sr	348.2	342.2	516.1	392.7	348.7
Y	0.266	0.258	0.452	0.318	0.286
Ba	107.1	97.0	158.9	109.6	81.8
La	3.35	2.93	5.19	3.72	3.19
Ce	4.72	4.14	7.21	5.16	4.33
Pr	0.393	0.394	0.730	0.506	0.398
Sm	0.174	0.161	0.275	0.191	0.121
Eu	1.12	1.01	1.71	1.32	1.06
Gd	0.107	0.069	0.456	0.157	0.178
Pb	2.00E+00	2.00E+00	2.00E+00	2.00E+00	2.00E+00
Th	1.42E-03	1.42E-03	1.42E-03	1.42E-03	1.42E-03
U	4.60E-04	4.60E-04	4.60E-04	4.60E-04	4.60E-04

Group:	Palea Kameni		Sample:	feldspar crystal (2) from dka-726AD
Age:	1273 a		Traverse:	from core to rim
EMP point	7	12	17	20
µm	76	140	204	242
Li	13.09	14.02	12.21	9.30
Be	0.83	0.88	0.84	0.82
Mg	9.52	8.54	9.06	9.15
K	859	1026	879	877
Ca	61911	55957	60950	61071
Fe	1963	1778	1979	1903
Rb	0.90	0.95	0.88	0.88
Sr	356.3	345.8	350.4	351.1
Y	0.302	0.279	0.291	0.289
Ba	81.2	92.0	80.9	77.1
La	3.08	3.34	3.07	2.98
Ce	4.52	4.60	4.45	4.30
Pr	0.387	0.378	0.427	0.390
Sm	0.189	0.217	0.176	0.247
Eu	1.04	1.08	1.06	1.09
Gd	0.192	0.118	0.078	
Pb	1.59E+00	1.59E+00	1.59E+00	1.59E+00
Th	1.22E-03	1.22E-03	1.22E-03	1.22E-03
U	5.93E-04	5.93E-04	5.93E-04	5.93E-04

Group:	Nea Kameni		**Sample:**	feldspar crystal (1) from dkf-1939
Age:	59-60 a		**Traverse:**	from core to rim
EMP point	1	5	11	14
µm	10	58	131	168
Li	8.48	8.18	8.44	7.83
Be	0.82	0.78	0.82	0.78
Mg	298.64	306.07	297.97	296.42
K	942	1017	1136	1068
Ca	58130	57542	53348	55201
Fe	2218	2283	2151	2196
Rb	0.95	1.03	0.98	1.01
Sr	364.9	376.1	355.8	354.4
Y	0.272	0.293	0.253	0.265
Ba	90.5	105.4	108.2	98.2
La	2.83	3.12	3.01	3.02
Ce	4.18	4.32	4.20	4.14
Pr	0.406	0.387	0.319	0.355
Sm	0.216	0.242	0.134	0.148
Eu	1.03	1.02	1.01	1.03
Gd	0.208	0.120	0.143	0.084
Pb	1.47E+00	1.47E+00	1.47E+00	1.47E+00
Th	8.89E-04	8.89E-04	8.89E-04	8.89E-04
U	7.11E-04	7.11E-04	7.11E-04	7.11E-04

Group:	Nea Kameni			**Sample:**	feldspar crystal (3) from dkf-1939	
Age:	59-60 a			**Traverse:**	from rim to rim	
EMP point	2	4	6	8	10	12
µm	39	116	193	270	347	424
Li	8.37	8.55	9.07	9.14	8.80	8.67
Be	0.86	0.80	0.82	0.83	0.79	0.81
Mg	301.70	305.90	301.15	296.85	287.90	302.70
K	952	890	994	1004	991	935
Ca	57989	59656	57127	56575	56929	58773
Fe	2018	2289	2094	2024	1967	2142
Rb	0.87	0.87	0.89	0.91	0.91	0.88
Sr	341.5	346.3	349.1	347.0	351.1	347.6
Y	0.262	0.251	0.259	0.254	0.274	0.266
Ba	76.4	69.8	86.8	77.1	74.5	77.1
La	2.52	2.26	2.68	2.70	2.78	2.55
Ce	3.56	3.45	3.82	3.77	3.90	3.67
Pr	0.284	0.277	0.337	0.373	0.373	0.371
Sm	0.125	0.127	0.195	0.135	0.120	0.112
Eu	0.88	0.93	0.91	0.91	1.00	0.89
Gd	0.050	0.000	0.100	0.134	0.182	0.074
Pb	1.25E+00	1.25E+00	1.25E+00	1.25E+00	1.25E+00	1.25E+00
Th	6.71E-04	6.71E-04	6.71E-04	6.71E-04	6.71E-04	6.71E-04
U	4.31E-04	4.31E-04	4.31E-04	4.31E-04	4.31E-04	4.31E-04

Group:	Nea Kameni		Sample:	feldspar crystal (3) from dkr-1940		
Age:	59-60 a		Traverse:	from rim to rim		
EMP point	2	4	6	8	10	12
µm	39	116	193	270	347	424
Li	8.37	8.55	9.07	9.14	8.80	8.67
Be	0.86	0.80	0.82	0.83	0.79	0.81
Mg	301.70	305.90	301.15	296.85	287.90	302.70
K	952	890	994	1004	991	935
Ca	57989	59656	57127	56575	56929	58773
Fe	2018	2289	2094	2024	1967	2142
Rb	0.87	0.87	0.89	0.91	0.91	0.88
Sr	341.5	346.3	349.1	347.0	351.1	347.6
Y	0.262	0.251	0.259	0.254	0.274	0.266
Ba	76.4	69.8	86.8	77.1	74.5	77.1
La	2.52	2.26	2.68	2.70	2.78	2.55
Ce	3.56	3.45	3.82	3.77	3.90	3.67
Pr	0.284	0.277	0.337	0.373	0.373	0.371
Sm	0.125	0.127	0.195	0.135	0.120	0.112
Eu	0.88	0.93	0.91	0.91	1.00	0.89
Gd	0.050	0.000	0.100	0.134	0.182	0.074
Pb	1.25E+00	1.25E+00	1.25E+00	1.25E+00	1.25E+00	1.25E+00
Th	6.71E-04	6.71E-04	6.71E-04	6.71E-04	6.71E-04	6.71E-04
U	4.31E-04	4.31E-04	4.31E-04	4.31E-04	4.31E-04	4.31E-04

Group:	Nea Kameni		Sample:	feldspar crystal (2) from dkr-1940		
Age:	59 a		Traverse:	from core to rim		
EMP point	10	8	7	5.2	5	4
µm	608	473	405	284	270	203
Li	8.81	9.15	8.72	8.93	7.28	7.43
Be	0.70	0.79	0.81	0.80	0.60	0.64
Mg	10.53	10.06	9.85	9.41	11.49	10.21
K	783	859	801	901	620	780
Ca	61814	59121	61013	57697	69257	64974
Fe	2182	2190	2012	1900	2202	2675
Rb	0.98	0.98	0.96	0.97	0.90	0.96
Sr	379.7	375.0	367.9	373.2	382.1	389.7
Y	0.250	0.258	0.301	0.270	0.271	0.224
Ba	88.9	87.3	79.5	74.4	58.3	53.6
La	2.72	2.93	2.90	3.18	2.12	1.76
Ce	3.83	4.08	4.32	4.37	3.27	2.71
Pr	0.333	0.323	0.385	0.391	0.295	0.277
Sm	0.161	0.176	0.206	0.214	0.197	0.173
Eu	0.88	0.96	0.89	0.90	0.90	0.72
Gd	0.174	0.136	0.160	0.160	0.119	0.063
Pb	1.34E+00	1.34E+00	1.34E+00	1.34E+00	1.34E+00	1.34E+00
Th	1.42E-03	1.42E-03	1.42E-03	1.42E-03	1.42E-03	1.42E-03
U	6.72E-04	6.72E-04	6.72E-04	6.72E-04	6.72E-04	6.72E-04

Group:	Nea Kameni	Sample:	feldspar crystal (1) from dkl-1950
Age:	49 a	Traverse:	from core to rim

	#1 (core)	#2	#3 (rim)
Li	8.29	8.32	7.36
Be	0.80	0.77	0.78
Mg	9.36	9.24	9.84
K	1254	1294	987
Ca	51251	50616	59943
Fe	1763	1756	2084
Rb	0.99	1.06	1.02
Sr	362.6	377.4	372.9
Y	0.220	0.215	0.319
Ba	90.6	135.7	92.7
La	2.96	3.36	3.04
Ce	4.27	4.54	4.32
Pr	0.389	0.403	0.402
Sm	0.202	0.197	0.164
Eu	1.08	1.19	1.06
Gd	0.059	0.119	0.144
Pb	2.04E+00	2.04E+00	2.04E+00
Th	1.24E-03	1.24E-03	1.24E-03
U	1.18E-03	1.18E-03	1.18E-03

Group:	Nea Kameni	Sample:	feldspar crystal (2) from dkl-1950
Age:	49 a	Traverse:	from core to rim

EMP point				1	4	8
µm	10	116	193	227	269	325
Li	5.17	2.26	1.62	2.89	2.43	1.72
Be	0.06	0.06	0.06	0.06	0.06	0.06
Mg	464.80	663.41	480.84	452.55	431.93	390.43
K	40	59	42	39	36	38
Ca	96044	95604	95604	96925	98600	98247
Fe	2602	3076	2659	2678	2691	2664
Rb	0.61	0.61	0.57	0.61	0.60	0.55
Sr	216.2	215.5	215.2	215.8	218.3	212.0
Y	0.041	0.107	0.051	0.052	0.053	0.056
Ba	5.4	6.1	5.7	5.8	5.8	4.8
La	0.17	0.21	0.18	0.20	0.23	0.15
Ce	0.23	0.27	0.25	0.28	0.35	0.28
Pr	0.028	0.039	0.026	0.035	0.054	0.036
Sm	0.029	0.014		0.015	0.013	0.015
Eu	0.12	0.10	0.10	0.10	0.12	0.09
Gd		0.072	0.038		0.048	0.007
Pb						
Th						
U						

Group:	Soufriere	Sample:	feldspar crystal (1) from STV354 of Heath et al. (1998)			
Age:	20 a	Traverse:	from core to rim			
EMP point	6	11	15	20	24	
µm	140	280	391	531	643	
Li						
Be						
Mg	437.84	498.25	338.72	424.36	408.15	
K	338	350	134	312	346	
Ca	66883	67592	92059	69660	65251	
Fe	2573	2847	3118	2692	2554	
Rb	0.677	0.702	0.690	0.738	0.673	
Sr	271.6	255.4	270.3	270.7	265.9	
Y	0.209	0.210	0.225	0.238	0.208	
Ba	23.4	20.4	14.1	23.2	24.4	
La	0.692	0.543	0.466	0.642	0.639	
Ce	1.20	1.00	0.99	1.28	1.23	
Pr	0.137	0.140	0.103	0.132	0.160	
Sm	0.130	0.097	0.084	0.278	0.134	
Eu	0.510	0.406	0.262	0.483	0.477	
Gd	0.092	0.099	0.070	0.156	0.141	
Pb						
Th						
U						

Group:	Soufriere	Sample:	feldspar crystal (2) from STV354 of Heath et al. (1998)			
Age:	20 a	Traverse:	from core to rim			
EMP point				1	3	6
µm	10	87	220	373	441	544
Li						
Be						
Mg	397.08	380.63	357.16	345.95	441.09	413.22
K	254	201	166	145	339	319
Ca	78463	85409	89412	93047	68719	70940
Fe	2716	2854	3050	3201	2765	2610
Rb	0.774	0.796	0.755	0.676	0.729	0.69
Sr	316.7	323.8	295.7	290.6	270.3	273.6
Y	0.179	0.171	0.268	0.204	0.179	0.246
Ba	19.4	17.0	15.6	11.8	23.0	23.3
La	1.048	0.974	0.709	0.497	0.611	0.68
Ce	1.59	1.70	1.27	0.83	1.10	1.30
Pr	0.173	0.163	0.129	0.116	0.104	0.151
Sm	0.069	0.167	0.039	0.086	0.063	0.099
Eu	0.460	0.443	0.443	0.227	0.295	0.54
Gd	0.114	0.042	0.048	0.145	0.138	0.003
Pb	8.50E-01	8.50E-01	8.50E-01	8.50E-01	8.50E-01	8.50E-01
Th	4.58E-04	4.58E-04	4.58E-04	4.58E-04	4.58E-04	4.58E-04
U	3.13E-04	3.13E-04	3.13E-04	3.13E-04	3.13E-04	3.13E-04

Group:	Soufriere	**Sample:**	feldspar crystal (3) from STV354 of Heath et al. (1998)			
Age:	20 a	**Traverse:**	from core to rim			
EMP point	2	9	18	27	29	
µm	25	198	420	643	692	
Li						
Be						
Mg	366.62	363.61	322.23	274.74	525.34	
K	34	33	39	35	55	
Ca	97623	97093	97977	98773	89223	
Fe	2731	2736	2648	2484	2831	
Rb	0.557	0.555	0.519	0.497	0.500	
Sr	205.9	202.9	200.5	186.1	176.7	
Y	0.082	0.064	0.064	0.066	0.087	
Ba	4.8	4.7	4.3	3.1	4.2	
La	0.119	0.106	0.102	0.085	0.088	
Ce	0.23	0.23	0.20	0.15	0.25	
Pr	0.030	0.027	0.031	0.024	0.029	
Sm	0.024	0.018	0.070	0.034	0.019	
Eu	0.087	0.067	0.091	0.084	0.094	
Gd	0.061	0.025	0.046		0.026	
Pb	3.19E-01	3.19E-01	3.19E-01	3.19E-01	3.19E-01	
Th	3.38E-04	3.38E-04	3.38E-04	3.38E-04	3.38E-04	
U	1.75E-04	1.75E-04	1.75E-04	1.75E-04	1.75E-04	

Group:	Nea Kameni		**Sample:**	pyroxene crystal (1) from dkf-1939	
Age:	59-60 a		**Traverse:**	from rim to rim	

	#1 (opx)	#2 (opx)	#3 (opx)	#4 (cpx)	#5 (cpx)	#6 (cpx)
Li	9.89	2.95	1.39	2.82	2.66	5.77
Be	0.040	0.041	0.061	0.220	0.168	0.178
K	0.634	0.629	0.865	2.99	1.77	1.40
Ca				146049	143443	144173
Fe	233892	212149	209405	94969	96126	99910
Sr	0.130	0.102	0.261	14.53	12.61	12.28
Y	9.00	7.87	15.76	61.0	54.2	57.7
Sn	0.290	0.195	0.698	1.80	1.03	1.09
Ba	0.005	0.005	0.028	0.061	0.026	0.043
La	0.022	0.018	0.065	3.47	3.03	2.99
Ce	0.112	0.097	0.386	14.16	12.45	13.05
Pr	0.031	0.034	0.122	2.91	2.61	2.71
Sm	0.252	0.174	0.473	8.09	7.02	7.27
Eu	0.074	0.056	0.157	1.85	1.48	1.57
Gd	0.532	0.614	1.24	10.58	9.60	10.45
Yb	2.47	1.80	3.44	7.32	6.51	7.12
Pb	8.29E-01	8.29E-01	8.29E-01			
Th	1.52E-03	1.52E-03	1.52E-03			
U	1.87E-03	1.87E-03	1.87E-03			

Group:	Nea Kameni		**Sample:**	clinopyroxene crystal (2) from dkf-1939
Age:	59-60 a		**Traverse:**	from rim to rim

EMP point	1.5	2.7	4.5
µm	23	77	158
Li	3.27	2.73	3.09
Be	0.192	0.179	0.181
K	2.51	2.37	1.48
Ca	142656	142656	142656
Fe	101005	97568	99338
Sr	11.77	11.66	12.29
Y	61.2	57.0	59.6
Sn	1.15	1.01	0.025
Ba	0.019	0.027	0.010
La	3.18	3.06	3.09
Ce	13.33	12.50	13.64
Pr	2.74	2.64	2.84
Sm	7.71	7.03	7.43
Eu	1.56	1.47	1.67
Gd	10.73	10.83	10.12
Yb	7.91	6.79	7.78
Pb	1.76E+00	1.76E+00	1.76E+00
Th	5.24E-02	5.24E-02	5.24E-02
U	1.69E-02	1.69E-02	1.69E-02

Group:	Nea Kameni		**Sample:**	clinopyroxene crystal (1) from dkr-1940			
Age:	59 a		**Traverse:**	from rim to rim			
EMP point	2	4	7.5	10	13	16	18	20
µm	22	65	140	194	259	324	367	410
Li	5.52	3.12	2.77	2.73	2.64	3.00	2.88	4.69
Be	0.175	0.175	0.182	0.171	0.170	0.209	0.186	0.188
K	1.98	2.46	1.45	4.17	1.57	1.37	1.70	2.20
Ca	142252	141228	140205	141228	140205	141228	140205	143275
Fe	96097	91082	95892	91798	93845	96915	98143	91082
Sr	12.49	13.00	12.18	12.08	11.97	12.49	11.97	13.41
Y	57.4	50.2	58.3	51.4	53.1	65.4	61.7	52.9
Sn	1.08	1.11	1.11	0.99	1.29	1.18	1.41	1.26
Ba	0.026	0.060	0.029	0.027	0.013	0.017	0.020	0.027
La	3.18	2.75	3.26	2.74	2.90	3.53	3.35	3.00
Ce	13.20	11.36	13.30	11.46	11.97	15.15	13.92	12.79
Pr	2.73	2.33	2.70	2.37	2.55	3.18	2.96	2.59
Sm	6.73	6.67	7.47	6.83	6.57	7.67	7.68	7.16
Eu	1.59	1.44	1.69	1.42	1.37	1.82	1.61	1.59
Gd	10.34	9.22	10.64	9.30	9.70	12.18	11.77	9.79
Yb	7.31	6.40	7.84	6.24	6.79	8.64	7.55	6.80
Pb	1.59E+00	1.59E+00	1.59E+00	1.59E+00	1.59E+00	1.59E+00	1.59E+00	1.59E+00
Th	3.45E-02	3.45E-02	3.45E-02	3.45E-02	3.45E-02	3.45E-02	3.45E-02	3.45E-02
U	1.11E-02	1.11E-02	1.11E-02	1.11E-02	1.11E-02	1.11E-02	1.11E-02	1.11E-02

Group:	Nea Kameni		**Sample:**	clinopyroxene crystal (1) from STV354 of		
Age:	59 a			Heath et al. (1998)		
			Traverse:	from core to rim		
	#1 (core)	#2	#3	#4	#5 (rim)	
Li						
Be						
K	1.98	6.94	1.32	15.13	1.36	
Ca	147444	147756	148173	144424	143383	
Fe	85717	84218	89008	91975	93975	
Sr	12.89	11.85	13.66	12.52	11.97	
Y	43.2	48.5	54.6	42.5	42.4	
Sn	1.46	0.95	2.01	1.31	0.97	
Ba	0.018	0.020	0.005	0.017	0.001	
La	1.71	1.75	1.73	1.06	1.04	
Ce	8.04	8.01	8.32	5.32	5.07	
Pr	1.80	2.00	1.96	1.28	1.26	
Sm	5.70	5.97	6.94	4.68	5.11	
Eu	1.18	1.33	1.74	1.38	1.37	
Gd	7.35	8.58	10.39	7.38	7.45	
Yb						
Pb	1.03E+00	1.03E+00	1.13E+00	1.13E+00	1.13E+00	
Th	1.43E-02	1.43E-02	1.27E-02	1.27E-02	1.27E-02	
U	6.08E-03	6.08E-03	7.97E-03	7.97E-03	7.97E-03	

Groundmasses for determination of partition coefficients

	Groundmass (next to crystal): dka (px-1)	dkf (px-1)	dkf (px-1)	dkf (px-1)	dkf (px-2)	dkr (px-1)
Li	19.75	21.13	27.04	23.21	26.22	13.54
Be	1.95	1.67	1.97	2.10	2.19	1.85
K	12563	15050	17.7	14920	15260	11124
Ca	19025	19065	10482	10501	10538	13604
Fe	25322	41412	30441	25250	40967	19227
Rb		53.3	66.0	56.1		
Sr	131	91.9	46.9	60.3	40.6	97.0
Y	32.1	40.3	40.4	32.7	36.8	26.3
Sn	9.28	8.06	10.51	9.91	9.05	6.81
Ba	368	356	372	346	311	428
La	22.4	25.6	25.2	20.2	21.8	19.2
Ce	43.9	54.5	51.6	40.9	44.0	37.5
Pr	5.17	6.42	5.89	4.88	5.12	4.32
Sm	4.73	6.12	6.17	4.42	5.40	3.70
Eu	1.08	0.76	1.01	0.95	0.91	0.49
Gd	6.33	7.17	7.55	5.91	6.78	4.39
Yb	5.41	6.82	5.85	4.76	5.67	3.95
Pb	46.8	32.3	35.1	29.9	35.0	46.1
Th	9.08	10.32	11.57	9.56	9.55	6.77
U	2.72	3.36	3.88	3.04	3.08	2.20

Groundmasses for determination of partition coefficients

	Groundmass (next to crystal): dkl (fsp-1)	dkl (fsp-1)	dkl (fsp-2)	dkl (px-2)	STV354	STV354	STV354
Li	24.1	24.9	25.8	22.0		13.0	7.61
Be	2.12	2.29	2.32	2.08		1.99	0.60
K	14322	16143	359	14126.7	4546	6582	3043
Ca	12030	8282	8766	11889	33057	27053	54785
Fe	44917	30829	28422	45320	55414	54991	27928
Rb	58.5	59.8	57.3	53.5	11.6	17.1	7.86
Sr	42.1	32.6	39.6	49.1	122	99.7	213
Y	45.2	40.8	35.6	37.2	26.0	33.8	13.8
Sn	10.10	10.28	9.15	9.17	4.29	6.22	2.15
Ba	352	342	330	305	125	166	91.1
La	15.9	24.6	21.5	21.4	6.73	8.54	4.06
Ce	56.0	50.7	43.0	44.2	16.4	22.3	9.86
Pr	6.77	5.97	5.02	5.17	2.30	3.24	1.46
Sm	6.78	6.14	5.29	5.26	3.43	4.28	1.59
Eu	0.85	0.87	0.86	0.88	1.03	1.25	0.75
Gd	8.15	7.49	6.76	5.61	4.25	6.72	2.83
Yb	6.73	5.57	4.93	5.60		4.46	2.12
Pb	33.8	41.5	40.4	31.3	10.4	13.9	6.73
Th	11.47	11.35	9.56	9.49	1.01	1.46	0.708
U	3.74	3.74	3.01	3.00	0.499	0.723	0.394

APPENDIX E

Trace element partition coefficients

In the following, partition coefficients between crystal rims and groundmass as determined by ion microprobe analysis are presented and compared with published data, thereby assessing the extend of crystal-groundmass equilibrium in terms of trace elements.

E1 Plagioclase partition coefficients

Plagioclase partition coefficients from Kameni dacite plagioclase rim - groundmass pairs are given in Figure E-1. For comparison, data from an andesite of Mt. Adams, Washington, are also given (Dun and Sen, 1994). In general, the data from the Kameni dacites are consistent with published values. Discrepancies for Pb, Th and U probably result from Pb contamination and melt inclusions in the mineral separates from Dun and Sen (1994). Due to background counts, which are significant at low concentration levels, ion microprobe partitioning data for U and Th in plagioclase are probably overestimates, i. e. maximum values. D_{Th} is constrained to less than 0.0002 and D_U to less than 0.0003 for plagioclases. All plagioclases have $40 < X_{An} < 50$, with the exception of dkl-fsp-2 which has $X_{An} > 90$ and is clearly not in equilibrium with the groundmass as indicated by consistently lower apparent partition coefficients.

Figure E-2 shows plagioclase partition coefficients of sample STV345 from Soufriere, St. Vincent, in comparison with the Kameni dacites. STV-fsp-1 ($60 < X_{An} < 85$) and STV-fsp-2 ($50 < X_{An} < 65$) show partition coefficients very similar to those of most Kameni dacite plagioclases. STV-fsp-3, however, with $X_{An} > 90$, is shifted towards dkl-fsp-2 and again clearly not in equilibrium with the groundmass.

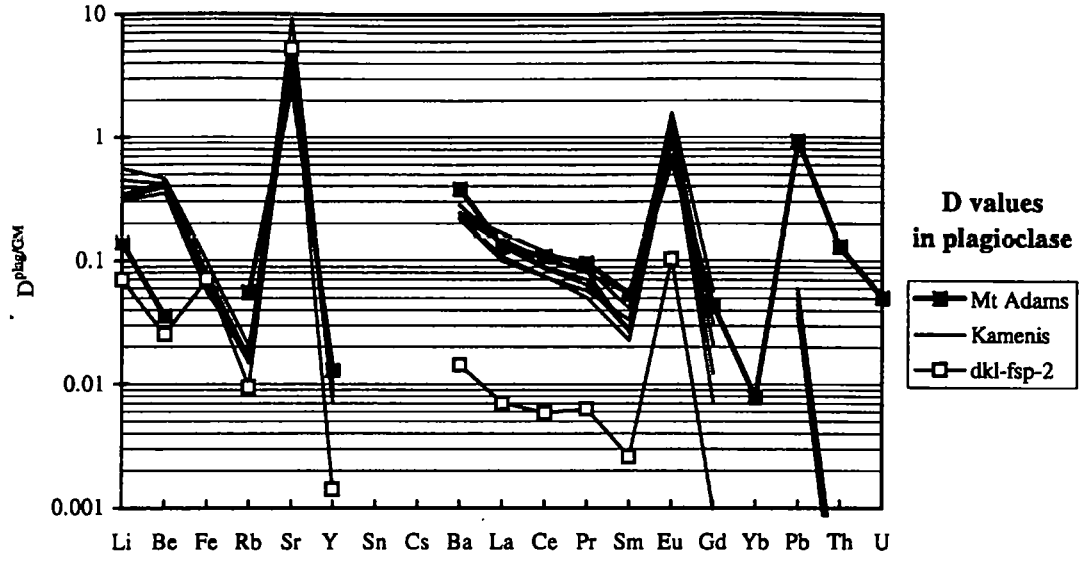

Figure E-1: Plagioclase partition coefficients for the Kameni island dacites

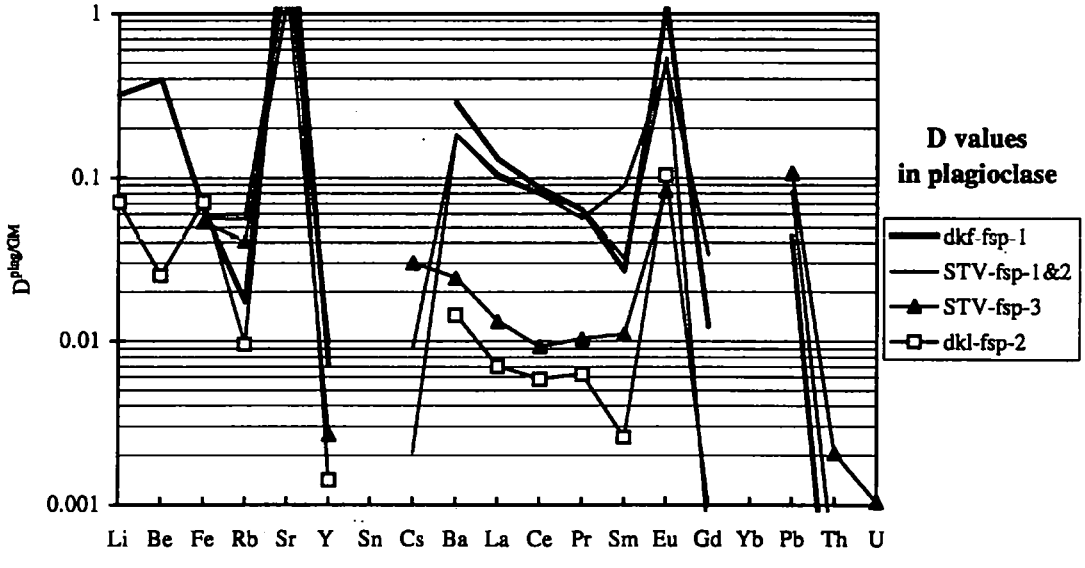

Figure E-2: Plagioclase partition coefficients for STV345 (Soufriere, St. Vincent, compared to the Kameni dacites

E2 Clinopyroxene partition coefficients

Clinopyroxene partition coefficients for all crystals analysed are shown in Figure E-3. There is no significant difference between cystals from the Kameni dacites and the crystal from Soufriere, St. Vincent. Partition coefficients lie between published data for basalts and lherzolites (Halliday et al., 1995) and those of rhyodacites, such as one from Twin Peaks, Utah (Nash and Crecroft, 1985), as expected from their andesitic to dacitic compositions. Data for Th and U is accurate to better than 10% and 15% (counting statistics) respectively, and background counts were <3% for Th and <5% for U.

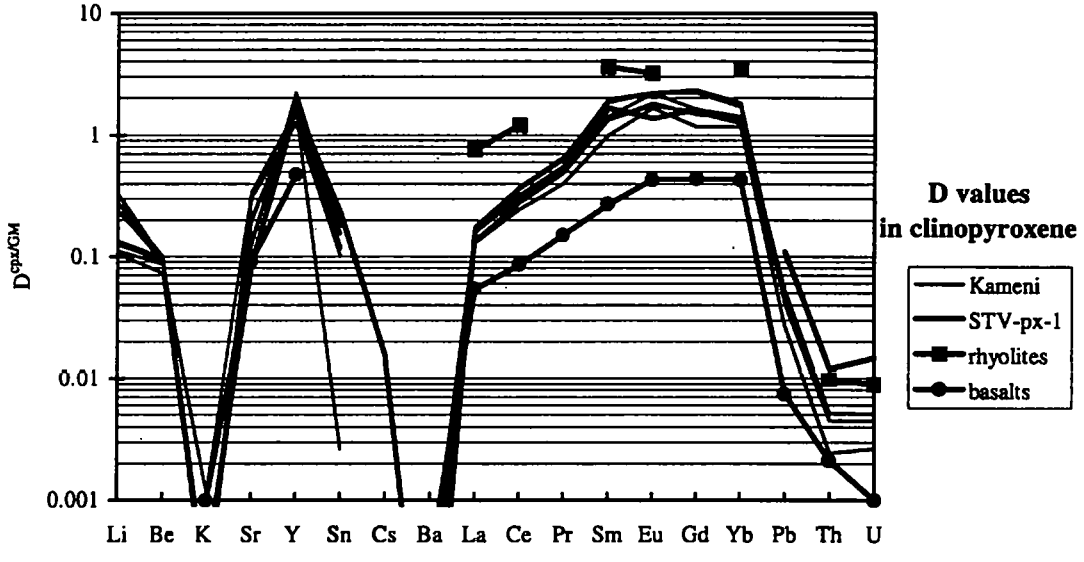

Figure E-3: Partition coefficients for clinopyroxene in the Kameni dacites and Soufriere, St. Vincent

E3 Orthopyroxene partition coefficients

Orthopyroxene partition coefficients for two Kameni dacites are shown in Figure E-4. Again, data are consistent with published data (Dun and Sen, 1994). D_{Th} and D_U are lower then 0.0003 and 0.001 respectively.

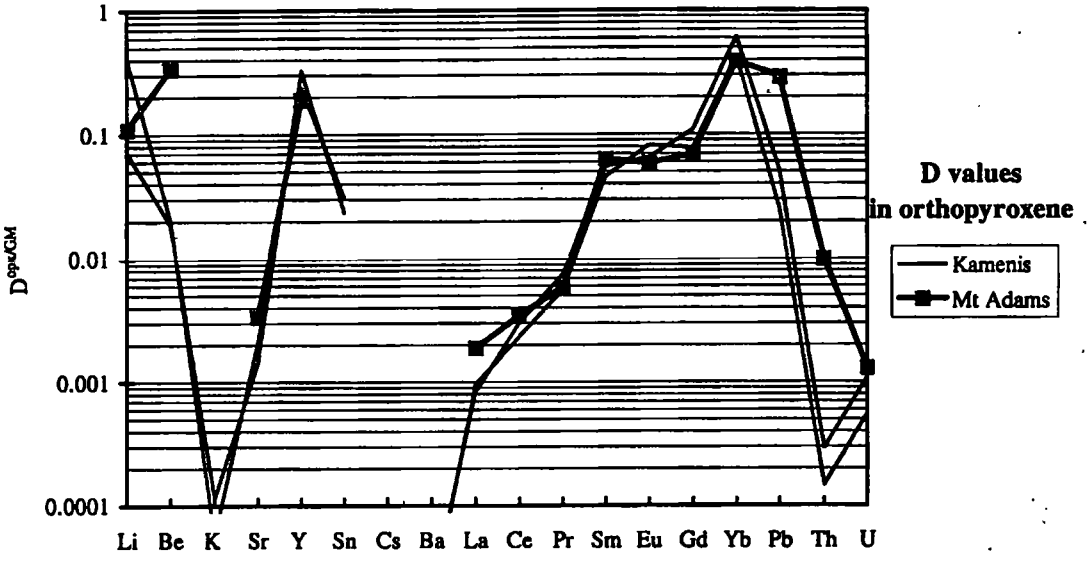

Figure E-4: Partition coefficients for orthopyroxene in the Kameni dacites